

Investigation of Key Parameters Affecting Ion-Capturing Abilities of Mixed-Ligand Protected Gold Nanoparticles

THÈSE N° 8105 (2017)

PRÉSENTÉE LE 18 DÉCEMBRE 2017

À LA FACULTÉ DES SCIENCES ET TECHNIQUES DE L'INGÉNIEUR

LABORATOIRE DES NANOMATÉRIAUX SUPRAMOLÉCULAIRES ET INTERFACES - CHAIRE CONSTELLIUM

PROGRAMME DOCTORAL EN SCIENCE ET GÉNIE DES MATÉRIAUX

ÉCOLE POLYTECHNIQUE FÉDÉRALE DE LAUSANNE

POUR L'OBTENTION DU GRADE DE DOCTEUR ÈS SCIENCES

PAR

Elif ERTEM BEKDEMIR

acceptée sur proposition du jury:

Dr L. Weber, président du jury
Prof. F. Stellacci, directeur de thèse
Prof. A. Fink, rapporteuse
Prof. F. Mancin, rapporteur
Prof. K. Severin, rapporteur



ÉCOLE POLYTECHNIQUE
FÉDÉRALE DE LAUSANNE

Suisse
2017

Learning never exhausts the mind

- Leonarda da Vinci

To my beloved family,

Dualariyla hayatta hep dimdik ayakta kalmami saglayan guzel annem, Lâle'ye
Davranislari ve öğretileriyle onurlu bir hayatın yolunu gosteren babam, Nejed'e
Yasadigimiz her seyi mutluluga donusturen, ellerimi hic birakmayan sevgili esim,
Ahmet'e

ACKNOWLEDGMENTS

Throughout the past five years of research at SUNMIL group, I had the overwhelming support of my advisor, my colleagues, and my relatives. Now, it is time to thank all of them since the results shown in this thesis would not exist without the guidance and encouragement from them.

First of all, I would like to express my sincere thanks to my supervisor, Prof. Francesco Stellacci, who gave me a chance to pursue my scientific enthusiasm in his laboratory. He tried to teach me how to become a good scientist by showing the proper ways of designing, and organizing the experiments to be able to reach a conclusion. His style of looking at things from completely different point of views made me amazed every time. He has been always kind and understanding, providing us a relaxed working environment.

I have been worked with brilliant people during my incredible journey at EPFL. Special thanks go to: Dr. Eun Seon Cho, who was the former PhD student initiating the project presented in this thesis. She also helped me to conduct the experiments presented in Chapter 5 of this thesis. I would like to state my sincere gratitude to Ahmet Bekdemir for his scientific advices and performing fractionation experiments as well as Zhi Luo who helped me with the MALDI-TOF experiments. A special mention goes to Prof. Paola Posocco for performing molecular simulations of our gold nanoparticles. I am grateful to Dr. Matej Janecek, who helped me to grammatically re-structure this thesis. In addition, he has been offering his valuable help all the time, showing his great curiosity and interest in scientific dialogue.

I have been also involved in different kinds of projects, whose results were not presented in this thesis due to mismatch of the research topics. However, I would like to thank here both my internal and external collobarators, whom I worked with within those interesting projects. A big thanks goes to Prof. Anna Roig, Dr. Nerea Murillo-Cremaes, Dr. Randy Patrick Carney, Dr. Anna Laromaine, Dr. Emma-Rose Janecek, Dr. Sergio Allegri, Dr. Qun Ren, and Dr. Beatrice Gutt for their excellent contributions and

guidance to obtain fruitful results from our projects. I have been very lucky to be part of these dynamic research teams.

I would like to express my appreciation to Dr. Quy Ong Khac, Dr. Paulo Jacob Silva, and Dr. Marta Diezcastellnou for sharing their valuable experiences with me, and giving me useful advises.

To the people of SUNMIL group, I have really prized our scientific discussions as much as the non-scientific ones. I was very lucky to be surrounded by brilliant people like you. We have a very friendly working environment, in which we have always been supported each other by all means. I really need to thank you all for the great time we spent together: Marta, Mauro, Javier, Juan José, Kislou, Kellen, Yun, Tam, Randy, Stefan, Sergio, Ahmet, Sam, Maria, Paulo, Marie, Anna, Alejandro, Rosie, Huayan, Pelin, Chiara, Nikos, Ozgun, Simone, Yulia, Matej, Bhadra, Pratap, Duc, Lina, Adam, Zhi, Evi, Quy, Ula, and Xiawong.

Chiara Donini has always been helpful and efficient to take care of my administrative problems. Thank you very much Chiara for helping me all these years!

A special thanks goes to my family for supporting me all the time to pursue my dreams. They never stop believing me, and stayed by my side no matter what I decide to do.

Finally, I would like to thank to my beloved husband, Ahmet Bekdemir. The actual motivation behind this work was his unconditional support, and love. You have been always very considerate and kind to me. Thank you for being in my life, and holding my hands all the time.

ABSTRACT

Over the past decades, there has been a dramatic change in the types and amounts of metal ions in the biosphere, since we have introduced huge amount of metal waste into our environment in the course of industrialization of our society. Most of the metal cations persist in ecological systems and in the food chain, exposing top-level predators. Therefore, there is a huge need to develop sensitive, cost-effective, portable, and rapid sensing systems for continuous monitoring of the metal ions in various aquatic environments.

The introduction of gold nanoparticles to the field of metal ion sensing has offered extensive opportunities to the design of miniaturized sensors with improved selectivity, limit of detection, signal-to-noise ratio, and response time. The ability to tune nanoparticles' properties by simple chemical modifications of their core or ligand shell was one of the key for their early successes in this field. In particular, the surface of gold nanoparticles (AuNPs) can be decorated with a wide range of organic ligands, which enables their selective interaction with a specific metal ion. A previous study from our group demonstrated that mixed-ligand coated gold nanoparticles in specific size and ligand compositions ranges were able to capture metal cations selectively.

The ultimate goal at this thesis was to develop an understanding of such mixed-ligand coated nanoparticles' binding to metal cations. To achieve this goal, the ion binding capability of mixed-ligand coated AuNPs were systematically studied for nanoparticles of different ligand shell composition, and core size of the nanoparticles. Our results revealed that the selectivity and the binding ability of the studied particles to the cation of interest (here Cd^{+2}) is strongly influenced by the parameter studies. We also found that the molecular conformation of the ligands for the particles in dry state has an unexpected and significant effect on the binding. In order to summarize the results obtained, a phase diagram was constructed. Understanding the concept behind the selectivity of our AuNPs in terms of ligand-shell conformation, which highly depends on the ligand composition and the size of AuNPs will enable researchers to develop selective sensors for detection of various metal ions.

Keywords: gold nanoparticles, mixed-ligand, metal ions, binding, sensors, phase diagram

RÉSUMÉ

Au cours des dernières décennies, il y a eu un changement radical dans les types et les quantités d'ions métalliques dans la biosphère, car nous avons introduit une énorme quantité de déchets métalliques dans notre environnement au cours de l'industrialisation de notre société. La plupart des cations métalliques persistent dans les systèmes écologiques et dans la chaîne alimentaire, en exposant les prédateurs de haut niveau. Par conséquent, il est grandement nécessaire de développer des systèmes sensibles, rentables, portables et rapides pour la surveillance continue des ions métalliques dans divers milieux aquatiques.

L'introduction de nanoparticules d'or dans le domaine de la détection des ions métalliques a offert des possibilités étendues à la conception de capteurs miniaturisés avec meilleure sélectivité, limite de détection, rapport signal sur bruit et temps de réponse. La capacité de modifier les propriétés des nanoparticules par des modifications chimiques simples de leur cœur ou de leur coquille de ligands a été l'une des clés de leurs premiers succès dans ce domaine. En particulier, la surface des nanoparticules d'or (AuNP) peut être décorée avec une large gamme de ligands organiques, ce qui permet leur interaction sélective avec un ion métallique spécifique. Une étude précédente de notre groupe a démontré que les nanoparticules d'or revêtues de ligands mixtes, dans des gammes spécifiques de taille et de composition des ligands, peuvent capter sélectivement les cations métalliques.

Le but ultime de cette thèse était de développer une compréhension de la liaison de ces nanoparticules revêtues de ligands mixtes aux cations métalliques. Pour atteindre cet objectif, la capacité de liaison aux ions des AuNP revêtues de ligands mixtes a été systématiquement étudiée pour des nanoparticules avec une différente composition de la coquille et une différente taille des cœurs. Nos résultats ont révélé que la sélectivité et la capacité de liaison des particules étudiées au cation d'intérêt (ici Cd^{+2}) sont fortement influencées par les paramètres étudiés. Nous avons également constaté que la conformation moléculaire des ligands pour les particules à l'état sec a un effet inattendu et significatif sur la liaison. Afin de résumer les résultats obtenus, un diagramme de phase

a été construit. Comprendre le concept de la sélectivité de nos AuNP en termes de la conformation de la coquille, qui dépend fortement de la composition des ligands et de la taille des AuNPs, permettra aux chercheurs de développer des capteurs sélectifs pour la détection de divers ions métalliques.

Mots-clés: nanoparticules d'or, ligands mixtes, ions métalliques, liaisons, capteurs, diagramme de phase

LIST of ABBREVIATIONS

2D	Two-dimensional
AuNPs	Gold nanoparticles
ATC	Automatic temperature compensation
ATR	Attenuated reflection mode
AES	Atomic emission spectroscopy
AAS	Atomic absorption spectroscopy
AFS	Atomic fluorescence spectroscopy
DGU	Density gradient ultracentrifugation
EPA	Environmental Protection Agency
FRET	Fluorescence Resonance Energy Transfer
FTIR	Fourier Transform Infrared Spectroscopy
LOL	Limit of linearity
LOD	Limit of detection
LOQ	Limit of quantification
ITC	Isothermal titration calorimetry experiments
MALDI	Matrix-assisted laser desorption/ionization
TOF-MS	Time of flight-mass spectroscopy
NAA	Neutron Activation Analysis
NLO	Nonlinear optical
NMR	Nuclear magnetic resonance
OEG	Ethylene glycol oligomers
PRET	Plasmonic resonance energy transfer
ROS	Reactive oxygen species
SAMs	Self-assembled monolayers

SERS	Raman scattering spectroscopy
TEM	Transmission electron microscopy
TGA	Thermogravimetric analysis
WHO	World health organization

Table of Contents

Acknowledgements	ii
Abstract	iv
Résumé	v
List of Abbreviations	vii
1 CHAPTER 1 : Introduction -1.....	1
1.1 Metal Ions in Biology	3
1.1.1 General Chemistry of Metal Ions in Aqueous Solutions	3
1.1.2 Importance of Metal Ions in Biology	5
1.1.3 Toxicity of Metal Ions	6
1.2 Metal Ions in Environment	9
1.2.1 Why is it crucial to check routinely the metal ion concentration in aquatic systems?	9
1.2.2 Conventional methods for routine monitoring of metal ion levels	11
1.3 Sensing Systems for Detection of Metal Ion Levels	16
1.4 Gold Nanoparticles as Sensing Probes	18
1.4.1 Detection of Mercuric Ions	19
1.4.2 Detection of Lead Ions	22
1.4.3 Detection of Cadmium Ions	24
1.4.4 Detection of Copper Ions	25
1.4.5 Detection of Other Hazardous Heavy Metal Ions	27
2 CHAPTER 2 : Introduction -2	30
2.1 Self-Assembled Monolayers (SAMs) on Gold Nanoparticles	30
2.2 Structure of Mixed Composition SAMs on Highly Curved Gold Surfaces	32
2.3 Host-Guest Interactions in Solution	35
2.3.1 Concept of Complexation and Lock-Key Analogy	35
2.3.2 Factors that Promote Thermodynamical Selectivity by Stabilizing the Metal-Ligand Complex	37
2.3.3 Tunable Binding Ability of Crown Ethers Towards Metal Ions	40
2.4 General Scope of the Work	42
2.4.1 Previous Work Conducted by Our Group	42
2.4.2 Theoretical Explanation for Ion-Capturing by Striped AuNPs	45
2.5 The Motivation and the Aim of Our Study	46
REFERENCES	48
3 CHAPTER 3 : Synthesis and Characterization of Mixed-Ligand Coated Gold Nanoparticles	57
3.1 Synthesis and Purification of Mixed Ligand Coated Gold Nanoparticles	57

3.2	Characterization of Mixed Ligand Coated Gold Nanoparticles	68
3.2.1	<i>Ligand-Shell Composition Determination</i>	69
3.2.2	<i>Size Distribution Analysis</i>	71
3.2.3	<i>Constructing 2-D Map of Size and Ligand Ratio for the Synthesized AuNPs</i>	72
3.2.4	<i>Thermogravimetric Analysis (TGA) and Ligand Density Calculations</i>	75
3.2.5	<i>Fourier Transform Infrared (FT-IR) Spectrometry to Probe Conformation of EG2 Ligands on the Surface of AuNPs</i>	81
3.2.5.1	Basic Principles of FTIR	81
3.2.5.2	Structural Studies of Oligo(Ethylene Glycol) Terminated Self-Assembled Monolayers on Gold Surfaces	83
3.2.5.3	Solid-State Spectroscopic Characterization of EG2:HT Protected AuNPs	87
3.2.5.4	Analysis and categorization of FTIR spectra	89
3.2.5.5	Aqueous-State Spectroscopic Characterization of EG2:HT AuNPs by ATR mode	94
3.3	Comparison of Sum-of-Squares Residual (SSR) Values of Synthesized AuNPs	95
3.4	Molecular Simulations of Synthesized AuNPs	97
3.5	Evaluations and Comparisons of the Results Obtained from Solid-State FTIR, SSR Values, and Molecular Simulations	101
	REFERENCES	102
4	CHAPTER 4 : Investigation of Metal Ion Binding Abilities by Mixed-Ligand Protected AuNPs	105
4.1	Conductometric Titrations to Inspect Ion-Binding Abilities of Synthesized AuNPs	105
4.1.1	<i>Fundamentals of Conductometry and Its Applications in the Complexation Studies</i>	106
4.1.2	<i>Experimental Design of Conductometric Tests</i>	109
4.1.3	<i>Experimental Results of Conductometric Tests</i>	110
4.1.4	<i>Interpretation of the Results Acquired from Conductivity Tests</i>	111
4.1.5	<i>Investigation of Selectivity Profiles of Each Regime by Conductivity Tests</i>	114
4.2	Isothermal Titration Calorimetry (ITC) Experiments - Determination of Association Constants Between AuNPs and Metal Ions	116
4.3	Fourier Transform Infrared (FTIR) spectrometry - Investigation of Conformational Changes After Cd ²⁺ Binding	118
4.4	Correlation Between Surface Properties of EG2 Ligands and Binding Abilities	120
	REFERENCES	122
5	CHAPTER 5 : Ion-Binding Properties of EG3:HT Protected AuNPs Fractionated by Their Size	123
5.1	Working Principle of Fractionation	123

5.2	Experimental Details	124
5.3	Results and Discussion on Ion-Binding Properties of EG3:HT Protected AuNPs	126
REFERENCES		130
6	CHAPTER 6 : Conclusion and Future Work	131
6.1	Conclusion	131
6.2	Future Work	133
6.2.1	<i>Applicability of the AuNPs to the Real-World Systems</i>	<i>134</i>
REFERENCES		136
7	APPENDIX :	137
A.1	NMR Spectra of EG2-n AuNPs	137
A.2	Representative TEM images and size distributions of EG2-n AuNPs.....	141
A.3	FTIR Spectra of EG2-n AuNPs.....	149
A.4	Conductivity Plots of EG2-n AuNPs	160

CHAPTER 1

Introduction-1

We are reminded of our metal-rich environment each time we taste our salty tears, or instinctively lift a cut finger to our mouths recognizing the metallic taste of our blood. Natural evolution has integrated many metal ions into critical biological functions in our body. While some of metal ions are simply toxic like, cadmium, others like, copper and zinc, are both essential and toxic. The toxicity effect of essential metal ions cannot be grasped well without the statement of Paracelsus, the father of the toxicology, as “Everything is poisonous, and nothing is not; only the dose ensures that something is not poisonous.” Therefore, the concentration of metal ions that we are exposed to throughout our daily life is important for the sake of our healthy body functioning. On the other hand, metals are vital for humans not only physiologically, but also economically, as they play crucial roles in the improvement of civilizations. Over the past decades, there has been a dramatic increase in the types and amounts of existing metal ions in the biosphere since we have introduced huge amount of metal waste into our environment in the course of industrialization. Thus, there is a huge requirement to develop sensitive, cost-effective, portable, and rapid sensing systems for monitoring of these metal ions in various aquatic environments.

The introduction of nanostructured materials such as noble metal nanoparticles to the field of metal ions sensing has offered extensive opportunities to the design of miniaturized sensors with enhanced sensitivity and selectivity. Among various nanomaterials, gold nanoparticles (AuNPs) represent an excellent scaffold for the fabrication of metal ion-sensors due to their ease of synthesis, modification, stabilization, and distinctive physical and optical properties. Previous study of our group¹ revealed that mixed-ligand coated AuNPs of specific size and ligand composition can be of great utility by creating new recognition processes, and thus being able to capture metal cations selectively and sensitively.

The present study is a continuation of our previous work. The ion-binding capabilities of AuNPs are investigated by shining light on the role of ligand composition, size of the NPs and the resulting conformation of self-assembled monolayers (SAMs).

The significance of the study conducted in this thesis cannot be appreciated without knowing the background information presented in **Chapter 1** and **2**. Firstly, **Chapter 1** introduces to the reader the role and the importance of metal ions in our body. Secondly, it provides background to understanding of the toxicity of these ions. The advantages and disadvantages of conventional techniques used to determine the metal ion concentrations in aquatic medium are outlined. A comprehensive literature review of the current state-of-the-art of AuNP based metal ion sensing systems is presented.

1.1 Metal Ions in Biology

1.1.1 General Chemistry of Metal Ions in Aqueous Solutions

The ionization energies of all elements are positive, which means that the formation of cations in gaseous form is not an energetically favorable process.²



First ionization energies of the elements range from 90 kcal mol⁻¹ for Cesium, up to 567 kcal mol⁻¹ for Helium. Metals are elements with lower ionization energies so that they are more likely to form positive ions.^{2,3} When a metal is transferred into a solution, solvation of the metal ion (Mⁿ⁺) can offset the unfavourability of the gas phase ionization process to a greater or lesser extent. From toxicological or biological viewpoint, the environment of a metal cation in aqueous solution is important³, and can be roughly divided into several layers as depicted in **Fig.1.1**.²

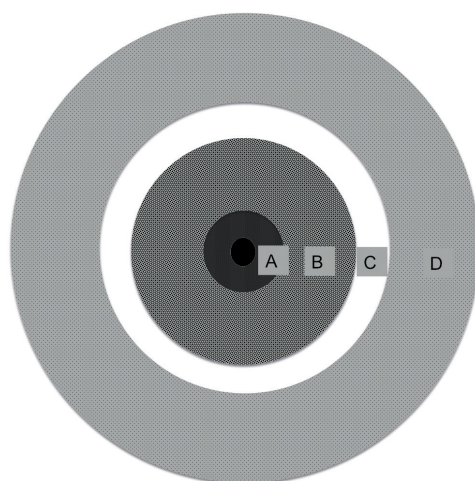


Figure 1.1: The metal ion environment in water. The black sphere is metal cation; **A)** primary water; **B)** secondary water; **C)** disordered water; **D)** bulk water. This model only applies fully in very dilute solutions (lower than 0.1 M for a 1:1 electrolyte).

Fig.1.1.A represents the first hydration shell of the metal cation. This contains water molecules directly interacting or bonding with the cation.² The secondary hydration shell is shown in **Fig.1.1.B**. In this shell, the cation has an influence on the order of water molecules. Electron-withdrawing effect of the cation on tightly bound water molecules in first solvation shell encourages them to make hydrogen bonding with secondary water of hydration.^{2,3} The volume of secondary solvation shell is highly affected by the charge and the size of the metal ion, being large for small ions of high charge and small or negligible for large ions of low charge.²

Fig.1.1.C depicts a disordered zone, separating the ordered region of **Fig.1.1.A** and **Fig.1.1.B** from differently ordered region of **Fig.1.1.D**. The extent of this zone can vary depending on the charge density of the metal ion.²

Bulk water can be assigned to the region shown in **Fig.1.1.D**. The scenario depicted in **Fig.1.1** can only be applied to very dilute solutions where there are sufficient water molecules to surround each cation. The existence of the anion is ignored in the case of the dissolution of ionic salt since it is possible to treat the cation as isolated in dilute conditions. When the concentration of the ionic salt increases, there comes a time when the interaction between cation-anion can no longer be ignored. In that case, anion may enter the primary hydration shell of the cation.^{2,3}

The zones depicted in **Fig 1.1.B, C, and D** can fuse undetectably into each other. This also may be true for the zones shown in **Fig.1.1.A**, and **B**, but a differentiation between these two regions can be made. For metal ions of high charge density, the rate of exchange of water molecules between region demonstrated in **Fig.1.1.A**, and the other regions is sufficiently slow for a real physical distinction to be possible, for example by the use of NMR spectroscopy.^{2,3}

In non-aqueous polar solvents, such as methanol, ethanol, or formamide, the typical picture of **Fig.1.1** still applies. Since non-aqueous solvents are much less structured than water, the distinctions between the properties of bulk solvent, and those of hydration shell zones will be less important.²

1.1.2 Importance of Metal Ions in Biology

Since most biological molecules, such as DNA and proteins, are electron rich, there is a tendency of metal cations for biological molecules. In light of this information, it is not surprising that natural evolution has integrated many metals into critical biological functions.^{4,5}

There are ten essential metals in human body, which perform a broad variety of tasks.⁶ The deficiency of an *essential metal* results in abnormalities in biological functions and it can be relieved *only* by supplementing that metal ion.^{4,6,7} The rest of the metals, which are not at all vital for proper functioning of the human body are called **non-essential metals**.⁸

Four of the essential metals, potassium, sodium, calcium and magnesium contribute almost 99% of the metal ion content of the human body. Therefore, they can be considered as '**bulk elements**'.⁹ Copper, cobalt, zinc, iron, manganese, and molybdenum are the other six metals that are crucial for human life, yet their abundance is much lower than the bulk elements, so they are called '**trace elements**'.⁹

The function of metal ions is regulated evolutionary depending on their properties. Mobility and strength of binding of the metal ions to organic ligands are two main factors that determine their main tasks in human body.⁹ **Table 1.1** shows the correlation between mobility, ligand-binding affinity, and biological functions of essential metals.^{8,9}

Metal Ions	Mobility	Binding Strength	Biological Function
Na ⁺ , K ⁺	High	Weak	As charge carriers; they ensure the maintenance of cellular osmotic balance, signal transduction and neurotransmission by generating ionic gradients across biological membranes.
Mg ²⁺ , Ca ²⁺	Semi-mobile	Moderate	Mg ²⁺ has structural & catalytic roles in phosphoryl transfer & hydrolysis reactions as an enzyme co-factor, it stabilizes polyphosphate compounds within the cell, and binds to ATP (adenosine tri-phosphate) to activate it. Ca ²⁺ act as a messenger in cascade signaling reactions within the cell, and is present within the biominerals that constitute bone and teeth.
Zn ²⁺	Moderate	Strong	Zinc plays prominent catalytic and structural roles in enzymes. In addition, as a Lewis acid; it organizes the tertiary structure of nucleic acid binding proteins via the structural motifs known as 'zinc fingers'.
Co, Cu, Fe, Mn, Mo*	Low	Strong	They participate in a wide range of oxidation and reduction reactions. Fe, Cu also play an important role in oxygen-binding proteins involved in oxygen activation, as well as in oxygen transport and storage .
<ul style="list-style-type: none"> • Charge is not given, varies with oxidation state. 			

Table 1.1: Relationship between mobility, strength of ligand-binding, and general biological roles of essential metals ^{7,8}

1.1.3 Toxicity of Metal Ions

Metal ions, essential for human body, like zinc and iron, as well as the non-essential metals, like mercury, cadmium and lead, may exert toxic effects if the dose of consumption or exposure exceeds certain levels. ^{7,8,10}

For both the essential and the non-essential metals, **Fig.1.2** envisages the relationship between the metal concentration and the physiological response. ^{7,11} There are concentration ranges that allow the optimum physiological response, whilst concentrations above and below this range are detrimental to life. These concentration levels are referred to 'critical levels'. The concentration levels labeled as **A**, **B** and **C** in **Fig.1.2.A and B** can be assigned to critical levels. ^{7,11}

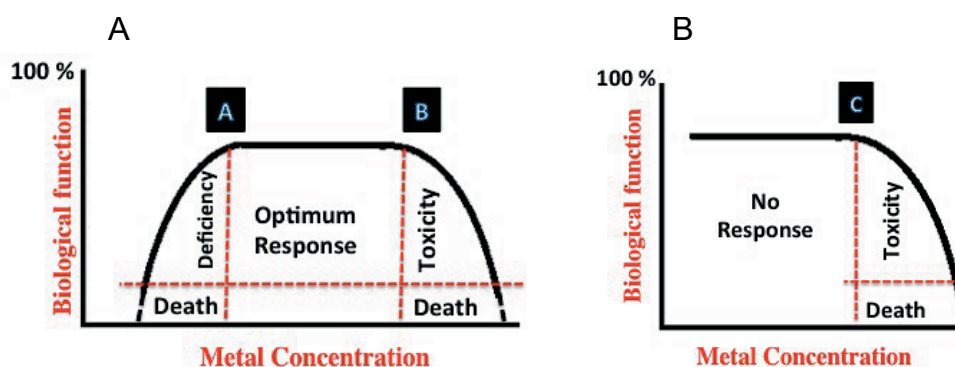


Figure 1.2: Dose-response relationships for (A) essential and (B) nonessential elements.

Although all essential metals follow a general trend in terms of their toxicity effects, which is shown in **Fig.1.2.A**, the critical levels of the metal ions vary largely depending on their functions.¹² **Table 1.2** shows the estimated concentration levels of essential metals in human body that helps to understand how the abundance of an essential metal ions change with respect to type of the metal ion.⁷ The origin of the toxicity of an essential metal is the shift from physiological equilibrium state concentrations to a condition of excess caused by an environmental or other factors.⁷

For instance, acute overexposure to cobalt leads to toxicity and the severe consequences were observed in the 1960s among heavy beer drinkers (15–30 beers per day), when Co^{2+} salts were utilized in beers as foam stabilizers, resulting in severe and often lethal cardiomyopathy.⁸ Another example is manganese; it is highly neurotoxic in large doses. Since neurons are more vulnerable than other cells to manganese-induced toxicity, manganese tends to accumulate in the brain resulting in the condition known as manganism. It is first spotted in miners during the 19th century who showed Parkinson’s disease-like symptoms.^{8,10} **Fig.1.2.B** describes the response of the body against the non-essential metal ions. Among them, there are highly toxic heavy metals (metals with specific density more than 5 g/cm^3) like lead (**Pb**), cadmium (**Cd**), mercury (**Hg**), arsenic (**As**) and chromium (**Cr**) for which the critical level “C” is lower than critical level “B” in **Fig. 1.2**.^{10,12–15} These metals have a tendency to form complexes with bio-macromolecules containing sulfur, nitrogen, and oxygen such as enzymes, nuclear proteins or DNA.¹⁶

Metal Ions	The Predominant Elemental Form at pH 7 *	Serum Concentration	Recommended Daily Intake
Na	Na ⁺	140 mM	1-2 g
K	K ⁺	4 mM	2-5 g
Mg	Mg ²⁺	0.8 mM	0.3 g
Ca	Ca ²⁺	2.4 mM	0.8 g
Zn	Zn ²⁺	14 μM	15 mg
Co	Co ²⁺	2 nM	3 μg vitamin B12
Cu	Cu ²⁺	17 μM	3 mg
Fe	Fe(OH) ₃	17 μM	10-20 mg
Mn	Mn ²⁺	10 nM	3 mg
Mo	MoO ₄ ²⁻	6 nM	0.2 mg

* Many of the elements do not exist as their predominant elemental form in the serum since they may bind to other entities. For instance, Fe³⁺ does not precipitate as the hydroxide but is retained by tightly chelating ligands.

Table 1.2: Approximate concentrations of essential metal ions found in a 70 kg adult.⁶

As a consequence, the bio-chemical life cycle of the cells is distorted due to enzyme inhibition, protein structure alteration or hydrogen bond rupture.^{12,15,16} For example, cadmium ions inhibit enzymes that are involved in repairing errors that produce DNA mismatches.^{12,15} These mutations in genes get amplified due to lack of that enzyme, resulting in cancer. Another important mechanism of the carcinogenic and toxic outcomes of heavy metals such as those affecting the central nervous system (**Hg²⁺**, **Pb²⁺**, **As³⁺**); liver or the kidneys (**Cd²⁺**, **Hg²⁺**, **Pb²⁺**); bones, skin, or teeth (**Cd²⁺**, **Cr³⁺**) is reactive oxygen species (ROS) production and oxidative stress.¹⁶ Unlike the other metals heavy metals get excreted gradually through liver, kidney or spleen due to strong interaction of these metals with metallothioneins (a family of cysteine-rich proteins).¹⁵

1.2 Metal Ions in Environment

1.2.1 Why is it crucial to check routinely the metal ion concentration in aquatic systems?

Being natural elements, metal ions are ubiquitous in the environment. The concentration levels of the metal ions in various parts of the ecosystem can be changed by natural means such as weathering of the earth's crust, volcanic eruptions, soil erosion etc.¹³ However, in recent times, there has been a great disturbance of the natural levels of metal ions mostly due to anthropogenic activities. Because of the exponential increase in the consumption of metals in numerous industrial, domestic, agricultural, and technological applications, metal ions have become significant environmental pollutants.^{10,13} Mercury, arsenic, cadmium, chromium, and lead rank among the prime metals of public health significance due to their critical concentration levels, which are



Figure 1.3: One of the victims of itai-itai disease. (1 September 2017) Retrieved from <http://2009.igem.org/Team:Cornell/Project/Background>

lower than that of other metals and as such exhibit serious toxicity.^{8,12,13} Since these metals are not biodegradable, when the free or complexed forms of them find their way into fresh and marine waters, including underground water, they accumulate in the biosphere exposing top-level predators to high levels of pollution.¹⁶ For example, in 1950's, the residents of the Jinzu River basin in Toyama territory, Japan were exposed to a serious form of cadmium poisoning due to consumption of the crops, especially rice, irrigated by cadmium polluted water over a period of many years.^{13,17} The point source of the pollution was found to be a zinc mine located in the upper part of the Jinzu River. Bone softening leading to easy fracturing (72 fractures in one victim) and kidney failure was the most serious consequences of the disease, which is called as **itai-itai disease**.^{8,12,13,17} One of the victims of the disease (**Fig.1.3**) shows how serious the skeletal deformities were. Unfortunately, disposal of cadmium and

cadmium containing products into the world ecosystem (18,400 tons in 2003; 20,400 tons in 2007) has progressively increased due to heavy utilization of cadmium in the industrialized world.¹⁷

Another severe example is mercury poisoning of the local people living near Minamata city in southern Japan in 1956.⁸ The primary cause of the disease was the dumping of industrial wastewater contaminated with methylmercury by a chemical manufacturer to Minamata Bay. Then, methylmercury accumulated in aquatic food chain, reaching its highest concentrations in fish and shellfish, which when eaten by the local people lead to mercury poisoning.^{8,17} There were officially 2265 victims, of which 1784 passed away, suffered from neurological symptoms like loss of field of vision, hearing and talking abilities, and overall muscle weakness.¹⁷ In the rural areas of Iraq in 1971 to 1972, consumption for 2-3 months of bread made from seed wheat treated with mercury positive fungicide caused more than 6500 hospital admissions and 500 deaths.⁸ Today, methylmercury is predominantly found in aquatic sediments and soils as a result of the methylation of inorganic mercury.¹⁷ It is very dangerous since it is easily absorbed from the diet and within a few days spreads throughout the body. It is mainly present in the body as a water-soluble complex with L-cysteine, and it can therefore easily cross the blood-brain barrier, targeting the central nervous system.¹⁷ As the industrialization of our society progressed, there have been several other chronic and acute poisoning cases due to increased levels of both essential and non-essential metals.¹⁵ The introduction of huge amounts of metals into the environment has raised a lot of questions among the public. Hence, Environmental Protection Agency (EPA) and World Health Organization (WHO) have defined safe concentration limits of highly toxic heavy metals in drinking water.^{10,12} **Table 1.3** demonstrates the typical concentrations within the safe limits for heavy metals of primary concern.

Bearing in mind that postponement in detection and evaluation of these metal ion contaminants in aquatic environments has been the cause of several serious health problems for living organisms,^{14,15,18} especially for humans, there is an immense necessity to monitor the metal ion concentrations in water bodies.

Metals	WHO (mg/L)	EPA (mg/L)
Ni	0.07	0.04
Cu	2	1.3
Zn	3	5
Cd	0.003	0.005
Hg	0.001	0.002
Pb	0.010	0.015
As	0.010	0.010

Table 1.3: Safe concentration limits for heavy metals in drinking water suggested by WHO and EPA^{9,12}

1.2.2 Conventional methods for routine monitoring of metal ion levels

Today, the main challenge in analytical chemistry is to develop accurate, precise, rapid, and cost effective techniques for routine analysis of various metal ions in aqueous environments with mass fractions of around 10^{-11} (0.01 ppb) or below.^{19,20} Analysis of metal ions at trace levels involves a degree of sophistication, depending on the metal ion of interest, the matrix, and the concentration level.²¹ Many instrumental analytical methods now exist for trace analysis.^{19,20,22} However, these methods may suffer from bias with respect to each other and to the true value.¹⁹ To understand the potentials and limitations of these methodologies, it is crucial to consider what analytical techniques are available to the researchers.

The most prevalent analytical methods have shown to be applicable in trace level analysis of various metal ions in a variety of matrices can be divided into four main categories.^{19,23}

(I) Electrochemical Methods: *Potentiometry* and *stripping voltammetry* are two main electrochemical techniques that have seen significant development in trace metal analysis within the last few years.²³

The principle of **Potentiometric sensors** is based on monitoring the changes in the equilibrium voltage between two electrodes while the electric current between the

electrodes is maintained under an almost zero-current condition.^{19,23,24} Depending on the activity of the ion of interest, equilibrium potential of the indicator electrode changes as a Nernstian function:^{19,23}

$$E_{\text{ISE}} = E^0 + (RT / zF) \ln \alpha_{\text{M (aq)}}$$

E_{ISE} is the interfacial potential of the electrochemical cell at zero current, E^0 is the standard cell potential; T , R and F are absolute temperature, the gas constant and the Faraday constant, respectively; α is the ion activity of the target metal M that has charge z . It is important to understand that the activity of the ion describes the *concentration of uncomplexed or free analyte*, which can be orders of magnitude smaller than the total concentration.^{19,23,24} Most commonly utilized indicator electrodes (ISEs) possess ion-selective membranes whose electrical potential provides an analytical response that is highly specific to the measured ion. In order to ensure getting specific analytical response, the membranes are doped with either sensing components such as ionophores that can selectively chelate with the analyte or with ion exchanger moieties that attract a fixed concentration of analyte and conserve charge balance into the membrane phase.²³

ISEs have been used for detection of more than 60 ions so far and they have been well established for clinical evaluation of electrolytic ions such as Na^+ , K^+ , Mg^{2+} , Ca^{2+} , and Cl^- in blood or plasma with micro-molar (μM) range detection limits.²³ Since Pb^{2+} selective electrodes with picomolar (pM) detection limit has been reported by Ceresa et al. in 2001, there has been significant development in trace analysis.^{23,25} However, there is still a huge room for the improvement because the presence of interfering ions becomes more pronounced at trace analyte levels. Interfering ions in solutions can be either present at high concentration, or have a high affinity to the indicator electrode, which results in a significant positive bias on measurement results.^{19,23}

The variety of ISEs with low detection limits needs to be expanded either by use of novel ion-selective materials (ionophores), effective electrode design and robust calibration of the systems. In addition, since the technique allows us to detect free metal ions, environmental samples should be pre-treated (etc. buffering to low pHs) to ensure that all metal ions are uncomplexed, and therefore it might result in a lengthy protocol. On

the other hand, the system is highly cost effective and suitable for miniaturization, which can be utilized in very small sample volumes.^{19,23,24}

Stripping voltammetry is another common electrochemical technique for trace metal analysis that is based on the redox behavior of the analyte on the electrode.²⁴ It is a two-stage technique in which the first stage is the accumulation of a chemical species on the surface of the electrode at a constant potential by either a faradaic (cathodic or anodic) or non-faradaic (absorptive) manner.^{19,23} In the second step, the voltage is varied in a systematic manner, which results in stripping (electrolytic dissolution) of electro-active species back into the solution at distinctive potentials. The current-potential profiles at electrode surface are measured at each stripping step and the follow-on current is proportional to the concentration of the analyte of interest.¹⁹

Mercury electrodes that can be configured as either a hanging drop or a thin film have been extensively used in the area. The technique uses the advantage of amalgam formation, therefore; trace level analysis of many metal ions such as lead ions is possible at sub-ppb level.¹⁹ However, these techniques require high safety precautions regarding recovery of the mercury element after each experiment. In addition, the accumulation in the first step is time consuming when very low element concentrations is concerned since long accumulation times are needed to build up enough material at the electrode to be accurately measured.¹⁹

The range of detectable elements with this method is limited to around 20 elements due to the overlap of characteristic stripping peaks of interfering elements in the sample.¹⁹ Moreover, the method is not able to measure the concentration of elements bound within compounds whose reduction (or oxidation) potential is outside the sweeping potential applied during pre-concentration. Its response is only to the presence of *free ions or elements in labile complexes*.¹⁹

(II) Atomic Spectroscopic Methods: In these methods, the elements are atomized or ionized at very high temperatures (at furnace or plasma) and then the constituent atomic fragments are analyzed by their interaction with electromagnetic radiation (absorption, emission, or fluorescence), or by their mass-to-charge ratio.^{19,24,26}

These methods remain the most popular approach since they allow the trace or ultra-trace level elemental detection regardless of the matrix and of the element of interest. Unlike the electrochemical techniques mentioned in previous section, these methods do not provide the concentration of free ions in the matrix, instead; they provide analysis of the total amount of element present in the sample.¹⁹ The technique can also provide chemical state or speciation data if it is coupled with a chromatographic column.²¹

Atomic spectroscopy can be subdivided into four approaches, namely; atomic emission spectroscopy (AES), atomic absorption spectroscopy (AAS), atomic fluorescence spectroscopy (AFS), mass spectroscopy (MS) based on the detection principle.²⁴ Among all the approaches, the most advantageous technique is inductively coupled plasma-mass spectroscopy (ICP-MS), providing access to the lowest limit of detection (parts-per-trillion (ppt) ranges) currently obtainable in routine analytical chemistry.¹⁹ In addition, it is a multi-element detection system, which allows a broad detection range of elements. ICP-MS uses argon plasma as a source to dissociate the elements, therefore; complete atomization of the elements is ensured. The ions that are released from the plasma are directed to mass filters (either a quadrupole or a magnetic sector) where they are separated according to their atomic mass-to-charge ratio.²⁷

On the other hand, the ICP-MS is a very expensive, large and bulky instrument making it challenging for an on-site and real-time detection. In addition, to prevent the overlapping peaks from interfering species and to minimize the matrix effect, huge amount of time has to be dedicated to sample preparation.¹⁹ Moreover, since the instruments are sophisticated, specialized personnel are needed to carry out the operational procedures.

(III) X-Ray Methods: A frequently used method in this area is the X-ray fluorescence (XRF) a physical phenomenon involving the interaction of X-rays with the sample. It can be utilized to measure the total content of any metal in the sample at its trace level (ppt range).²⁷

When high-energy photons, or electrons strike an atom, it induces removal of inner orbital electrons. Since the atom becomes unstable, outer orbital electrons fill the orbital vacancies in the inner shell. As a result of this phenomenon, X-ray photons are emitted

because the outer shell electrons have a higher energy than the replacing electron. XRF is based on the measurement of the energy (wavelength) and intensity of these photons. The energy of X-ray fluorescence peak is associated to a specific element because the energy levels for each element are different.^{19,26,27}

Quantitation is usually accomplished by the addition of an internal standard, a single element that is not present in the sample itself. Large systematic errors may arise due to the lack of robustness in the calibration methods.¹⁹ Compared to the atomic spectroscopic techniques, the cost of instrument is high and the instrument is not suitable for relocation. Direct measurement of liquid samples is not possible since they need to be in the form of a thin film for this technique.^{19,26}

(IV) Neutron Activation Analysis (NAA): The NAA method has been effectively applied to measure the total metal amount in different sample matrices at trace or ultra-trace levels.²⁷ In this technique, neutrons are used to irradiate the target element producing radionuclides with characteristic half-lives. As these radionuclides decay to a lower energy state, they emit delayed gamma rays with specific energies for each element. Quantitative measurement of the metal concentrations is based on determination of the intensities of these gamma rays emitted from the radioactive isotopes by a suitable detector.^{19,27}

NAA is as a robust technique, which provides very accurate results, and allows for simultaneous determination of multi-elements at very low concentrations (limit of detection for some metals can be mass fraction of 10^{-15} or below).²⁶ However, the instrument is very expensive even compared with ICP-MS and it is not applicable to carry to the field for the analysis. In addition, the throughput of NAA techniques is low. In terms of sample preparation, it is similar to XRF^{16,28,29}, and the liquid samples should be dried before measurements, which is a time-consuming step for routine analysis.¹⁹

1.3 Sensing Systems for Detection of Metal Ion Levels

A chemical sensor is a “sensing device” that can report the presence or the concentration of an analyte by physical means as a result of a chemical stimulation.²⁸ Various key

improvements, which have been initiated in modern world, are based on chemical sensors. They have found broad applications in many fields, such as medical diagnosis, process control, or environmental monitoring.²⁹ A chemical sensor should be distinguished from complex analytical systems such as infrared and mass spectrometers, which might sometimes be referred to chemical sensors. However, a chemical sensor is typically more handy and inexpensive than conventional instrumentation.²⁸ In addition, Janata *et al.* states that a chemical sensor must provide “*a real time insight into the chemical composition of the system*” and combine “*recognition and amplification*” with a resulting analytical signal.³⁰ Sensing systems generally contain two functional parts (**Fig 1.4**): **a receptor part**, which provides selectivity for the desired ions and/or molecules, and **a transducer part**, which gives analytically useful signal upon binding event.^{16,29}

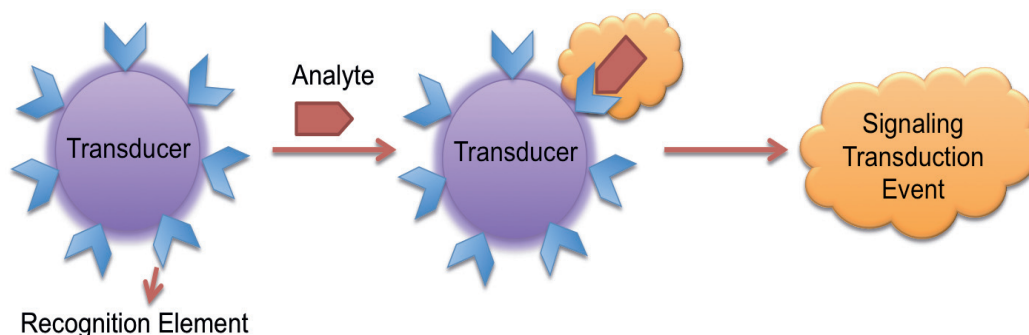


Figure 1.4: Schematic illustration of a sensing systems. Adapted from **Ref. 17** with permission from American Chemical Society.

In the **receptor** part of a sensor, chemical information is transformed into a form of energy that can be measured by the transducer. The chemical information may originate from a chemical reaction of the analyte or from a physical property of the system investigated.^{16,29} Various principles can be employed in the receptor part of the chemical sensors. It can be based on **physical** means such as change in mass, temperature, refractive index, absorbance, conductivity, where there is no chemical reaction between receptor and the analyte.³¹ Or, it can be **chemical**, in which a chemical reaction between recognition moiety and the analyte gives rise to the analytical signal. **Biochemical** process can be also the source of analytical signals.³²

The **transducer** is a device capable of transforming the energy carrying the chemical information about the sample into a useful analytical signal. The transducer as such does

not show selectivity. Operating principle of the transducers could be optical, mechanical (mass), thermal, magnetic, or electrical.^{16,29}

Recently, there has been a high demand for highly **selective**, **sensitive**, and portable chemical sensors with low **detection limit** and large **dynamic range** for routine metal analysis in environmental systems.²⁹

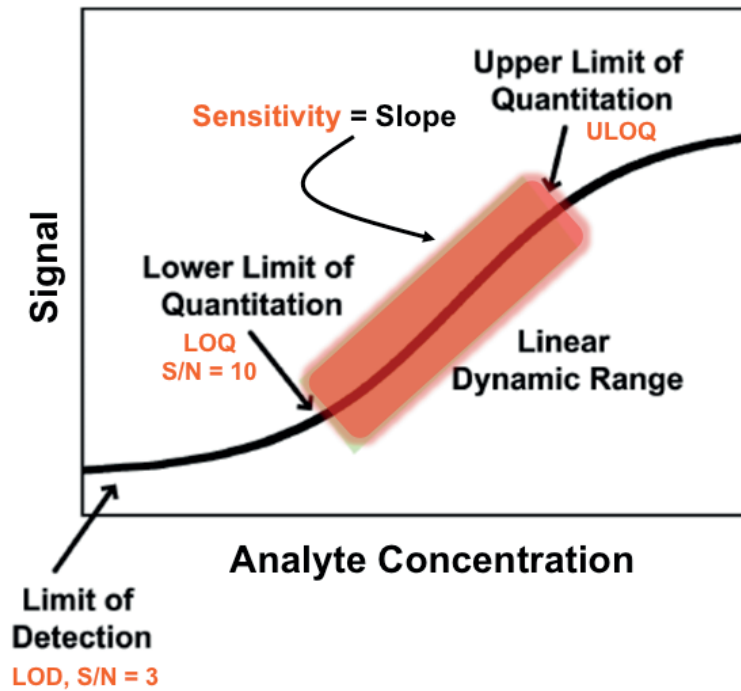


Figure 1.5: Response curve of a chemical sensor displaying sensitivity, LOD (limit of detection, $S_{bl} + 3s_{bl}$ of the blank), dynamic range, LOQ (lower limit of quantitation, $S_{bl} + 10s_{bl}$ of the blank), and ULOQ (upper limit of quantitation, 5 % deviation from linearity). S_{bl} is signal of the blank, s_{bl} is standard deviation of the blank signal, and S/N is signal to noise ratio.

The calibration curve is a plot that shows how a sensor responds the changes in the concentration of the analyte. From a practical point of view, it is formulated as the linear regime of the binding isotherm. **Upper limit of quantitation (ULOQ)** defines the upper limit of the dynamic range. Above ULOQ, the saturation of the receptor starts, and therefore linear response depending on the change in the concentration of the analyte cannot be observed.

The change in output of the sensor per unit change in the concentration of the analyte shows the **sensitivity** of the sensor.²⁷ In other words, sensitive sensors have high ability to

discriminate between small differences in analyte concentration at a particular concentration. Sensitivity is often confused with the **limit of detection (LOD)**, which is the concentration of the analyte giving a signal equal to the blank plus three times the standard deviation of the blank. In other words, it is the minimum concentration of analyte that can be detected with a specific technique at a known confidence level. However, the lower limit of quantitative measurements is generally taken to be equal to the concentration of the analyte giving a signal equal to the blank plus ten times the standard deviation of the blank, which is referred as **lower limit of quantitation (LOQ)**. Another important parameter for the sensor to detect wide range of concentrations is the **linear dynamic range** of the sensor, which is the maximum concentration range over which an accurate measurement can be made. Response curve of a chemical sensor presented in **Fig.1.5** offers better understanding to these five concepts.²⁷ Sensors are also desired to be highly **selective** which shows the discriminating power of the system against the analyte over the interferences.³³

1.4 Gold Nanoparticles as Sensing Probes

The superior physicochemical properties of nanomaterials, which are materials **in the feature unit of 1-100 nm**, have drawn a great deal of attention in the scientific community due to their tremendous potentials as sensing probes.³⁴ The multifaceted and tunable properties of nanomaterials, which are based on their size, shape, surface functionalization, and the environment has allowed researchers to develop innovative sensing systems with enhanced sensitivity, selectivity and robustness.^{34,35} Among nanomaterials, gold nanoparticles (AuNPs) provide extensive opportunities in the detection of various analytes since they can be utilized as a dual component both for transduction and recognition processes.^{16,29} The surface of AuNPs can be decorated with a wide range of organic ligands or biomacromolecules by using the toolbox of surface modification techniques, which enables the selective interaction with the analyte. On the other hand, AuNPs are versatile transducers due to the fact that they possess distinctive physical and optical properties such as surface plasmon resonance (SPR), distance-dependent fluorescence enhancement or quenching, high electrical conductivity, redox

behavior, surface enhanced Raman scattering (SERS) and, nonlinear optical (NLO) properties, which can be altered upon binding to generate a detectable signal.^{16,29,34,35}

Here, I will focus on the recent advancements and the new trends in sensing strategies based on multifunctionalization of AuNPs with a wide range of organic ligands for the detection of metal ions. Among all the strategies, my choice of literature examples is mostly based on the improvements in detection limit, selectivity, applicability to real samples and the novelty in transduction mechanisms. I also highlight the necessity of generation of more robust and portable online monitoring systems with low detection limits. As it is stated in previous sections, heavy metal ions such as Hg, As, Cd, Cr, Cu, Ni, and Pb rank among the prime metals that are of public health significance.^{6,14,36} Consequently, the development of AuNPs-based sensing strategies has been mostly dedicated to detection of the concentration of these heavy metal ions.^{14,36}

1.4.1 Detection of Mercuric Ions

Most part of the work in the field of metal ion sensing systems in the literature has been dedicated to detection of mercuric ions due to its serious health consequences even at very low concentrations. Chelating ligands containing amino or carboxy groups³⁷⁻⁴⁴ as well as thiophilic groups⁴⁵, which have been shown to have higher affinity towards Hg^{2+} than other metal ions have been employed to modify AuNPs for sensing of Hg^{2+} via ligand- Hg^{2+} coordination and they are applied as very advantageous dual probes. Chen *et. al* reported a simple but highly selective colorimetric assay based on exploitation of 3-nitro-1H-1, 2, 4-triazole (NTA)-functionalized AuNPs as a transducer.⁴⁶ They showed that citrate capped AuNPs do not resist the aggregation induced by 2-amino-2-hydroxymethyl-propane-1,3- diol (Tris), however; the NTA can stabilize the AuNPs against Tris-induced aggregation through covering the AuNPs (**Fig.1.6**). The colorimetric technique used in this work is based on the shift of the surface plasmon resonance (SPR) peak of AuNPs upon a binding event. For example, it is known that in their dispersed state, AuNPs show a prominent red color, while upon a binding event that induces colloidal instability in the dispersion, purple color can be visible as a direct consequence of the agglomeration. Therefore, the technique benefits a simple readout by

the visual color change and can be quantitative as the peak intensity is related to the concentration of the analyte. Chen and co-workers used this methodology. And, it resulted in very low LODs (limit of detection) of 7 nM (1.4 ppb) and 50 nM (10 ppb), which can be read by spectrophotometer and by direct visualization, respectively.⁴⁶ In addition, no response was detected in the presence of other metal ions whose concentrations are up to 100 mM in the absence of masking agents. They also applied their detection system to the real environmental sample (Jurong Lake water, Singapore) and the results showed good agreement with those determined by ICP-MS.⁴⁶



Figure 1.6: A) Color changes of the citrate-capped AuNPs upon the addition of Tris buffer, NTA, and Hg²⁺, respectively. B) Color changes of the NTA-AuNP probes upon the addition of various metal ions. Adapted from Ref. 46 with permission from The Royal Society of Chemistry.

Later, Darbha *et al.* presented for the first time that hyper-Rayleigh scattering technique, which can be 2-3 orders of magnitude more sensitive than the typical colorimetric technique, could be used for rapid and reliable detection of Hg²⁺ in aqueous solutions.⁴⁷ This work is one of the few examples in which the authors studied the effect of homoligand vs. mixed-ligand functionalized AuNPs, finding that the mixed monolayer of mercaptopropionic acid (MPA) and homocysteine (HCys), in the presence of the chelating ligand 2,6-pyridinedicarboxylic acid (PDCA), is more selective for Hg²⁺ ions over other alkali, alkali earth and transition heavy metal ions. Thanks to the combination of mixed-ligands cooperativity on the nanoparticle surface and the high sensitivity of the

HRS technique, a limit of detection (LOD) of 5 ppb for Hg^{2+} ions was achieved. Although this methodology has a huge potential for analysis of environmental samples, it remains to be demonstrated that the sensing system is applicable to real samples. Meanwhile, trimercaptotriazine-modified gold nanoparticles were applied as a SERS probe⁴⁸ by taking advantage of the fact that a contrasting response was observed for selected vibrational bands in the SERS profiles in the presence of heavy metal ions like Hg^{2+} and Cd^{2+} . This enables direct quantitative evaluation by utilizing relative peak intensity ratios instead of internal standards. However, the study is published as a proof of concept since the sensitivity of the probe is not shown to be high enough to detect the concentration levels of Hg^{2+} and Cd^{2+} defined by EPA (Environmental Protection Agency) and also the selectivity of the probe is not evaluated towards the particular type of ion.

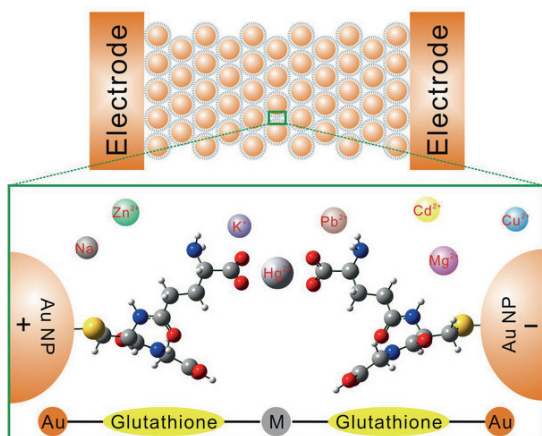


Figure 1.7: Thin film of GSH capped AuNPs between microelectrodes (top) and complexation of two glutathione molecules with Hg^{2+} via carboxylic groups between two Au NPs (bottom). Reproduced from **Ref. 49** with permission from Nature Publishing Group.

An electrochemical approach has been published by Guo *et al.* by using a thin film of glutathione (GSH) functionalized AuNPs between interdigitated microelectrodes.⁴⁹ Complex formation of metal ions with two terminal carboxylic acid groups of GSH results in bridging the molecular gaps between the AuNPs within the thin film accompanied by an increase in the conductance of the thin film (**Fig. 1.7**). The fabricated molecular-gap device demonstrates high selectivity toward Hg^{2+} with a low detection limit down to 1 nM.

Recently, Chen *et al.* took advantage of the high affinity of mercury ions for soft donors such as sulfur to create an innovative colorimetric detection system able to perform mercury speciation analysis.⁵⁰ The sensing system is based on two main components: 13

nm diameter citrate-stabilized AuNPs and the sulfur-containing ligand diethyldithiocarbamate (DDTC), which form a stable complex with Cu^{2+} ions. In the presence of mercury species, they replace the Cu^{2+} ions in the DDTC complex, and form Hg-DDTC complexes, which possess free sulfur groups that can displace the citrate molecules from the nanoparticle surface and lead to the nanoparticle aggregation.

In this work, the originality can be assigned to the discriminating power of the sensor towards three organic mercury species (methyl, ethyl, and phenyl mercury) over inorganic derivatives of Hg^{2+} in the presence of masking agent, ethylenediaminetetraacetic acid (EDTA). The detection limit of the sensor was found to be 10 nM for Hg^{2+} ions and 15 nM for MeHg^+ , and the real-world applicability was investigated for drinking water samples confirming the huge potential of the sensor for the determination of organic mercury species.⁵⁰

Within the same year, Maiti *et al.* developed a completely different approach based on generation of fluorescence signal in the presence of Hg^{2+} ions.⁵¹ In this system, recognition moiety (thymine nucleotide) is not bound to the nanoparticles, so AuNPs acts only as a transducer by quenching the signal of a fluorescence anionic probe. This is a different approach to the various nanoparticle-based detection systems, which are typically based on the presence of recognition element in the monolayer of AuNPs.⁵¹ The protected monolayer is made of positively charged 1,4,7-triazacyclononane (TACN)- Zn^{2+} head groups that promote the multivalent interactions with a fluorescent anionic probe, whose fluorescence is quenched by the gold core. The presence of Hg^{2+} ions resulted in the ternary complex formation with two thymine nucleotide molecules. The complex has an increased affinity for the positively charged nanoparticle surface due to electrostatic forces. As a consequence, fluorescence anionic probe is displaced from the surface leads to an increase in fluorescence. The system shows an excellent selectivity towards Hg^{2+} ions due to high affinity of thymine nucleotide for mercuric ions and it can generate a linear response curve in the low nM concentration range.⁵¹ Since the signal transduction pathway of the system is designed in an ingenious manner, it possesses a good potential for development of modified detection systems for various analytes.

1.4.2 Detection of Lead Ions

Detection of lead ion levels has also attracted much attention due to its high toxicity to human beings. Pb^{2+} ions are very hazardous especially for children since it causes mental retardation. U.S. Environmental Protection Agency (EPA) defines the maximum concentration level of lead ions in drinking water as 72 nM, however, it can lead to brain and neuro-developmental deficiencies among children at even lower concentrations.⁵² As a consequence, it is essential to generate ultrasensitive sensors for the detection of lead ions.⁵² The proposed sensing systems for the detection of Pb^{2+} ions are mostly built on colorimetric assays that manipulate the SPR peak of AuNPs. One of the early examples is based on the aggregation of gallic acid-capped AuNPs (GA-AuNPs) in the presence of Pb^{2+} ions due to coordination of phenolic hydroxyl groups of GA with the cation.⁵³ However, the detection limit of the system was not satisfactory (in μM range) with respect to its use for public health. In addition, LOD was found to be higher depending on the concentration of interfering ions, which suggests an insufficient selectivity profile. Later, the LOD (down to 10 nM) and the selectivity of the system was improved by another group⁵⁴ by reducing the mean diameter as well as the size distribution of the GA-AuNPs and by minimizing the interparticle repulsion between each GA-AuNPs with the addition of NaOCl_4 salt. Moreover, the feasibility of the assay has been evaluated in drinking water, which offers a huge potential as a practical sensor in the field. Similar colorimetric detection mechanisms that are based on metal induced aggregation of nanoparticles have been proposed by using glutathione⁵⁵, cysteamine⁵⁶, maleic acid⁵⁷, triazole-acetate⁵⁸, and mercaptoundecanoic acid⁵⁹ functionalized AuNPs to detect Pb^{2+} ions in aqueous solutions.

Wang *et al.* proposed a different sensing strategy based on Fluorescence Resonance Energy Transfer (FRET) between cysteamine capped CdTe-Quantum dots (CA-CdTe-QDs) and 11-mercaptoundecanoic acid (MUA-AuNPs) capped AuNPs.⁶⁰ In the absence of Pb^{2+} ions, the negatively charged QDs and positively charged AuNPs can form FRET donor-acceptor pairs due to electrostatic interactions, which leads to the effective quenching of the photoluminescence intensity (PL) of the QDs (**Fig.1.8** (A)). MUA-AuNPs are congregated in the presence of Pb^{2+} , which decrease the efficiency of FRET between QDs and AuNPs and yield higher PL intensity as the concentration of Pb^{2+}

increases (**Fig. 1.8 (B)**). The method has been shown to be working very well in the range of 0.22–4.51 ppm with a relatively high selectivity. The selectivity of the system can be further improved by replacing MUA with more selective recognition units. Recently, citrate covered AuNPs were applied as a SERS probe by exploiting the affinity of the Pb^{2+} ions to carboxylate and hydroxyl moieties of citrate molecules.⁶¹ Upon complexation with the cation, the spectral bands that correspond to the $\nu_{\text{as}}(\text{COO}^-)$, $\nu_{\text{s}}(\text{COO}^-)$ and $\nu(\text{C-OH})$ are perturbed, and this enables to detect Pb^{2+} ions over a linear range of 25 ng/L–1000 ng/L. The effect of presence of interfering ions has been shown against only three types of ions (Cd^{2+} , Ni^{2+} , and Hg^{2+}), and therefore it is difficult to evaluate the practicability of the sensor in the reported form for real environmental samples.

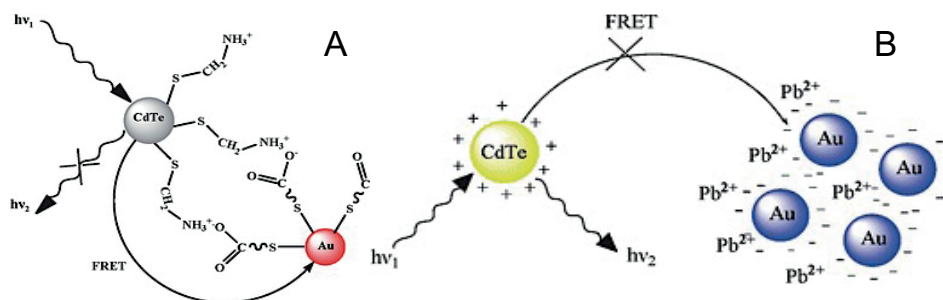


Figure 1.8: Schematic representation of the (A) FRET donor–acceptor pair of positively charged CA-CdTe-QDs and negatively charged MUA-AuNPs, (B) Inhibition of FRET efficiency between QDs and AuNPs in the presence of Pb^{2+} . Reproduced from **Ref. 60** with permission from Royal Society of Chemistry.

1.4.3 Detection of Cadmium Ions

Colorimetric detection methodologies have been developed to sense Cd^{2+} ions by using mercaptoundecanoic acid⁵⁹, 4-amino-3-hydrazino-5-mercapto-1,2,4-triazole⁶² modified AuNPs as a dual sensing probe. Xue *et al.* demonstrated the advantage of using mixed-ligand coated AuNPs for colorimetric detection of Cd^{2+} .⁶³ The working principle of the assay is based on Cd^{2+} induced aggregation of 6-mercaptonicotinic acid (MNA) and L-Cysteine (L-Cys) functionalized AuNPs (**Fig.1.9**). An important aspect of the work is to show a better performance of the mixed-ligand coated AuNPs compared with the that coated by either MNA or L-Cys, which pave the way for novel sensing probes just by

modifying two different ligand types. The detection limit of the system is reported as 100 nM with promising selectivity, and practicality of the system was validated through analysis of lake water samples.

In another study⁶⁴, quinoline is attached to the surface of AuNPs through click chemistry and the fluorescence response of the molecule is tracked depending on the concentration of Cd²⁺.

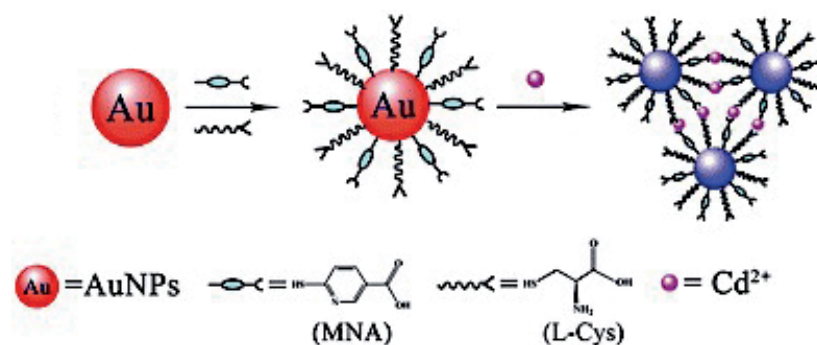


Figure 1.9: Schematic representation of aggregation induced colorimetric response of MNA-L-Cys-AuNPs in the presence of Cd²⁺. Reproduced from **Ref. 63** with permission from Royal Society of Chemistry.

When there is no Cd²⁺ in the solution, the fluorescence of quinoline is quenched by AuNPs due to electron transfer between AuNPs and quinoline. However, when Cd²⁺ coordinates with quinoline, it blocks the electron transfer and switches on the fluorescence. Although the design of this fluorescent probe is quite sophisticated, the detection limit is quite high (10 μM) in terms of EPA standards. Recently, an innovative electrochemical sensor based on covalent attachment of mixed aryldiazonium salts coated AuNPs to gold electrodes for the detection of Cd²⁺ has been proposed.⁶⁵ 4-nitrophenyl and 4-carboxylphenyl were used to functionalize the surface of AuNPs, which were then anchored on gold electrodes to obtain Au-Ph-AuNP interfaces. Glutathione (GSH), which can selectively bind Cd²⁺, was finally attached on the surface to create Au-Ph-AuNP-GSH sensing interface. This interface served as electronic bridge for anodic stripping voltammetry to detect Cd²⁺ over the concentration range from 0.1 nM to 100 nM. The proposed sensor was tested against three different environmental samples; tap water, marine water and river water with accuracy comparable to that of ICP-MS. The

idea behind this sensor can lead to fabricate various electrochemical sensors for the online monitoring of trace amounts of metals.²⁹

1.4.4 Detection of Copper Ions

Colorimetric AuNPs based sensors have been effectively employed for the detection of Cu^{2+} ions by using cysteine⁶⁶, malonamide dithiocarbamate⁶⁷ groups as a recognition unit on the surface of AuNPs. Recently, Nath *et al.* constructed a portable, power-free, and inexpensive nanosensor based on a visible color change on paper strip.⁶⁸ In addition, colorimetric detection strategies based on the copper catalyzed click chemistry have been described.^{69,70} This method is based on crosslinking of azide functionalized AuNPs with each other in the presence of a ascorbic acid and a dialkyne due to copper(i)-catalyzed azide-alkyne cycloaddition 'click' reaction. Although the sensitivity of the methods are not excellent, the practicality of the systems is worth mentioning since this technique allows the naked eye, without the help of any sophisticated instrument, to assay for the presence of Cu^{2+} ions. There are also other colorimetric and fluorescence based techniques, in which AuNPs were only used as a transducer, and the recognition process was not take place on the surface of AuNPs.^{71,72}

An ultrasensitive detection method has been proposed by Foroushani *et al.*, which is based on the increase of a tunneling current through the network of L-cysteine functionalized core-satellite AuNPs upon complexation with Cu^{2+} .⁷³ The L-cysteine can selectively coordinate with copper ion by the carboxyl group and amine group (**Fig.1.10**). The chelation with copper ions produces the formation of GNP/L-cysteine/ Cu^{2+} /L-cysteine/GNP molecular junctions and results in a significant increase in the conductance through the networks. Uniform size AuNPs was shown to perform less sensitive and selective than core-satellite AuNPs. The system was shown to respond over ten orders range of copper ion concentrations and the effectiveness of the system was verified in environmental samples, such as tap water, lake water, and pure distilled water spiked with a known concentration of Cu^{2+} ion.⁷³

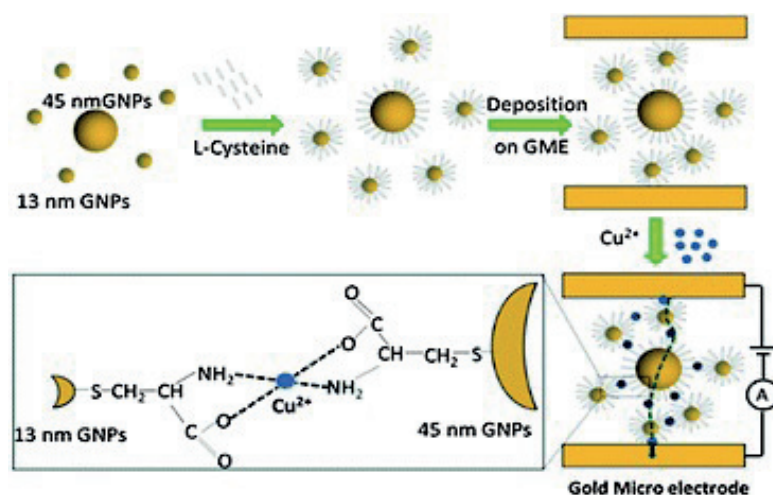


Figure 1.10: Schematic illustration of L-cysteine modified core–satellite AuNPs sensor. Reproduced from Ref. 73 with permission from Royal Society of Chemistry.

Another innovative approach towards Cu²⁺ ion detection is the nanospectroscopic metal ion recognition method based on chelation chemistry and *plasmonic resonance energy transfer (PRET)* that should be mentioned in terms of novelty of the approach.⁷⁴ Lee and co-workers have utilized resonant quenching in the Rayleigh scattering of a AuNP when the frequency of the electronic absorption band of a metal-ligand complex on the surface of the AuNPs matches with the frequency of the Rayleigh scattering of a gold nanoparticle. The detection system is applied for Cu²⁺ ions sensing in aqueous solutions using ethylenediamine ligands. There is no spectral overlap between ethylenediamine and the AuNPs (**Fig. 1.11, left**). When the electronic absorption frequency of metal ligand coordination complex matches with the Rayleigh scattering frequency, the selective energy transfer is stimulated by this spectral overlap (**Fig. 1.11, middle**) and the distinct resonant quenching on the resonant Rayleigh scattering spectrum is observed (**Fig. 1.11, right**). It makes the detection of Cu²⁺ ions feasible at concentrations down to 1 nM.

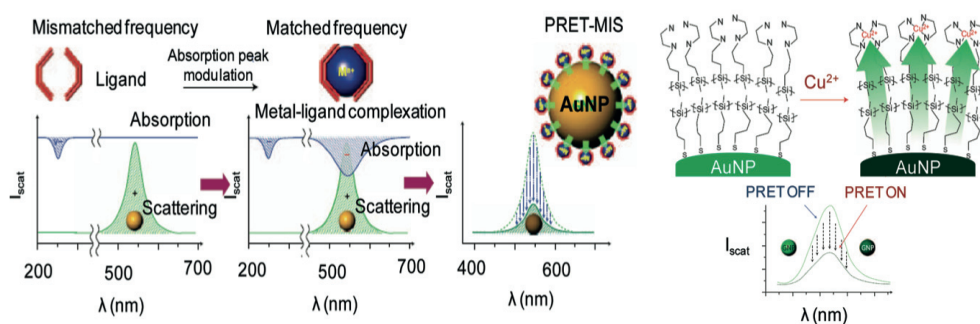


Figure 1.11: A schematic illustrating the detection of Cu^{2+} via plasmonic resonance energy transfer (PRET) between a single AuNP and conjugated resonant complexes and the expected Rayleigh scattering profile. Reproduced from **Ref. 74** with permission from Royal Society of Chemistry.

1.4.5 Detection of Other Hazardous Heavy Metal Ions

There are numerous AuNP based colorimetric and fluorometric assays for detection of hazardous Cr^{3+} ions.^{36,75,76} Recently, the modification of the surface of AuNPs with mixed ligands of citrate and thiourea yielded better performance of the colorimetric assay with relatively low detection limit, $0.05 \mu\text{M}$ compared to the that with one type of ligand.⁷⁵ In order to demonstrate the potential of the colorimetric Cr^{3+} assays for construction of cheaper sensors, the citrate stabilized AuNPs were transformed on the paper based platform.⁷⁷

Another toxic heavy metal is arsenic, exposure to which can even at very low concentrations result in abdominal pain, skin cancer, renal failure, lungs and liver diseases.³⁶ As^{3+} has a huge affinity for sulphur containing ligands, and therefore most of the colorimetric AuNP based detection systems have taken the advantage of this strong affinity.^{78,79} One example of this strategy was published recently by Shrivastava *et al.* by using lauryl sulphate functionalized AuNPs to create a colorimetric assay with the detection limit of $5 \mu\text{g L}^{-1}$.⁸⁰ Recently, a novel colorimetric sensor was developed to detect As^{5+} by utilization of citrate-capped AuNPs as a transduction unit.⁸¹ The resulting aggregation of the AuNPs, which leads to the color change, is due to the inhibition of acid phosphatase activity in the presence of As^{5+} .

Nickel ions have been shown to be carcinogenic, and causing skin allergies at high concentrations, and thus, the continuous and accurate detection of concentration of Ni^{2+} ions is crucial.^{82,83} However, there has not been an extensive study on AuNP based sensing systems for Ni^{2+} ions. An innovative surface sandwich platform composed of nitrilotriacetic acid (NTA)-functionalized gold surface and polyhistidine-functionalized AuNPs allowed researchers to detect Ni^{2+} ions at concentrations as low as 50 ppt by taking advantage of nanoparticle-enhanced surface plasmon resonance (SPR) technique.⁸³ The selectivity was achieved by using two different types of ligands, which are highly selective towards Ni^{2+} ions. Another study focused on development of AuNP-

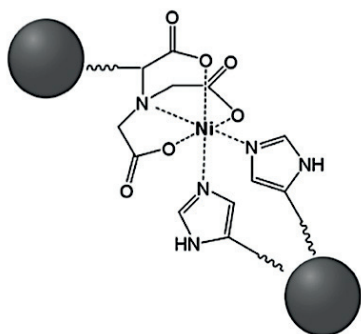


Figure 1.12: Aggregation of the AuNPs due to the formation of the octahedral complex, when Ni^{2+} ion is coordinated between NTA and histidine groups existing at the particle surface. Reproduced from **Ref. 82** with permission from John Wiley and Sons.

based sensing systems, which exploit both colorimetric and SERS techniques.⁸² NTA and L-carnosine (a dipeptide of histidine and β -alanine) functionalized AuNPs are utilized in the system. The compounds resulted in the aggregation of the particles in the presence of Ni^{2+} ions due to the strong affinity of the ligands on the surface of AuNPs for the Ni^{2+} ions (**Fig.1.12**). Aggregation of AuNPs leads to an alteration of the extinction profile along with an increase in SERS intensity of the Raman reporter. The colorimetric and SERS measurements result in the relative detection limits of 5 ppm and 0.5 ppm, respectively.⁸²

In conclusion, organic ligands, which are used as recognition elements on the surface of AuNPs are more stable under various conditions and also inexpensive compared to biomacromolecules like DNA, peptides etc. Re-visiting and exploring (new) the physicochemical properties of gold nanoparticles enable researchers to develop novel transducing strategies, which decrease the detection limits by enhancing signal to noise ratio. There is also a need to increase the selectivity and enable the detection of multi-elements simultaneously. One may accomplish this by, for example, developing array-based systems composed of AuNP based various recognition units.

CHAPTER 2

Introduction-2

Ligands on the surface of AuNPs enable the selective interaction with the specific metal ion, therefore; knowledge on self-assembled monolayers (SAMs) is important to be reviewed. In addition, the concept of selectivity for the supramolecular complexation agents is visited. Finally, the previous work done by our group, which forms the basis of this thesis, is analyzed and the similar systems in the field are reviewed.

2.1 Self-Assembled Monolayers (SAMs) on Gold Nanoparticles

Self-assembled monolayers provide a convenient, simple, and adaptable system with which one can tailor and fine-tune a surface of interest.⁸⁴ Therefore, they can be regarded as a toolbox of surface modifications, and they are available for designing highly selective surfaces towards detection of metal ions or other target analytes. SAMs are highly ordered 2-D organic assemblies that are formed spontaneously on variety of solid surface by adsorption of organic molecules from gas or solution phases.⁸⁴ Since the adsorption of organic molecules lowers the surface free energy of bare surfaces of metal and metal oxides, the formation of SAMs is thermodynamically favorable.⁸⁵

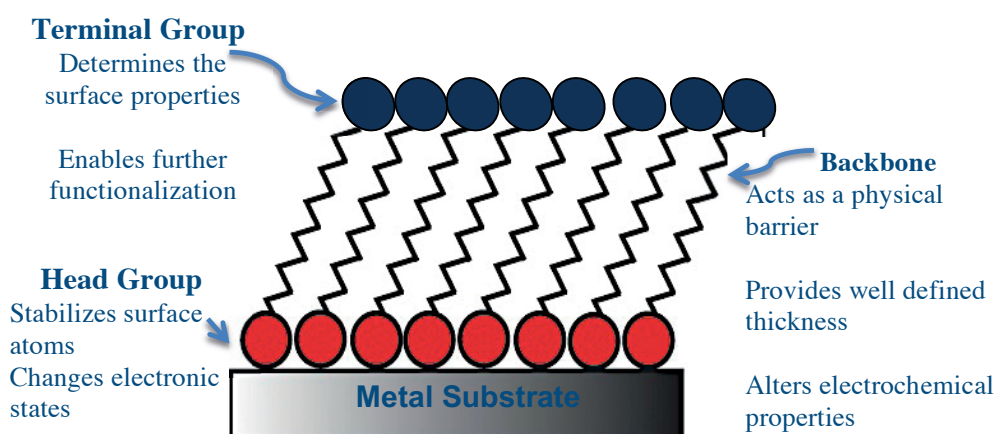


Figure 2.1. Schematic illustration of an ideal, single-crystalline SAM structure on a metal substrate. The characteristics of the SAM are highlighted.

As shown in Fig.2.1, the organic molecules that constitute SAMs possess typically three parts; **the head group** with a specific affinity for the surface, **the backbone** made of hydrocarbon chains that are mostly responsible for the molecular ordering via non-covalent lateral interactions between the chains, and **the terminal group with** functional moieties, which determine the specific properties of outer interface, such as wettability, topography, surface energy, chemical reactivity, and others.^{84–86}

In this work, I utilized thiolated ligands on the surface of AuNPs because the bond between the gold substrate and the sulfur head group is quite strong (-40 - 50 kcal/mol).⁸⁵ This semi-covalent bond gives rise to a robust but modifiable interactions in a wide range of temperature and solvents.

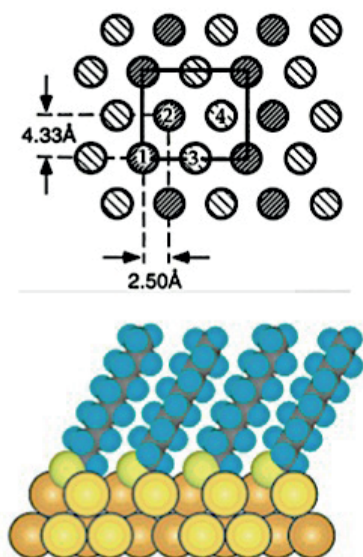


Figure 2.2: (Top) The standard model of the $c(4 \times 2)$ phase of a SAM assumes a single sulfur on top of a hollow site on an unreconstructed gold surface. The two kinds of shading symbolize molecules that are different within the $c(4 \times 2)$ unit mesh (rectangle). Molecules 1 and 2 are equivalent but different from molecules 3 and 4. (Bottom) cross section of a SAM formed from decanethiol. **T. Bürgi, *Nanoscale*, 2015, 7, 15553–15567-** Published by The Royal Society of Chemistry.

Considering the ubiquitous use of the gold–sulfur interface, it is not unexpected that the nature of the Au–S interfaces has intrigued researchers.⁸⁷ The electron diffraction studies conducted in the late 80s and 90s revealed the hexagonal arrangement of thiolates on gold surfaces with sulphur–sulphur distance of 4.97 \AA . The arrangement is a $(\sqrt{3} \times \sqrt{3}) R30^\circ$ structure where the sulphur atoms are positioned in the to the threefold hollow sites of the (111) surface. Additional X-ray studies discovered a $c(4 \times 2)$ superlattice of the $\sqrt{3} \times \sqrt{3} R 30^\circ$ lattice (**Fig.2.2**).^{85,87} The diffraction patterns furthermore indicated that two of the four molecules of the unit mesh are distinct to a certain extent.

Over the past 20 years, numerous atomic constructions for the gold–sulfur interface of the close-packed thiolate-SAM on Au(111) have been proposed (Fig.2.3). Surprisingly, recent single crystal X-ray structures of thiolate-protected gold clusters show staple motifs depicted by gold ad-atoms sandwiched between two sulphur atoms (Fig.13).⁸⁸ In addition, although it contradicted with the older work on SAMs, it is proposed that the nature of the Au–S interfaces in curved and flat surfaces are quite similar in terms of staple motifs. A key feature of SAMs has been recently proposed as its dynamic behavior, including a reconstruction of the Au(111) surface, lateral diffusion, and conformational isomerism in response to surroundings.⁸⁸

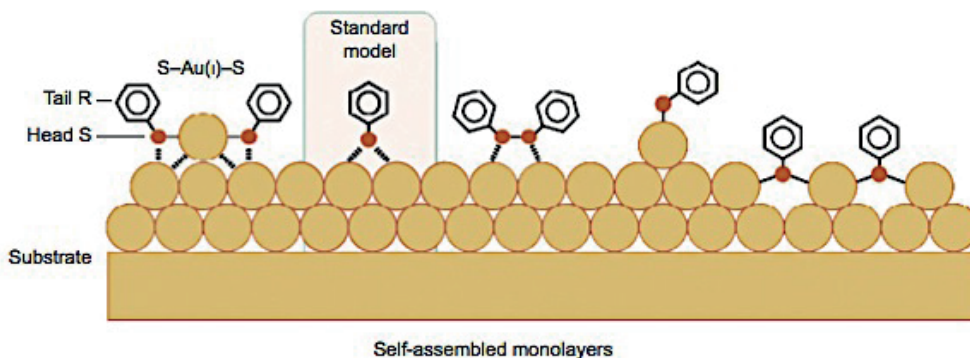


Figure 2.3: Recently proposed bonding patterns between Au and S atoms. The **standard model** defining a monothiolate binding has been challenged by (**from middle to right**): disulfide bonding; a complex comprising an Au adatom and a thiolate; or a sulfur-gold polymeric chain. Recent calculations and experiments demonstrated that the staple motifs (RS-Au(I)-SR) described above are the most abundant structure elements in the low- and medium-coverage SAMs (**left**). Reproduced from **Ref. 88** with permission from Nature Publishing Group.

2.2 Structure of Mixed Composition SAMs on Highly Curved Gold Surfaces

When a mixture of thiolates is assembled onto a small, highly curved 3D objects such as nanoparticles, geometric constraints regulate how the molecules phase separate.⁸⁹ Phase separation on the curved surfaces with formation of domains of distinctive sizes and shapes was experimentally evidenced by a variety of characterization methods such as scanning tunneling microscopy (STM),^{90,91} nuclear magnetic resonance (NMR)

spectroscopy,⁹² Fourier transform infrared spectroscopy (FT-IR),⁹³ mass spectrometry,⁹⁴ electron spin resonance (ESR),⁹⁵ transmission electron microscopy (TEM),⁹⁶ and neutron scattering.⁹⁷ The discovery of the different surface structures was theoretically envisaged by thermodynamic arguments.⁸⁹

The system equilibrates itself to reach a minimum Gibbs free energy through a trade-off between entropy maximization that drives random mixing, and enthalpy minimization which favors constructive intermolecular contacts of similar molecules, and drives phase separation.^{89,98} The competing driving forces for separation and mixing determine the degree of phase separation or lack of it. The balance between separation and mixing depends on the characteristics of ligands and the size of nanoparticles (the curvature effect).^{89,98}

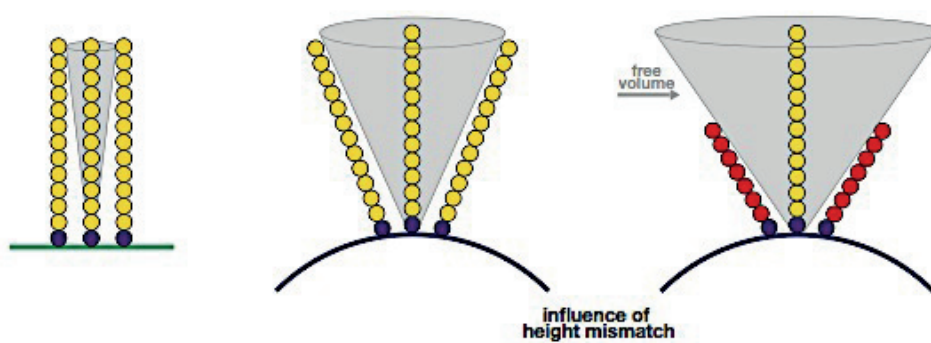


Figure 2.4: Schematic view of the free-volume gain on curved surfaces compared to flat ones. For ligands with a mismatch in height, conformational entropy increase in longer ligands results in microphase separation. Reproduced from <http://dx.doi.org/10.5075/epfl-thesis-5859>

For example, when the ligands have similar characteristics, both enthalpy and entropy of mixing dominate resulting in the lack of phase separation (randomly mixed). On the other hand, side-by-side packing of two dissimilar ligands is enthalpically non-favorable, when thiolated ligands significantly differ in hydrophilicity, length, and chemical functionality.^{89,98} Therefore, macrophase separation is expected in order to minimize the interface between dissimilar ligands (enthalpic contributions dominate over entropy of mixing). Within a certain size range of the nanoparticles, on the other hand; when ligands have a size-mismatch, there is a gain in conformational entropy for the taller

ligands otherwise unavailable in side-by-side packing with the identical ligands (**Fig. 2.4**).^{89,98} This favors tall/short interfaces and leads to a microphase separation, whereby ligands form nano-structured domains. Under particular conditions, ordered ribbon-like domains (referred to as stripes), with alternation of two dislike ligands have been observed (**Fig.2.5**). These special arrangements of the ligand on the surfaces can confer interesting interfacial properties to the nanoparticles.^{89,98}

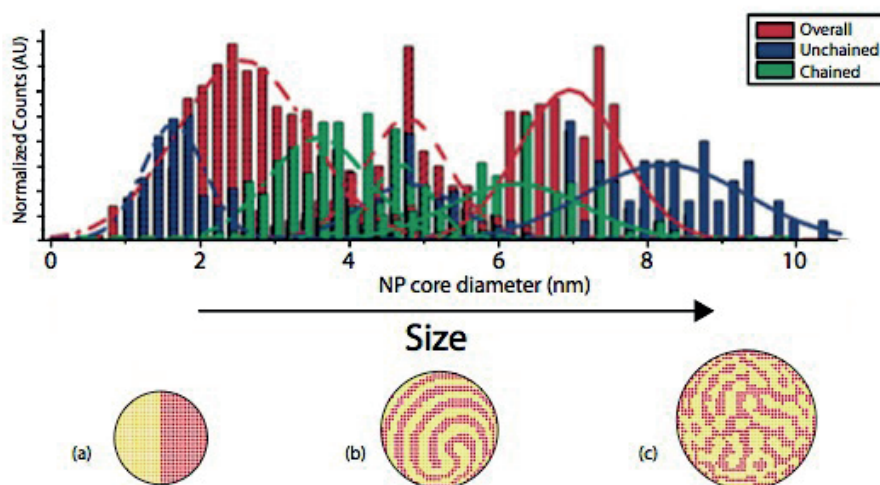


Figure 2.5: Schematic representation for a monolayer on a particle. Phase separation in mixtures of co-adsorbed ligands of different length on nanoparticles of increasing sizes, ranging from Janus to striped to randomly mixed. Reproduced from <http://dx.doi.org/10.5075/epfl-thesis-5859>

Our group has previously demonstrated that AuNPs exhibiting ordered nano-structured domains at their surface could have distinct properties, such as improved cell permeability,⁹⁹ peculiar catalytic properties,¹⁰⁰ monotonic solubility scaling non-monotonically with relative ligand concentration,⁹¹ and atypical interfacial energy.¹⁰¹ In addition, previous study of our group showed that striped patterned AuNPs of specific ligand composition, which can be of great utility in creating new recognition processes, are able to capture metal cations selectively and sensitively.¹ The system described in that work forms the basis of this thesis and will be discussed in greater detail in the following chapters.

2.3 Host-Guest Interactions in Solution

2.3.1 Concept of Complexation and Lock-Key Analogy

Chemistry found in living organisms provides a great source of inspiration for understanding of assemblies of molecules held together by non-covalent forces.¹⁰² On a molecular level, the receptors in our body, which has an ideal size, shape, and positions of the binding sites specific to certain molecules selectively catch and bind to the substrate.^{102,103} For example, while genes, enzymes, antibodies, and ionophores can be counted as receptors; inhibitors, co-factors, drugs or antigens can act as substrates.^{102,104} The highly specific, selective, hierarchical and cooperative biological chemistry, which allows our body to sustain itself in a dynamic equilibrium, forms the basis of molecular recognition chemistry which is also called **host-guest chemistry**.¹⁰³⁻¹⁰⁵ **Host** is considered to be a large molecule with a sizeable pocket or central cavity, which possesses convergent binding sites, such as Lewis basic donor atoms. On the other hand, **guests** are smaller entities (in our case, Lewis acidic metal cation), which have divergent binding sites. When host and guest entities experience an attractive force, they bind to each other to produce ‘ a host-guest complex’ or ‘a supermolecule’. The main hypothesis associated with host-guest chemistry is the “lock and key” model developed in 1894 by Emil Fisher based on his study of the binding of enzymes to substrates. In his model, the enzyme is described as the lock and the substrate as the key. The lock and key principle states that the host (lock) should be complementary to the guest (key) sterically and electronically. A schematic illustration of this idea is shown **Fig. 2.6**.¹⁰³⁻¹⁰⁵

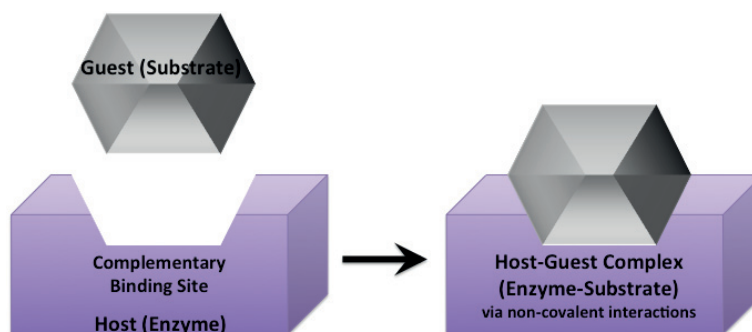


Figure 2.6: Schematic representation for lock and key principle proposed by Emil Fisher, which form the basis of host-guest chemistry

After the lock and key theory was proposed, four macrocyclic hosts to capture metal cations were synthesized by the groups of Curtis, Busch, Jäger, and Pedersen in mid-to-late 1960s, which may be seen as having taken inspiration from natural macrocyclic hosts, such as hemes, porphyrins, and ionophores. These four systems shown in **Fig. 2.7** enabled researches to develop a vast variety of analogues with varying selectivity for a large number of guests.¹⁰⁵

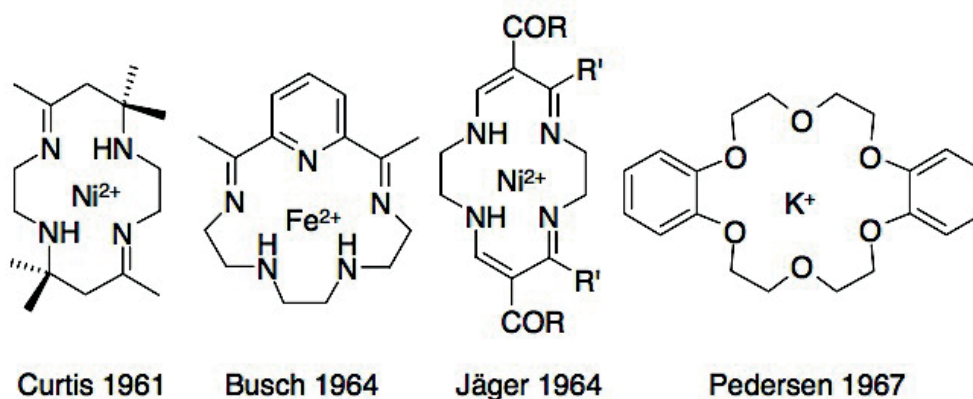


Figure 2.7: Four host molecules of fundamental importance, which form the basis of host-guest chemistry. Reproduced from **Ref. 106** with permission from John Wiley and Sons.

The non-covalent interaction between a metal, **M** as a guest and a ligand, **L** as a host is an equilibrium process.^{105,106} The equilibrium constant of this interaction is termed as 'binding constant' and it provides information about the affinity between metal and ligand. The affinity refers to the strength of interaction between M-L and the thermodynamic stability of the M-L complex. When we ignore activity effects, the binding constant for a simple 1:1 M-L system is described by **Equation 2.2**.^{105,107} In order to determine the binding constant, we need to have information about the concentration of M-L complex as a function of varying concentration of M or L (**Equation 2.2**). Depending on the existing transduction element in the system, binding constants can be calculated from titration data by using various techniques like NMR, fluorescence and UV-Vis spectroscopy, potentiometry, and calorimetry.^{105,107} While choosing the proper technique, one of the limitations is that the sensitivity of the instrument should be high enough to be able to detect the concentrations at which

significant amounts of bound and free host and guest are in equilibrium.¹⁰⁵

As I stated before, binding constants provide thermodynamic parameters to predict the stability of the complex because of its link to Gibbs free energy (Eq. 2.3).^{105,107}



$$K = \frac{[ML^{m+}]}{[M(H_2O)_n^{m+}][L]} \quad (2.2)$$

$$\Delta G = -RT \ln K$$

$$\Delta G = \Delta H - T\Delta S \quad (2.3)$$

Therefore, any binding event can be seen as interplay between entropy and enthalpy.¹⁰⁵ For both cyclic and acyclic host molecules, the complexation process is mainly enthalpy favorable since there is an electronic affinity between M and L. On the other hand, entropy change is negative in most cases (sometimes, it is positive for crown ethers). Thus, complexation can happen only when entropy loss ($T\Delta S$) is surpassed by enthalpy gain (ΔH).¹⁰⁵

2.3.2 Factors that Promote Thermodynamical Selectivity by Stabilizing the Metal-Ligand Complex

When a ligand exhibits a strong affinity for a particular metal ion, it is assured to show some degree of selectivity towards these particular metal ions. The designs of the host molecules in nature ((integral membrane) transport proteins, enzymes, ionophores, and others) are the most successful examples of selective systems.¹⁰²⁻¹⁰⁵ For example, selectivity of voltage gated potassium and sodium channels towards potassium, and sodium respectively is of a paramount importance to maintain our body functioning properly and

it is originated from high discrimination power of the binding sites (pockets) of integral membrane proteins.^{102,105}

From a thermodynamical viewpoint, selectivity is the ratio of the binding constants for interfering guests (**Equation 2.4**). This means that when ligand (host) molecule is selective towards a specific ion, the Gibbs free energy of the M-L complex is very low compared to that with other ions. In other words, the factors, which increase the selectivity of L towards specific M, also enhance the stability of M-L complex.¹⁰⁵

$$\text{Selectivity} = \frac{K_{\text{metal ion 1}}}{K_{\text{metal ion 2}}} \quad (2.4)$$

Thermodynamic stability of M-L complex can be enhanced by the “**chelate effect**”.^{105,106} When the ligand has multiple convergent binding sites that are covalently linked to each other, it forms more stable M-L complex than a ligand with similar binding sites that are not connected. In order to achieve this effect, there should not be any steric strain between the binding sites upon binding.^{105,106} Another way of further increase the stability of M-L complex is the introduction of an element of preorganization. If a ligand (host) has a certain degree of rigidity so that it doesn't undergo significant conformational readjustment in the fashion of most complementary to the metal ion, the ligand is said to be “**preorganized**” (**Fig.2.8**).^{104,105} Since preorganization of the ligand contribute a major enhancement to the stability of M-L complex (decrease in the free energy), it is a fundamental concept. When a host is preorganized, it does not need to pay the energy penalty due to the loss of its entropy upon binding. One of the wise ways to make the ligand (host) rigid is to introduce a preformed cavity to the system that has a matched size with the size of the metal ion. This arrangement, which is traditionally termed as “**macrocyclic effect**” can be achieved by using ligands, composed of large rings or macrocycles within its structure (**Fig 2.8**).¹⁰⁵

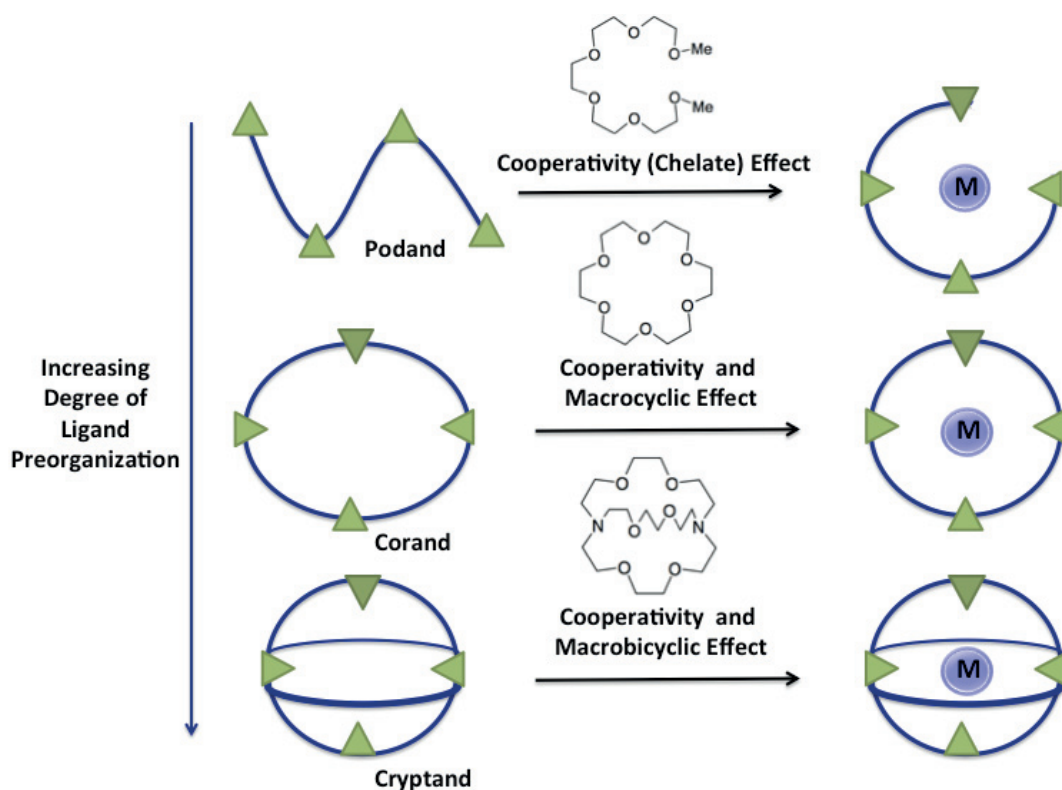


Figure 2.8: As the preorganization of the ligand increases from podand to cryptand, the ligand shows enhanced binding affinity towards a specific metal ion due to “preorganization” effect. Examples of host molecules that are designed according to each effect are shown above the arrows. Adapted from **Ref. 106** with permission from John Wiley and Sons.

In addition to the degree of preorganization, “**electronic complementary**” is the prominent factor to determine the affinity of the ligand molecule to the metal ion. According to Pearson’s hard and soft acids and bases (HSAB) theory, depending on the polarisability of the electron density of acids and bases, they can be hard or soft.^{104–106} Soft acids and bases are much more polarizable than hard acids and bases. As a general chemistry rule, hard acids prefer to bind to hard bases, whereas soft acids prefer to bind to soft bases, demonstrating the complementarity between like species (**Fig.2.9**).^{104–106} To illustrate, the soft transition metal ions like Hg^{2+} are bound more strongly by the softer sulphur atoms of the thio-crown ethers than the harder oxygen atoms of crown ethers.¹⁰⁶

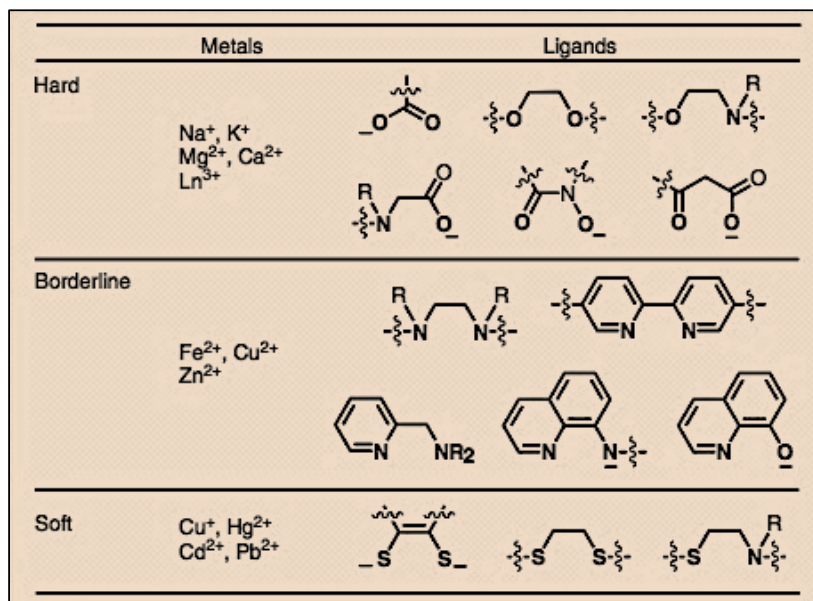


Figure 2.9: Categorization of chosen metal ions (as Lewis acids) and representative ligand motifs (as Lewis bases) based on HSAB theory. Reproduced from **Ref. 107** with permission from John Wiley and Sons.

2.3.3 Tunable Binding Ability of Crown Ethers Towards Metal Ions

Crown ethers are macrocyclic ligands composed of ethyleneoxy repeating units, and they were discovered by Charles Pedersen, a chemist working at the American du Pont de Nemours company in 1967.^{102,104,105} This discovery brought Pederson a share of 1987 Nobel Prize for chemistry. At the time of the discovery, naturally occurring ionophores like valinomycin had been known to form stable complexes with specific metal ions. Therefore, a lot of attention from researchers was given to ligands that are capable of selectively incorporating metal ions. They were seen as models of natural ionophores like gramicidin and valinomycin for the study of ion-transport routes in cell membranes, especially for sodium and potassium ions.¹⁰³ The electric dipole moments of the C–O–C ether groups result in a large electrostatic potential in the cavity, enabling binding to the metal ion. Since then, the crown ethers have become very popular as cation holding hosts due to the cooperativity effect and the partial preorganisation resulting from their macrocyclic structure. After earlier work on crown ethers, a huge variety of crown analogues (amine derivative (azacrowns), sulphur derivatives (thioethers)) and

functionalized crown ethers with different binding profiles towards specific ions have been obtained (Fig 2.10).¹⁰⁵

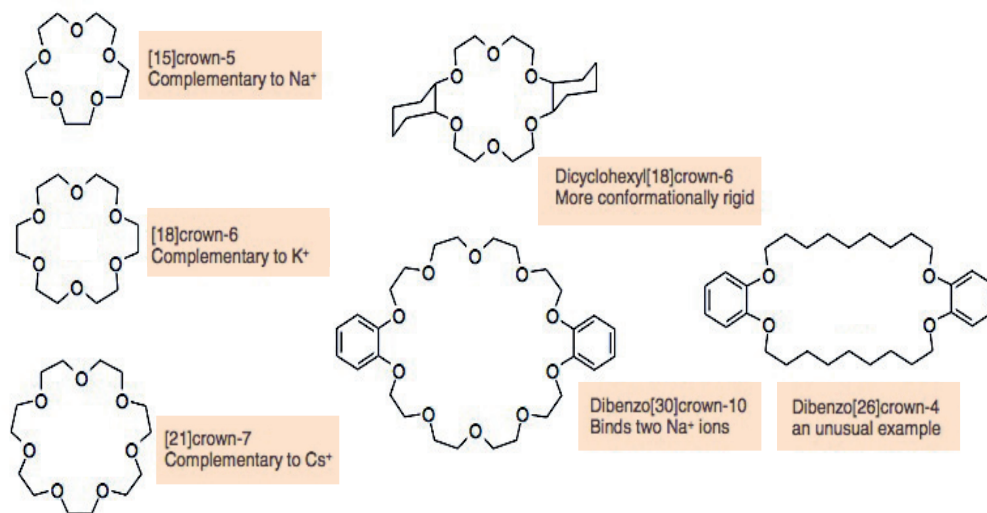


Figure 2.10: Examples of some common crown ethers. Adapted from Ref. 106 with permission from John Wiley and Sons.

One of the key criteria to ensure stable metal-ligand complex is to have a host organized in proper geometry so that it allows the metal ions to bind to all of the donor atoms at the optimal metal–ligand distance.^{105,106} Therefore, the shape and size of the cavity within crown ethers confer selectivity for complementary ions that fit in it.

Crown Ether	Cavity Diameter (Å)	Na ⁺ (1.90 Å)	K ⁺ (2.66 Å)	Rb ⁺ (3.04 Å)	Cs ⁺ (3.38 Å)	Ca ²⁺ (2.20 Å)
[12]Crown-4	1.20-1.50	1.70	1.30	-	-	-
[15]Crown-5	1.70-2.20	3.24	3.43	-	2.18	2.36
[18]Crown-6	2.60-3.20	4.35	6.08	5.32	4.70	3.90
[21]Crown-7	3.40-4.30	2.52	2.35	-	5.02	2.80

Table 2.1: Comparison of cavity diameter of various crown ethers and metal ions, binding constants of various metal-crown ether complexes (log K, Methanol, 20 °C)¹⁰³

Crown ethers can be synthesized in different sizes, so they can incorporate ions of

different sizes. However, since the crown ethers have some degree of flexibility, they do not hold a constant size cavity. This results in **plateau selectivity** of crown ethers, which means that they have a similar affinity for several metal ions with similar radius. This may lead to poor discrimination between Na⁺ and K⁺, or Rb⁺ and Cs⁺, which have similar radius. The phenomenon is more pronounced with the larger crown ethers due to their highly flexible nature.^{103–105} **Table 2.1** shows the binding constants for a selection of metal ions with various sizes of crown ethers. In addition, when the metal ion is too large to fit inside the cavity of the crown ether, sandwich complexes with metal/crown ratios at 1:2 and 2:3 can be formed.¹⁰⁵

In order to interpret the binding profile of crown ethers, “the size-match” criterion alone is not enough. We should consider the interplay of all the factors mentioned in previous section 2.3.2 that affect the thermodynamical stability of M-L complex. The magnitude of binding constant depends on the number of donor atoms, ligand bite angle, the charge on the metal cation, the nature of the solvent (solvation degree of ligand and cation), as well as the nucleophilicity of the counter-ion, and degree of electronic complementarity of the donor atoms with the metal.^{104–106} In addition, the comparative strain energies of the crown ethers in different conformations may also contribute.¹⁰⁶

2.4 General Scope of the Work

2.4.1 Previous Work Conducted by Our Group

A pioneer study on the development of low-cost, ultrasensitive and portable class of solid-state sensors for the detection of heavy metal cations in environmental samples has been published by our group in *Nature Materials* on 9 September 2012.¹ Beyond the proof-of-principal stage, they also demonstrated the applicability of the sensors by detecting atto to picomolar concentrations of methylmercury in tap water, lake water and fish.¹

The solid-state sensor consists of 150-nm-thick films of crosslinked networks of gold nanoparticles, and the platform is depicted in **Fig.2.11**. The films were formed via drop-casting method in the 50- μ m gaps between two sputtered gold microelectrodes on glass

(Fig. 2.11 (Left)).¹ The gold nanoparticles used in this work were coated with binary mixtures of hexanethiol (HT) and alkanethiols terminated with ethylene glycol (EG) units.

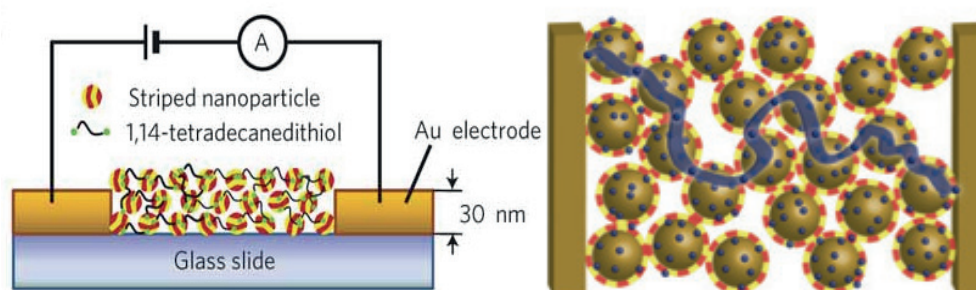


Figure 2.11: (Left) Side view of the crosslinked film of striped gold nanoparticles. (Right) An example of a conductive path after metal ion binding (dark blue line). Reproduced from Ref. 1 with permission from Nature Publishing Group.

Based on the change of tunneling current across the films of gold nanoparticles upon complexation of metal ions, ultrahigh sensitive detection of CH_3Hg^+ ions were achieved. The sensors were extremely selective as a result of their highly ordered ligand–shell architecture. The remarkable low limit of detection of their solid-state sensors (an unmatched attomolar limit for the detection of CH_3Hg^+) derives from the formation of

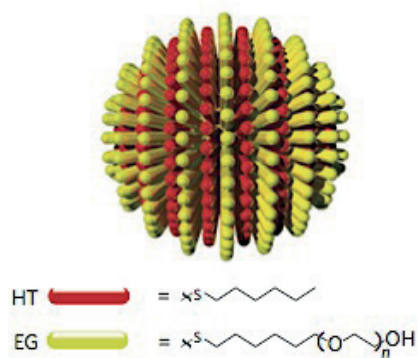


Figure 2.12: An idealized scheme of a striped nanoparticle. Reproduced from Ref. 1 with permission from Nature Publishing Group.

conductive pathways percolating the nanoparticle films due to local increase in tunneling current over individual NP-SAM/cation/NP-SAM bridges upon binding event (Fig.2.11 (right)). Heterogeneity of the nanoscale gold nanoparticle film expands the range of the cation-affinity constants, which leads to non-linear broad dynamic range of detection. Alternating arrangements of striped patterned SAMs (Fig.2.12) of these binary ligands generates supramolecular pockets that are able to selectively trap ions.¹

In this study, solution based conductometric titrations were performed for further verification of cation binding. As I will describe the details later in this thesis, they titrated the AuNP suspensions with salt solutions. The solution of HT/EG3 coated AuNPs were used for these experiments. Conductivity of the nanoparticle solution was expected to increase linearly as the salt was added (with a slope related to the cation's valence) if the cations do not bind to AuNPs. On the other hand, if conductivity initially increased only slowly before the binding sites were saturated, and the increase become linear afterwards, then this can be taken as an indication of binding. The results obtained from these solution-based experiments were mirroring the solid-state data, which evidenced the binding of Cs^+ cations, not the other ions. On the other hand, the extremely toxic CH_3Hg^+ was not used in these titration experiments since the quantity required to conduct solution-based experiments was really high, and therefore it was extremely dangerous for the people working in the laboratory environment. The results obtained from conductometric titrations are shown in **Fig.2.13**.

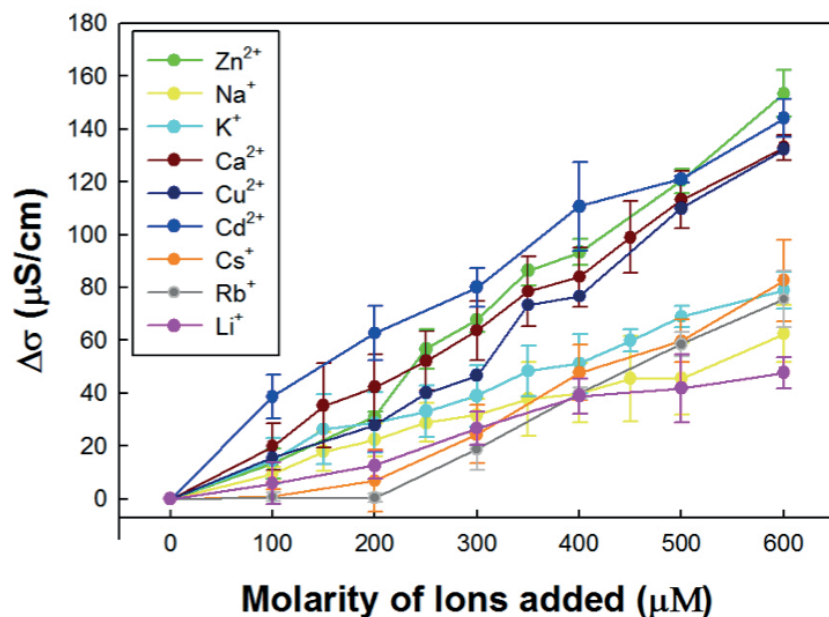


Figure 2.13: Conductometric titration plots for HT/EG3 coated AuNPs with various cations. The conductivity change was measured by adding different cation solutions into aqueous dispersion of AuNPs. Adapted from **Ref. 1** with permission from Nature Publishing Group.

2.4.2 Theoretical Explanation for Ion-Capturing by Striped AuNPs

To understand the concept behind the changes in the electronic structure of the molecular bridges between neighboring nanoparticles, quantum-mechanical calculations for a fragment of NP surface comprising two nearby EGN stripes and an HT stripe between them were performed.¹ They found that the highest occupied molecular orbital (HOMO) close to the nanoparticle surface and the lowest unoccupied molecular orbital (LUMO) on the EGN chains were involved in electron transport. They also showed that upon cation binding, the energy (ΔE) required for electron ejection from HOMO to LUMO is reduced. The smallest values of ΔE generally reflect the detection specificity observed in the experiments. In addition, the molecular dynamic simulations also revealed that energy gaps (ΔE) are lower when the binding sites of cations are located at the edges of the stripes than when these cations are fully buried within the EGN stripes (Fig.2.14). Thus, **the free space provided by HT** is crucial for the sensitivity of the sensor.¹

The decrease in energy gaps between the frontier orbitals (ΔE) upon cation binding increases the electronic conductance of a NP-SAM/cation/NP-SAM molecular bridge. These local increases in electron transport ability result in the formation of global conductive paths percolating the nanoparticle films when multiple cations bind into the NP film. Due to the heterogeneity of the structure of the film, the change in the conductance of the film on cation binding becomes nonlinear; ultimately leading to remarkable wide range of sensitivity. In other words, heterogeneity in the thin film gives rise to binding pockets with not a single but many different affinity constants.¹ The first binding pockets to be occupied at low concentrations are the ones with low dissociation constants, whereas binding pockets with high dissociation constants are saturated at much higher concentrations. This phenomena account for the very low detection limit and notable dynamic range of the sensor designed by our group. To sum up, our group provided an innovative point of view for solid-state sensing and enables low cost, sensitive and portable sensors for environmental analysis.¹

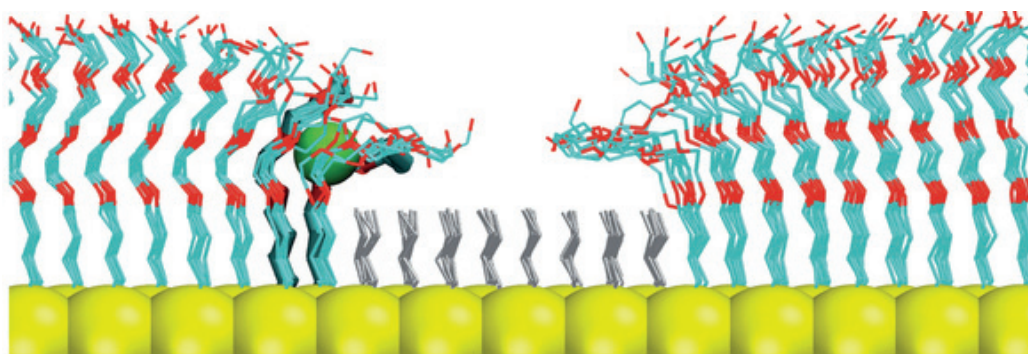


Figure 2.14: Typical cation-trapping scenario, where a metal ion (green ball) is bound near the edge of an EGN stripe. Reproduced from **Ref. 1** with permission from Nature Publishing Group.

2.5 The Motivation and the Aim of Our Study

The Cho study¹ showed that mixed-ligand coated AuNPs of specific size and ligand composition have a huge potential as selective and sensitive metal-ion sensors. The idea behind this work is mainly based on creating supramolecular binding pockets similar to that of crown ethers by using a correct combination of two dissimilar ligands, a hydrophilic and a hydrophobic ligand, on the surface of AuNPs. While the hydrophilic ligand participates in the chelation process, the hydrophobic ligand plays a crucial role in the formation of the “binding pockets” by providing a free space between the neighboring hydrophilic ligands, which would be impossible for single ligand coated nanoparticles.

On the other hand, a fundamental modeling of the binding process is needed in order to develop new recognition processes towards different metal ions. Therefore, the main motivation of this project was to obtain a clear and accurate understanding of the selective ion binding abilities of the AuNPs depending on the physicochemical properties of the particles. To achieve this goal, the ion binding capability of AuNPs are studied by shining light on the role of ligand composition, size of the NPs and the conformation of self-assembled monolayers (SAMs), which changes with respect to varying particle size and composition.

The chemical structure and abbreviation of the ligands utilized in this work is shown in **Fig. 2.15**. Two dissimilar ligands were used to form SAMs on the nanoparticle surface.

The hydrophobic shorter ligand was 1-hexanethiol (**HT**). The other ligand was hydrophilic alkanethiol containing two ethylene glycol terminal groups, 2-(2-((6-mercaptohexyl)oxy)ethoxy)ethanol (**EG2**). The two ligands were selected in such a way to mimic crown ethers, which are well known for selectively chelating metal ions. The whole work presented in **Chapter 3** and **4** is based on AuNPs coated with the combinations of **HT** and **EG2** ligands. In **Chapter 5**, 2-(2-(2-(((6-mercaptohexyl)oxy)ethoxy)ethoxy)ethoxy)ethanol (**EG3**) was used in the synthesis of AuNPs instead of **EG2** since more soluble particles were needed for the special technique that was used to fractionate the particles with respect to their size. Detailed explanation will be given in **Chapter 5**.

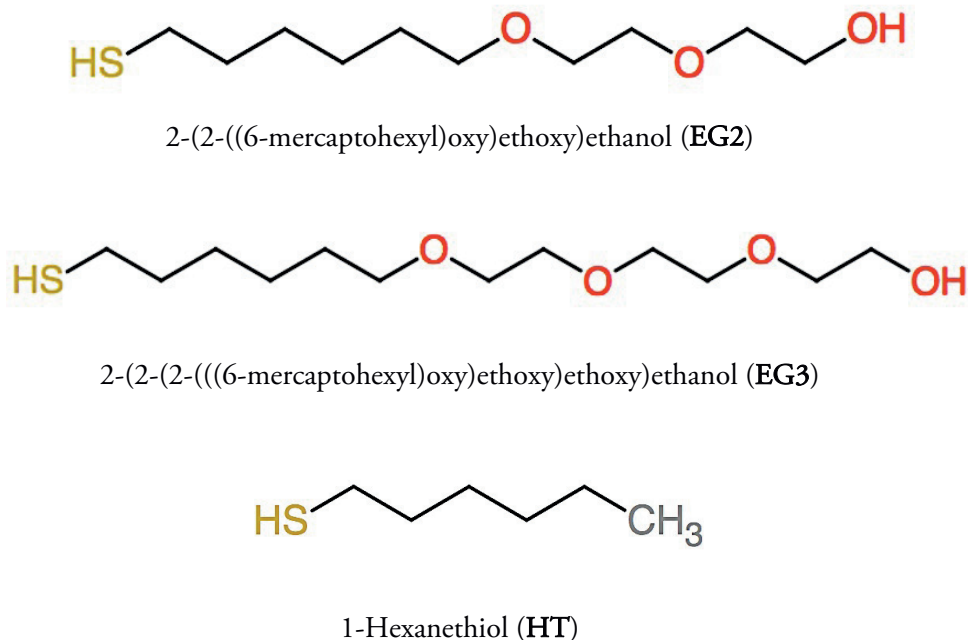


Figure. 2.15: The chemical structure and abbreviation of the ligands on the surface of AuNPs

REFERENCES

- (1) Cho, E. S.; Kim, J.; Tejerina, B.; Hermans, T. M.; Jiang, H.; Nakanishi, H.; Yu, M.; Patashinski, A. Z.; Glotzer, S. C.; Stellacci, F.; Grzybowski, B. A. Ultrasensitive Detection of Toxic Cations through Changes in the Tunnelling Current across Films of Striped Nanoparticles. *Nat. Mater.* 2012, 11 (11), 978–985.
- (2) Burgess, J. (1978). *Metal Ions in Solution*. New York, USA: Ellis Horwood.
- (3) Williams, D. R. (1971). *The Metals of Life: The Solution Chemistry of Metal Ions in Biological Systems*. New York, USA: Van Nostrand Reinhold.
- (4) Maret, W. The Metals in the Biological Periodic System of the Elements: Concepts and Conjectures. *Int. J. Mol. Sci.* 2016, 17 (1), 1–8.
- (5) Glusker, J. P.; Katz, A. M. Y. K.; Bock, C. W. Metal Ions in Biological Systems. *Rigaku J.* 1999, 16 (2), 8–17.
- (6) Chellan, P.; Sadler, P. J. The Elements of Life and Medicines. *Philos. Trans. A. Math. Phys. Eng. Sci.* 2015, 373, 1-56.
- (7) Martin, R. B. (2006). Metal Ion Toxicity. *Encyclopedia of Inorganic Chemistry*. New Jersey, USA: John Wiley & Sons.
- (8) Crichton, R. R. (2017). *Metal Toxicity - An Introduction*. Cambridge, UK: Royal Society of Chemistry.
- (9) Crichton, R. R. (2012). “An Overview of Metals and Selected Nonmetals in Biology”. *Biological Inorganic Chemistry*. Elsevier.
- (10) Fernández-Luqueño, F.; López-Valdez, F.; Gamero-Melo, P.; Luna-Suárez, S.; Aguilera-González, E.; Martínez, A.; García-Guillermo, M.; Hernández-Martínez, G.; Herrera-Mendoza, R.; Álvarez-Garza, M.; Pérez-Velázquez, I. Heavy Metal Pollution in Drinking Water - a Global Risk for Human Health: A Review. *African J. Environ. Sci. Technol.* 2013, 7 (7), 567–584.
- (11) Strohfeldt, K. A. (2015). *Essentials of Inorganic Chemistry: For Students of Pharmacy, Pharmaceutical Sciences and Medicinal Chemistry*. New Jersey, USA: John Wiley & Sons.
- (12) Bhargavi, M.; Sethuraman, S.; Maheswari, U. Detection of Heavy Metal Ions in Water – An Electrochemical Approach. *Sensors Actuators B. Chem.* 2015, 213, 515–533.
- (13) Tchounwou, P. B.; Yedjou, C. G.; Patlolla, A. K.; Sutton, D. J. (2012).

Molecular, Clinical and Environmental Toxicology. Basel: Springer.

- (14) Singh, R.; Gautam, N.; Mishra, A.; Gupta, R. Heavy Metals and Living Systems: An Overview. *Indian J. Pharmacol.* 2011, 43 (3), 246.
- (15) Jaishankar, M.; Tseten, T.; Anbalagan, N.; Mathew, B. B.; Beeregowda, K. N. Toxicity, Mechanism and Health Effects of Some Heavy Metals. *Interdiscip. Toxicol.* 2014, 7 (2), 60–72.
- (16) Aragay, G.; Merkoç, A. Recent Trends in Macro-, Micro-, and Nanomaterial-Based Tools and Strategies for Heavy-Metal Detection. 2011, 3433–3458.
- (17) Drost, W.; Agency, F. E. (2011). “Metals in the Environment”. *Biological Inorganic Chemistry*. Elsevier.
- (18) Martell, A. E. Chemistry of Carcinogenic Metals. *Environ. Health Perspect.* 1981, Vol. 40, 207–226.
- (19) Brown, R. J. C.; Milton, M. J. T. Analytical Techniques for Trace Element Analysis: An Overview. *Trends Anal. Chem.* 2005, 24, 266–274.
- (20) Mao, S.; Chang, J.; Zhou, G.; Chen, J. Nanomaterial-Enabled Rapid Detection of Water Contaminants. *Small.* 2015, 11 (40), 5336–5359.
- (21) Kot, A.; Namiesn, J. The Role of Speciation in Analytical Chemistry. *Trends Anal. Chem.* 2000, 19, 69–79.
- (22) Zhao, W. W.; Xu, J. J.; Chen, H. Y. Photoelectrochemical Detection of Metal Ions. *Analyst* 2016, 141 (14), 4262–4271.
- (23) Radu, A.; Diamond, D. Ion-Selective Electrodes in Trace Level Analysis of Heavy Metals: Potentiometry for the XXI Century. *Compr. Anal. Chem.* 2007, 49 (6), 25–52.
- (24) Ahuja, S. Overview. *Compr. Anal. Chem.* 2006, 47 (6), 1–13.
- (25) Ceresa, A.; Bakker, E.; Hattendorf, B.; Günther, D.; Pretsch, E. Potentiometric Polymeric Membrane Electrodes for Measurement of Environmental Samples at Trace Levels: New Requirements for Selectivities and Measuring Protocols, and Comparison with ICPMS. *Anal. Chem.* 2001, 73 (2), 343–351.
- (26) Helaluddin, A.; Khalid, R. S.; Alaama, M.; Abbas, S. A. Main Analytical Techniques Used for Elemental Analysis in Various Matrices. *Trop. J. Pharm. Res.* 2016, 15 (2), 427.
- (27) Skoog, D. A.; Leary, J. J. (1992) *Principles of Instrumental Analysis*. Philadelphia, USA: Saunders College Pub.
- (28) Adam H.; S. G.; F. I. Commission on General Aspects of Analytical Chemistry

- and Chemical Sensors. *Pure Appl. Chem.* 1991, 63 (9), 1247–1250.
- (29) Saha, K.; Agasti, S.; Kim, C.; Li, X.; Rotello, V. Gold Nanoparticles in Chemical and Biological Sensing. *Chem. Rev.* 2012, 112, 2739–2779.
 - (30) Janata, J.; Josowicz, M. Conducting Polymers in Electronic Chemical Sensors. *Nat. Mater.* 2003, 2 (1), 19–24.
 - (31) Takahashi, T.; Takei, K.; Gillies, A. G.; Fearing, R. S.; Javey, A. (2011). “Nanoparticles and Sensors”. *Chemosensors: Principles, Strategies, and Applications*. New Jersey, USA: John Wiley & Sons.
 - (32) Almeida, M. P. De; Baptista, P. V. (2014). “Gold Nanoparticles as (Bio) Chemical Sensors”. *Gold Nanoparticles in Analytical Chemistry*. Elsevier Science.
 - (33) Peveler, W. J.; Yazdani, M.; Rotello, V. M. Selectivity and Specificity: Pros and Cons in Sensing. *ACS Sensors.* 2016, 1 (11), 1282–1285.
 - (34) Lin, Y. W.; Huang, C. C.; Chang, H. T. Gold Nanoparticle Probes for the Detection of Mercury, Lead and Copper Ions. *Analyst.* 2011, 136 (5), 863–871.
 - (35) Wang, Z.; Ma, L. Gold Nanoparticle Probes. *Coord. Chem. Rev.* 2009, 253, 1607–1618.
 - (36) Priyadarshini, E.; Pradhan, N. Gold Nanoparticles as Efficient Sensors in Colorimetric Detection of Toxic Metal Ions: A Review. *Sensors Actuators B Chem.* 2016, 238, 888–902.
 - (37) Chansuvarn, W.; Tuntulani, T.; Imyim, A. Colorimetric Detection of mercury(II) Based on Gold Nanoparticles, Fluorescent Gold Nanoclusters and Other Gold-Based Nanomaterials. *TrAC Trends Anal. Chem.* 2015, 65, 83–96.
 - (38) Ma, Y.; Jiang, L.; Mei, Y.; Song, R.; Tian, D.; Huang, H. Colorimetric Sensing Strategy for Mercury (II) and Melamine Utilizing Cysteamine-Modified Gold Nanoparticles. *Analyst.* 2013, 138 (18), 5338.
 - (39) Huang C. C.; Chang H. T. Selective Gold-Nanoparticle-Based “Turn-On” Fluorescent Sensors for Detection of Mercury (II) in Aqueous Solution. *Anal. Chem.* 2006, 78 (24), 8332–8338
 - (40) Yu, C. J.; Tseng, W. L. Colorimetric Detection of Mercury (II) in a High-Salinity Solution Using Gold Nanoparticles Capped with 3-Mercaptopropionate Acid and Adenosine Monophosphate. *Langmuir.* 2008, 24 (21), 12717–12722.
 - (41) Huang, C. C.; Chang, H. T. Parameters for Selective Colorimetric Sensing of Mercury in Aqueous Solutions Using Mercaptopropionic Acid-Modified Gold Nanoparticles. *Chem. Commun.* 2007, No. 12, 1215–1217.

- (42) Tan, Z.; Liu, J.; Liu, R.; Yin, Y.; Jiang, G.; Wu, Y.; Jiang, G. B. Visual and Colorimetric Detection of Hg²⁺ by Cloud Point Extraction with Functionalized Gold Nanoparticles as a Probe. *Chem. Commun.* 2009, 81 (45), 7030.
- (43) Huang, C. C.; Yang, Z.; Lee, K.-H.; Chang, H.-T. Synthesis of Highly Fluorescent Gold Nanoparticles for Sensing Mercury (II). *Angew. Chemie Int. Ed.* 2007, 46 (36), 6824–6828.
- (44) Su, D.; Yang, X.; Xia, Q.; Chai, F.; Wang, C.; Qu, F.; Watt, A. A. R.; Huo, Q.; Wang, Y. S.; Yu, R. Q. Colorimetric Detection of Hg²⁺ Using Thiocetic Acid Functionalized Gold Nanoparticles. *RSC Adv.* 2013, 3 (46), 24618.
- (45) Kim, Y. R.; Mahajan, R. K.; Kim, J. S.; Kim, H. Highly Sensitive Gold Nanoparticle-Based Colorimetric Sensing of Mercury (II) through Simple Ligand Exchange Reaction in Aqueous Media. *ACS Appl. Mater. Interfaces.* 2010, 2 (1), 292–295.
- (46) Chen, X.; Zu, Y.; Xie, H.; Kemas, A. M.; Gao, Z.; Ray, P. C.; Fan, C.; Li, G.; Fan, C. Coordination of Mercury (II) to Gold Nanoparticle Associated Nitrotriazole towards Sensitive Colorimetric Detection of Mercuric Ion with a Tunable Dynamic Range. *Analyst.* 2011, 136 (8), 1690.
- (47) Darbha, G. K.; Singh, K.; Rai, U. S.; Yu, E.; Yu, H. T.; Ray, P. C. Selective Detection of Mercury (II) Ion Using Nonlinear Optical Properties of Gold Nanoparticles. *J. Am. Chem. Soc.* 2008, 130 (25), 8038–8043.
- (48) Zamarion, V. M.; Timm, R. A.; Araki, K.; Toma, H. E. Ultrasensitive SERS Nanoprobes for Hazardous Metal Ions Based on Trimercaptotriazine-Modified Gold Nanoparticles. *Inorg. Chem.* 2008, 47 (8), 2934–2936.
- (49) Guo, Z.; Liu, Z.-G.; Yao, X.-Z.; Zhang, K.-S.; Chen, X.; Liu, J.-H.; Huang, X.-J. A Molecular-Gap Device for Specific Determination of Mercury Ions. *Sci. Rep.* 2013, 3, 3115.
- (50) Chen, L.; Li, J.; Chen, L. Colorimetric Detection of Mercury Species Based on Functionalized Gold Nanoparticles. *ACS Appl. Mater. Interfaces.* 2014, 6 (18), 15897–15904.
- (51) Maiti, S.; Pezzato, C.; Garcia Martin, S.; Prins, L. J. Multivalent Interactions Regulate Signal Transduction in a Self-Assembled Hg²⁺ Sensor. *J. Am. Chem. Soc.* 2014, 136 (32), 11288–11291.
- (52) Ding, N.; Cao, Q.; Zhao, H.; Yang, Y.; Zeng, L.; He, Y.; Xiang, K.; Wang, G. Colorimetric Assay for Determination of Lead (II) Based on Its Incorporation into Gold Nanoparticles during Their Synthesis. *Sensor.* 2010, 10 (12), 11144–11155.
- (53) Karuvath Y.; Binil I. I.; Cherumuttathu H. S.; Thomas G. In Situ Synthesis of

- Metal Nanoparticles and Selective Naked-Eye Detection of Lead Ions from Aqueous Media. *J. Phys. Chem. C*. 2007, 111 (34), 12839–12847.
- (54) Huang, K. W.; Yu, C. J.; Tseng, W. L. Sensitivity Enhancement in the Colorimetric Detection of Lead (II) Ion Using Gallic Acid-capped Gold Nanoparticles: Improving Size Distribution and Minimizing Interparticle Repulsion. *Biosens. Bioelectron.* 2010, 25 (5), 984–989.
- (55) Chai, F.; Wang, C.; Wang, T.; Li, L.; Su, Z. Colorimetric Detection of Pb²⁺ Using Glutathione Functionalized Gold Nanoparticles. *ACS Appl. Mater. Interfaces* 2010, 2 (5), 1466–1470.
- (56) Li, L.; Yuan, Z.; Peng, X.; Li, L.; He, J.; Zhang, Y. Highly Selective Colorimetric Detection of Copper Ions Using Cysteamine Functionalized Gold Nanoparticles. *J. Chinese Chem. Soc.* 2014, 61 (12), 1371–1376.
- (57) Ratnarathorn, N.; Chailapakul, O.; Dungchai, W. Highly Sensitive Colorimetric Detection of Lead Using Maleic Acid Functionalized Gold Nanoparticles. *Talanta*. 2015, 132, 613–618.
- (58) Lee, I. L.; Sung, Y. M.; Wu, S. P. Triazole-Acetate Functionalized Gold Nanoparticles for Colorimetric Pb (II) Sensing. *RSC Adv.* 2014, 4 (48), 25251.
- (59) Youngjin K.; Robert C. J., and; Hupp, J. T. Gold Nanoparticle-Based Sensing of “Spectroscopically Silent” Heavy Metal Ions. *Nano Letters*. 2001, 1 (4), 165–167.
- (60) Wang, X.; Guo, X. Ultrasensitive Pb²⁺ Detection Based on Fluorescence Resonance Energy Transfer (FRET) between Quantum Dots and Gold Nanoparticles. *Analyst*. 2009, 134 (7), 1348.
- (61) Frost, M. S.; Dempsey, M. J.; Whitehead, D. E. Highly Sensitive SERS Detection of Pb²⁺ Ions in Aqueous Media Using Citrate Functionalized Gold Nanoparticles. *Sensors Actuators B Chem.* 2015, 221, 1003–1008.
- (62) Wang, A. J.; Guo, H.; Zhang, M.; Zhou, D. L.; Wang, R. Z.; Feng, J. J. Sensitive and Selective Colorimetric Detection of cadmium (II) Using Gold Nanoparticles Modified with 4-Amino-3-Hydrazino-5-Mercapto-1,2,4-Triazole. *Microchim. Acta* 2013, 180 (11–12), 1051–1057.
- (63) Xue, Y.; Zhao, H.; Wu, Z.; Li, X.; He, Y.; Yuan, Z. Colorimetric Detection of Cd²⁺ Using Gold Nanoparticles Cofunctionalized with 6-Mercaptonicotinic Acid and L-Cysteine. *Analyst*. 2011, 136 (18), 3725.
- (64) Yao, Y.; Sun, Z.; Zou, Z.; Li, H. Quinolono-Triazole Linked Gold Nanoparticles as Sensitive “Turn-on” Fluorescent Cd²⁺ Probes. *Nanotechnology* 2011, 22, 1–5.
- (65) Liu, G.; Zhang, Y.; Qi, M.; Chen, F. Covalent Anchoring of Multifunctionized

- Gold Nanoparticles on Electrodes towards an Electrochemical Sensor for the Detection of Cadmium Ions. *Anal. Methods* 2015, 7 (13), 5619–5626.
- (66) Yang, W.; Gooding, J. J.; He, Z.; Li, Q.; Chen, G. Fast Colorimetric Detection of Copper Ions Using L-Cysteine Functionalized Gold Nanoparticles. *J. Nanosci. Nanotechnol.* 2007, 7 (2), 712–716.
- (67) Mehta, V. N.; Basu, H.; Singhal, R. K.; Kailasa, S. K. Simple and Sensitive Colorimetric Sensing of Cd²⁺ Ion Using Chitosan Dithiocarbamate Functionalized Gold Nanoparticles as a Probe. *Sensors Actuators, B Chem.* 2015, 220, 850–858.
- (68) Nath, P.; Arun, R. K.; Chanda, N. Smart Gold Nanosensor for Easy Sensing of Lead and Copper Ions in Solution and Using Paper Strips. *RSC Adv.* 2015, 5 (84), 69024–69031.
- (69) Zhou, Y.; Wang, S.; Zhang, K.; Jiang, X. Visual Detection of Copper (II) by Azide- and Alkyne-Functionalized Gold Nanoparticles Using Click Chemistry. *Angew. Chemie - Int. Ed.* 2008, 47 (39), 7454–7456.
- (70) Hua, C.; Zhang, W. H.; De Almeida, S. R. M.; Ciampi, S.; Gloria, D.; Liu, G.; Harper, J. B.; Gooding, J. J. A Novel Route to Copper (II) Detection Using “Click” Chemistry-Induced Aggregation of Gold Nanoparticles. *Analyst* 2012, 137 (1), 82–86.
- (71) Ye, Y.; Lv, M.; Zhang, X.; Zhang, Y. Colorimetric Determination of Copper Ions Using Gold Nanoparticles as a Probe. *RSC Adv.* 2015, 5, 102311–102317.
- (72) He, X.; Liu, H.; Li, Y.; Wang, S.; Li, Y.; Wang, N.; Xiao, J.; Xu, X.; Zhu, D. Gold Nanoparticle-Based Fluorometric and Colorimetric Sensing of Copper (II) Ions. *Adv. Mater.* 2005, 17 (23), 2811–2815.
- (73) Foroushani, A.; Zhang, Y.; Li, D.; Mathesh, M.; Wang, H.; Yan, F.; Barrow, C. J.; He, J.; Yang, W. Tunnelling Current Recognition through Core–satellite Gold Nanoparticles for Ultrasensitive Detection of Copper Ions. *Chem. Commun.* 2015, 51 (14), 2921–2924.
- (74) Choi, Y.; Park, Y.; Kang, T.; Lee, L. P. Selective and Sensitive Detection of Metal Ions by Plasmonic Resonance Energy Transfer-Based Nanospectroscopy. *Nat. Nanotechnol.* 2009, 4 (11), 742–746.
- (75) Long, D.; Yu, H. A Synergistic Coordination Strategy for Colorimetric Sensing of Chromium (III) Ions Using Gold Nanoparticles. *Anal. Bioanal. Chem.* 2016, 408 (29), 8551–8557.
- (76) Liu, D.; Wang, Z.; Jiang, X. Gold Nanoparticles for the Colorimetric and Fluorescent Detection of Ions and Small Organic Molecules. *Nanoscale* 2011, 3

- (4), 1421–1433.
- (77) Elavarasi, M.; Rajeshwari, A.; Chandrasekaran, N.; Mukherjee, A. Simple Colorimetric Detection of Cr (III) in Aqueous Solutions by as Synthesized Citrate Capped Gold Nanoparticles and Development of a Paper Based Assay. *Anal. Methods* 2013, 5 (21), 6211–6218.
- (78) Kalluri, J. R.; Arbneshi, T.; Afrin Khan, S.; Neely, A.; Candice, P.; Varisli, B.; Washington, M.; McAfee, S.; Robinson, B.; Banerjee, S.; Singh, A. K.; Senapati, D.; Ray, P. C. Use of Gold Nanoparticles in a Simple Colorimetric and Ultrasensitive Dynamic Light Scattering Assay: Selective Detection of Arsenic in Groundwater. *Angew. Chemie Int. Ed.* 2009, 48 (51), 9668–9671.
- (79) Domínguez-González, R.; González Varela, L.; Bermejo-Barrera, P. Functionalized Gold Nanoparticles for the Detection of Arsenic in Water. *Talanta*. 2014, 118, 262–269.
- (80) Shrivastava, K.; Shankar, R.; Dewangan, K. Gold Nanoparticles as a Localized Surface Plasmon Resonance Based Chemical Sensor for on-Site Colorimetric Detection of Arsenic in Water Samples. *Sensors Actuators B Chem.* 2015, 220, 1376–1383.
- (81) Zhang, J.; Zhang, C.-L. L.; Yu, S.-H. H. Tuning Gold Nanoparticle Aggregation through the Inhibition of Acid Phosphatase Bioactivity: A Plasmonic Sensor for Light-Up Visual Detection of Arsenate (V). *Chempluschem* 2016, 81 (11), 1147–1151.
- (82) Krpetic Z.; Guerrini, L.; Larmour, I. A.; Reglinski, J.; Faulds, K.; Graham, D. Importance of Nanoparticle Size in Colorimetric and SERS-Based Multimodal Trace Detection of Ni (II) Ions with Functional Gold Nanoparticles. *Small* 2012, 8 (5), 707–714.
- (83) Kim, E. J.; Chung, B. H.; Lee, H. J. Parts per Trillion Detection of Ni (II) Ions by Nanoparticle-Enhanced Surface Plasmon Resonance. *Anal. Chem.* 2012, 84 (22), 10091–10096.
- (84) Casalini, S.; Bortolotti, C. A.; Leonardi, F.; Biscarini, F. Self-Assembled Monolayers in Organic Electronics. *Chem. Soc. Rev.* 2017, 46 (1), 40–71.
- (85) Love, J. C.; Estroff, L. a.; Kriebel, J. K.; Nuzzo, R. G.; Whitesides, G. M. Self-Assembled Monolayers of Thiolates on Metals as a Form of Nanotechnology. *Chem. Rev.* 2005, 105 (4), 1103–1170
- (86) Vericat, C.; Vela, M. E.; Benitez, G.; Carro, P.; Salvarezza, R. C. Self-Assembled Monolayers of Thiols and Dithiols on Gold: New Challenges for a Well-Known System. *Chem. Soc. Rev.* 2010, 39 (5), 1805.
- (87) Bürgi, T. Properties of the Gold–sulphur Interface: From Self-Assembled

- Monolayers to Clusters. *Nanoscale* 2015, 7 (38), 15553–15567.
- (88) Häkkinen, H. The Gold–sulfur Interface at the Nanoscale. *Nat. Chem.* 2012, 4 (6), 443–455.
- (89) Singh, C.; Ghorai, P. K.; Horsch, M. A.; Jackson, A. M.; Larson, R. G.; Stellacci, F.; Glotzer, S. C. Entropy-Mediated Patterning of Surfactant-Coated Nanoparticles and Surfaces. *Phys. Rev. Lett.* 2007, 99 (22), 226106.
- (90) Ong, Q. K.; Reguera, J.; Silva, P. J.; Moglianetti, M.; Harkness, K.; Longobardi, M.; Mali, K. S.; Renner, C.; De Feyter, S.; Stellacci, F. High-Resolution Scanning Tunneling Microscopy Characterization of Mixed Monolayer Protected Gold Nanoparticles. *ACS Nano* 2013, 7 (10), 8529–8539.
- (91) Jackson, A. M.; Myerson, J. W.; Stellacci, F. Spontaneous Assembly of Subnanometre-Ordered Domains in the Ligand Shell of Monolayer-Protected Nanoparticles. *Nat. Mater.* 2004, 3 (5), 330–336.
- (92) Liu, X.; Yu, M.; Kim, H.; Mameli, M.; Stellacci, F. Determination of Monolayer-Protected Gold Nanoparticle Ligand-Shell Morphology Using NMR. *Nat. Commun.* 2012, 3, 1182.
- (93) Uzun, O.; Hu, Y.; Verma, A.; Chen, S.; Centrone, A.; Stellacci, F.; Centrone, A.; Chen, S.; Uzun, O.; Hu, Y.; Verma, A.; Chen, S.; Centrone, A.; Stellacci, F. Water-Soluble Amphiphilic Gold Nanoparticles with Structured Ligand Shells. *Chem. Commun.* 2007, 2, 196–198.
- (94) Harkness, K. M.; Balinski, A.; McLean, J. A.; Cliffel, D. E. Nanoscale Phase Segregation of Mixed Thiolates on Gold Nanoparticles. *Angew. Chem. Int. Ed. Engl.* 2011, 50 (45), 10554–10559.
- (95) Lucarini, M.; Pasquato, L. ESR Spectroscopy as a Tool to Investigate the Properties of Self-Assembled Monolayers Protecting Gold Nanoparticles. *Nanoscale*. 2010, 2 (5), 668–676.
- (96) Wang, Y.; Zeiri, O.; Neyman, A.; Stellacci, F.; Weinstock, I. A. Nucleation and Island Growth of Alkanethiolate Ligand Domains on Gold Nanoparticles. *ACS Nano*. 2012, 6 (1), 629–640.
- (97) Moglianetti, M.; Ong, Q. K.; Reguera, J.; Harkness, K. M.; Mameli, M.; Radulescu, A.; Kohlbrecher, J.; Jud, C.; Svergun, D. I.; Stellacci, F. Scanning Tunneling Microscopy and Small Angle Neutron Scattering Study of Mixed Monolayer Protected Gold Nanoparticles in Organic Solvents. *Chem. Sci.* 2014, 5 (3), 1232.
- (98) Carney, R. P.; DeVries, G. A.; Dubois, C.; Kim, H.; Kim, J. Y.; Singh, C.; Ghorai, P. K.; Tracy, J. B.; Stiles, R. L.; Murray, R. W.; Glotzer, S. C.; Stellacci,

- F. Size Limitations for the Formation of Ordered Striped Nanoparticles. *J. Am. Chem. Soc.* 2008, 130 (3), 798–799.
- (99) Verma, A.; Uzun, O.; Hu, Y.; Hu, Y.; Han, H.-S.; Watson, N.; Chen, S.; Irvine, D. J.; Stellacci, F. Surface-Structure-Regulated Cell-Membrane Penetration by Monolayer-Protected Nanoparticles. *Nat. Mater.* 2008, 7 (7), 588–595.
- (100) Ghosh, A.; Basak, S.; Wunsch, B. H.; Kumar, R.; Stellacci, F. Effect of Composition on the Catalytic Properties of Mixed-Ligand-Coated Gold Nanoparticles. *Angew. Chem. Int. Ed. Engl.* 2011, 50 (34), 7900–7905.
- (101) Kuna, J. J.; Voitchovsky, K.; Singh, C.; Jiang, H.; Mwenifumbo, S.; Ghorai, P. K.; Stevens, M. M.; Glotzer, S. C.; Stellacci, F. The Effect of Nanometre-Scale Structure on Interfacial Energy. *Nat. Mater.* 2009, 8 (10), 837–842.
- (102) Kralj, M.; Tusek, B. L.; Frkanec, L. Biomedical Potentials of Crown Ethers: Prospective Antitumor Agents. *ChemMedChem.* 2008, 3 (10), 1478–1492.
- (103) Ariga, K.; Kunitake, T. (2006). *Supramolecular Chemistry - Fundamentals and Applications: Advanced Textbook*; Verlag Berlin Heidelberg: Springer.
- (104) Vögtle, F.; Alfter, F. (1991). *Supramolecular Chemistry: An Introduction*. New Jersey, USA: John Wiley & Sons.
- (105) Steed, J. W.; Atwood, J. L. (2009). *Supramolecular Chemistry*. New Jersey, USA: John Wiley & Sons.
- (106) Lee, D. Metal Chelation Chemistry. *Chemosens. Princ. Strateg. Appl.* 2011, 1, 41–64.
- (107) Thordarson, P. Determining Association Constants from Titration Experiments in Supramolecular Chemistry. *Chem. Soc. Rev.* 2011, 40, 1305–1323.

CHAPTER 3

Synthesis and Characterization of Mixed-Ligand Protected Gold Nanoparticles

One of the first objectives of this project was to succeed in the nanoparticle synthesis in order to better control their size and ligand ratio while also increasing reproducibility. As was soon evident, the size and ligand ratio of the nanoparticles greatly affects their ion-binding abilities. In order to understand the relationship between metal binding properties and the physical properties of AuNPs, we constructed a 2-D map of nanoparticle size and ligand ratio. Therefore, the size and the ligand ratio of the particles were varied by using different synthetic protocols. This chapter deals with the synthetic protocols and their variations to obtain a series of mixed ligand (EG2:HT) coated gold nanoparticles. In addition, the characterization tools of synthesized particles are introduced. These characterization techniques functioned as the mainstay of nearly all of the measurements and results in this thesis. Being able to accurately characterize the particles was essential for our understanding of the factors that needed to be controlled or altered in order to achieve the desired properties.

3.1 Synthesis and Purification of Mixed Ligand Coated Gold Nanoparticles

Synthesis of gold nanoparticles protected by thiolate groups were achieved by various methods.^{1,2} The most common approaches are based on reduction of gold ions in liquid phase in the presence of protective ligands. Typically, those techniques can be divided into two main categories as “the ligand exchange method” and “the direct synthesis method”.^{1,2}

For a long time, **the ligand exchange method** was used to synthesize thiolated AuNPs. In 1951, Turkevich developed the synthesis of ~10-20 nm AuNPs stabilized by sodium citrate ($\text{Na}_3\text{C}_3\text{H}_5\text{O}(\text{COO})_3$) molecules. In this synthesis, chloroauric acid (HAuCl_4) is reduced by citrate molecules that also function as a capping ligand of nanoparticles.³ Then, thiolate molecules, which are stronger capping agents, can be replaced with citrate molecules on the surface of the particles.

In 1994, Brust *et al.* developed **the direct synthesis method**, where gold ions are reduced by strong reducing agent in the presence of thiolate ligands.⁴ The original approach depicted in **Fig. 3.1** consists of a two-phase synthesis: the dissolution of a gold salt in aqueous phase, followed by a phase transfer into the organic phase, then the addition of thiolated molecules to form gold-thiol polymer complex and reduction by sodium borohydride (NaBH_4).^{2,4} This technique results in polydispersed nanoparticles in a range of ~1-7 nm and the average size of the particles can be controlled by several parameters like the Au to thiol ratio, the type of chemical functionality (R in **Fig.3.1**), the reduction rate and the temperature of the reaction.

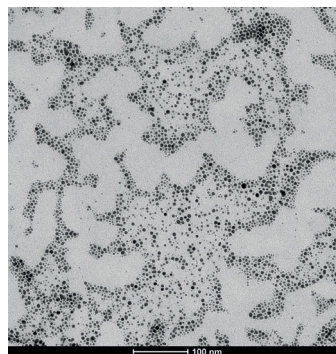
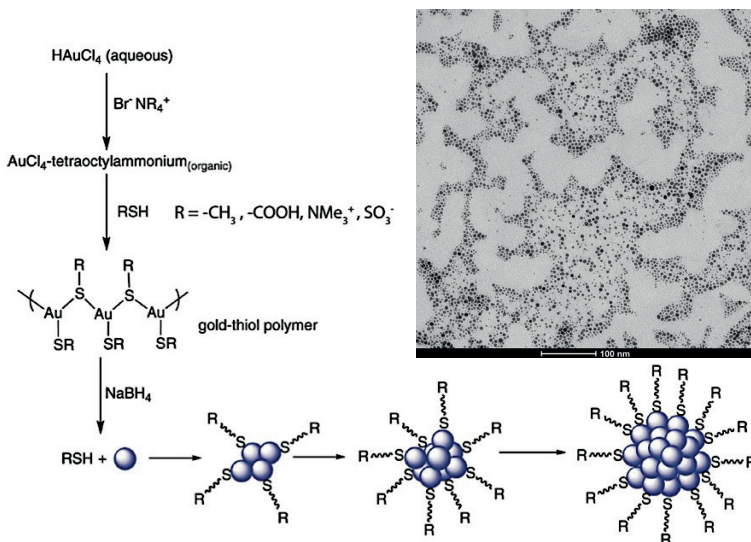


Figure 3.1: The original direct synthetic scheme of conventional gold nanoparticles proposed by Brust *et al.* A TEM micrograph of a typical synthesis using EG2 ligands is shown to exemplify the size distribution of the particles. Reproduced from **Ref. 2** with permission from American Chemical Society.

To synthesize water-soluble AuNPs, the phase transfer stage can be omitted, and the gold salt (HAuCl_4) can be directly dissolved in ethanol, followed by addition of the thiolated ligands (in our case, mixture of two thiolated ligands). After a short period of time, typically 10 to 30 minutes, a solution of NaBH_4 is added to the reaction medium. NaBH_4 leads to nucleation of the thiol-gold complex and grow into nanoparticles. This protocol is called the “**one-phase synthesis method**” and it can be utilized to generate a wide variety of water-soluble monolayer-protected nanoparticles.^{5,6}

Given our interest in mixed-ligand AuNPs to study their metal binding abilities, one-phase synthesis gives us the opportunity to control and reconcile the solubility of two disparate molecules. Therefore, the **one-phase synthesis method** was chosen to produce the nanoparticles used in this work. The synthesis of nanoparticles can be sensitive to a number of factors. Ultimately, the interplay between the chemical potential of the dissimilar species in the solution and the kinetic barriers governs the outcome. Several conditions using one-phase technique were tested to obtain different size of AuNPs with different ligand ratio on the surface. Here, I give all the details about the synthesis protocols to produce all types of particles mentioned in this thesis.

Prior to synthesis, all glassware was rinsed with a freshly prepared aqua regia solution (3:1 $\text{HCl}:\text{HNO}_3$) in order to smooth out the glass and to improve the reproducibility. Aqua regia is a yellow-orange fuming liquid, which can dissolve gold metal. This step is important since the leftover AuNPs stuck on the glassware surface from previous synthesis can cause an additional nucleation, which results in high size polydispersity in the sample. Then, glassware was washed with tap water, Micro-90® concentrated alkaline cleaning solution (International Products Corp.), tap water, acetone, ethanol, and ultrapure MQ water, respectively. Finally, they were kept in the oven at 55 °C for couple of hours to ensure the removal of water.

Throughout my syntheses attempts, I defined the following parameters as having a large effect on the size of the nanoparticles. **The reaction temperature, the type and addition rate of reducing agent, the polarity of the solvent, ligand ratio, the concentration of the reactants and reaction time** (time of stirring after reduction is complete) were found to

have enormous impact on the final properties of AuNPs in terms of ligand size and ligand ratio. In addition, the relative amount of two dissimilar ligands on the surface of the particles varies depending on certain synthetic factors. In order to be able to synthesize desired nanoparticles with certain size and ligand ratio, it is really important to analyze and rationalize all of these parameters.

Longer reaction time (Ex. EG2-2 vs. EG2-3) Gold-thiol complex and reduction @ lower temperatures (Ex. EG2-3 vs. EG2-4) Reduction under argon (Ex. EG2-25 vs. EG2-51) Non-polar solvents like chloroform (Ex. EG2-21 vs. EG2-22) Weaker reducing agents (Ex. EG2-36 vs. EG2-48)	leads to	increase in the size of AuNPs
Polar solvents like methanol (Ex. EG2-8 vs. EG2-40)	leads to	decrease in the size of AuNPs
Immediate (all in once) and dropwise addition of reducing agent (Ex. EG2-27 vs. EG2-28)	leads to	similar average size of AuNPs
Longer reaction time (Ex. EG2-11 vs. EG2-22) Lower EG2 to HT feed ratio (strong correlation, but not linear) (Ex. EG2-22 vs. EG2-25)	leads to	lower EG2 ratio on the surface of NPs

Table 3.1: The codes of the samples are provided below. The synthetic parameters that vary across separate syntheses of EG2:HT coated AuNPs were observed to have significant impact on the final properties of AuNPs. Examples are given in the parenthesis, however; more examples can be found after careful investigation of the relationship between reaction conditions and properties of different AuNPs. The reactions were highly sensitive the external factors like the temperature of the environment (it varied from season to season, or even from day to day), the stirring rate, dust in the reaction medium, the cleanliness of the glassware, the source of the reagents, purity of the reagents etc. Therefore, starting with one set of parameters to synthesize desired nanoparticles with certain size and ligand ratio, then altering conditions under the guidance of table 3.1 would be helpful. Throughout the syntheses of the series, it was important not to take the reagents from different sources (stick with the same bottle of certain reagent).

The schematic representation of the synthesized gold nanoparticles coated with EG2:HT ligands is shown in **Fig.3.2**. As a **general synthesis protocol** to synthesize those particles,

0.225 mmol of $\text{HAuCl}_4 \cdot 3\text{H}_2\text{O}$ (%99.9 trace metal basis, Sigma-Aldrich) (88.6 mg) was dissolved in 10 ml of ethanol, followed by the addition of total 0.225 mmol of thiol mixtures (e.g. 37.5 mg EG2 (Prochimia Surfaces) + 8.35 μL HT (Sigma-Aldrich, 99%) for 3:1 EG2:HT mole ratio) in 10 ml of ethanol. This was a critical step in determining ligand ratio, because a yellow gold-thiol complex forms, which is evidenced by the increasing turbidity of the mixture. After 20 minutes of stirring, 2.5 mmol of NaBH_4 from Sigma-Aldrich (94.5 mg) in 37.5 ml of ethanol was added to the reaction dropwise. The addition started with 0.3 mm outer diameter needle for the first 10 min, and followed by 0.5-0.6 mm outer diameter needle until all the solution was added. The reaction was stirred for additional 3 hours after the reducing agent addition was completed. After completing the reaction, diethyl ether (50 ml) was poured in the flask, and the mixture was kept in the 4 $^\circ\text{C}$ fridge overnight to precipitate the nanoparticles.

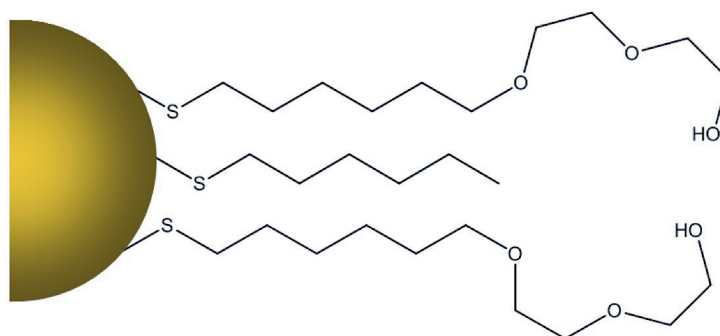


Figure 3.2: The schematic cartoon of the synthesized gold nanoparticles coated with EG2:HT ligands

Batch numbers were assigned to all the batches shown in the 2-D map of nanoparticle size vs. ligand ratio (Fig.3.13) as “EG2-n” where n is an integer. **There were several parameters varied for each synthesis, and only the changed conditions were indicated. Unless otherwise is indicated, the parameters in general synthetic protocol were followed.**

Synthesis of EG2-1: Gold-thiol complex stirring time: 30 minutes / Addition rate of reducing agent: Immediate (not dropwise, all in once) / EG2:HT mole ratio: 3:1 / Reaction time: 48 hours / Double scale of the general synthesis protocol (0.45 mmol HAuCl_4 in 20 ml EtOH+ 0.45 mmol ligands mixture in 20 ml ethanol EtOH + 5 mmol NaBH_4 in 75 ml EtOH)

Synthesis of EG2-2: Gold-thiol complex stirring time: 30 minutes / EG2:HT mole ratio: 3:1 / Reaction time: 48 hours / Double scale of the general synthesis protocol (0.45 mmol H_{Au}Cl₄ in 20 ml EtOH+ 0.45 mmol ligands mixture in 20 ml EtOH + 5 mmol NaBH₄ in 75 ml EtOH)

Synthesis of EG2-3: Gold-thiol complex stirring time: 30 minutes / EG2:HT mole ratio: 3:1 / Double scale of the general synthesis protocol (0.45 mmol H_{Au}Cl₄ in 20 ml EtOH+ 0.45 mmol ligands mixture in 20 ml EtOH + 5 mmol NaBH₄ in 75 ml EtOH)

Synthesis of EG2-4: Gold-thiol complex stirring time: 30 minutes / EG2:HT mole ratio: 3:1 / Addition rate of reducing agent: Immediate / Temperature: Gold-thiol complex stirring @ 0 °C, reduction @ 0 °C, 30 min stirring @ 0 °C, 3 hours stirring @ room temperature / Reaction time: 3.30 hours / Double scale of the general synthesis protocol (0.45 mmol H_{Au}Cl₄ in 20 ml EtOH+ 0.45 mmol ligands mixture in 20 ml EtOH + 5 mmol NaBH₄ in 75 ml EtOH)

Synthesis of EG2-5: Gold-thiol complex stirring time: 30 minutes / EG2:HT mole ratio: 3:1 / Temperature: Gold-thiol complex stirring @ 0 °C, reduction @ 0 °C, 30 min stirring @ 0 °C, 3 hours stirring @ room temperature / Reaction time: 3.30 hours / Double scale of the general synthesis protocol (0.45 mmol H_{Au}Cl₄ in 20 ml EtOH+ 0.45 mmol ligands mixture in 20 ml EtOH + 5 mmol NaBH₄ in 75 ml EtOH)

Synthesis of EG2-6: Gold-thiol complex stirring time: 30 minutes / EG2:HT mole ratio: 5:1 / Addition rate of reducing agent: Immediate / Reaction time: 24 hours / Double scale of the general synthesis protocol (0.45 mmol H_{Au}Cl₄ in 20 ml EtOH+ 0.45 mmol ligands mixture in 20 ml EtOH + 5 mmol NaBH₄ in 75 ml EtOH)

Synthesis of EG2-7: Gold-thiol complex stirring time: 30 minutes / EG2:HT mole ratio: 7:1 / Addition rate of reducing agent: Immediate / Reaction time: 24 hours / Double scale of the general synthesis protocol (0.45 mmol H_{Au}Cl₄ in 20 ml EtOH+ 0.45 mmol ligands mixture in 20 ml EtOH + 5 mmol NaBH₄ in 75 ml EtOH)

Synthesis of EG2-8: EG2:HT mole ratio: 3:1 / Reaction atmosphere: Gold-thiol complex stirring under nitrogen

Synthesis of EG2-9: EG2:HT mole ratio: 3:1 / Reaction atmosphere: Gold-thiol complex stirring under nitrogen

Synthesis of EG2-10: EG2:HT mole ratio: All EG2 (0.225mmol EG2) / Reaction atmosphere: Gold-thiol complex stirring under nitrogen

Synthesis of EG2-11: Addition rate of reducing agent: Immediate / EG2:HT mole ratio: 3:1 / Reaction time: 48 hours / Solvent mixture: 5 ml EtOH + 5 ml CHCl₃ to dissolve ligands

Synthesis of EG2-12: Addition rate of reducing agent: Immediate / EG2:HT mole ratio: 5:1 / Reaction time: 48 hours / Solvent mixture: 5 ml EtOH + 5 ml CHCl₃ to dissolve ligands

Synthesis of EG2-13: Addition rate of reducing agent: Immediate / EG2:HT mole ratio: 7:1 / Reaction time: 48 hours / Solvent mixture: 5 ml EtOH + 5 ml CHCl₃ to dissolve ligands

Synthesis of EG2-14: EG2:HT mole ratio: 6:1 / Reaction time: 48 hours / Solvent mixture: 5 ml EtOH + 5 ml CHCl₃ to dissolve gold salt

Synthesis of EG2-15: EG2:HT mole ratio: 4:1 / Reaction time: 48 hours / Solvent mixture: 5 ml EtOH + 5 ml CHCl₃ to dissolve gold salt

Synthesis of EG2-16: Double scale of the synthesis protocol of EG2-37 (0.45 mmol HAuCl₄ + 0.45 mmol ligands mixture in 40 ml of EtOH + 5 mmol NaBH₄ in 75 ml EtOH) except the precursor (common one was used, %99.9 trace metal basis HAuCl₄.3H₂O)

Synthesis of EG2-17: Double scale of the synthesis protocol of EG2-28 (0.45 mmol HAuCl_4 + 0.45 mmol ligands mixture in 40 ml of EtOH + 5 mmol NaBH_4 in 75 ml EtOH)

Synthesis of EG2-18: EG2:HT mole ratio: 5:1 / Reaction atmosphere: Gold-thiol complex stirring under nitrogen / Solvent mixture: 5 ml EtOH + 5 ml toluene to dissolve ligands

Synthesis of EG2-19: Gold-thiol complex stirring time: 30 minutes / EG2:HT mole ratio: 3:1 / Reaction atmosphere: Gold-thiol complex stirring under nitrogen / Solvent mixture: 9 ml EtOH + 1 ml CHCl_3 to dissolve ligands, 45 ml EtOH to dissolve NaBH_4

Synthesis of EG2-20: Gold-thiol complex stirring time: 30 minutes / EG2:HT mole ratio: 3:1 / Temperature: Gold-thiol complex stirring @ RT, reduction @ 0 °C, 3 hours stirring @ room temperature / Volume of the solvent used for gold-thiol complex: 80 ml EtOH, 150 ml EtOH to dissolve NaBH_4

Synthesis of EG2-21: EG2:HT mole ratio: 3:1 / Reaction atmosphere: Gold-thiol complex stirring under nitrogen / Solvent mixture: 5 ml EtOH + 5 ml CHCl_3 to dissolve ligands

Synthesis of EG2-22: Addition rate of reducing agent: Immediate / Gold-thiol complex stirring time: 30 minutes / EG2:HT mole ratio: 3:1 / Double scale of the general synthesis protocol (0.45 mmol HAuCl_4 in 20 ml EtOH + 0.45 mmol ligands mixture in 20 ml EtOH + 5 mmol NaBH_4 in 75 ml EtOH)

Synthesis of EG2-23: EG2:HT mole ratio: 5:1 / Reaction atmosphere: Gold-thiol complex stirring under argon / Solvent mixture: 5 ml EtOH + 5 ml CHCl_3 to dissolve ligands

Synthesis of EG2-24: EG2:HT mole ratio: 7:1 / Reaction atmosphere: Gold-thiol complex stirring under argon / Solvent mixture: 5 ml EtOH + 5 ml CHCl₃ to dissolve ligands

Synthesis of EG2-25: EG2:HT mole ratio: 3:1 / Reaction atmosphere: Gold-thiol complex stirring under argon / Solvent mixture: 3 ml EtOH + 7 ml CHCl₃ to dissolve ligands

Synthesis of EG2-26: EG2:HT mole ratio: 3:1 / Reaction atmosphere: Gold-thiol complex stirring under argon / Solvent mixture: 10 ml CHCl₃ to dissolve ligands

Synthesis of EG2-27: Addition rate of reducing agent: Immediate / EG2:HT mole ratio: 3:1 / Reaction atmosphere: Gold-thiol complex stirring under argon / Solvent mixture: 10 ml CHCl₃ to dissolve ligands

Synthesis of EG2-28: Addition rate of reducing agent: Immediate / EG2:HT mole ratio: 7:1 / Reaction time: 15 minutes

Synthesis of EG2-29: Gold-thiol complex stirring time: 35 minutes / EG2:HT mole ratio: 6:1 / Temperature: Gold-thiol complex stirring @ RT for first 20 min, then @ 0 °C for 15 min , reduction @ 0 °C, 1 hour stirring @ room temperature / Solvent mixture: 20 ml CHCl₃ + 20 ml EtOH to dissolve ligands / Volume of the solvent used: 40 ml EtOH for gold salt, 75 ml EtOH to dissolve NaBH₄ / Reaction time: 1 hour

Synthesis of EG2-30: Gold-thiol complex stirring time: 35 minutes / EG2:HT mole ratio: 7:1 / Temperature: Gold-thiol complex stirring @ RT for first 20 min, then @ 0 °C for 15 min , reduction @ 0 °C, 1 hour stirring @ room temperature / Solvent mixture: 5 ml CHCl₃ + 5 ml EtOH to dissolve ligands / Reaction time: 1 hour

Synthesis of EG2-31: EG2:HT mole ratio: 7:1 / Temperature: Gold-thiol complex stirring @ 0 °C , reduction @ 0 °C, 3 hours stirring @ room temperature / Solvent

mixture: 10 ml CHCl_3 + 10 ml EtOH to dissolve ligands / Volume of the solvent used: 20 ml EtOH for gold salt, 75 ml EtOH to dissolve NaBH_4

Synthesis of EG2-32: Gold-thiol complex stirring time: 30 minutes / EG2:HT mole ratio: 10:1 / Reaction atmosphere: Gold-thiol complex stirring under argon / Solvent mixture: 5 ml CHCl_3 + 5 ml EtOH to dissolve ligands / Volume of the solvent used: 45 ml EtOH to dissolve NaBH_4

Synthesis of EG2-33: Gold-thiol complex stirring time: 30 minutes / EG2:HT mole ratio: 5:1 / Temperature: Gold-thiol complex stirring @ RT, reduction @ 0 °C, 3 hours stirring @ room temperature / Solvent mixture: 20 ml CHCl_3 + 20 ml EtOH to dissolve ligands / Volume of the solvent used: 40 ml EtOH for gold salt, 45 ml EtOH to dissolve NaBH_4

Synthesis of EG2-34: EG2:HT mole ratio: 5:1 / Reaction atmosphere: Gold-thiol complex stirring under nitrogen / Solvent mixture: 5 ml EtOH + 5 ml CHCl_3 to dissolve ligands / Volume of the solvent used: 47.5 ml EtOH to dissolve NaBH_4

Synthesis of EG2-35: Addition rate of reducing agent: Immediate / EG2:HT mole ratio: 5:1 / Precursor: Different than the common one, %99.999 trace metal basis $\text{HAuCl}_4 \cdot x\text{H}_2\text{O}$

Synthesis of EG2-36: Addition rate of reducing agent: Immediate / EG2:HT mole ratio: 7:1 / Precursor: Different than the common one, %99.999 trace metal basis $\text{HAuCl}_4 \cdot x\text{H}_2\text{O}$

Synthesis of EG2-37: EG2:HT mole ratio: All EG2 (0.225mmol EG2) / Solvent mixture: 10 ml MeOH + 10 ml EtOH mixture to dissolve gold-thiol complex, 10 ml MeOH + 27.5 ml EtOH to dissolve NaBH_4 / Precursor: Different than the common one, %99.999 trace metal basis $\text{HAuCl}_4 \cdot x\text{H}_2\text{O}$

Synthesis of EG2-38: EG2:HT mole ratio: 12:1 / Solvent mixture: 7 ml methanol (MeOH) + 13 ml EtOH mixture to dissolve gold-thiol complex / Reaction time: 1 hour / Precursor: Different than the common one, %99.999 trace metal basis H_{Au}Cl₄.xH₂O

Synthesis of EG2-39: Addition rate of reducing agent: Immediate / EG2:HT mole ratio: 3:1 / Solvent mixture: 5 ml MeOH + 5 ml EtOH for gold salt

Synthesis of EG2-40: EG2:HT mole ratio: 4:1 / Temperature: Gold-thiol complex stirring @ RT for first 20 min, then @ 0 °C for 15 min, reduction @ 0 °C, 1 hour stirring @ room temperature / Solvent mixture: 5 ml CHCl₃ + 5 ml EtOH to dissolve ligands / Reaction time: 1 hour

Synthesis of EG2-41: Addition rate of reducing agent: Immediate / Temperature: Gold-thiol complex stirring @ 0 °C, reduction @ 0 °C / EG2:HT mole ratio: All EG2 (0.225mmol EG2)

Synthesis of EG2-42: Double scale of the synthesis protocol of EG2-25 except EG2:HT mole ratio: 8:1 / (0.45 mmol H_{Au}Cl₄ in 20 ml EtOH+ 0.45 mmol ligands mixture in 13 ml EtOH + 7 ml CHCl₃ + 5 mmol NaBH₄ in 50 ml EtOH) / Reaction atmosphere: Gold-thiol complex stirring and whole reduction step under nitrogen

Synthesis of EG2-43: Double scale of the synthesis protocol of EG2-25 except EG2:HT mole ratio: 10:1 / (0.45 mmol H_{Au}Cl₄ in 20 ml EtOH+ 0.45 mmol ligands mixture in 13 ml EtOH + 7 ml CHCl₃ + 5 mmol NaBH₄ in 50 ml EtOH) / Reaction atmosphere: Gold-thiol complex stirring and whole reduction step under nitrogen

Synthesis of EG2-44: Addition rate of reducing agent: Dropwise / Temperature: Gold-thiol complex stirring @ 0 °C, reduction @ 0 °C / EG2:HT mole ratio: 7:1

Synthesis of EG2-45: Addition rate of reducing agent: Dropwise / Temperature: Gold-thiol complex stirring @ 0 °C, reduction @ 0 °C / EG2:HT mole ratio: 12:1

After the synthesis, the nanoparticles needed to be purified and the impurities such as excess reducing agent, unreacted ligands, and residual solvents removed. **Vacuum filtration purification method**, which is a common purification practice for synthetic chemistry, was utilized for the purification of AuNPs. Following the completion of the reaction, a solvent that caused to precipitation of particles was added into the reaction, and the solution was stored at 4 °C overnight. In our case, diethyl ether was utilized as the precipitation solvent after testing the solubility of the nanoparticles in a number of common solvents. After supernatant of the solution was removed, the particles were filtered through a filter paper under the vacuum. Then, a large amount of solvents (ethanol and acetone, respectively) were used to dissolve out impurities. As a final step, AuNPs on the filter paper were dried under the vacuum and the black powder was collected. I also used other cleaning techniques that for extra purification prior to certain characterization techniques, where existence of extra ligands could cause inaccurate results.

3.2 Characterization of Mixed Ligand Coated Gold Nanoparticles

Careful characterization of physical and chemical properties of the synthesized AuNPs was required as these properties dictate the function of AuNPs. Therefore, the particle characterization served as the pillar of nearly all of the results in this thesis. Appropriate characterization of the synthesized AuNPs is necessary for our understanding of the parameters that need to be controlled or changed in order to attain the anticipated properties. This section of the thesis explains the characterization techniques employed in the study of family of EG2:HT coated AuNPs.

Numerous techniques can be used to characterize the nanoparticles. The three most basic characterization techniques applied to all the synthesized AuNPs were the transmission electron microscopy (TEM), the nuclear magnetic resonance (NMR), and the Fourier transform infrared spectroscopy (FTIR). These three methods allowed me to obtain the average size of the particles, the actual ligand composition, and the molecular conformation of the ligands on the surface, respectively. In addition, thermogravimetric analysis (TGA) was utilized to calculate the organic percentage of the synthesized

nanoparticles, which in turn was used to determine the ligand density on the surface of the particles.

3.2.1 Ligand-Shell Composition Determination

¹H-NMR spectroscopy was used to determine the actual ratio of two dissimilar ligands (EG2:HT) on the surface of the particles. The molar ratio of two ligands that are used during the synthesis is called “feed ratio” and feed ratio is not necessarily the same as the ratio of two ligands on the surface after the synthesis. Therefore, NMR spectroscopy was used to check which ligands are present on the surface of NPs, quantifying the real ratio of the ligands. This technique was chosen to determine the identity and the quantity of the ligands on the surface thanks to chemical resolution provided by chemical shift and the direct correlation between NMR signal integration and spin population.

Solution based ¹H-NMR spectroscopy previously utilized in the field to evaluate the kind and amount of ligands on noble metal NPs.⁷ Moreover, the ligand concentration on the surface of AuNPs found by NMR has been compared with other techniques like ICP-OES, revealing high correlation between two methods within a 95% confidence interval.⁸

However, the direct analysis of nanoparticle solution for quantitative results is not possible since the ligands attached to the surface of the NPs experience an amplified relaxation time, broadening their NMR peaks. For this reason, the metal core of the NPs has to be etched prior to measurement to release the ligands from the surface.

If the particles are clean, one should not expect any sharp peak in the spectra of NP solutions except the solvent peaks. Sharp peaks overlaid on broad ones are characteristically an indication of free ligands present in solution due to inefficient cleaning.

To avoid incorrect results, the nanoparticles had to be cleaned from their impurities. Thus, after the standard cleaning procedure that is mentioned in previous **Section.3.1**, the powder of AuNPs was centrifuged with acetone several times (7*40 ml), and the sample was sonicated and vortexed between each wash cycle. This residue was then dried under vacuum. Then, 12 mg of nanoparticles was suspended in 0.5 mL of DMSO-d₆

(Sigma) to check if there was any free ligand left. In the beginning, in order to decide the cleaning procedure, this step was repeated for every NP that was synthesized. Later, the protocol was set to assure the cleanliness of each particle. In **Fig.3.4**, one spectrum of a synthesized nanoparticle batch is shown as an example to see what a spectrum of clean nanoparticle sample looks like. After this stage, if nanoparticles were clean, the ligands were liberated from the surface for increased resolution.

Chemical decomposition of the gold core was performed by iodine etching. An etching solution of 4 mg of Iodine (Acros) in 100 μ L DMSO- d_6 was added previously prepared nanoparticle solution. Then, the NMR tube with the mixture of etchant and nanoparticles was sonicated for 70 minutes prior to the measurement. This protocol was applied to all series of synthesized EG2:HT coated AuNPs.

To calculate the actual ligand ratio, the area of a peak assigned to each ligand was integrated, normalized by the number of protons on the particular group, and compared to each other. The peaks, which were interfered by solvent peaks, were unsuitable to be utilized. Therefore, we turned our attention to the alkyl region. For the HT ligand, the terminal CH_3 group was used (3H, 0.87 ppm). In the region that spans from 1.2 ppm to 1.65 ppm, the peaks corresponding to the alkyl part of both EG2 and HT were overlapping (8H from EG2, 8H from HT). The positions of chemical shifts of each hydrogen within both HT and EG2 are shown in **Fig. 3.3** in detail. The choice of integration area was crosschecked by mixing two pure ligands together in known molar ratios, which revealed the accurate match between measured and feed ratio.

After careful processing of NMR data, it was shown that the ligand feed ratio was not necessarily the same as the real ligand ratio on the surface of the nanoparticles. It is highly recommended to visit **Section 3.1** to examine the correlation between the feed ratio and the real ratio depending on the reaction conditions.

NMR spectra of all the synthesized batches are shown in **Appendix, Fig.A.1-A.5**. The missing batch numbers are corresponding to All-EG2 covered AuNPs, which can be found in **Fig.3.3F**.

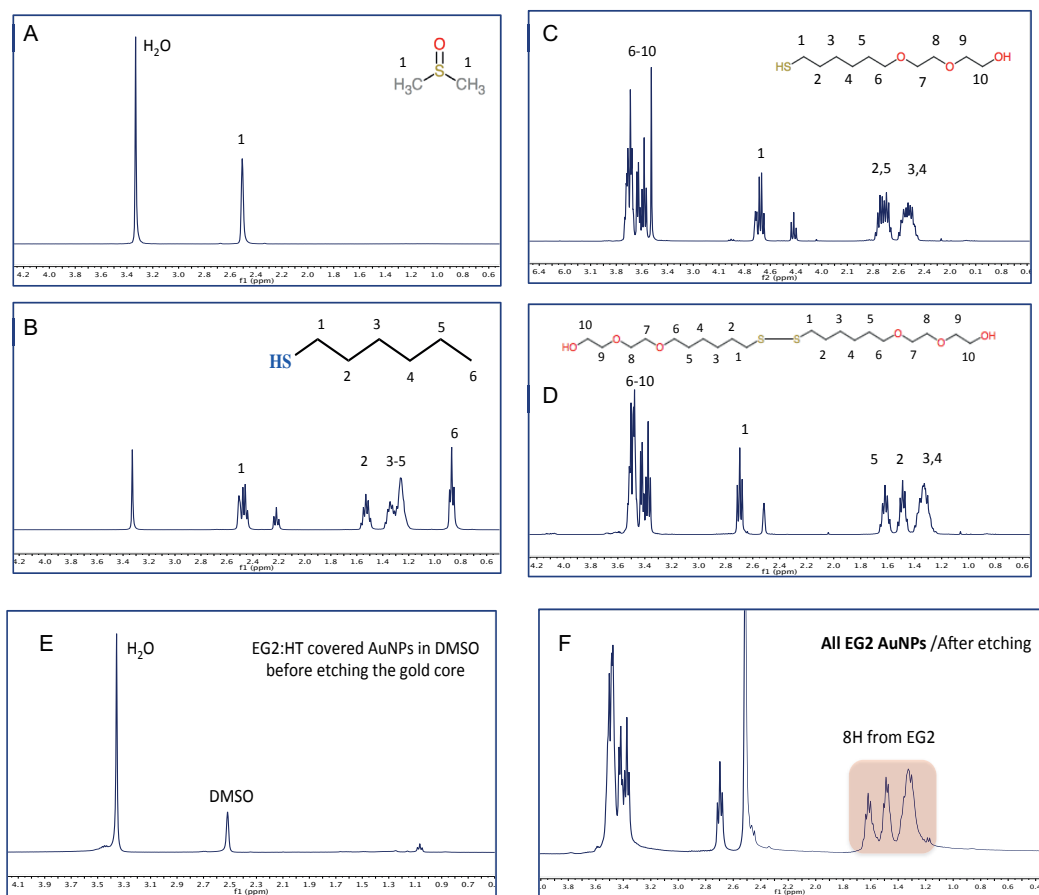


Figure 3.3 Representative NMR spectra of **A)** DMSO-d₆, **B)** Pure HT ligand in DMSO-d₆, **C)** Pure EG2 ligand in DMSO-d₆, **D)** Pure EG2 ligand in DMSO-d₆ + iodine, ligands were shown to form disulfide species in our group due to oxidizing nature of iodine. **E)** EG2:HT covered AuNPs in DMSO-d₆ without iodine etching, the spectrum didn't show any peak corresponding to EG2 or HT ligand, **F)** All-EG2 covered AuNPs in DMSO-d₆ after etching with iodine.

3.2.2 Size Distribution Analysis

Transmission electron microscopy (TEM) is the most direct technique to analyze the mean core diameter of metal nanoparticles.⁹ TEM image is produced as a result of the interaction of the electrons transmitted through an ultra-thin specimen. This technique is able to provide images at a significantly higher resolution than light microscopes due to the small de Broglie wavelength of electrons.

TEM images of whole series of EG2:HT coated AuNPs was routinely acquired in a

Tecnai Spirit BioTWIN electron microscope. A TEM sample was prepared by drop-casting the diluted solution of AuNPs on a 400 mesh carbon-coated copper grid. Depending on the actual EG2:HT ratio on the surface of AuNPs, their solubilities varied in ethanol, methanol, and water. The most suitable solvent in which NPs are more dispersible was used to prepare the nanoparticle solutions. And, prior to analysis, the solvent was left to evaporate. TEM images were obtained in a Tecnai Spirit BioTWIN with the acceleration voltage of 80 kV. The size distributions were obtained using a threshold based particle analysis in the program “ImageJ”, which also applied watershed filter in order to separately analyze the particles whose surfaces were in contact.

Size distributions and representative TEM images of the synthesized EG2:HT coated AuNPs used in this thesis is shown in **Appendix, Fig.A.6-A.14**. While calculating the mean diameter of each synthesized batches, it is important that the calculated value should reflect the whole nanoparticle population. If the particles have perfect Gaussian size distribution, then the calculated mean diameter represents well the whole particle population. However, the synthesis method used in this thesis were prone to produce more than one size population as it can be seen in most of the TEM histograms of EG2-n particles (**Appendix, Fig.A.6-A.14**). Origin Pro (9.1) was used to determine the mean diameter of each size population by fitting each distribution to a Gaussian function. As a result, two different mean diameters were calculated to represent one nanoparticle batch if size distribution of the particles are bimodal. Each mean diameter was reported with standard deviation of the population.

3.2.3 Constructing 2-D Map of Size and Ligand Ratio for the Synthesized AuNPs

After characterization of each synthesized batch with NMR and TEM in order to determine the real EG2:HT mole ratio on the surface and the mean diameter of the core size, we decided to transform this information into a 2-D plot (**Fig.3.4**). **The plot provided a clear picture about the range of the size and ligand ratio of the particles that are used in this thesis for further binding experiments.** Data corresponding to each point in the 2-D plot can be found in **Table 3.2** and **Table 3.3**. In addition, batch numbers are

added in Table 3.2 and Table 3.3 to aid finding out synthesis method of batch of interest.

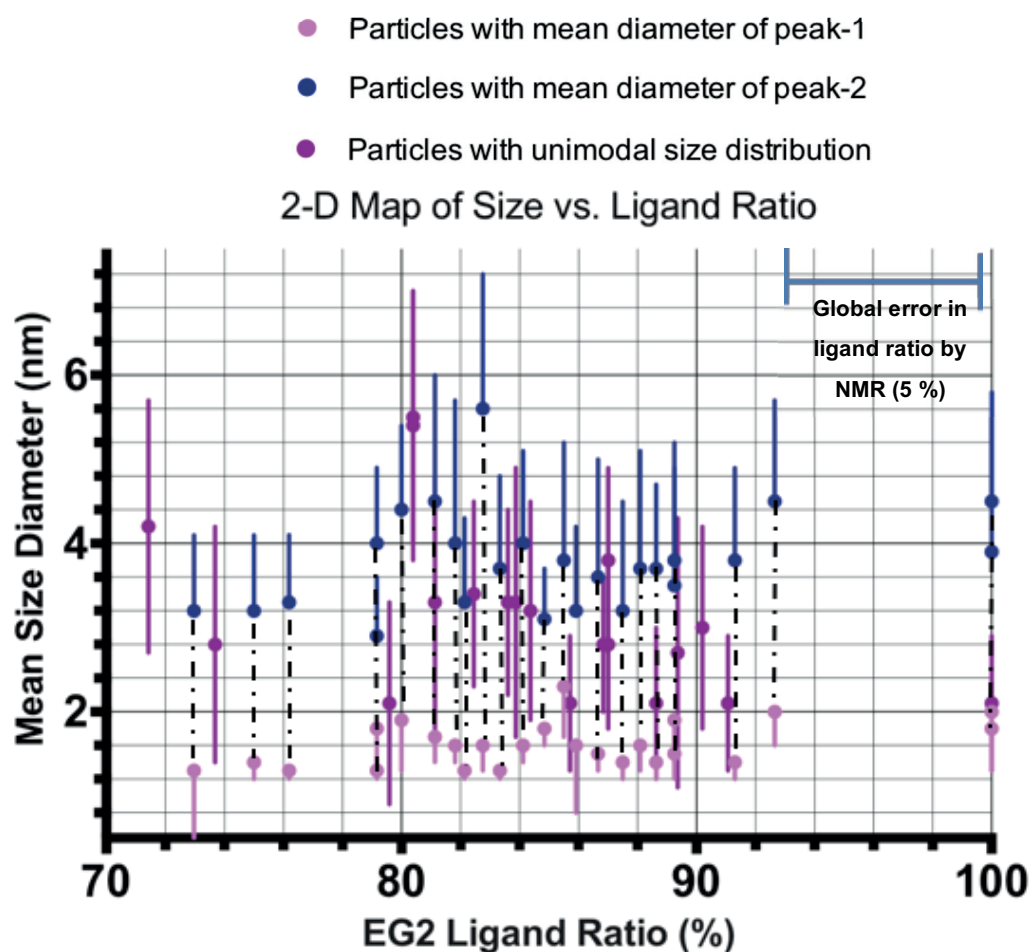


Figure 3.4: Size and ligand ratio (in terms of moles) of the synthesized AuNPs demonstrated in 2-D format. Bimodal particles were represented by two different mean diameters (navy and pink dots connected with black dashed line) assuming the same ligand ratio for each nanoparticle population. Upper and lower error bars shown for the y-axis is the standard deviation of mean size diameter of that population. Corresponding mean diameters, standard deviations, fitting of peak 1 and peak 2 can be found in Appendix, Fig.A.6-A.14.

The mean diameters of each nanoparticle population within the same batch (mean diameters of peak 1 and peak 2) can be found in Appendix, Fig.A.6-A.14. While plotting Fig.3.4, we assumed that both nanoparticle populations within the same AuNP batch have the same EG2 ligand ratio on their surfaces. The population of the particles with mean diameter of peak-1 is much lower compared to the particles with mean diameter of

peak-2. In addition, mean diameter of peak-1 is similar for all the bimodal nanoparticle batches. Therefore, from this point on in this thesis, each AuNPs batch will be represented by the mean diameter of peak-1 (navy dots in **Fig.3.4**).

Mean Size Diameter (nm)	Deviation from Mean Size (nm)	EG2:HT Mole Ratio	EG2 Ligand Ratio (Mole %)	The codes in the thesis-EG2-n
3.2 / 1.4 (Bimodal)	0.9 / 0.2	3	75.00	1
2.8	1.4	2.8	73.68	2
2.1	1.2	3.9	79.59	3
4.0 / 1.6 (Bimodal)	1.1 / 0.2	5.3	84.13	4
5.6 / 1.6 (Bimodal)	1.6 / 0.3	4.8	82.76	5
2.8	0.8	6.6	86.84	6
3.7 / 1.4	1.0 / 0.2	7.8	88.64	7
2.7	1.6	8.4	89.36	8
4.0 / 1.6 (Bimodal)	1.7 / 0.2	4.5	81.82	9
3.9 / 1.8	1.6 / 0.5	100	100.00	10
3.2 / 1.3 (Bimodal)	0.9 / 0.1	2.7	72.97	11
3.3 / 1.3 (Bimodal)	0.8 / 0.1	3.2	76.19	12
3.3 / 1.3 (Bimodal)	1.0 / 0.1	4.6	82.14	13
2.9 / 1.3 (Bimodal)	0.7 / 0.1	3.8	79.17	14
3.1 / 1.8 (Bimodal)	0.6 / 0.2	5.6	84.85	15
2.8	1	6.7	87.01	16
3.3	1.5	4.3	81.13	17
3.4	1.1	4.7	82.46	18
4.0 / 1.8 (Bimodal)	0.9 / 0.5	3.8	79.17	19
4.4 / 1.9 (Bimodal)	1.0 / 0.6	4	80.00	20
3.3	1.6	5.2	83.87	21
3	1.2	9.2	90.20	22
3.2 / 1.4 (Bimodal)	1.3 / 0.2	7	87.50	23
3.7 / 1.6 (Bimodal)	1.4 / 0.3	7.4	88.10	24
3.6 / 1.5 (Bimodal)	1.4 / 0.2	6.5	86.67	25
3.2 / 1.6 (Bimodal)	1.0 / 0.8	6.1	85.92	26

Table 3.2: Mean size diameters (nm), standard deviation of the core sizes (nm), EG2:HT mole ratios on the surface of AuNPs, mole percentages of EG2 on the surface of AuNPs are shown for EG2-n (n, 1-26)

Mean Size Diameter (nm)	Deviation from Mean Size (nm)	EG2:HT Mole Ratio	EG2 Ligand Ratio (Mole %)	The codes in the thesis-EG2-n
3.2	1.3	5.4	84.38	27
3.8	1.1	6.7	87.01	28
3.8 / 2.3 (Bimodal)	1.4 / 0.6	5.9	85.51	29
3.5 / 1.9 (Bimodal)	1.4 / 0.5	8.3	89.25	30
3.8 / 1.5 (Bimodal)	1.4 / 0.3	8.3	89.25	31
3.8 / 1.4 (Bimodal)	1.1 / 0.3	10.5	91.30	32
3.3	1.1	5.1	83.61	33
3.7 / 1.3 (Bimodal)	1.1 / 0.1	5	83.33	34
2.1	0.8	6	85.71	35
2.1	0.8	10.2	91.07	36
2.1	0.8	100	100.00	37
2.1	0.9	7.8	88.64	38
2.2	1	6.9	87.34	39
4.2	1.5	2.5	71.43	40
4.5 / 2.0 (Bimodal)	1.3 / 0.3	100	100.00	41
5.5	1.5	4.1	80.39	42
5.4	1.6	4.1	80.39	43
4.5 / 1.7 (Bimodal)	1.5 / 0.3	4.3	81.13	44
4.5 / 2.0 (Bimodal)	1.2 / 0.4	12.6	92.65	45

Table 3.3: Mean size diameters (nm), standard deviation of the core sizes (nm), EG2:HT mole ratios on the surface of AuNPs, mole percentages of EG2 on the surface of AuNPs are shown for EG2-n (n, 27-45)

3.2.4 Thermogravimetric Analysis (TGA) and Ligand Density Calculations

The multi-technique evaluation by Terrill *et al.* (1995) was among the first applications of TGA to monolayer-protected AuNPs.¹⁰ It was utilized to calculate the organic percentages of NPs covered with one type alkanethiol with similar core size but increasing in ligand length. Results from TGA and elemental analysis showed excellent agreement on the weight percentages of organics on the surface of NPs (19.74% and 20.67 %, respectively for C8-terminated AuNPs). After early studies, TGA has become a gold standard for calculating the organic content of monolayer-protected AuNPs and gold clusters in order to estimate the number of Au-S bonds (ligand density) and surface coverage. This method has been widely accepted in the field since it allows for the direct determination of the weight of the organic layer on the surface compared to the inorganic core.^{11,12}

The general mechanism of TGA is based on recording weight loss or gain of a sample upon heating due to loss of volatiles (moistures, ligands etc.), decomposition or oxidation. The temperature of the sample in a crucible is linearly ramped up under stream of inert (or reactive, not for our purpose) gas. Here, it is important to understand the experimental set-up of TGA since a mass loss observed during the measurement under N₂ flow, in an open crucible cannot be attributed to boiling phenomena, but rather evaporation, desorption or sublimation. The maximum temperature was chosen as 600 °C in this study. Typically, it is chosen in such a way that there is no further decomposition of carbon materials above that temperature.

The amount of sample used for the analysis should be in the powder form and it generally ranges from 2 mg to 30 mg (depending on the organic percentage, if the percentage is low then the amount should be increased to obtain a smooth curve). Unfortunately, it is a destructive technique, which means you cannot recover the sample after the measurement.

Inorganic impurities within the samples result in high-error measurements. Since there was high amount of salt present in our synthesis, we needed to be sure that all the salts were washed away. Therefore, particles were washed several times with MilliQ water

using Amicon® Ultra-15 Centrifugal Filter Devices (10k or 30k NMWL). Before the washing procedure, particles were suspended in water 5-7 days to ensure complete dissolution of the salts. The particles were then suspended in a small amount of water (~0.5 mL) and, then precipitated with the aid of acetone and hexane mixture. After the supernatant was poured off, the precipitate was stored under vacuum for 2 days to ensure complete removal of solvents. Characteristic heating rates in the literature are 5-20° C/min especially for carbon materials, and an increase in rate was associated to poor reproducibility and high error. Therefore, we used 5° C/min for our measurements.

We used TGA 4000 from Perkin Elmer in this work, and **Fig. 3.5** shows analyses of recently synthesized EG2:HT covered nanoparticles. NPs of different sizes were analyzed by TGA. The TGA data is obtained in form of absolute weight differences; however, it is mostly reported as percentage loss after normalization of absolute value by the initial weight of sample.

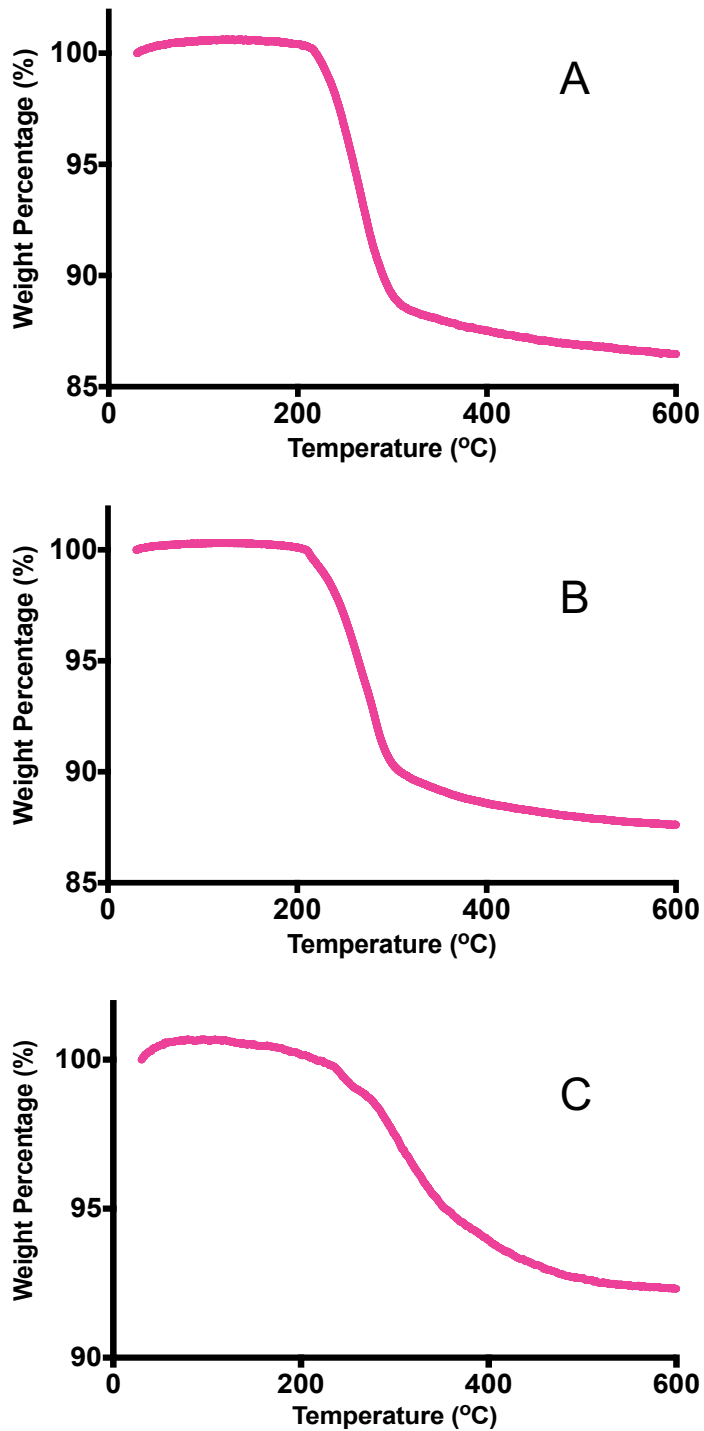


Figure 3.5: TGA curves of recently synthesized EG2:HT covered AuNPs, 30 min temperature equilibration at 30 °C to remove all the solvents are not represented A) % 13.9 organic percentage for EG2-14, B) % 12.4 organic percentage for EG2-27, C) 7.7 % organic percentage for EG2-43. Organic percentages were calculated by subtracting weight percentage @ 600 °C from 100 %.

Unfortunately, TGA of all the batches could not be obtained due to experimental reasons. In the beginning of this study, the organic percentages obtained for the particles were quite low (< 7 %), then it was shown with the aid of Inductively Coupled Plasma-Mass Spectroscopy (ICP-MS) (weight percentages, wt 4.3 % Na, 0.2 % B) that there was a remarkable amount of inorganic salt present after the routine cleaning protocol.

The cleaning protocol mentioned above gave relatively high amount of organic percentages, and the conductivity of nanoparticle solutions showed that there was no (or little) amount of salt present. However, the efficiency of this protocol was very low in terms of the amount of particles obtained. The most of the particles were stacked in the membrane of centrifugal device, and a large amount of particles was lost in that stage. Since TGA required high amount of particles (~6-8 mg in our case), it wasn't possible to obtain TGA plots for all the particles. Therefore, different sizes of particles were analyzed in order to understand the variations through the particle size. Since 2-nm particles passed through the membrane of the centrifugal filter device (10k NMWL), that size range could not be analyzed.

Knowing the number of ligands on unit surface area of the particles was important in order to develop the relationship between functions and properties. Murray and collaborators reported TGA-based ligand density calculations, which are one of the earliest studies in the field, by using various size of spherical AuNPs (1.5–5.2 nm) covered by different thiolated ligands.¹⁰ They showed that ligand density change only slightly with respect to particle size. To illustrate, dodecanethiol (DDT) ligand densities were found to be around 4.6 ligands per nm² for both 5.2 nm and 2.8 nm of AuNPs. On the other hand, the ligand identity was demonstrated to have a pronounced effect on the densities. For example, larger ligands like α -methoxy- ω -mercapto-poly(ethylene glycol) (PEGSH, molecular weight (MW) = 5 kDa) formed lower ligand densities (2.88 ligands per nm²) on similarly sized AuNPs (2.8 nm), indicating that larger ligands may pack less densely on the surface of AuNPs.¹³ It is also possible to use different techniques to calculate organic percentages. Colvin and his colleagues compared TGA with analytical ultracentrifugation (AU) and total organic carbon analysis (TOC) to calculate the ligand

density of various thiolated PEG molecules. The authors discovered that ligand densities were comparable for all three methods.¹⁴

On the other hand, considering the bulk quantification strategies (NMR for ligand ratio, TGA for organic percentages, TEM for size distribution), the accuracy of ligand density values is fundamentally restricted by the size distribution of the AuNPs. An ideal method would be to work on single particles; however, current analytical methods have not yet been advanced to reach single particle analysis for ligand density calculations.¹³

In order to calculate ligand densities, the general tactic was to divide the total amount of ligands by the total amount of particle surface area. Therefore, the size of the particles, the molecular weight of the ligands (ligand ratio is needed in the case that there are two different ligands on the surface), and the organic percentage had to be obtained experimentally.¹³ In this thesis, the ligand density was calculated using **Equation 3.1** by using data obtained from TGA, NMR and TEM analysis.¹³

TGA provided the relative weight percentage of ligand shell (wt % shell) compared to the weight percentage of the pure gold core (wt % core). To calculate the total number of ligands, the total mole of ligands on the surface was calculated first by taking ligand shell mass (wt % shell) and dividing it by molecular weight of the ligand ($=$ (mole ratio of HT obtained by NMR*MW of HT + mole ratio of EG2 obtained by NMR*MW of EG2)/ (total number of moles)). Then, it is multiplied by Avogadro's number (N_A) to find out the total ligand number. The denominator needs a degree of the total particle surface area in the sample, which can be found by multiplying the total number of particles with the surface area of one single particle ($4\pi r^2$). The number of particles is derived from weight percentage of the pure gold core (wt % core) divided by the mass per particle, which corresponded to the product of the volume of a single particle ($4/3\pi r^3$, radius by TEM) and the density of bulk gold ($\sigma_{\text{core}} = 19.6 \text{ g/cm}^3$).

$$\text{Ligand Density} = \frac{\frac{\text{wt}\%_{\text{shell}}}{\text{wt}\%_{\text{core}}} \rho_{\text{core}} \frac{4}{3} \pi r_{\text{core}}^3 N_A}{MW 4\pi r_{\text{core}}^2} \quad (\text{Equation 3.1})$$

The ligand densities of EG2-14, EG2-27 and EG2-43 were found to be 4.1 ligands per nm², 4.3 ligands per nm², 4.3 ligands per nm², respectively. Although, smaller EG2-14 particles were expected to have higher densities due to high radius of curvature, which can provide more space, experimental data did not confirm this phenomenon. We concluded that ligand density of EG2:HT covered AuNPs with almost similar ligand ratios doesn't vary much within the nanoparticle size range from 2.6 nm to 5.4 nm.

As stated before, it is difficult to speculate on the accuracy of the values since it is calculated based on bulk quantification. In addition, triplicate measurements could not be performed due to experimental restrictions. Combination of errors originating from different techniques may result in high error values. However, our results showed good agreement with the values found in the literature. For example, Zheng *et al.* analyzed a similar system that is presented on this thesis by using TGA. They reported the density of tetra (ethylene glycol, EG4-SH) on the surface of 3.4 nm of AuNPs as 4.2 ligands per nm².¹³

3.2.5 Fourier Transform Infrared (FT-IR) Spectrometry to Probe Conformation of EG2 Ligands on the Surface of AuNPs

Fourier transform infrared spectroscopy (FTIR) is a robust technique to probe the nanoparticle' surfaces, providing information on the configuration of ligand molecules. In our study, it has been utilized to assess the average orientation of ligands within SAMs. We will then discuss evidence correlating the molecular conformation of EG2 ligands that are on the surface of AuNPs with the ability of these AuNPs to bind metal ions.

3.2.5.1 Basic Principles of FTIR

The entire internal energy of a molecule can be distributed into translational, rotational, electronic and vibrational energy levels. In the infrared region, the electromagnetic waves largely couple with the molecular vibrations, resulting a molecule excited to a higher vibrational state. Absorption of electromagnetic radiation takes place at frequencies that correlates to the vibration of specific sets of chemical bonds within a sample molecule. As a result, an infrared spectrum is generally acquired by passing infrared radiation through a sample and determining what fraction of the incident radiation is absorbed at a specific energy. The resulting spectrum is therefore very valuable since it provides molecular fingerprint of the sample. Like a fingerprint, each unique molecule produces the different infrared spectrum depending on the characteristic of the molecule. The essential requirement for infrared activity is that electric dipole moment of the molecule must change during the vibration.¹⁵

It can be imagined that there is an infinite number of vibrations of a molecule, which in real world would lead to a completely chaotic model for interpretation. Therefore, a molecule can be seen as a system of masses connected by bonds with spring-like properties. By using this model, a minimum set of fundamental vibrations (stretching and bending movements), are described as the normal modes of vibration based on a threefold set of coordinate axes. The number of normal modes can be calculated as $3N-6$ ($3N-5$ for linear molecules, where N is number of atoms). In reality, the number of vibrational modes is observed is much more lower then calculated value. The reason is

that several vibrational modes require the same amount of energy.¹⁵

Vibrations comprise either an alteration in bond length (stretching) or bond angle (bending). There are different types of stretching and bending modes presented in **Fig. 3.6**.

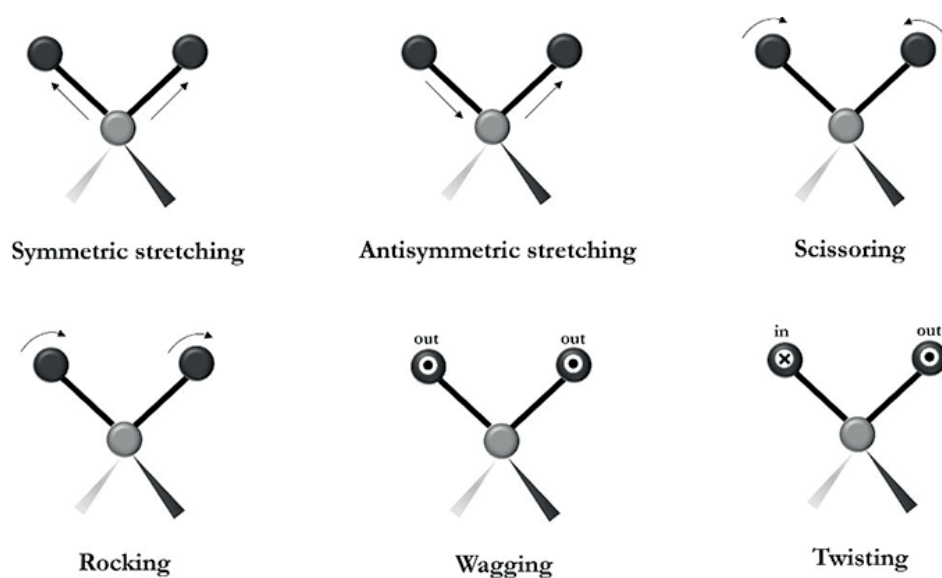


Figure 3.6: Fundamental vibrational modes of a molecule. Scissoring, rocking, wagging and twisting shows different types of bending vibrations.

The intensity of an absorption bands in IR spectrum rely on the change in the dipole moment of the bond and the number of the particular bonds existing. On the other hand, the frequency of absorption bands can be assessed based on our system of masses joined by bonds with spring-like properties. **Hooke's law (Equation 3.2)** defines the motion of a vibrating spring.¹⁵

$$\nu = \frac{1}{2\pi c} \left[\frac{f(m_1 + m_2)}{m_1 m_2} \right]^{1/2} \quad (\text{Equation 3.2})$$

It demonstrates the relationships between wavenumber (ν) and the masses of the atoms (m_1, m_2), the force constant of the bond (f). For example, we can deduce from Hooke's law that heavier atoms and weaker bonds lead to lower frequencies. Or, bending modes frequencies are lower than that of stretching frequencies since it is easier to bend a bond than to stretch it.

3.2.5.2 Structural Studies of Oligo(Ethylene Glycol) Terminated Self-Assembled Monolayers on Gold Surfaces

Pale-Grosdemange *et al.* for the first time considered the assembly properties of OEG-terminated alkanethiolates on gold surfaces.¹⁶ Later, Grunze and co-workers investigated in great detail the conformations of the OEGs on dissimilar supporting lattices, reporting the existence of two stable conformers – a helical on gold and an all trans on silver.¹⁷ The length of OEGs was also found to be critical in determining ligand configuration on the surface. For instance, Prime and Whitesides investigated nonspecific protein adsorption on SAMs of $\text{HS}(\text{CH}_2)_{11}\text{O}(\text{EG})_x\text{OH}$, where $x=1-7$. Protein adsorption was discovered to be inhibited when $x \geq 3$ since they were shown to have helical conformation, which accommodates water molecules within SAMs.¹⁶

On the other hand, it has been shown for huge series of OEGs that they have not been existed on gold surfaces by a single (pure) phase. Instead, IR spectra showed the coexistence of different phases like helical, all trans, or amorphous.^{18,19} **Fig. 3.7** illustrates the pure helical and all-trans form of EG3 oligomers, which are two of the possible crystalline configurations of OEG moieties. Therefore, interpretation of the IR spectra of ethylene glycol oligomers (OEGs) is not straightforward since multiple conformations may give rise to many peaks in the spectra. In addition, overlap of the bands because of the alkyl and oxyethylene moieties may make the analysis further challenging.²⁰⁻²²

In order to understand the effect of size and ligand ratio of AuNPs on the configuration of OEG ligand, we characterized all of the synthesized batches with solid-state FTIR spectroscopy. However, we first decided to start with establishing conformation of the EG2 chains in aqueous solution and as neat liquid. This may help us to elucidate conformational states of the EG2 moieties on the nanoparticle surface. In addition, we

tried to benefit from the previous studies conducted on conformations of OEGs on gold surfaces. **Table 3.4** displays the IR bands in the spectra at 1150-800 cm^{-1} , and **Fig. 3.8** shows the corresponding IR spectra of that compounds. The spectra were recorded in attenuated reflection mode (ATR).

The IR spectra of the ethylene glycol oligomers (OEG-SAMs) display two characteristic spectral regions, having the origin in (1) the CH stretching region of both alkyl and ether parts of the ligands (2800-3000 cm^{-1}), (2) the finger print region of OEGs, which includes different modes of in-plane bending, wagging, twisting, rocking, as well as skeletal vibrations of the oligomer parts (1500-800 cm^{-1}).^{17,22} However, I will focus on the changes in the bands at 1150 - 800 cm^{-1} , which correspond mostly to -C-O-C- stretching vibrations. One reason behind the close examination of the bands at 1150 - 800 cm^{-1} is that this part of the fingerprint region possesses the most resolved and intense IR peaks, which are relatively easy to interpret. Another reason is that a pronounced difference in the peak positions and relative intensities were observed in that region with respect to changing nanoparticle size.

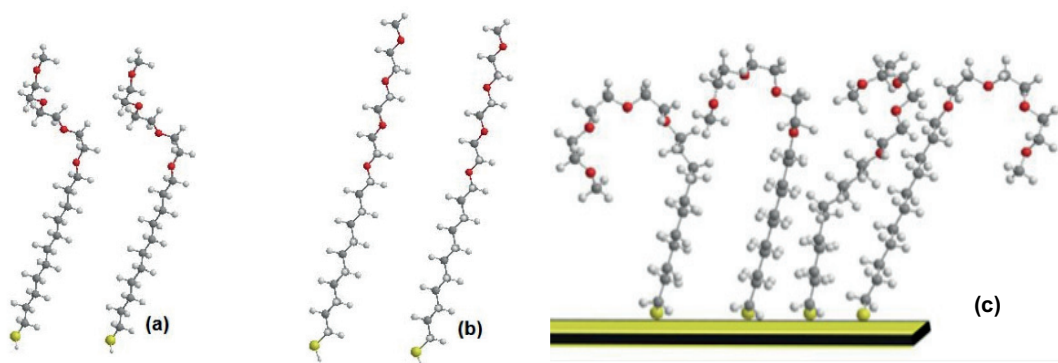


Figure 3.7: Schematic drawing of $\text{HSC}_{11}(\text{EG})_3\text{OCH}_3$ SAMs on Au, **A)** The helical conformation of OEGs. The helical conformer is attained when all dihedral angles about C-O bonds are $\sim 180^\circ$ and those about C-C bonds are $60\text{-}70^\circ$ (-C-O-C-C-O-, TGT). **B)** The all trans conformation of OEGs. The all trans conformer is denoted when all dihedral angles about C-O and C-C bonds are close to 180° (-C-O-C-C-O-, TTT). **C)** The series of amorphous conformation of OEGs (i.e. -C-O-C-C-O-, GTG).²³

CH Stretching Region. This region contains the asymmetric and symmetric alkyl -CH stretching modes, which provide information about the molecular packing and the crystallinity of the alkyl part of the SAMs. For the discussion of the vibrational spectra, we can refer to the band assignments of unfunctionalized alkanethiols reported in the literature. For example, the entire C₁₅ series, the peaks at 2918 cm⁻¹ and 2851 cm⁻¹ suggest that the SAMs adopt an excellent all-trans crystalline structure in the alkyl underlayer. Another example is that if you see a asymmetric alkyl CH₂ stretching mode frequency of 2921 cm⁻¹, it indicates that the C₁₁-alkyl phase has more gauche defects than the unfunctionalized C₁₂-thiol (2919 cm⁻¹), but fewer than in the liquid phase (2926cm⁻¹). In **Table 3.4**, CH₂ stretching mode appearing at higher frequencies indicates slightly higher gauche content.^{17,20,21,23}

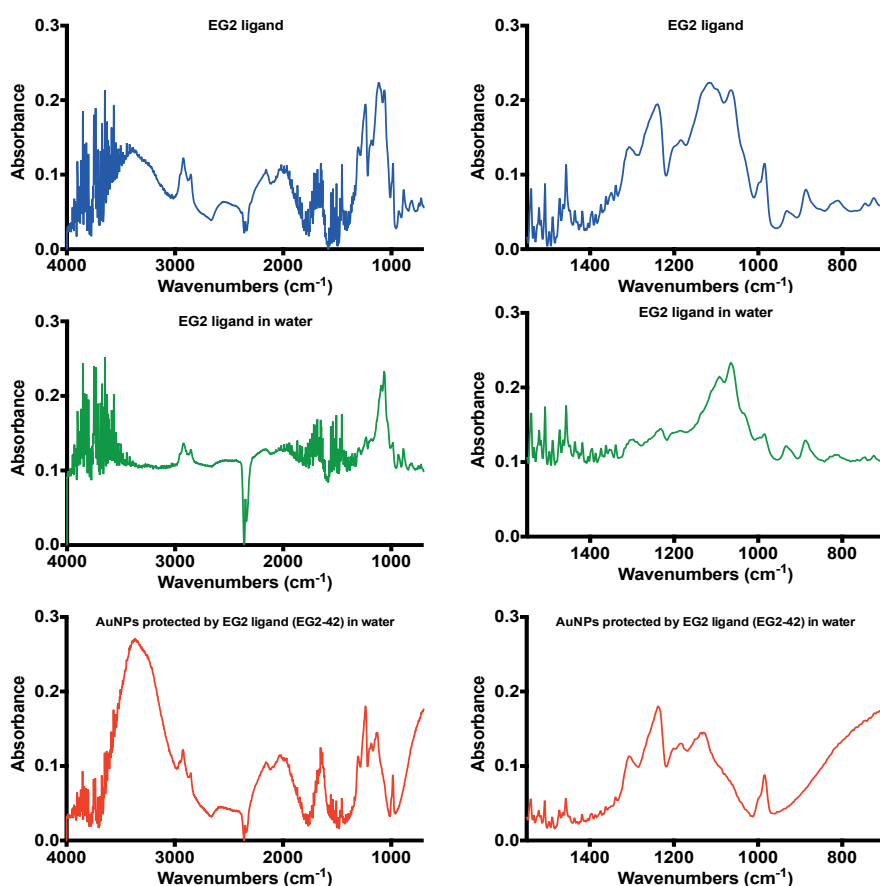


Figure 3.8: Left panel shows the wavenumbers in the range of 700-4000 cm⁻¹, Right panel shows the wavenumbers in the range of 700-1550 cm⁻¹. Comparison of spectral shifts corresponding to pure EG2 ligand/ EG2 ligand in water, and EG2 ligand on the surface of AuNPs in water.

The Name of the Compound	CH stretching region (cm ⁻¹)	OEG finger print region (1150-800 cm ⁻¹)	Relative Intensity -1	Relative Intensity -2
EG2-41 (All EG2-NPs-Solid state, 4.0 nm)	2926-2860	(1127, 1067 (sh), 1003) (943, 876, 827)	(2.5, 2.0, 1.0)	(1.0, 1.0, 1.0)
EG2-12 (All EG2-NPs-Solid state, 3.2 nm)	2923-2856	(1128, 1071 (sh), 1003) (947, 878, 825)	(1.7, 1.2, 1.0)	(1.3, 1.0, 1.3)
EG2-37 (All EG2-NPs-Solid state, 2.1 nm)	2923-2857	(1115, 1065 (sh)) (933, 880)	(1.0, 1.1)	(1.0, 1.0)
EG2 Ligand - Neat Liquid	2922-2856	(1114, 1064, 982) (930, 882, 810)	(2.0, 1.9, 1.0)	(1.0, 1.6, 1.3)
EG2 Ligand - Neat Liquid in Water	2922-2857	(1091 (sh), 1064, 983) (931, 885, 811)	(1.5, 1.6, 1.0)	(1.1, 1.2, 1.0)
EG2-12 (All EG2-NPs, 3.2 nm) in Water	2921-2855	(1127, 982)	(1.5, 1.0)	(-)

Table 3.4: Comparison of spectral shifts of EG2 ligands existing in different environments. The corresponding spectra are shown in **Fig.3.8**. Peak frequencies and intensities will be used as a reference in this study. Relative intensity-1 represents the ratios among the peaks at 1000 - 1130 cm⁻¹, and relative intensity-2 represents the ratios among the peaks at 800 - 1000 cm⁻¹. Sh-Shoulder peak

OEG Fingerprint Region. Assuming ordered alkyl chains, one would expect the OEG fingerprint bands, which display a more or less parallel alignment of the transition dipole moment with respect to the surface normal, to be dominating in the spectra. Here, we focused on the strong -C-O-C- asymmetric & symmetric skeletal stretching vibrations at ~ 1150 cm⁻¹ – 800 cm⁻¹.

First of all, we extracted all the useful data that we can use from the literature.

- ❖ Harder *et al.* found that the helical OEG-SAMs change their conformations to a predominantly amorphous phase when exposed to water, whereas; the all-trans OEG-SAMs retain a good conformational order when exposed to water and is affected mostly only within the methoxy terminal group of the OEG chains.¹⁷
- ❖ They also showed that the 1114 cm⁻¹ peak can be identified as a parallel polarized C-O-C stretching mode, a very distinctive sharp feature in spectra of helical crystalline PEG. In their system, the sharp peak appearing at 964 cm⁻¹ is also attributed to the CH₂ rocking mode of helical crystalline chains. In the molten state, PEG is enriched with gauche conformers, resulting in another rocking mode, appearing as a weak and broad low frequency shoulder on the 964 cm⁻¹ peak. In addition, C-O stretching

mode of the terminal C-OH group, can be seen also as a doublet at 1076/1061 cm^{-1} .^{18,19,24}

- ❖ An essentially different shape of C-O stretching mode at $\sim 1145 \text{ cm}^{-1}$ is seen for EG4 and EG2 ligands indicating that the chains are assembled predominantly in the all trans conformation.^{20,21,25}
- ❖ Previous studies suggested that amorphous and all-trans OEGs are expected to absorb in the 1125–1150 cm^{-1} region, and the shoulder(s) on the high frequency side therefore have been attributed to the presence of non-helical conformational (amorphous or trans) states in the OEG-SAMs.²²

In the light of this information, surprisingly, in contrast to the literature, the neat EG2 liquid holds preferentially helical conformation. The C-O-C stretching peak attributed to helical conformation at 1114 cm^{-1} disappears in water as suggested in the literature. Therefore, the spectral peaks observed in water can be seen as the vibrations related to amorphous like conformations (or with more gauche defects).

The peak around $\sim 1127 \text{ cm}^{-1}$ do not greatly change upon in touch with water, suggesting already amorphous like form, in which trans conformations may contribute more. On the other hand, peak at 1003 cm^{-1} seemed to be shifted to 982 cm^{-1} . The reason might be due to amorphous like orientation, in which gauche conformations may dominate. Here, it is really difficult to assign exact corresponding peak modes since there is no similar previous study on our system.

3.2.5.3 Solid-State Spectroscopic Characterization of EG2:HT Protected AuNPs

The transmission infrared spectra of the compounds were recorded on a Nicolet 6700 ThermoFischer Scientific FTIR spectrometer. 256 interferograms were averaged at 4 cm^{-1} resolution. The cleaning protocol prior to sample preparation was mentioned in **section 3.2.1**. 1.3 -1.5 mg of AuNPs as powder were mixed thoroughly with 150 mg of KBr in a mortar while grinding with the pestle. The fine powder was kept under vacuum for one night. The bottom of pellet die was covered with the powder, and then pressed at 5000-10000 psi to obtain homogenous pellet. The nanoparticle pellet was kept under vacuum

for one week prior to measurements to ensure the removal of bound water. In the beginning of this study, the time for keeping the pellet under vacuum was one day, however; as it is seen in the spectra presented in **Fig.3.9**, there is a huge peak around 1632-1635 cm^{-1} which can be attributed to the stretching and bending modes of adsorbed water molecules.²⁶ Spectra taken before and after drying protocol revealed that adsorbed water doesn't affect the vibrational bands in the fingerprint region, which is well correlated with the findings in the literature.

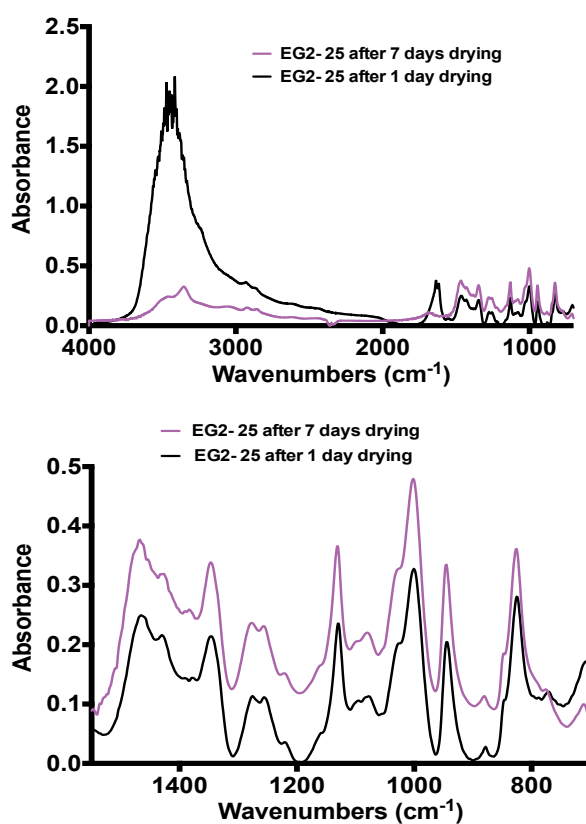


Figure 3.9: Adsorbed water molecules in the compound don't affect the conformation of the ligands on the surface.

FTIR spectra of all the synthesized AuNP batches are represented in **Appendix, Fig.A.15-A.25**. The corresponding vibrational peak frequencies and intensities that represent the region of interest can be found in **Table 3.5** presented in next section.

3.2.5.4 Analysis and Categorization of FTIR Spectra

The code in the thesis EG-n	CH stretching region (cm-1)	OEG finger print region (1150-800 cm-1)	Relative Intensity -1	Relative Intensity -2
EG2-1	2920-2854	(1116, 1068 (sh), -) (935, 878, 821)	(1.2, 1, -)	(1, 1.3, 1)
EG2-2	2917-2854	(1113, 1067 (sh), -) (935, 878, 824)	(1.3, 1, -)	(1.4, 2.3, 1)
EG2-3	2920-2858	(1125, 1069 (sh), 1001) (943, 878, 827)	(1.5, 1.1, 1.0)	(1.4, 1.0, 1.4)
EG2-4	2917-2855	(1123, 1069 (sh), 1000) (940, 878, 823)	(1.9, 1.4, 1.0)	(1.0, 1.1, 1.0)
EG2-5	2921-2855	(1125, 1071 (sh), 1004) (945, 877, 827)	(2.2, 1.6, 1.0)	(1.2, 1.0, 1.0)
EG2-6	2922-2863	(1126, -, 1003) (944, 877, 824)	(2.1, 1.5, 1.0)	(1.0, 1.0, 1.0)
EG2-7	2919-2856	(1128, 1071 (sh), -) (943, 878, 827)	(1.8, -, 1.0)	(1.0, 1.3, 1.0)
EG2-8	2925-2867	(1128, 1071 (sh), 1001) (943, 877, 824)	(1.5, 1.1, 1.0)	(1.2, 1.0, 1.1)
EG2-9	2916-2854	(1128, 1071 (sh), -) (943, 877, 824)	(1.4, -, 1.0)	(1.1, 2.4, 1.0)
EG2-10	2922-2858	(1128, 1067 (sh), 1001) (945, 878, 825)	(2.0, 1.7, 1.0)	(1.1, 1.0, 1.1)
EG2-11	2916-2855	(1128, 1071 (sh), 1003) (946, 878, 825)	(1.4, 1.0, 1.0)	(1.1, 1.0, 1.1)
EG2-12	2923-2856	(1128, 1071 (sh), 1003) (947, 878, 825)	(1.7, 1.2, 1.0)	(1.3, 1.0, 1.3)
EG2-13	2917-2855	(1128, 1071 (sh), 1002) (945, 878, 825)	(1.7, 1.2, 1.0)	(1.2, 1.0, 1.2)
EG2-14	2918-2857	(1124, 1071 (sh), 1003) (944, 883, 831)	(2.5, 1.6, 1.0)	(1.2, 1.0, 1.0)
EG2-15	2924-2859	(1123, 1071 (sh), 1002) (945, 880, 833)	(1.8, 1.3, 1.0)	(1.0, 1.8, 1.0)
EG2-16	2926-2859	(1127, -, 1003) (946, 880, 826)	(1.2, -, 1.0)	(1.2, 1.1, 2.0)
EG2-17	2910-2858	(1125, -, 1002) (945, 880, 825)	(1.7, -, 1.0)	(1.3, 1.0, 1.1)
EG2-18	2917-2854	(1128, -, 1002) (945, 878, 825)	(1.6, -, 1.0)	(1.0, 1.0, 1.0)
EG2-19	2823-2865	(1124, -, 1002) (945, 780, 826)	(2.2, -, 1.0)	(1.0, 1.0, 1.0)
EG2-20	2921-2856	(1130, 1079 (sh), 1003) (946, 877, 828)	(1.6, 1.0, 1.3)	(1.5, 1.0, 1.5)
EG2-21	2926-2859	(1130, 1079 (sh), 1001) (945, 881, 825)	(1.6, 1.0, 2.2)	(3.2, 1.0, 3.4)
EG2-22	2931-2864	(1130, 1079 (sh), 1002) (945, 877, 825)	(1.4, 1.0, 1.9)	(2.1, 1.0, 3.2)
EG2-23	2922-2861	(1130, 1079 (sh), 1003) (946, 883, 828)	(1.3, 1.0, 1.4)	(1.9, 1.0, 1.9)

EG2-24	2931-2865	(1130, 1076 (sh), 1001) (944, 877, 825)	(1.4, 1.0, 1.6)	(1.8, 1.0, 2.1)
EG2-25	2927-2858	(1130, 1079 (sh), 1002) (945, 880, 826)	(1.7, 1.0, 2.2)	(2.9, 1.0, 3.1)
EG2-26	2923-2858	(1130, 1078 (sh), 1003) (946, 879, 826)	(1.2, 1.0, 1.9)	(2.7, 1.0, 2.4)
EG2-27	2925-2859	(1130, 1079 (sh), 1004) (946, 879, 827)	(1.0, 1.1, 1.4)	(2.1, 1.0, 1.5)
EG2-28	2918-2863	(1129, 1069 (sh), 1002) (945, 878, 826)	(1.3, 1.0, 1.3)	(2.3, 1.0, 2.3)
EG2-29	2917-2859	(1129, 1079 (sh), 1002) (946, 876, 826)	(1.4, 1.0, 1.3)	(3.3, 1.0, 2.9)
EG2-30	2920-2862	(1128, 1079 (sh), 1001) (944, 878, 826)	(1.3, 1.0, 1.2)	(2.1, 1.0, 2.0)
EG2-31	2917-2858	(1130, 1079 (sh), 1003) (945, 883, 827)	(1.3, 1.0, 1.2)	(2.1, 1.0, 2.0)
EG2-32	2918-2850	(1117, 1065 (sh)) (923, 887)	(1.3, 1.0)	(1.0, 1.0)
EG2-33	2914-2847	(1118, 1066 (sh)) (927, 889)	(1.3, 1.0)	(1.0, 1.0)
EG2-34	2921-2855	(1118, 1063 (sh)) (923, 887)	(1.4, 1.0)	(1.0, 1.0)
EG2-35	2919-2857	(1116, 1065 (sh)) (933, -)	(1.2, 1.0)	(1.0, -)
EG2-36	2924-2859	(1113, 1067 (sh)) (933, 884)	(1.0, 1.1)	(1.0, 1.0)
EG2-37	2923-2857	(1115, 1065 (sh)) (933, 880)	(1.0, 1.1)	(1.0, 1.0)
EG2-38	2923-2859	(1117, 1069 (sh)) (-, 881)	(1.0, 1.0)	(-, 1.0)
EG2-39	2920-2855	(1117, 1069 (sh)) (-, 884)	(1.3, 1.0)	(-, 1.0)
EG2-40	2917-2852	(1113, 1064 (sh)) (926, 883)	(1.3, 1.0)	(1.0, 1.0)
EG2-41	2926-2860	(1127, 1067 (sh), 1003) (943, 876, 827)	(2.5, 2.0, 1.0)	(1.0, 1.0, 1.0)
EG2-42	2916-2853	(1117, 1068 (sh)) (925, 887)	(1.3, 1.0)	(1.0, 1.0)
EG2-43	2917-2857	(1116, 1067 (sh)) (924, 883)	(1.5, 1.0)	(1.0, 1.0)
EG2-44	2920-2854	(1116, 1064 (sh)) (927, 888)	(1.3, 1.0)	(1.0, 1.0)
EG2-45	2925-2862	(1123, 1071 (sh)) (944, 882)	(1.6, 1.0)	(1.0, 1.0)

Table 3.5: Comparison of spectral shifts of EG-n (1-45) AuNPs. The corresponding spectra are shown in Fig.3.19-3.30. The peak frequencies and intensities of region of interest are reported. Relative intensity-1 covers the range between 1000-1130 cm^{-1} . Relative intensity-2 covers the range between 800-1000 cm^{-1} . Sh is referred to shoulder peak.

Table 3.5 shows the corresponding vibrational peak positions and relative intensities of the peaks at region of interest. We need to systematically analyze and interpret all the spectra of synthesized AuNPs. We observed certain patterns between peak intensities and peak positions of different AuNPs, and therefore we benefited from principal component analysis (PCA) technique, which is a mathematical procedure that transforms a number of correlated variables into a smaller number of uncorrelated variables called principal components. It helped us to emphasize variation and bring out strong patterns in the dataset. PCA were performed by using six variables from the ratios of **relative intensity-1** and **relative intensity-2**. Based on PCA analysis, FTIR of 45 AuNP batches were patterned into 3 main regimes (**Fig. 3.10**, **FTIR regime-1**, 2, and 3).

The first two principal components account for as much of the variability in the data, therefore; only the pattern based on principal component 1 and 2 is presented (**Fig.3.10**).

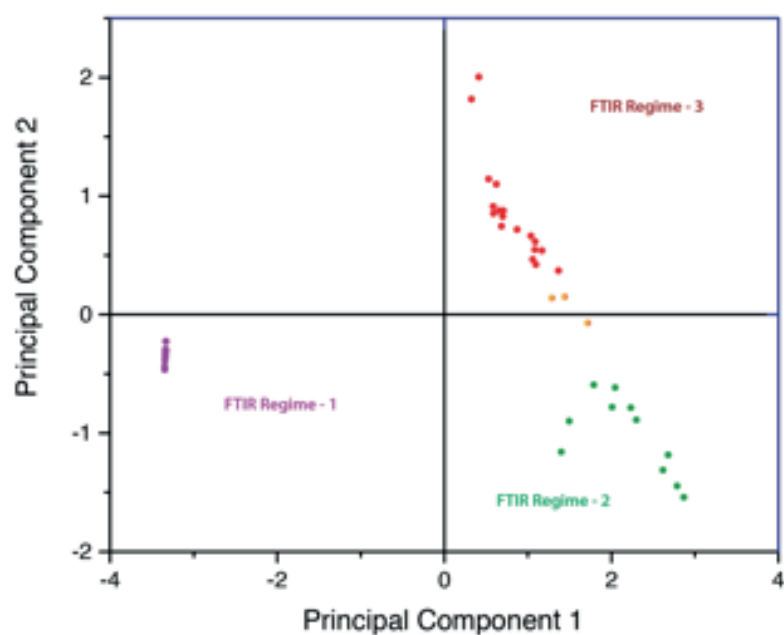


Figure 3.10: Principal component analysis of **relative intensities-1** and **2** of EG-n (1-45) AuNPs.

Representative FTIR spectra from each regime is shown in **Fig.3.11**.

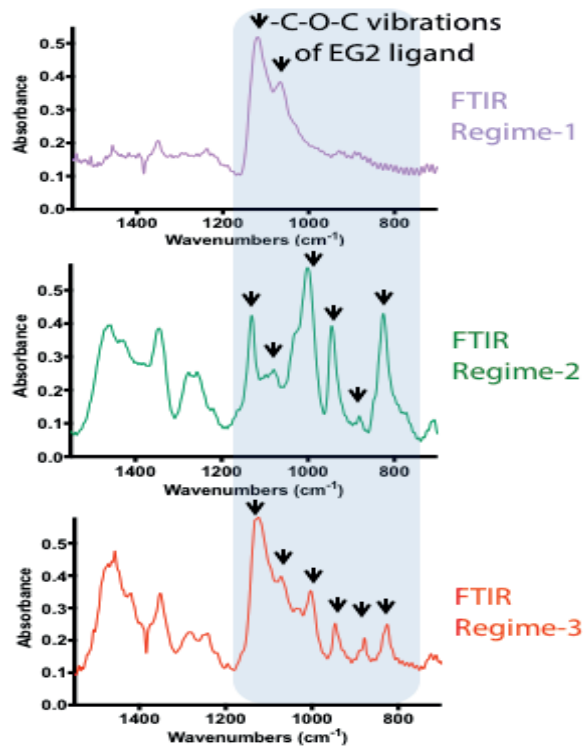


Figure 3.11: Representative FTIR spectra from each regime. Black arrows point out the spectral peaks of interest. Different FTIR regimes represent different configurational arrangement of EG2 ligands on the surface of synthesized AuNPs.

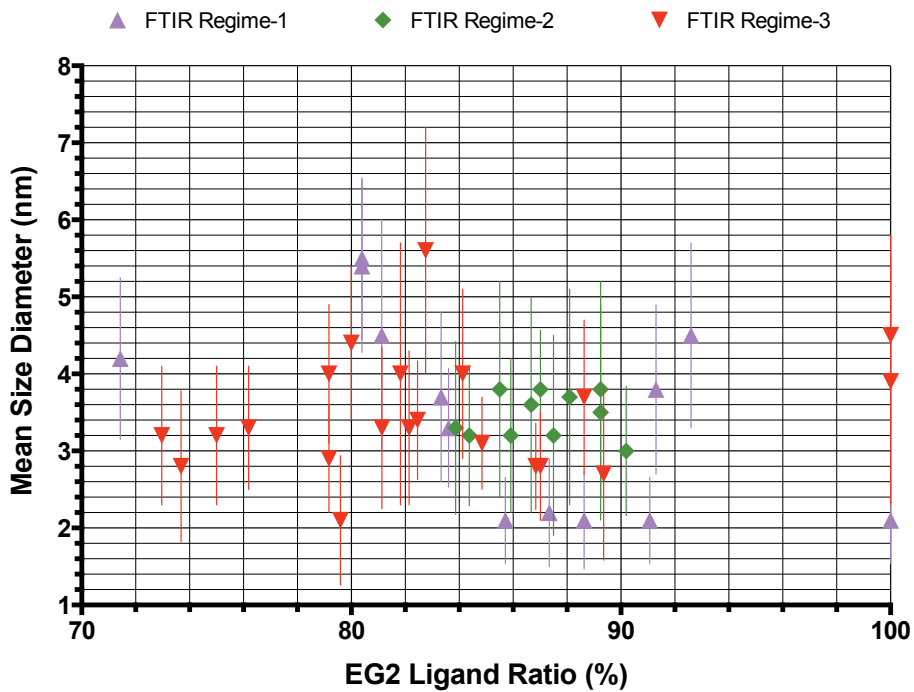


Figure 3.12 FTIR pattern of EG2 ligands on the surface of AuNPs depending on their size and EG2 ligand ratio. Upper and lower error bars shown for the y-axis is the standard deviation of mean size diameter.

In **Fig.3.12**, the knowledge obtained from PCA analysis regarding FTIR pattern of EG2 ligands is reflected on the 2-D size vs. ligand ratio plot, in order to understand how conformation of EG2 ligands varies with respect to size and ligand ratio of nanoparticles. As it can be seen from **Fig.3.12.**, there is generally a clustering of one type of **FTIR regime** within ranges of certain size and ligand ratio. On the other hand, it is possible to observe a nanoparticle batch, which corresponds three different FTIR regime within a narrow size and ligand ratio range. Or, it is also possible to observe particles from another FTIR regimes within a clustering of a specific FTIR regime (for example, appearance of red triangle within the clustering of green rhombus in **Fig.3.12.**). This observation can be explained by the recent findings of Ding and co-workers.²⁷ They used atomistic discrete molecular dynamics (DMD) simulations to calculate the equilibrium potential energies of the particles when SAMs on the surface results in certain structure and distribution (mixed, patch, and stripe). The conditions, which results in certain configurations of the ligands on the surface were evaluated by comparing the potential energies of each configuration. When they used **HT:EG2 ligand mixture** on the surface, the calculations concluded that the relative potential energies of different states are similar. This conclusion is very important since it tells us that even subtle changes in the synthetic protocol of those particles may results in different configuration on NP surface.

Now, we can turn our attention to understand how the conformation of EG2 ligands are changing among different FTIR regimes. Relative intensities of the peaks are critical in order to interpret the dominating conformation within SAMs. In addition, peak widths can be taken as an index of crystallinity. Broad peaks or shoulders are generally attributed to amorphous forms of the molecules. For example, although 2 nm All EG2 covered AuNPs possess –COC- stretching peaks for helical conformation, the peak has highly broad with shoulder at 1064 cm^{-1} , suggesting coexistence of both amorphous and crystalline state of the ligands. The intensity of the peaks at $\sim 940\text{ cm}^{-1}$ and $\sim 820\text{ cm}^{-1}$ (CH_2 rocking combined with COC stretching vibrations) are observed to be correlated with the intensity of the peak at $\sim 1001\text{ cm}^{-1}$.

Depending on the detailed explanation given in **Section 3.2.5.2**, we can only speculate about the results we obtained from this mathematical formulation. EG2 ligands, which belong to **FTIR regime-2**, can be said to have both helical and amorphous like

arrangement with more gauche defects around $-C-O-C-$ bonds compared to the AuNPs from other regimes. On the other hand, EG2 ligands, which belong to **FTIR regime-3**, can be said to have helical and amorphous like arrangement with more trans defects around $-C-O-C-$ bonds compared to the AuNPs from other regimes.

3.2.5.5 Aqueous-State Spectroscopic Characterization of EG2:HT AuNPs by ATR mode

As I stated in **Section 3.2.5.2**, helical like arrangements of OEG ligands results in having amorphous like conformation upon contact with water. I collected representative AuNP powders from each FTIR regime, and dissolved them in water. Under the attenuated transmission reflection (ATR) mode, an FTIR spectrum of each batch was recorded. We observed no difference in terms of conformation of EG ligands on the surface upon contact with water (**Fig. 3.13**).

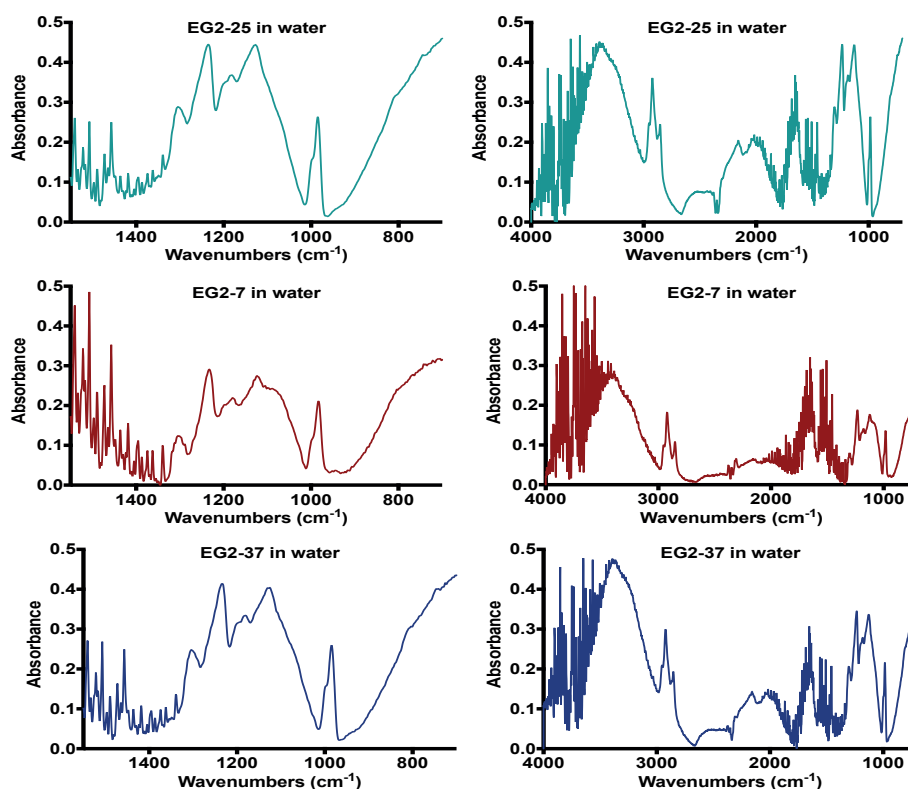


Figure 3.13: Right panel shows the wavenumbers in the range of 700-4000 cm^{-1} , Left panel shows the wavenumbers in the range of 700-1550 cm^{-1} . Representative FTIR spectra of synthesized AuNPs in water from each FTIR regime.

3.3 Comparison of Sum-of-Squares Residual (SSR) Values of Synthesized AuNPs

Mass spectrometry (MALDI-TOF-MS) has been recently explored as a simple and reliable tool to investigate the ligand ratio as well as ligand shell morphology of gold nanoparticles Harkness *et al.* presented the fundamental theory behind it. MALDI generates fragments from AuNP' surfaces that are composed of a number of gold atoms linked together with a number of thiolated ligands. The central hypothesis in this approach is that these fragments represent a statistical sampling of the surface. Thus, the mass distribution pattern of dissimilar fragments provides structural information of ligand shell morphology.²⁸

The most abundant fragment, i.e. gold-thiolate complex, Au_4L_4 was used for our calculations. Other types fragments have weak intensities, and therefore they are not suitable for accurate for quantitative analysis. For a ligand shell containing mixed-ligands, the Au_4L_4 fragment would have five dissimilar ligand combinations ($Au_4L_xL'_{4-x}$). The probability distribution of these combinations depends on the ligand shell arrangement (morphology).^{28,29} By analyzing the mass distribution pattern of such fragments, it is possible to deduce the morphology of the ligand shell. The value of sum-of-squares residual (SSR) has been proposed to quantify the differences in the mass distribution pattern. Luo *et al.* explained the calculation of SSR in this way: "The SSR is calculated by squaring and summing the residual between the normalized experimental intensity of each fragment and that of a given morphology."²⁹ Therefore, one can calculate the degree of phase separation of the two ligands on NP' surfaces by quantifying the deviation from binomial distribution (random morphology).

It has been established that if the SSR is less than 1.0×10^{-2} , the ligand shell are expected to have random distribution. On the other hand, if SSR is above 1.0×10^{-1} , it means that there are significant big domains or Janus type morphology on the surface. SSR in between 1.0×10^{-2} and 1.0×10^{-1} represents patchy or stripe-like morphology on the surface.²⁹

The AuNP batches analyzed by MALDI-TOF-MS technique were selected randomly based on the availability of the samples. MALDI results showed that there is lower EG2 ligand ratio on the surface of AuNPs than NMR predicts it (Table 3.5). Both NMR and MALDI-TOF results are consistent within each method. On the other hand, MALDI-TOF technique might be more reliable since residual free ligands that might be present even after the cleaning protocol do not have significant effect on the results.

AuNP Batch #	% EG2 (NMR)	% EG2 (MALDI)	SSR	Size (nm) Diameter	FTIR Regime
EG2-33	83	81	0.065	3.3	FTIR REGIME-1
EG2-45	92	85	0.050	3.8	
EG2-36	91	69	0.254	2.1	
EG2-38	88	78	0.208	2.1	
EG2-28	87	79	0.155	3.8	FTIR REGIME-2
EG2-29	85	74	0.095	3.7	
EG2-30	89	83	0.080	3.3	
EG2-1	75	68	0.042	2.8	FTIR REGIME-3
EG2-7	88	82	0.013	2.6	
EG2-18	82	81	0.036	3.3	
EG2-19	79	79	0.034	3.2	

Table 3.5: SSR values of different AuNPs' systems calculated by MALDI-TOF-MS technique. Molar ratio of EG2 is reported as %, which is determined by both NMR and MALDI-TOF-MS. For different FTIR regimes assigned to each particle, please refer to **Appendix, Fig.A.15-A.25**.

Table 3.5 reported calculated SSR values for selected AuNPs' systems. As it is explained above, we can refer to SSR values in order to compare the surface arrangements of the ligands. The ligand shell of the AuNPs corresponding to FTIR Regime-3 shows minimal phase separation compared to other systems. On the other hand, ligands from FTIR regime-2 tends to have patchier surfaces. When we looked at EG2-36, and EG2-38, they can be said that they probably have Janus type domain. Ligand shell structures of the

particles from FTIR regime-1 have two different kinds of arrangements depending on the core size, showing the high curvature effect of 2-nm particles on EG2 configuration.

3.4 Molecular Simulations of Synthesized AuNPs (In collaboration with Prof. Paola Posocco. University of Trieste, Italy.)

Selected **EG2-n** systems were analyzed at molecular level by computational techniques. For this purpose, we choose to work with different size of particles but with similar EG2:HT ratio on the surface. EG2-19, EG2-28, and EG2-38 were analyzed. For molecular simulations, we used the results from MALDI-TOF experiments. The EG2 molar amount for all three batches simulated is ~79 %.

To gain insights into the organization of such mixed monolayers nanoparticles (NPs), we resorted to a multiscale molecular simulation protocol, that is, a combination of atomistic/coarse-grained (CG) calculations. Initially, CG dissipative particle dynamics calculations were applied to predict the self-assembled ligand arrangement. This is a compulsory choice since the long times required for chain organization on the gold surface cannot be accessed by other computational approaches. Icosahedral shaped gold cores of appropriate diameter were considered and a proper number of **EG2** and **HT** ligands were placed around the AuNP core in order to reproduce the experimental grafting density (i.e., the number of ligands for nm² of surface, 4.5 ligands per nm²) and **EG2/HT** ratio. Ligands were initially placed in different relative configurations (i.e., completely random or completely phase separated) to guarantee that the thermodynamic equilibrium structure is achieved. Solvent molecules were explicitly considered at this stage to mimic the synthetic conditions.

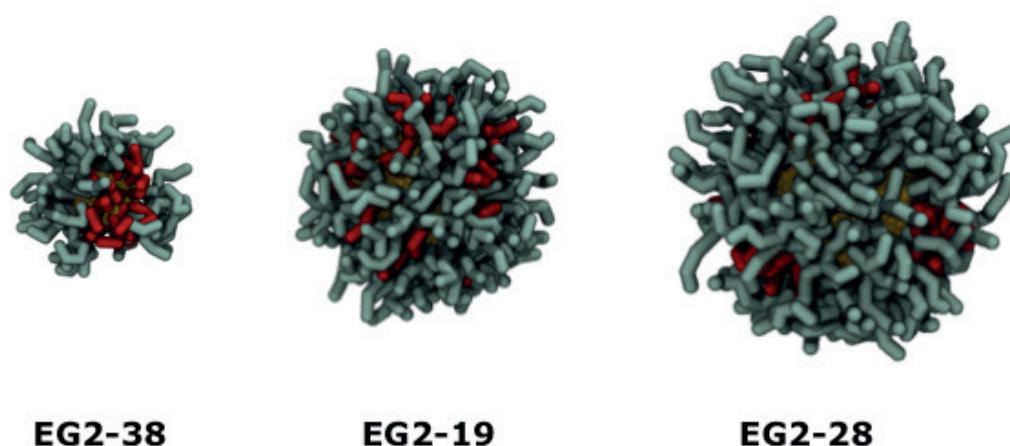


Figure 3.14: Representative morphology (arrangement) of the ligand shell of EG2-n AuNPs obtained by mesoscale simulation in water. EG2, grey sticks; HT, red sticks; gold core, yellow.

The results of the simulations shown in **Fig.3.14** are summarized in **Table 3.6**. Equilibrium surface arrangement of EG2:HT ligands on the surface show differences with respect to varying size of AuNPs.

AuNP Batch #	% EG2 (MALDI)	SSR	Size (nm) Diameter	FTIR Regime	Morphology
EG2-38	78	0.208	2.1	FTIR REGIME-1	Elongated HT domain-Janus
EG2-28	79	0.155	3.8	FTIR REGIME-2	Patches
EG2-19	79	0.034	3.2	FTIR REGIME-3	Random

Table 3.6: Size and molar EG2 % ratio of simulated AuNP systems. Morphology (arrangements on the surface) of the ligand shell were found by mesoscale simulations.

Results pointed out that the synthesized AuNPs might possess different ligand arrangements (morphology) on the surface with respect to the size of gold core. As previously stated in **Section.2.2**, phase separation on the curved surfaces with formation of domains of distinctive sizes and shapes was experimentally observed. Simulations suggested that HT ligands are randomly distributed on the surface of EG2-19. On the

other hand, they were observed to form small batches among EG2 ligands of EG2-28 particles. For smaller AuNPs (EG2-38), complete phase separation was observed to results in Janus arrangement of the ligands. If we turn our attention back to corresponding SSR values of these particles in **Table 3.5**, it can be seen that results show a good agreement.

Once the ligand-shell structures were equilibrated, we mapped the averaged ligand positions back onto an atomistic shell configuration with the aim of accurately deriving molecular related properties. Thus, **EG2** NPs were firstly relaxed in water and then, after solvent deletion, in vacuum to match the experimental spectroscopic environment. Trans/gauche distribution of dihedral angles in **EG2** ligands was later extracted from the hydrated/dehydrated systems to characterize molecular conformation and order/disorder state of the mixed monolayer (**Table 3.7**). CG calculations were carried out with LAMMPS software, and atomistic simulations were run using the AMBER package. In-house python scripts were developed for trans/gauche analysis. Careful calculations of dihedral angles of EG2 ligands on the surface of AuNPs revealed no remarkable differences in water. Dihedral angle distribution (%) for EG2 ligands in water is shown left panel of **Table 3.7**. Results are mirroring what we obtained from solution state ATR measurements of different AuNP' batches. FTIR spectra of synthesized AuNPs in water showed also no differences in terms of configuration of the ligands (**Fig. 3.13**).

Dihedral angle distribution (%) for EG2 ligands in vacuum is shown right panel of **Table 3.7**. More pronounced differences are obtained in the positions highlighted in red color in **Table 3.7**. Based on experimental solid-state FTIR measurements (**Appendix, Fig.A.15-A.25**) on EG2-38, EG2-19, and EG2-28, they are belonging to FTIR regime-1, FTIR regime-3, and FTIR-regime-2, respectively. Our conclusions for solid-state FTIR spectra of AuNPs matched with the calculated dihedral angle distributions in terms of the contribution of trans/gauche mode to the overall conformation state of EG2 ligand. For example, for EG2-28, we predicted more gauche states of $-C-O-C$ bond; whereas, for EG2-19, we predicted more trans states of $-C-O-C$ bond. This finding is reflected well in **Table 3.7**.

Atomistic structures

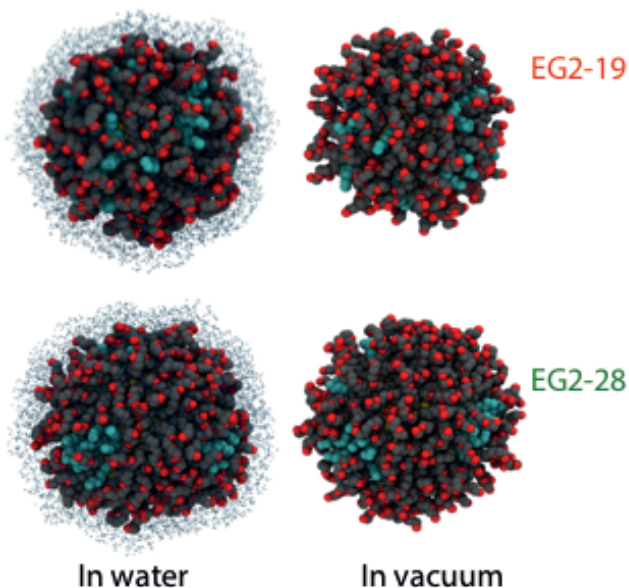


Figure 3.15: Atomistic structures of EG2-19 and EG2-28 in water and in vacuum. EG2 ligands are depicted as grey spheres and oxygen atoms are highlighted in red; HT ligands appear as cyan spheres. Some water molecules are shown as blue dots. Hydrogen atoms are not shown for sake of clarity.

		EG2-38	EG2-19	EG2-28			EG2-38	EG2-19	EG2-28		
1	S-C-C-C	Trans	49.2 (6.6)	49.7 (3.2)	50.8 (2.9)	1	S-C-C-C	Trans	55.1 (4.2)	54.9 (2.5)	51.7 (2.1)
		Gauche	50.8 (6.6)	50.3 (3.2)	49.2 (2.9)			Gauche	44.9 (4.2)	45.1 (2.5)	48.3 (2.1)
2	C-C-C-C	Trans	82.3 (5.5)	82.7 (3.4)	84.4 (2.8)	2	C-C-C-C	Trans	85.7 (3.9)	87.7 (2.1)	84.6 (1.7)
		Gauche	17.7 (5.5)	17.3 (3.4)	15.6 (2.8)			Gauche	14.3 (3.9)	12.3 (2.1)	15.4 (1.7)
3	C-C-C-C	Trans	80.7 (5.3)	82.3 (3.6)	81.5 (3.0)	3	C-C-C-C	Trans	87.8 (4.0)	77.1 (1.9)	81.5 (1.5)
		Gauche	19.3 (5.3)	17.7 (3.6)	18.5 (3.0)			Gauche	12.2 (4.0)	22.9 (1.9)	18.5 (1.5)
4	C-C-C-C	Trans	79.4 (6.0)	80.6 (3.4)	81.3 (3.0)	4	C-C-C-C	Trans	87.8 (3.7)	79.5 (2.2)	76.5 (1.6)
		Gauche	20.6 (6.0)	19.4 (3.4)	18.7 (3.0)			Gauche	12.2 (3.7)	20.5 (2.2)	23.5 (1.6)
5	C-C-C-O	Trans	46.5 (7.1)	46.6 (4.2)	46.6 (3.6)	5	C-C-C-O	Trans	44.6 (3.4)	49.3 (2.4)	51.0 (1.7)
		Gauche	53.5 (7.1)	53.4 (4.2)	53.4 (3.6)			Gauche	55.4 (3.4)	50.7 (2.4)	49.0 (1.7)
6	C-C-O-C	Trans	74.0 (6.6)	75.0 (3.8)	75.0 (3.5)	6	C-C-O-C	Trans	65.5 (4.0)	66.2 (2.3)	67.2 (1.3)
		Gauche	25.9 (6.6)	25.0 (3.8)	24.9 (3.5)			Gauche	34.5 (4.0)	33.8 (2.3)	32.8 (1.3)
7	C-O-C-C	Trans	69.6 (6.6)	70.5 (4.1)	70.0 (3.6)	7	C-O-C-C	Trans	62.4 (3.1)	61.0 (2.6)	61.5 (1.7)
		Gauche	30.4 (6.6)	29.5 (4.1)	30.0 (3.6)			Gauche	37.6 (3.1)	39.0 (2.6)	38.5 (1.7)
8	O-C-C-O	Trans	31.1 (6.9)	35.3 (4.4)	36.6 (3.8)	8	O-C-C-O	Trans	52.8 (3.1)	62.0 (1.8)	42.2 (1.7)
		Gauche	68.9 (6.9)	64.7 (4.4)	63.4 (3.8)			Gauche	47.2 (3.1)	38.0 (1.8)	57.8 (1.7)
9	C-C-O-C	Trans	68.2 (6.5)	67.6 (4.2)	67.8 (3.7)	9	C-C-O-C	Trans	61.8 (3.0)	62.4 (2.3)	62.1 (1.6)
		Gauche	31.8 (6.5)	32.4 (4.2)	32.3 (3.7)			Gauche	38.3 (3.0)	37.6 (2.3)	37.9 (1.6)
10	C-O-C-C	Trans	75.6 (5.9)	75.7 (4.0)	75.7 (3.3)	10	C-O-C-C	Trans	68.1 (3.3)	67.9 (1.9)	67.9 (1.7)
		Gauche	24.4 (5.9)	24.3 (4.0)	24.3 (3.3)			Gauche	31.9 (3.3)	32.1 (1.9)	32.1 (1.7)
11	O-C-C-O	Trans	11.7 (4.3)	13.4 (3.2)	13.3 (2.5)	11	O-C-C-O	Trans	33.3 (3.2)	43.8 (2.2)	25.2 (1.5)
		Gauche	88.3 (4.3)	86.6 (3.2)	86.8 (2.5)			Gauche	66.7 (3.2)	56.2 (2.2)	74.8 (1.5)

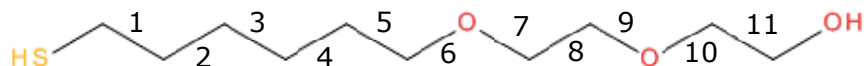


Table 3.7: Dihedral angle distribution (%) for EG2 ligands in water (left) and in vacuum (right). Values in parenthesis indicate standard deviation. The chemical structure of EG2 is depicted under the table. Numbers are assigned to different bond positions in EG2 molecule.

3.5 Evaluation and Comparison of the Results Obtained from Solid-State FTIR, SSR Values, and Molecular Simulations

Solid-state FTIR experiments showed that three different FTIR regimes could be identified for the configuration of EG2 ligands on the nanoparticles' surfaces depending on size and ligand ratio of the particles. Both SSR values and mesoscale simulations suggested that different ligand-shell morphologies could be observed for the synthesized AuNPs from each different FTIR regime. There is a high probability of that different ligand arrangements on the surface (different morphologies) may lead to different configuration of EG2 ligands in solid state. However, more research is needed in order to directly correlate the conformation of the ligands with the ligand morphology on the nanoparticles' surfaces.

When we consider revising what kind of differences are observed for EG2 ligands' conformation depending on the surface morphology, we can refer to both solid-state FTIR experiments and -C-O-C dihedral angles calculations by molecular simulations.

REFERENCES

- (1) M.C. D.; Astruc, D. *Gold Nanoparticles: Assembly, Supramolecular Chemistry, Quantum-Size-Related Properties, and Applications toward Biology, Catalysis, and Nanotechnology*. 2003.
- (2) Sardar, R.; Funston, A. M.; Mulvaney, P.; Murray, R. W. *Gold Nanoparticles: Past, Present, and Future*. *Langmuir* 2009, 25 (24), 13840–13851.
- (3) Turkevich, J.; Stevenson, P. C.; Hillier, J. A Study of the Nucleation and Growth Processes in the Synthesis of Colloidal Gold. *Discuss. Faraday Soc.* 1951, 11 (0), 55.
- (4) Brust, M.; Walker, M.; Bethell, D.; Schiffrin, D. J.; Whyman, R. Synthesis of Thiol-Derivatized Gold Nanoparticles in a Two-Phase Liquid-Liquid System. *J. Chem. Soc., Chem. Comm.* 1994, 0, 801-802.
- (5) Centrone, A.; Hu, Y.; Jackson, A.; Zerbi, G.; Stellacci, F. Phase Separation on Mixed-Monolayer-Protected Metal Nanoparticles: A Study by Infrared Spectroscopy and Scanning Tunneling Microscopy. *Small*. 2007, 3 (5), 814–817.
- (6) Carney, R. P.; DeVries, G. A.; Dubois, C.; Kim, H.; Kim, J. Y.; Singh, C.; Ghorai, P. K.; Tracy, J. B.; Stiles, R. L.; Murray, R. W.; Glotzer, S. C.; Stellacci, F. Size Limitations for the Formation of Ordered Striped Nanoparticles. *J. Am. Chem. Soc.* 2008, 130 (3), 798–799.
- (7) Marbella, L. E.; Millstone, J. E. NMR Techniques for Noble Metal Nanoparticles. *Chem. Mater.* 2015, 27 (8), 2721–2739.
- (8) Smith, A. M.; Marbella, L. E.; Johnston, K. A.; Hartmann, M. J.; Crawford, S. E.; Kozycz, L. M.; Seferos, D. S.; Millstone, J. E. Quantitative Analysis of Thiolated Ligand Exchange on Gold Nanoparticles Monitored by ¹H NMR Spectroscopy. *Anal. Chem.* 2015, 87 (5), 2771–2778.
- (9) Hayat, M. A. *Basic Techniques for Transmission Electron Microscopy*; Academic Press, 1986.
- (10) Terrill, R. H.; Postlethwaite, T. A.; Chen, C. H.; Poon, C. D.; Terzis, A.; Chen, A.; Hutchison, J. E.; Clark, M. R.; Wignall, G.; Londono, J. D.; Superfine, R.; Falvo, M.; Johnson, C. S.; Samulski, E. T.; Murray, R. W. Monolayers in Three Dimensions: NMR, SAXS, Thermal, and Electron Hopping Studies of Alkanethiol Stabilized Gold Clusters. *J. Am. Chem. Soc.* 1995, 117 (50), 12537–12548.
- (11) Daglar, B.; Aydogan, N. Fluorocarbon-Hydrocarbon Hybrid Gold NPs

Synthesized by Bulk Exchange Reactions and Surface Coatings of Fluorocarbon Coated Gold NPs Are Increased. *Colloids Surfaces A Physicochem. Eng. Asp.* 2013, 419, 257–262.

- (12) Mansfield, E.; Tyner, K. M.; Poling, C. M.; Blacklock, J. L. Determination of Nanoparticle Surface Coatings and Nanoparticle Purity Using Microscale Thermogravimetric Analysis. *Anal. Chem.* 2014, 86 (3), 1478–1484.
- (13) Smith, A. M.; Johnston, K. A.; Crawford, S. E.; Marbella, L. E.; Millstone, J. E.; Hamers, R. J.; Wild, U.; Knop-Gericke, A.; Su, D.; Schlögl, R.; Superfine, R.; Falvo, M.; Johnson, C. S.; Samulski, E. T.; Murray, R. W. Ligand Density Quantification on Colloidal Inorganic Nanoparticles. *Analyst* 2017, 142 (1), 11–29.
- (14) Benoit, D. N.; Zhu, H.; Lillierose, M. H.; Verm, R. A.; Ali, N.; Morrison, A. N.; Fortner, J. D.; Avendano, C.; Colvin, V. L. Measuring the Grafting Density of Nanoparticles in Solution by Analytical Ultracentrifugation and Total Organic Carbon Analysis. *Anal. Chem.* 2012, 84 (21), 9238–9245.
- (15) Coates, J. Interpretation of Infrared Spectra, A Practical Approach Interpretation of Infrared Spectra , A Practical Approach. *Encycl. Anal. Chem.* 2000, 10815–10837.
- (16) Pale-Grosdemange, C.; Simon, E. S.; Prime, K. L.; Whitesides, G. M. Formation of Self-Assembled Monolayers by Chemisorption of Derivatives of Oligo(ethylene Glycol) of Structure HS(CH₂)₁₁(OCH₂CH₂)_mOH on Gold. *J. Am. Chem. Soc.* 1991, 113 (1), 12–20.
- (17) Harder, P.; Grunze, M.; Dahint, R.; Whitesides, G. M.; Laibinis, P. E. Molecular Conformation in Oligo(ethylene Glycol)-Terminated Self-Assembled Monolayers on Gold and Silver Surfaces Determines Their Ability To Resist Protein Adsorption. *J. Phys. Chem. B* 1998, 102 (2), 426–436.
- (18) Valiokas, R.; Svedhem, S.; Svensson, S. C. T.; Liedberg, B. Self-Assembled Monolayers of Oligo(ethylene Glycol)-Terminated and Amide Group Containing Alkanethiolates on Gold. *Langmuir* 1999, 15 (10), 3390–3394.
- (19) Malysheva, L.; Onipko, A.; Valiokas, R.; Liedberg, B. First-Principle DFT and MP2 Modeling of Infrared Reflection - Absorption Spectra of Oriented Helical Ethylene Glycol Oligomers. *J. physical Chem. B* 2005, 109 (27), 13221–13227.
- (20) Pertsin, A. J.; Grunze, M.; Garbuzova, I. A. Low-Energy Configurations of Methoxy Triethylene Glycol Terminated Alkanethiol Self-Assembled Monolayers and Their Relevance to Protein Adsorption. *J. Phys. Chem. B* 1998, 102 (25), 4918–4926.

- (21) Feldman, K.; Hähner, G.; Spencer, N. D.; Harder, P.; Grunze, M. Probing Resistance to Protein Adsorption of Oligo(ethylene Glycol)-Terminated Self-Assembled Monolayers by Scanning Force Microscopy. *J. Am. Chem. Soc.* 1999, 121 (43), 10134–10141.
- (22) Malysheva, L.; Klymenko, Y.; Onipko, A.; Valiokas, R.; Liedberg, B. Ab Initio Calculations of Equilibrium Geometries and Vibrational Excitations of Helical Ethylene-Glycol Oligomers: Application to Modeling of Monolayer Infrared Spectra. *Chem. Phys. Lett.* 2003, 370 (3–4), 451–459.
- (23) Lee, H. Structural Studies of Oligo (Ethylene Glycol) -Containing Assemblies on Gold; 2012. *Phys. Chem. B*, 2005, 109 (7), 2934–2941.
- (24) Malysheva, L.; Onipko, A.; Fyrner, T.; Lee, H. H.; Valiokas, R.; Konradsson, P.; Liedberg, B. Spectroscopic Characterization and Modeling of Methyl- and Hydrogen-Terminated Oligo(ethylene Glycol) Self-Assembled Monolayers. *J. Phys. Chem. C* 2012, 116 (22), 12008–12016.
- (25) Vanderah, D. J.; Meuse, C. W.; Silin, V.; Plant, A. L. Synthesis and Characterization of Self-Assembled Monolayers of Alkylated 1-Thiahexa(ethylene Oxide) Compounds on Gold. *Langmuir* 1998, 14 (24), 6916–6923.
- (26) Zughul, M. B.; Derwish, G. A. W. Infrared Spectroscopic Study of the Role of Water in Crown Ethers and Their Molecular Complexes with 3- and 4-Nitrophenol. 1997, 245–258.
- (29) Ge, X.; Ke, P. C.; Davis, T. P.; Ding, F. A Thermodynamics Model for the Emergence of a Stripe-like Binary SAM on a Nanoparticle Surface. *Small*. 2015, 37 (11), 4894-4899.
- (28) Harkness, K. M.; Balinski, A.; McLean, J. A.; Cliffel, D. E. Nanoscale Phase Segregation of Mixed Thiolates on Gold Nanoparticles. *Angew. Chem. Int. Ed. Engl.* 2011, 50 (45), 10554–10559.
- (29) Luo, Z.; Hou, J.; Menin, L.; Ong, Q. K.; Stellacci, F. Evolution of the Ligand-Shell Morphology during Ligand-Exchange Reaction on Gold Nanoparticles. *Angew. Chemie Int. Ed.* 2017, 56(43), 13521-13525.

CHAPTER 4

Investigation of Metal Ion Binding Abilities by Mixed-Ligand Protected AuNPs

The ultimate goal of our study is to understand the relationship between metal-ion binding properties and physical properties of mixed ligand coated AuNPs. For this purpose, we focused our attention to examining the differences between metal ion capturing abilities of synthesized AuNPs both qualitatively and quantitatively. **Primary choice of metal ion** in this work is Cd^{2+} ion since there is a great need to monitor the concentration levels of this highly toxic and carcinogenic ion. Similarly, other environmentally relevant metal ions were tested against the produced AuNPs to assess their selectivity profiles. This thesis envisaged establishing conductometry as an analytical method to evaluate qualitatively the binding capabilities of EG2:HT protected AuNPs. In addition, isothermal titration calorimetry (ITC) was utilized to define the thermodynamic parameters of the interaction between Cd^{2+} ions and synthesized AuNPs. Finally, spectral changes of ligand moieties upon complexation were observed by FTIR spectroscopy, which supported the results obtained by conductometry and ITC.

4.1 Conductometric Titrations to Inspect Ion-Binding Abilities of Synthesized AuNPs.

Many experimental techniques have been described in the literature for the study of complex formation of cations with inorganic and organic ligands (UV-VIS, Fluorescence, NMR etc.), however, not all of them are applicable to find out association constant of reaction between metal ions and AuNPs due to the nature of the gold nanoparticles.¹ As a major qualitative tool, conductometric titrations were used to verify the interaction between synthesized AuNPs and metal ions.

4.1.1 Fundamentals of Conductometry and Its Applications in the Complexation Studies

Conductivity is a measure of how well a solution conducts electricity. To conduct electricity, a solution must contain ions, or charged particles.² Ohm's law, which describes the conductance in both electrolytes and metals, forms the basis of conductivity measurements. According to Ohm's law, the current (I, amperes) passing through a conductor is mathematically equal to the electromotive force (E, volts) divided by the resistance of the path (R, ohms) ($I=E/R$). And, conductance is the reciprocal ($1/R$) of the resistance, and its unit is ohm^{-1} or mho. Friedrich Kohlrausch first designed conductivity meters, where two electrodes are separated by a fixed distance. This way, the specific conductance can be obtained when the area of the electrodes (A) and their distance apart (L) are known (Equation 4.1). According to Kohlrausch's law of independent migration of ions, each ion contributes the specific conductivity of the solution independently, and the specific conductivity therefore can be expressed in terms of chemical properties of the ions (Equation 4.1).²

$$\kappa = G \cdot (L/A) \text{ where } \kappa \text{ is specific conductivity [S/cm]}$$

$$\kappa = \sum c_i \lambda_i \quad \text{where } \lambda_i = z_i \mu_i F$$

$$c_i = \text{concentration [mol/L]} \quad \text{(Equation 4.1)}$$

$$Z_i = \text{valence number}$$

$$\lambda_i = \text{molar conductivity [S*cm}^2 \text{ /mol]}$$

As it can be deduced from Equation 4.1, the extent of observed conductivity (G) of the electrolyte solution depends directly on the concentration and mobility of the ions. Therefore, the interactions that can change the mobility or the concentration of free ions in solutions can be tracked with the help of conductometry, which is a modest and low-cost experimental technique.

Conductometry has been used widely to examine the complex formation between metal cations and crown ethers in solution.^{3,4} The benefit of this technique is that the

measurements can be carried out with great precision at low concentration in solution systems. Valuable knowledge can be obtained about the metal ion-crown ether interaction by measuring the change in conductivity of a metal salt solution to which crown ether is added (common practice in the field).⁴ When metal salt is fully dissociated in the solution, a large cationic complex of metal ion and crown ether is formed upon complexation. This complex can have less mobility in solution than the uncomplexed metal cation, causing the reduced capacity of charge transport and hence the reduced conductivity of the solution. This titration study provides information about the affinity constant of crown ethers for cations and the stoichiometry of complexation. It is also counted as one of the most reliable approaches for acquiring the formation constants of cation-macrocyclic complexes.^{4,5} One of the recent examples that applied conductometry was published by Barman *et.al* in order to study the inclusion complex formation of hollow circular hosts,⁵ 18-crown-6 (18C6) and dibenzo-18-crown-6 (DB18C6) with 1-methyl-3-octylimidazolium tetra- fluoroborate (**Fig. 4.1**).

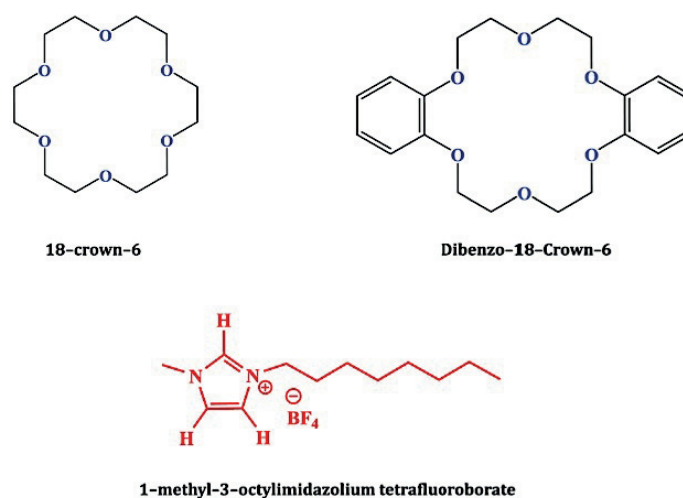


Figure 4.1: Chemical structures of the imidazolium cation and crown ethers. Reproduced from **Ref. 5** with permission from The Royal Society of Chemistry.

The molar conductance (λ) of the 0.5 mM imidazolium cation in acetonitrile solution was measured as a function of the crown ether to cation molar ratio. Plots of the resultant molar conductance vs. crown ether/cation molar ratio are demonstrated in **Fig. 4.2**. In

both cases of 18C6 and DB18C6, there is a steady decrease in the molar conductance of imidazolium cation with increasing crown ether concentration. This observation implies that the inclusion complex is less mobile than the free imidazolium cation in acetonitrile. From the titration plots in **Fig. 4.2**, they determined the stoichiometric ratio between the cation and the crown ether in the complex as 1:1, by determining the leveling off point of the curve.

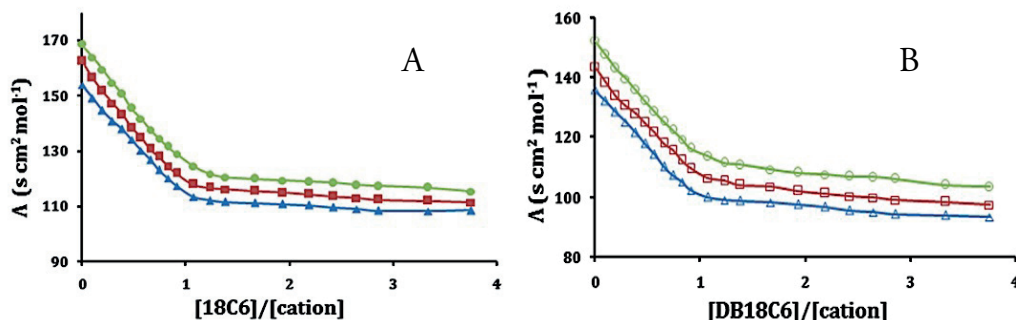


Figure 4.2: The plots of change in molar conductance of imidazolium cation against **A**) [18C6]/[cation] at 298.15 K, **B**) [DB18C6]/[cation] at 298.15 K. Reproduced from **Ref. 5** with permission from The Royal Society of Chemistry.

In addition, the authors followed the mathematical approach proposed by Evans *et al.* (1972) to calculate the association constant.⁶ Although all steps were not presented here, the resulting formulation to calculate association constant is demonstrated in **Equation 4.2**.

$$K_f = \frac{[MC^+]}{[M^+][C]} = \frac{(\Lambda_M - \Lambda_{obs})}{(\Lambda_{obs} - \Lambda_{MC})[C]} \quad \text{(Equation 4.2)}$$

$$[C] = C_C - \frac{C_M(\Lambda_M - \Lambda_{obs})}{(\Lambda_M - \Lambda_{MC})}$$

Equation 4.2 can be applied to any host-guest interaction. Here, K_f is the complex formation constant; λ_M is the molar conductance of the guest before the addition of host;

λ_{MC} is the molar conductance of the complexed guest; λ_{obs} is the molar conductance of the solution during titration; C_C is the concentration of the host added and C_M is the concentration of the guest. Both λ_{MC} and K_f can be assessed by applying **Equation 4.2** after performing conductometric titrations. K_f calculated for both crown ethers is around 10^3 at 25 °C.

4.1.2 Experimental Design of Conductometric Tests

The design of our conductivity experiments was different to the one used to study the interactions of crown ethers, perhaps the most common ones found in the literature. The main reasons for the design change are experimental limitations of our system (i.e the heterogenous nature of AuNPs). The schematic illustration of our experimental set up is shown in **Fig. 4.3A**. Experiments were carried out by titrating solution of AuNPs with a metal ion solution in MQ water. Then, the conductivity of AuNPs solution was measured after each addition of the metal salt.

Such a titration may give rise to different conductometric effects depending on the binding capability of AuNPs. In theory, addition of strong electrolyte solution to the highly homogenous AuNPs system may give rise to different scenarios depicted in **Fig. 4.3**. In the case that AuNPs are not able to bind/capture the added metal ions, linear increase in the solution conductivity is expected since it is directly proportional to concentration. When AuNPs are able to capture metal ions from the solution an increase in the conductivity is observed after initial additions of the metal salt depending on the affinity constant between AuNPs and metal ions. Then, a plateau region (where the conductivity would not increase) will be observed upon further addition of metal ions in case of the ion trapping. The reason for this observation is that added metal ions cannot contribute the increase in conductivity since they are stuck in the ligand moieties of AuNPs, resulting in immobile complexes. We expect that this plateau region would be observed until all binding sites are occupied.

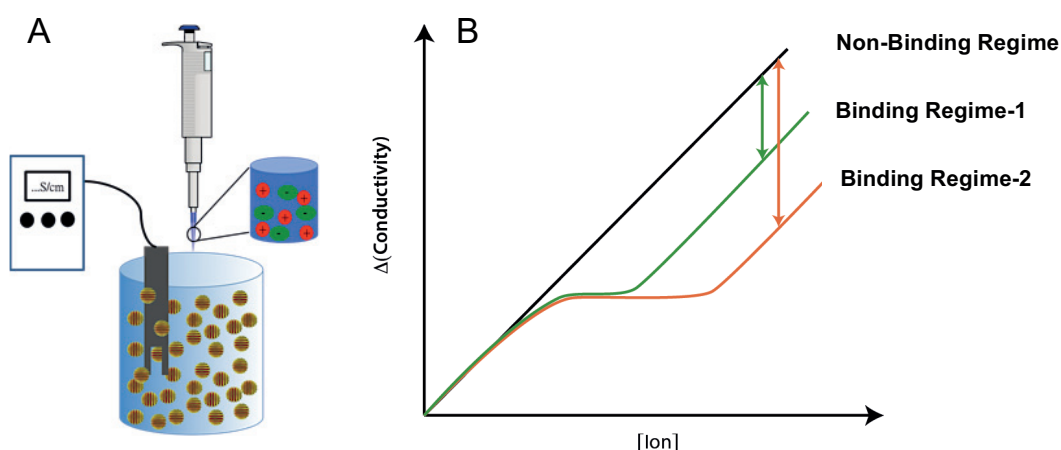


Figure 4.3: **A)** The schematic drawing of conductivity measurement set up, **B)** Theoretical plot of change in solution conductivity upon addition of metal ions. Based on the assumption that all three batches have the same amount of EG2 ligands (which possess donor atoms for ion-binding) on the surface, three different regimes can be inferred from the plot. Non-binding regime, which shows linear increase with the increasing concentration of metal salt does not hold any binding pocket on the surface. Binding regime-1 has fewer binding pockets on the surface than that of binding Regime-2. (This interpretation is valid if binding regimes have similar association constants.)

4.1.3 Experimental Results of Conductometric Tests

All of the synthesized AuNPs were tested against Cd^{2+} ion in order to evaluate their binding capabilities qualitatively. Chloride ions were used as counter ions. MQ water without any AuNPs was used as a reference for all the measurements. Experiments were conducted with a Mettler Toledo SevenGo™ conductivity meter with automatic temperature compensation (ATC) coupled with 4-pole graphite conductivity probe (Inlab 738). Each measurement was done in triplicates, and average values were plotted with standard deviations represented by error bars. For each replicate, a fresh AuNP powder was taken from the synthesized batch and weighted separately, and then diluted with water.

Based on the ligand density calculations shown in **Chapter 3**, we assumed that all the batches have the same ligand density, ~ 4.3 ligands/ nm^2 . In addition, to calculate number

of binding pockets in AuNPs solutions, we assumed that two EG2 ligands would interact with one metal ion like crown ethers, forming one binding pocket.

Before performing the conductivity tests, AuNPs were dissolved in 12.5 ml of MQ water to give ~0.18 mM EG2 pairs. The solutions were then allowed to equilibrate in MQ water for 3-5 hours to ensure good dispersion of the particles within a solution. Metal ion solutions (0.05 M) were prepared freshly just before the titrations, and added to nanoparticle solutions as small aliquots (10-20 μ L each time). Here, it was important to not to change the volume of the solution, which would disturb the equilibrium and linearity in conductivity measurements. This is why conductivity experiments were not performed until the saturation point is reached. An alternative way to avoid changing the volume of solution, might be to prepare concentrated solutions of metal salts, however; the solubility of CdCl₂ salt decreases dramatically above 0.05 molar concentration, leading to high error measurements.

Conductivity plots corresponding to entire EG-n series are presented in **Appendix, Fig.A.26-A.31**. EG2-10, EG2-37, and EG2-41 batches, which possess only EG2 ligands on the surface were tested as a control. MQ water without adding of AuNPs was presented in all plots as a control.

Delta conductivity (Δ) in the y-axis of the plots represents the conductivity of the solution from which the initial conductivity value is subtracted. Concentration of added metal salt is represented in x-axis as molarity (M).

4.1.4 Interpretation of the Results Acquired from Conductivity Tests

Before detailed analysis, it is important to see different capturing modes of synthesized AuNPs towards Cd²⁺ ions under the same conditions. Detailed explanation for the interpretation of the experimentally obtained conductivity plots was provided in section 4.1.2. The theoretical plot represented in **Fig. 4.3B** is designed to understand the experimental results presented in this thesis. Our system does not follow a perfect plot, like the one represented in **Fig.4.3B** due to heterogenous nature of synthesized AuNPs. Since the clear plateau region and saturation point could not be observed clearly, it is

difficult to speculate about the association constants between AuNPs and Cd^{2+} ions. On the other hand, what we can infer from the plots is the number of binding pockets of different AuNPs batches since similar concentrations of EG2 pairs were present in each solutions. However, it should be kept in mind that this comparison is valid if the batches have similar binding constants. Soon it will be evident by isothermal titration calorimetry experiments (ITC) that the association constants of binding regime-1 and binding regime-2 are similar, and no association was observed for non-binding regime. Therefore, deviation from this straight line corresponding to MQ water can be seen as an index to judge number of binding pockets on the surface of AuNPs.

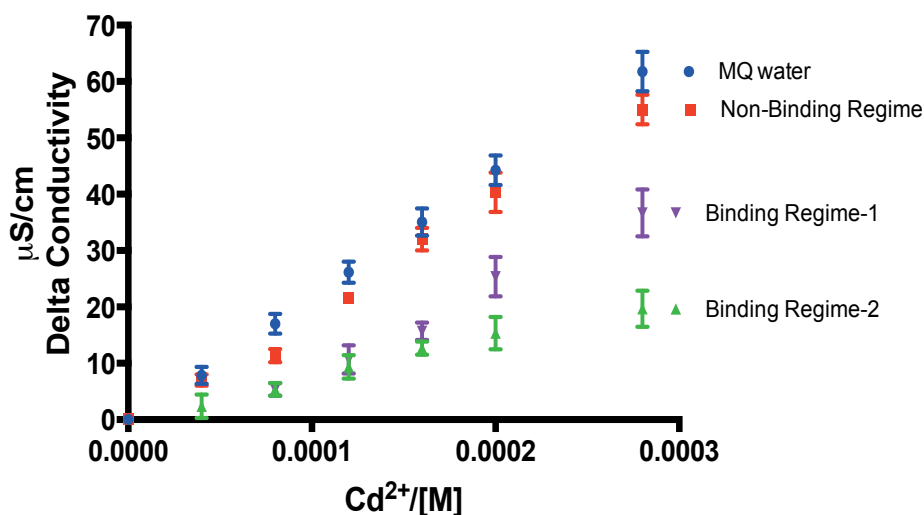


Figure 4.4: Three different binding regimes identified after conductivity measurements. One result from each regime is represented for the clarity. Each set of measurements were done three times and the average values were plotted with standard deviations represented by error bars.

In order to systemize our results, we mathematically defined this deviation, identifying three different binding behaviors of the particles. Values that correspond to last titration points of synthesized AuNPs were compared with the last titration point of MQ water. The values of deviations in the range of 5-15 $\mu\text{S/cm}$, 20-30 $\mu\text{S/cm}$, and 35-45 $\mu\text{S/cm}$ are assigned as **non-binding regime**, **binding regime-1**, and **binding regime-2**, respectively. These numbers are specific to concentration range of metal salt as well as concentration of AuNPs used in this study. In other words, they may change in another platform depending on the concentration of metal salt and AuNPs. According to this

arrangement, from EG2-1 to EG2-40, and EG2-41; from EG21 to EG2-31; from EG2-32 to EG2-45 (except EG2-41) falls in the category of **non-binding regime**, **binding regime-2**, and **binding regime-1**, respectively. AuNPs that belong to **binding regime-2** can be interpreted as the ones possessing the greater amount of binding pockets for Cd²⁺ ions.

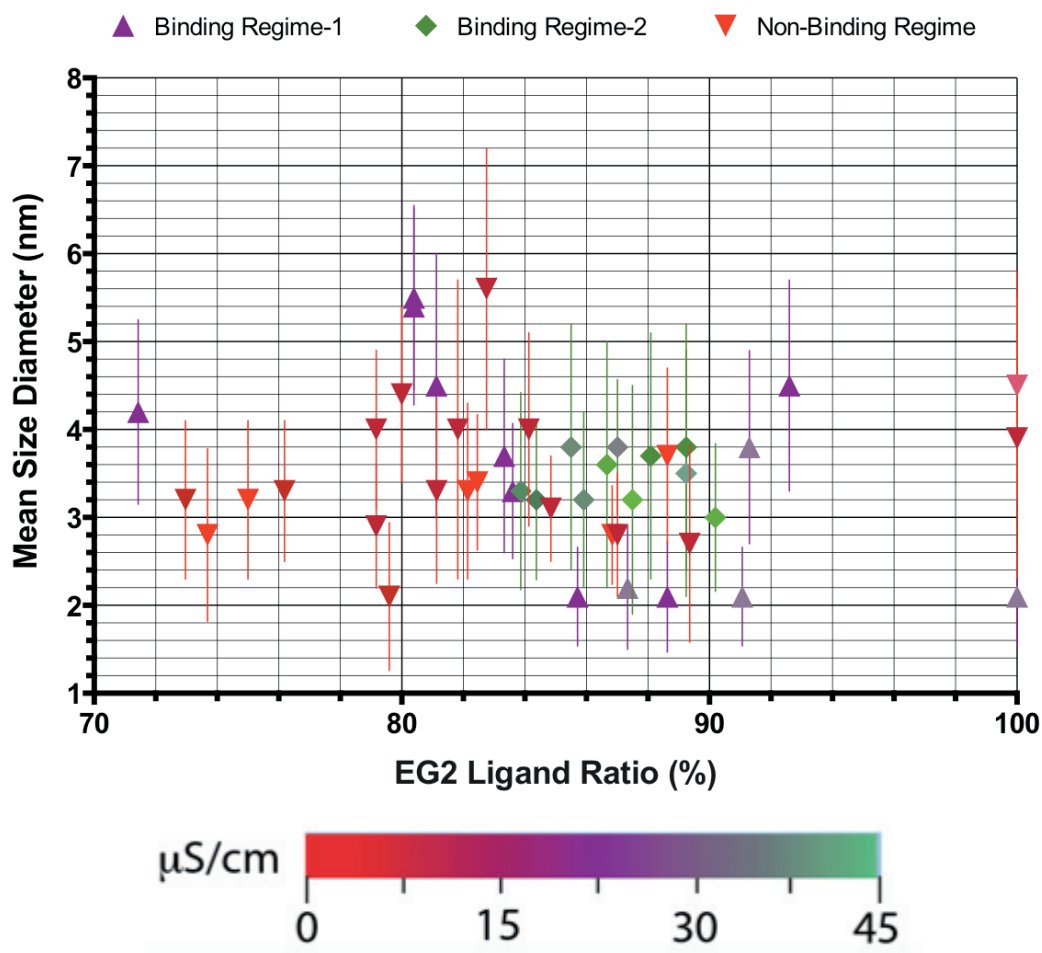


Figure 4.5: Results on conductivity experiments projected on color coded 2-D map of size vs. ligand ratio of synthesized AuNPs. Color map (bottom panel) defines how color of each batch changes with respect to the amount of deviation from the control (MQ water).

Since the primary interest in this study to investigate the factors that affect binding properties of AuNPs, the information obtained from conductivity experiments are projected on **2-D map of size vs. ligand ratio** of synthesized AuNPs, resulting in phase diagram of Cd²⁺ binding behavior (Fig. 4.5). It is important to understand that each

AuNP types show different binding behavior towards Cd^{2+} ion depending on its size and ligand ratio.

4.1.5 Investigation of Selectivity Profiles of Each Regime by Conductivity Tests

In these experiments, we screened the ion-binding abilities of our AuNPs against environmentally relevant ions other than Cd^{2+} . The experimental set up and the protocol was exactly the same as is described in **Section 4.1.2**. We selected random AuNPs batches from each regime, assuming similar behavior within each system, and tested them against different kind of metal ions, namely; Ca^{2+} , Li^+ , Cs^+ , Zn^{2+} , Co^{2+} , Ni^{2+} , K^+ , and Na^+ . I could not perform these experiments against all kind of EG2-n batches (n=1-45) since the amount of particles left for each batches after characterization and binding studies were not enough to perform these experiments. Results are presented in **Fig. 4.6**.

Selectivity, the power of the AuNP ligand shell to discriminate between metal ion of interest over other ions, is essential for correctly measuring the concentration of the desired metal ion in real world systems. Also, since we can now correlate the surface properties of EG2 ligands with their binding abilities, investigation of their binding profiles may provide an opportunity to design more selective systems. While none of the systems show any remarkable interactions towards Ca^{2+} , Li^+ , and Cs^+ ions, they have noteworthy affinity towards Zn^{2+} . Non-binding regime AuNPs, which is named based on their behavior towards cadmium ions, unexpectedly showed affinity towards Zn^{2+} . In the field, Zn^{2+} has always been one of the primary interfering ions for Cd^{2+} measurement, and therefore AuNPs in this regime would be great candidates to sense Zn^{2+} ions, selectively. **Regime-1** and **Regime-2** show different profiles towards transition and alkaline metals. AuNPs in the binding regime-1 showed binding towards transition metal ions (Zn^{2+} , Co^{2+} , Ni^{2+}), however; AuNPs in binding regime-2 bound alkaline metals better (K^+ , and Na^+).

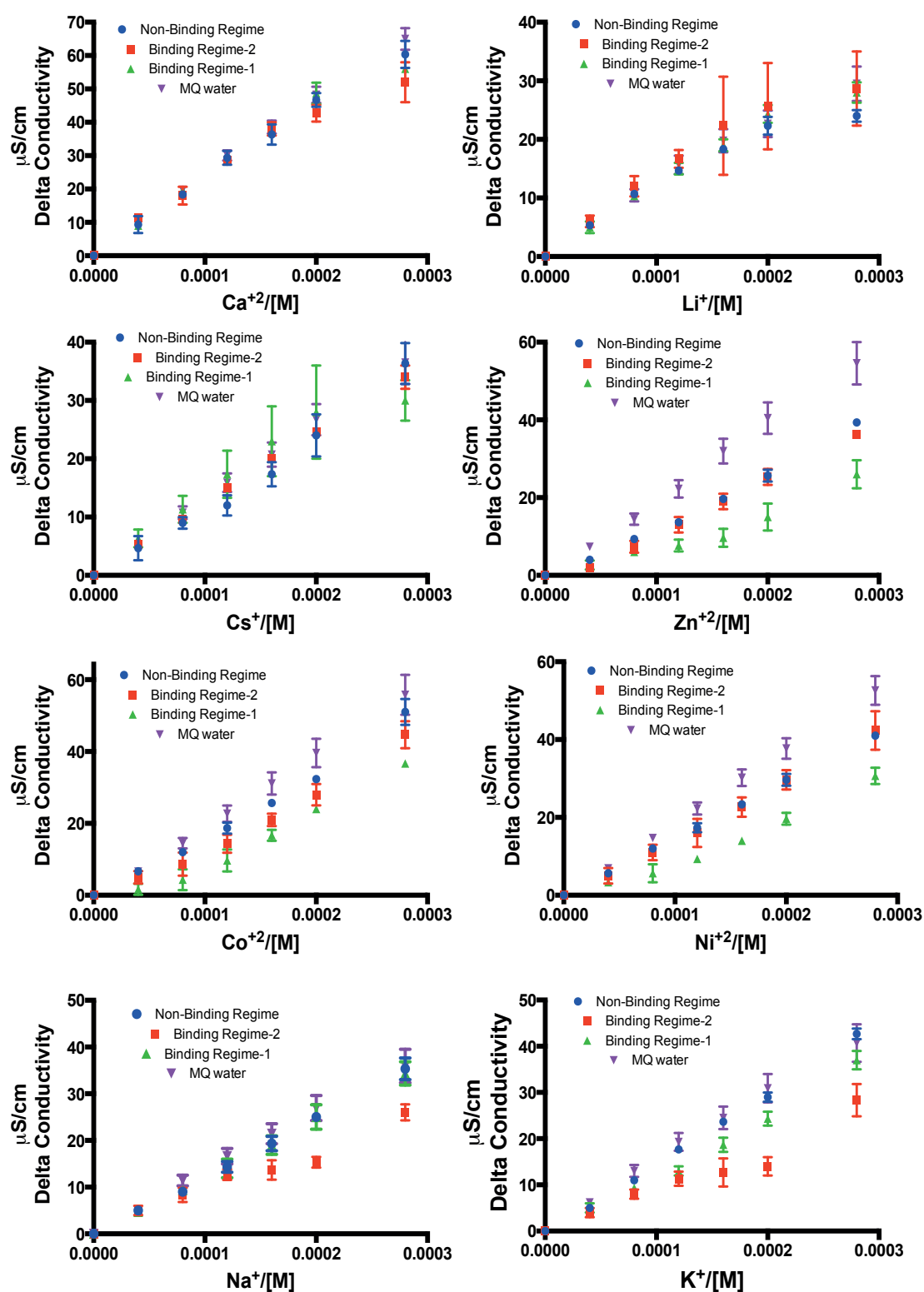


Figure 4.6: Selectivity tests of three different binding regimes by conductometry. Each regime is named according to their behavior towards Cd^{2+} . One result from each regime is represented for the clarity. Each measurements were done three times resulting in each plot their average values with standard deviations represented by error bars.

Regime Code	Cd^{2+}	Ca^{2+}	Li^+	Na^+	K^+	Cs^+	Co^{2+}	Ni^{2+}	Zn^{2+}
Non-Binding	Grey	Grey	Grey	Grey	Grey	Grey	Grey	Black	Black
Binding-1	Black	Grey	Grey	Grey	Grey	Grey	Black	Black	Black
Binding-2	Black	Grey	Grey	Black	Black	Grey	Grey	Black	Black

Figure 4.7: Summary of selectivity tests of three different binding regimes by conductometry. Each regime is named according to their behavior towards Cd^{2+} . Black color (binding observed), Grey color (no binding observed).

4.2 Isothermal Titration Calorimetry (ITC) Experiments - Determination of Association Constants Between AuNPs and Metal Ions

To derive a clear picture of the process of AuNPs-metal ions interaction from a thermodynamic point of view, it is essential to combine more than one technique. ITC is a thermodynamic technique that directly measures the heat released or absorbed in an intermolecular interaction.⁷ An ITC experiment consists of a calorimetric titration of a specific volume of one of the reagents (metal ion solution in our case), with adding controlled quantities of the other reagents (AuNPs) at constant temperature and pressure.⁷ Thus, the measured heat during the titration corresponds to the enthalpy of such interaction. An ITC experiment allows a complete and precise thermodynamic characterization of the binding event.

As it is stated above, our conductivity plots do not provide us with any quantitative results in terms of binding constant. The aim of the ITC experiments was to support the data obtained from the conductivity experiments. Therefore, random batches from each regime were chosen to be tested against Cd^{2+} ion. The thermograms that resulted from these titrations are shown in **Fig. 4.8**. The data are provided as the baseline-corrected heat flow vs. time in the upper panel, and the integrated concentration-normalized molar heat per injection vs. the molar ratio of titrant (AuNPs) to titrand (metal ions) in the lower panel. The thermodynamic values obtained from the experiments are presented

under the figure captions.

The ITC experiments were performed at 25 °C with 750 rpm stirring on a MicroCal™ ITC200 isothermal titration calorimeter (GE Healthcare). Titrant (18 mg/ml AuNPs) was delivered to the cell (50 μM CdCl₂ solution) in 20 times per 2 μL injections. Heats of dilution curves determined in the absence of reagents were subtracted from the titration data prior to curve fitting. Moreover, an initial 2 μL injection was discarded from each dataset to remove the effect of titrant diffusion across the syringe tip during the equilibration process. The data were analyzed using a one set of sites model provided in Origin 7.0 software by MicroCal.

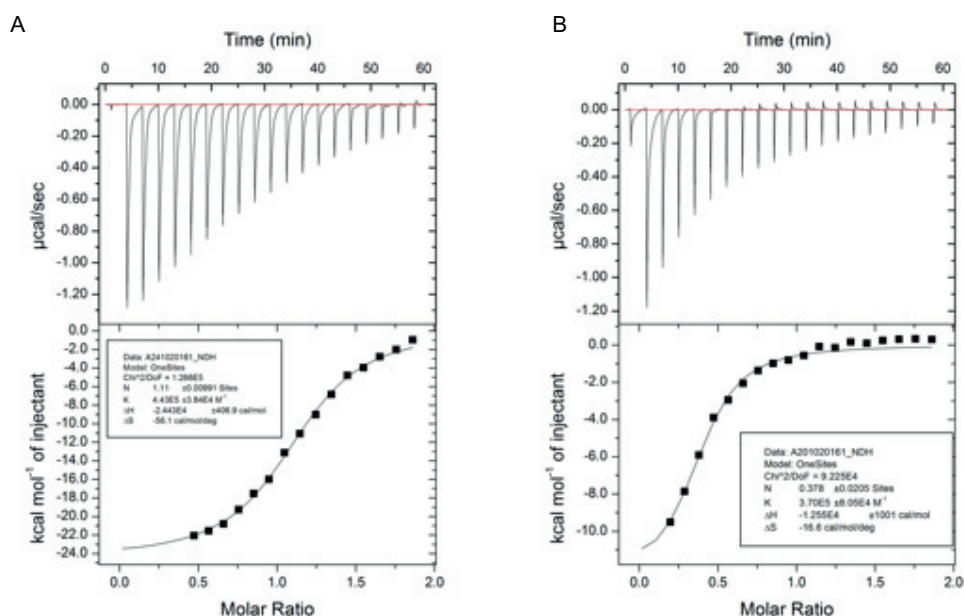


Figure 4.8: ITC results for A) EG2:HT AuNPs (**binding regime-2**) with Cd²⁺ : N=1.1, K=4.4*10⁵ ± 3.8*10⁴ M⁻¹, ΔH=-2.4*10⁴ cal mol⁻¹, ΔS=-56.1 cal mol⁻¹deg⁻¹ B) EG2:HT AuNPs (**binding regime-1**) with Cd²⁺ : N=0.4, K=3.7*10⁵ ± 8.1*10⁴ M⁻¹, ΔH=-1.26*10⁴ cal mol⁻¹, ΔS=-16.6 cal mol⁻¹deg⁻¹. The solid line represents the least squares fitting of the binding isotherm.

In order to use information obtained from conductivity plots for comparison of the number of binding pockets created by EG2 ligands on the surface of different AuNPs, knowledge on association constants is important. ITC experiments revealed similar binding constants (~4*10⁵) for AuNPs corresponding to both **binding regime-1** and **2**. Both binding process shows exothermic behavior, suggesting spontaneous complex formation between EG2 ligands and Cd²⁺ ions at room temperature. No binding

phenomenon was observed for AuNPs that belong the category of **non-binding regime**, supporting information acquired from conductivity plot (data is not shown).

As it is mentioned in previous sections, the concentration of the ligand was calculated based on the assumption that two EG2 pair bind one Cd^{2+} ion to form a binding pocket similar to the ones in crown ethers. In order to fit the data obtained from ITC curves, same amount of EG pair was written as an input, which gives lower stoichiometric binding ratio (N) for **binding regime-2**. This data correlates well with the results obtained from conductometric titrations, which suggests that binding regime-1-AuNPs posses lower binding pockets compared to **binding regime 2**-AuNPs.

4.3 Fourier Transform Infrared (FTIR) spectrometry - Investigation of Conformational Changes After Cd^{2+} Binding

Solid-state FTIR measurements were performed in order to further verify the binding event. Three representative samples from each binding regime were taken. AuNP solutions were prepared based on experimental details given in **Section 4.1.3**. Then, in order to ensure the complete saturation of all-binding pockets on the surfaces, titration of the AuNPs were ended with 10 times more concentrated Cd^{2+} solution. When titration of AuNPs with Cd^{2+} salt was finished, particles were precipitated via centrifugation at 5000 rpm for 45 minutes. Then, the pellets were dried under vacuum for 2 days. In order to prepare the KBr pellet of AuNPs for FTIR analysis, the protocol described in **Section 3.2.5.3** were followed.

Depending on the categorization showed in **Section 4.2.4**, EG2-7, EG2-25, and EG2-37 belong to **non-binding regime**, **binding regime-2**, and **binding regime-1**, respectively. For the particles in **binding regimes**, there is a huge shift of the $-\text{C}-\text{O}-\text{C}-$ stretching band to the $\sim 1130 \text{ cm}^{-1}$ after binding to Cd^{2+} ions (**Fig.4.9**). On the other hand, $-\text{C}-\text{O}-\text{C}$ stretching band of EG2-7 already appears at $\sim 1130 \text{ cm}^{-1}$, and there is no remarkable shift observed after addition of the Cd^{2+} ions (**Fig.4.9**). As we explained before, the position $-\text{C}-\text{O}-\text{C}$ spectral band at $\sim 1130 \text{ cm}^{-1}$ might be assigned to domination of more trans state

of $-C-O-C$ bonds. After binding, we observed a shift of EG2 ligand configuration to more trans-state form. This might be the reason behind the incapability of EG2-7 particles to bind Cd^{2+} ions since there is not enough space for EG2 ligand to change its configuration upon binding.

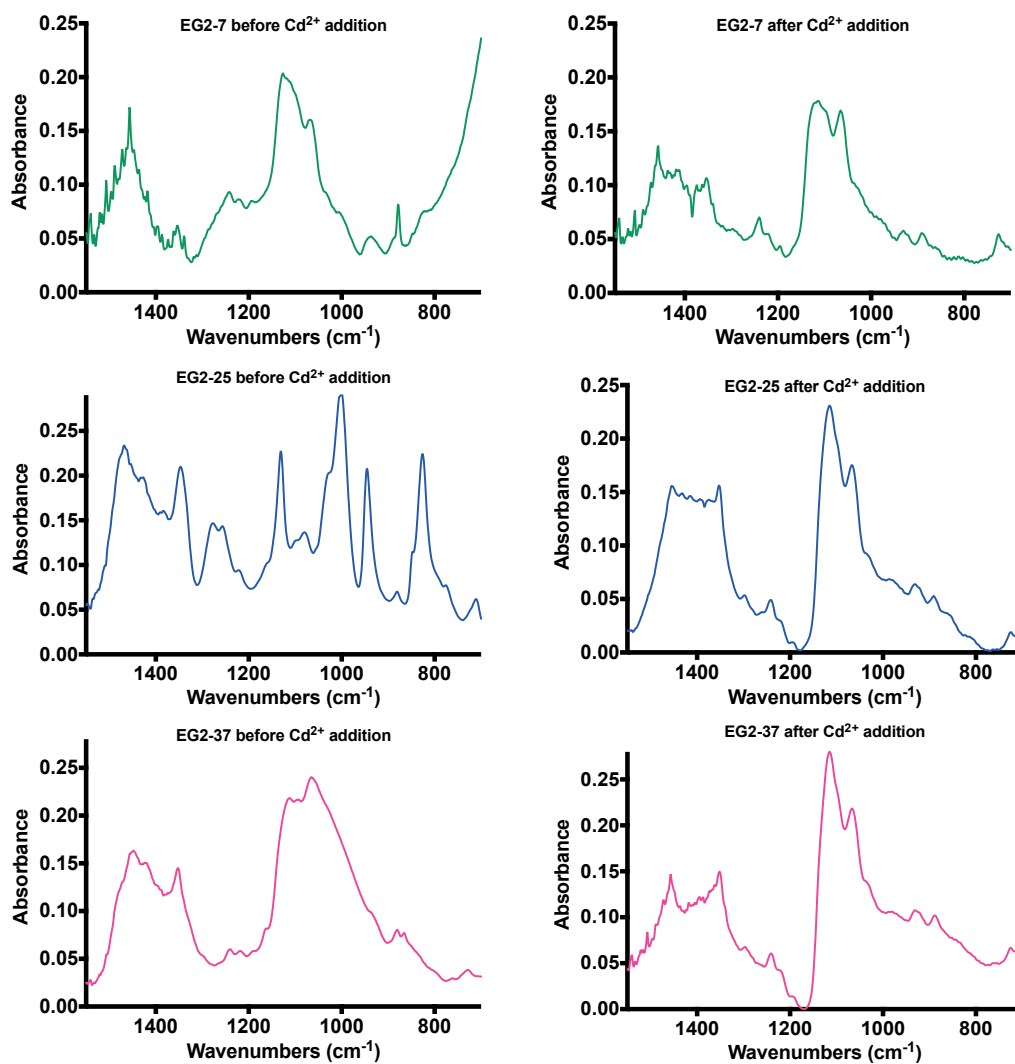


Figure 4.9: Left panel shows the FTIR spectra of the representative AuNPs (700-1550 cm^{-1}) before addition of Cd^{2+} , Right panel shows the FTIR spectra of the representative AuNPs (700-1550 cm^{-1}) after addition of Cd^{2+} .

4.4 Correlation Between Surface Properties of EG2 Ligands and Binding Abilities

In Chapter 3, the synthesized AuNPs were categorized with respect to the surface properties of EG2 ligands, resulting 3 different conformation of the ligand (**FTIR Regime 1, 2, and 3**). Then, it is shown in a 2-D plot that resulting conformation of EG2 ligands vary with respect to core size and ligand ratio.

In similar manner, Cd^{2+} binding abilities of synthesized AuNPs were arranged to give 3 different behaviors in binding (**non-binding, binding regime-1, and 2**), and they were also found to depend on core size and ligand ratio. In addition, particles from each binding regime have different selectivity profiles. Now, it is time to see, if there is a direct relationship between solid-state configuration of EG2 ligands and binding abilities. For this purpose, two 2-D plot shown previously to compare binding abilities and ligand conformation is shown in **Fig.4.10**.

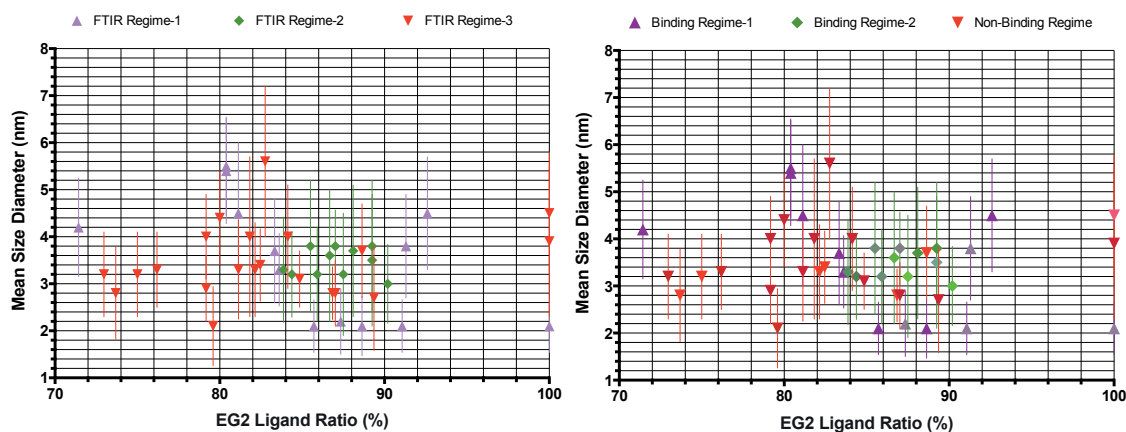


Figure 4.10: Left figure shows three different FTIR regimes that represent different conformations of EG2 ligands on the surface of synthesized AuNPs, Right figure shows three different binding regimes that vary based on size and ligand ratio of synthesized AuNPs. Upper and lower error bars shown for the y-axis is the standard deviation of mean size diameter.

Surprisingly, there is a good match between each binding regime and FTIR regime. In other words, when EG2 ligands have specific conformation on the surface, these AuNPs

have different binding abilities. According to **Fig.4.10**, AuNPs from **binding regime-1** holds EG2 ligands on the surface with the specific conformation corresponding to **FTIR Regime-1**. Likewise, AuNPs from **binding regime-2**, and **non-binding regime** holds EG2 ligands on the surface with the specific conformation corresponding to **FTIR regime-2**, and **FTIR regime-3**, respectively.

It is obvious that the ion-binding abilities and selectivity profiles of AuNPs are highly dictated by conformation of EG2 ligands on AuNPs. However, the differences observed in the conformation of the ligands were valid for solid-state experiments. Ion-binding experiments were conducted in water, and EG2 ligands' conformations show no difference in the presence of water (**Fig.3.13**). Therefore, binding abilities of AuNPs cannot be simply associated to conformation of EG2 ligands. However, it is quite obvious that conformation of EG2 ligands at solid-state acts like some kind of index which is directly related to binding capabilities.

In sections **3.3-3.5**, detailed explanations were given to show there is a relationship between the solid-state conformation of EG2 ligands and ligand-shell morphology. Although huge amounts of efforts and further experiments are needed to completely understand the extent of this relationship, we can conclude to few important points from our experiments and simulations.

The particles from **binding regime-2** tend to have patchier surfaces, whereas the particles from non-binding regime show more random distributions of the ligands on the surface. Particles from **binding regime-1** are special in a sense that although all of them (regardless of their size) were assigned to same **FTIR regime-1**, they possess different surface morphology. Due to high curvature of 2-nm particles, the ligands on the surface are much more free compared to the ones on the other NPs. Therefore, it is not surprising to observe similar EG2 conformation on the surfaces of those particles in **FTIR regime-1**. This means that binding behavior is not simply associated with the surface morphology. On the other hand, it is clear that there is a kind of relation between two. For now, it is not easy to show evidences to show a direct correlation between binding capabilities and surface morphology, or ligand configuration of EG2. Therefore, from now on, we can

only think about reasons behind by considering previous works done in the field. Now, if we re-visit the theoretical explanation for ion-capturing behavior of previously synthesized striped AuNPs (**Section 2.4.2, Fig.2.14**), there, the binding ability is related to free space provided by shorter, HT ligands. Therefore, we may say that configuration of EG2 ligands measured at solid state can be an index to judge free space in the vicinity of EG2 ligands. And, that index also can be used as a guide to differentiate surface morphologies.

REFERENCES

- (1) Thordarson, P. Determining Association Constants from Titration Experiments in Supramolecular Chemistry. *Chem. Soc. Rev* 2011, 40, 1305–1323.
- (2) Jaffrezic-Renault, N.; Dzyadevych, S. V. Conductometric Microbiosensors for Environmental Monitoring. *Sensors* 2008, 8 (4), 2569–2588.
- (3) Ijeri, V. S.; Srivastava, A. K. The Complexation Behaviour of Crown Ethers with Some Divalent Transition Metal and Silver Ions in a 40%(v/v) Ethanol + Water Medium. *Eur. J. Inorg. Chem.* 2001, 2001 (4), 943–947.
- (4) Christy, F. A.; Shrivastav, P. S. Conductometric Studies on Cation-Crown Ether Complexes: A Review. *Crit. Rev. Anal. Chem.* 2011, 41 (3), 236–269.
- (5) Barman, S.; Roy, M. N. Hollow Circular Compound-Based Inclusion Complexes of an Ionic Liquid. *RSC Adv.* 2016, 6 (80), 76381–76389.
- (6) Evans, D. F.; Wellington, S. L.; Nadis, J. A.; Cussler, E. L. The Conductance of Cyclic Polyether-Cation Complexes. *J. Solution Chem.* 1972, 1 (6), 499–506.
- (7) Brautigam, C. A.; Zhao, H.; Vargas, C.; Keller, S.; Schuck, P. Integration and Global Analysis of Isothermal Titration Calorimetry Data for Studying Macromolecular Interactions. *Nat. Protoc.* 2016, 11, 882-894.

CHAPTER 5

Ion-Binding Properties of EG3:HT Protected AuNPs Fractionated by Their Size

Unlike proteins or small molecules, most nanoparticles have some degree of polydispersity in size and molecular weight. Therefore, structure – property relationships that are attributed to nanoparticles can be described as average representations of the whole nanoparticle distribution. Fractionation is a post-synthetic separation technique to obtain monodisperse particles from initially polydisperse distributions. In this chapter, monodispersed EG3:HT coated AuNPs were obtained after the fractionation method, and their ion-binding capabilities were investigated. The experiments were conducted in order to crosscheck our argument regarding the effect of size of the AuNPs on ion-binding abilities.

5.1 Working Principle of Fractionation

In order to decrease the heterogeneity of nanoparticles size distribution, various post-synthetic separation methods have been developed.¹ Based on the core material, size, colloidal stability and desired efficiency in separation of nanoparticles, different strategies can be applied. For example, filtration is a high-throughput method for most nanoparticles but suffer from inability to isolate multiple sizes at a time while size exclusion chromatography allows retention of different fractions in one experiment.¹ In this regard, recently, density gradient ultracentrifugation (DGU) has been utilized as high-resolution separation method particularly for small and less dense nanomaterials that have relatively narrow size/density distributions such as nanodiamonds, carbon nanotubes and gold nanoparticles.²⁻⁴

DGU is a centrifugation-based method where heterogeneous sample is introduced into a continuous density gradient solution under high centrifugal fields (**Figure 5.1**).⁵ The

fundamental principle is that larger particles sediment faster than smaller ones. Density gradient in the medium slows down the sedimentation process. As the particles travel through the density gradient, the faster-sedimenting particles move ahead, until a number of zones are created by particles of similar size. Through gradient, the medium increases in density with distance from the rotor center. Therefore, sedimentation is slowed down, ideally in a uniform manner for all sizes of particles, leading to increased separation resolution under the right conditions. Finally, when the solute separates into bands, it can be selectively fractionated with a variety of commercially available fractionators.

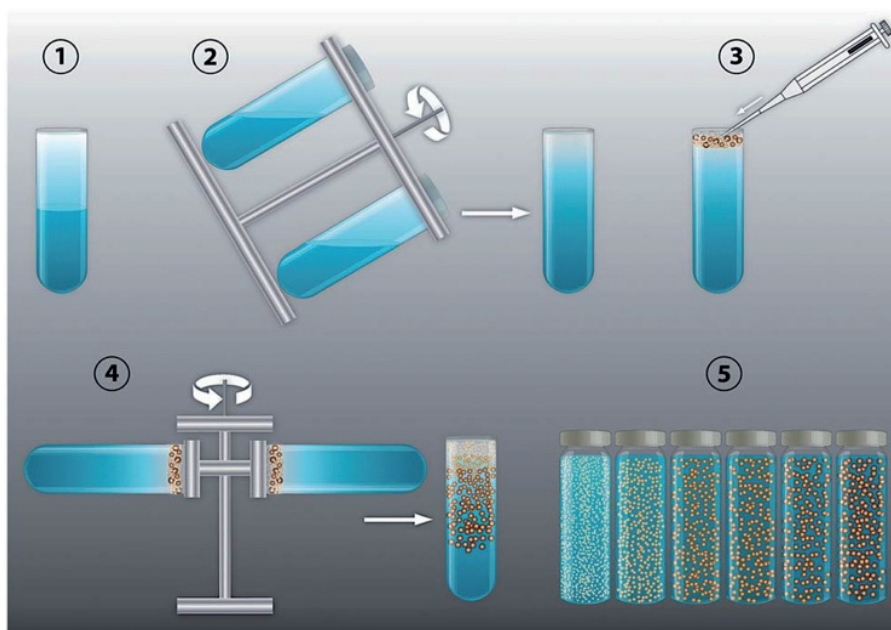


Figure 5.1: Schematic illustration of density gradient fractionation: 1) layering a less dense solution over a more dense one (sucrose); 2) tube tilt and rotation to form a continuous density gradient; 3) seeding the nanoparticle solution; 4) ultracentrifugation; 5) fraction collection. Reproduced from **Ref. 2** with permission from Royal Society of Chemistry.

5.2 Experimental Details

In this section, we applied DGU to show further the size effect on ion-binding for our model nanoparticles (EG3:HT covered AuNPs). Although the work presented in this thesis based on investigation of structure-property relationship of EG2:HT coated AuNPs, the solubility of these particles is not sufficient to be fractionated. Although

different density gradients were tried, because of limited solubility of those particles, they tend to aggregate and sediment together. For this reason, more soluble EG3:HT protected AuNPs were chosen as model particles. Our group already reported the ion-binding properties of those particles, showing affinity of those particles towards Cs⁺ ions.⁶ The gold particles covered by 2-(2-(2-((6-mercaptohexyl)oxy)ethoxy)ethoxy)ethanol (EG3) and 1-hexanethiol (HT) with a molar ratio of 3:1 (hereafter referred to EG3:HT AuNPs) were synthesized by using the general synthesis protocol described in **section 3.1** for EG2-n AuNPs. The synthesized particles are schematically depicted in **Fig.5.2**.

Concentrated nanoparticles solution (10 mg/ml) were layered on top of the gradient solution and subjected to ultracentrifugation (typically at 32 krpm, SW32 Ti Rotor™, Beckman Coulter) for 1-2 hours at 20 °C. Density gradients can be formed with different materials (ethylene glycol, silica microgels, etc.) and in order to separate EG3:HT AuNPs. We employed sucrose gradients from 20% to 50% (w/v). Sucrose has low molecular weight and thus it is easy to wash away after fractionation. In the end, larger nanoparticles travel further down the tube than smaller nanoparticles due to the fact that density of gold nanoparticles is strictly a function of size in diameter. Nanoparticles' bands in the sucrose gradient were subsequently separated in a desired number of fractions using piston operated Biocomp Gradient Station® (New Brunswick, Canada). All fractions were thoroughly washed with deionized water using 15 ml Amicon® centrifugal filter tubes (30kDa MWCO) under 5000 g centrifugation until removal of residual sucrose is ensured. Presence of sucrose molecules can be checked by NMR prior to the etching of the gold cores.

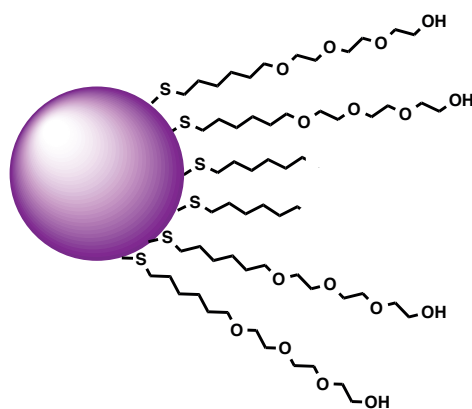


Figure 5.2: Schematic illustration of EG3:HT protected AuNPs

5.3 Results and Discussion on Ion-Binding Properties of EG3:HT Protected AuNPs

The HT:EG3 gold nanoparticles were divided into five different batches (Fig.5.4, Fractions A-E), and each TEM image is shown in Fig.5.4. The mean diameter is calculated by counting at least 300 particles per batch, and it is distributed from 2.96 nm to 5.44 nm. The EG3:HT ligand molar ratio on the surface of AuNPs is determined by ¹H Nuclear magnetic resonance (NMR) after etching the gold core with iodine solution by previously described method in the section 2.2.1. Corresponding ligand ratios are presented in Fig. 5.4.

The conductivity tests were performed for each fraction against Cs⁺ ions (also against K⁺ ions for raw batch as a control), and the results are illustrated in Fig. 5.4. The experimental set up and conditions are described in section 4.1.2. The only difference was the preparation of the replicates, as in this case, all the dilutions were performed from already prepared solutions of EG3:HT AuNPs.

Previous study conducted by our group showed that 4.9 nm EG3:HT AuNPs with 3:1 molar ratio had remarkable affinity ($K=3 \times 10^6$) towards Cs⁺ ions, whereas no binding of K⁺ ions was detected.⁶ Since EG3 ligand possess more electron donor atoms than EG2 ligand, this behavior of EG3:HT particles is reasonable. The reason behind is similar with what we observed in crown ethers, the bigger the size of the cavity within crown ethers, the bigger the ions that can fit in it.⁷

Our synthesized raw batch EG3:HT AuNPs also showed similar binding behavior towards Cs⁺ ions as it can be seen in Fig.5.4A. Among these fractions, we have seen differences in ion binding behaviors, which suggests that specific sizes of nanoparticles can be more determinant factor even within the same nanoparticle batch. The particles larger than 3.5 nm mean diameter were observed to have binding affinities toward Cs⁺ ions. This correlates well with the results we obtained for series of EG2-n AuNPs. Therefore, this study demonstrates the importance of size of mixed-ligand coated AuNPs for the binding affinities. However, it is difficult to speculate about ligand ratio since there is no clear correlation observed.

The phase diagram of EG3:HT AuNPs, which provides information about binding abilities depending on size and ligand ratio of the particles, seems to be different than that of EG2:HT AuNPs. This is also important to understand since depending on the nature of the ligand, the properties of the phase diagram can be shifted in terms of size and ligand ratio.

Due to practical reasons, the FTIR spectrum of the fractionated EG3:HT AuNPs to evaluate orientation of EG3 ligands on the surface could not be obtained. Fractionation is not a mass production technique, so the amount of particles obtained for each fraction for one cycle is really low (~1-4 mg). Then, for our solid state FTIR technique, we needed to precipitate them. However, the solubility of EG3:HT particles was quite high, and it was difficult to obtain them as a pellet. Therefore, we can only speculate about the indirect effect of size of AuNPs on the binding capabilities. Our group previously showed with the help of STM technique that EG3:HT ligands on the surface of 4.9 nm of AuNPs organized in striped pattern (**Fig.5.3**).⁶ Since the stripe domains have been shown to form in certain radius curvatures, we can correlate the observed binding behavior of EG3:HT AuNPs with changing surface arrangement of EG3 ligands for different size of AuNPs.^{8,9}

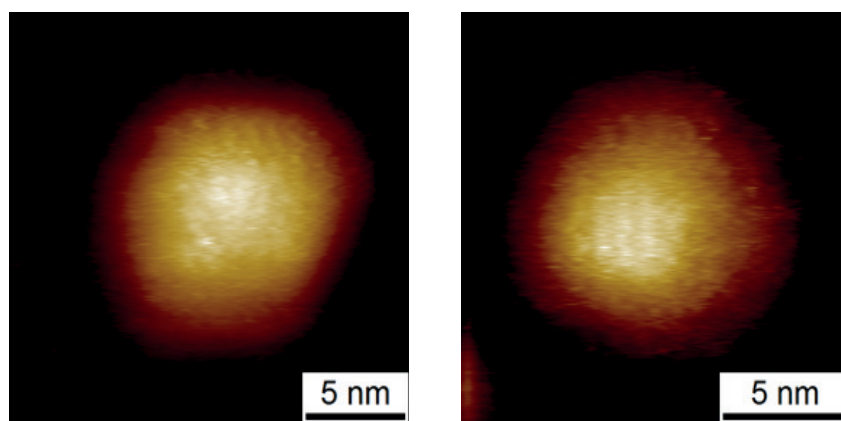
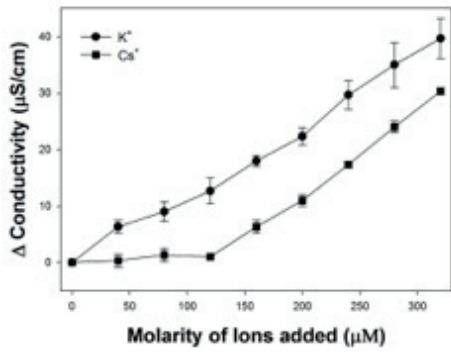
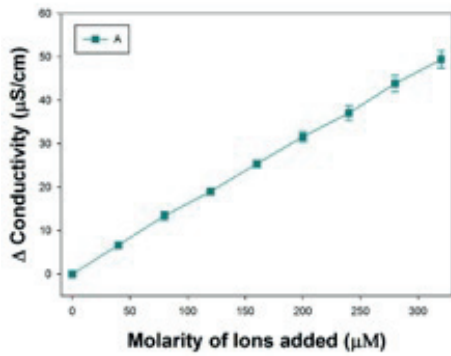
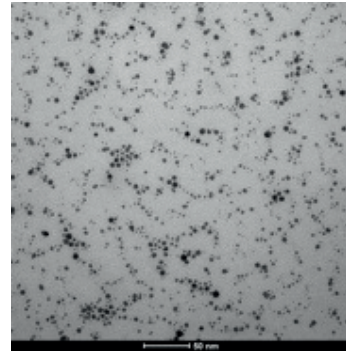


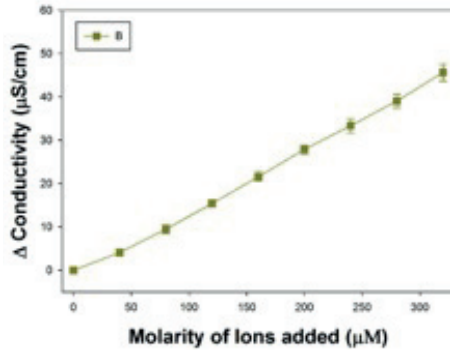
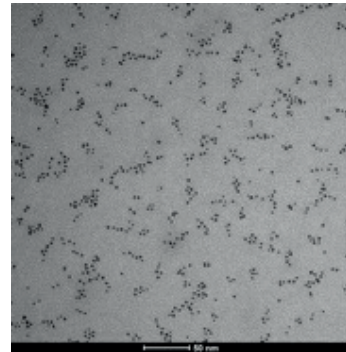
Figure 5.3: EG3:HT AuNPs examined by scanning tunnelling microscopy (STM): the width of both HT and EG3 stripes are 1.3 ± 0.1 nm. STM images were obtained by a Veeco multimode scanning probe microscope on a vibration-damping table (in an acoustic chamber, at room temperature, and in air). Reproduced from **Ref. 6** with permission from Nature Publishing Group.



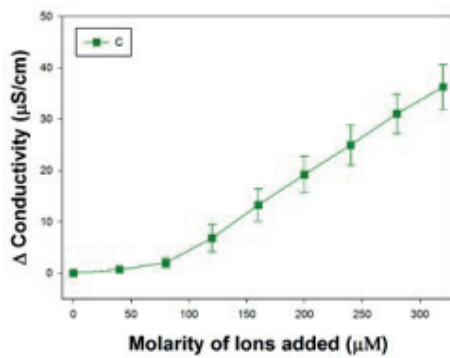
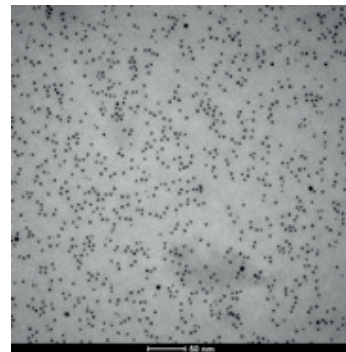
Size: 3.39 ± 0.60 nm
EG3: HT ratio (4.63:1)



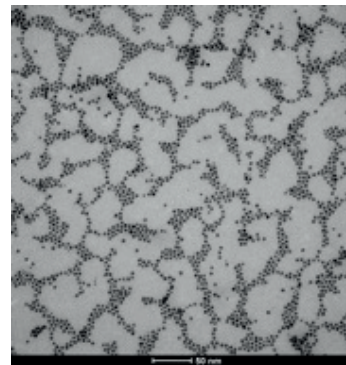
Size: 2.96 ± 0.60 nm
EG3: HT ratio (2.45:1)



Size: 3.52 ± 0.56 nm
EG3: HT ratio (2.44:1)



Size: 4.18 ± 0.64 nm
EG3: HT ratio (4.22:1)



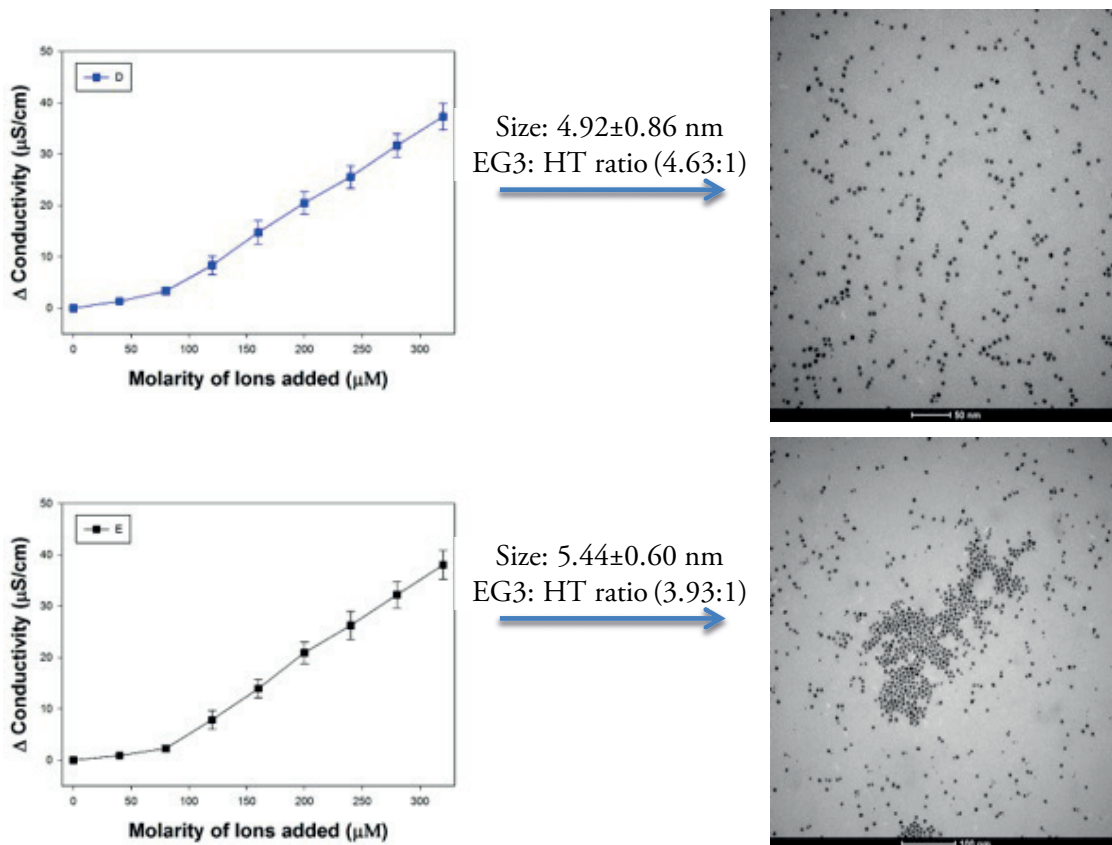


Figure 5.4: TEM images and the results of conductivity tests of fractions **A-E**. Mean diameters together with standard deviations of the core sizes and EG3:HT ligand ratio on the surface of the AuNPs are presented above the arrows.

In summary, these experiments showed the importance of the core size of AuNPs for ion-binding abilities. Detailed investigation is needed to understand the effect of ligand ratio as well as ligand configuration on the binding. Although the results show an agreement with our study based on EG2:HT AuNPs, it is obvious that they show different binding behavior in terms of core size and ligand ratio. Since 4.9 nm particles were showed to have stripe-like domains,⁶ it would be useful to calculate SSR values (**Section 3.3**) for all the fractionated batches by taking SSR value of 4.9 nm particles as a reference point. This may provide useful information in order to understand the correlation between surface arrangement and binding ability.

REFERENCES

- (1) Robertson, J. D.; Rizzello, L.; Avila-Olias, M.; Gaitzsch, J.; Contini, C.; Magoń, M. S.; Renshaw, S. A.; Battaglia, G. Purification of Nanoparticles by Size and Shape. 2016.
- (2) Peng, W.; Mahfouz, R.; Pan, J.; Hou, Y.; Beaujuge, P. M.; Bakr, O. M. Gram-Scale Fractionation of Nanodiamonds by Density Gradient Ultracentrifugation.
- (3) Ghosh, S.; Bachilo, S. M.; Weisman, R. B. Advanced Sorting of Single-Walled Carbon Nanotubes by Nonlinear Density-Gradient Ultracentrifugation. 2010.
- (4) Carney, R. P.; Young Kim, J.; Qian, H.; Jin, R.; Mehenni, H.; Stellacci, F.; Bakr, O. M. Determination of Nanoparticle Size Distribution Together with Density or Molecular Weight by 2D Analytical Ultracentrifugation. *Nat. Commun.* 2011, 2.
- (5) Carmignac, D. F. *Biological Centrifugation* J. Graham, BIOS Scientific Publishers Ltd., 201 Pp., £21-99, ISBN 1 85996 037 5 (2001). *Cell Biochem. Funct.* 2002, 20 (4), 357–357.
- (6) Cho, E. S.; Kim, J.; Tejerina, B.; Hermans, T. M.; Jiang, H.; Nakanishi, H.; Yu, M.; Patashinski, A. Z.; Glotzer, S. C.; Stellacci, F.; Grzybowski, B. A. Ultrasensitive Detection of Toxic Cations through Changes in the Tunnelling Current across Films of Striped Nanoparticles. *Nat. Mater.* 2012, 11 (11), 978–985.
- (7) Steed, J. W.; Atwood, J. L. *Supramolecular Chemistry*; Wiley, 2009.
- (8) Carney, R. P.; DeVries, G. A.; Dubois, C.; Kim, H.; Kim, J. Y.; Singh, C.; Ghorai, P. K.; Tracy, J. B.; Stiles, R. L.; Murray, R. W.; Glotzer, S. C.; Stellacci, F. Size Limitations for the Formation of Ordered Striped Nanoparticles. *J. Am. Chem. Soc.* 2008, 130 (3), 798–799.
- (9) Singh, C.; Ghorai, P. K.; Horsch, M. A.; Jackson, A. M.; Larson, R. G.; Stellacci, F.; Glotzer, S. C. Entropy-Mediated Patterning of Surfactant-Coated Nanoparticles and Surfaces. *Phys. Rev. Lett.* 2007, 99 (22), 226106.

CHAPTER 6

Conclusion and Future Work

6.1 Conclusion

Previous study done by our group already showed that it is possible to create selective binding pockets for metal ions like macro-cyclic rings have, by using mixed ligand strategy on the surface of AuNPs. However, there was a lack of understanding the ion-binding abilities of gold nanoparticles depending on their physicochemical properties.

The goal of this thesis was to generate a library of ion-binding gold nanoparticles and extract information about structure-selectivity relationships. To achieve this goal, the ion-binding behaviors of AuNPs towards specific ion (Cd^{2+}) were studied by shining light on the role of ligand composition, size of the NPs and the conformation of self-assembled monolayers (SAMs).

In **chapter 1 and 2**, the background information was introduced in order to help the reader to understand the motivation, the design and the novelty of our study. A broad literature review of the current state-of-the-art of AuNP based metal ion sensing systems was presented. Particular attention was paid to the additional effect of the ligand self-organization of the protecting monolayer that leads to the spontaneous formation of recognition units on the NP surface. The previous study of our group, which forms the basis of this thesis, was analyzed.

In **chapter 3**, the synthetic protocols and their variations were explained in order to obtain a series of mixed-ligand (EG2:HT) protected gold nanoparticles with different core size and ligand ratio. Important synthetic parameters that affect the final properties of AuNPs were identified. In addition, the characterization tools (NMR, TEM, TGA, FTIR) for analysis of physicochemical properties of synthesized AuNPs were presented in

detail. The ligand shell properties were studied by FTIR, and MALDI-TOF-MS techniques, revealing different conformations, and arrangements of the ligands on the nanoparticles' surfaces. The configurations of EG2 ligands in dry state were found to be changing with respect to particle core size and ligand composition. On the other hand, configurations of EG2 ligands on the surface of different AuNPs were showed to be similar in the presence of water. SSR values calculated from MALDI-TOF-MS method suggested that different ligand shell organizations (morphology) were possible depending on size and ligand ratio of AuNPs. In addition, molecular simulations helped us to relate the EG2 configurations in dry state with the ligand shell organizations on the surface.

In **chapter 4**, the binding capabilities of EG2:HT protected AuNPs towards Cd^{2+} ions were evaluated qualitatively by conductometric titration method. ITC was utilized to define the thermodynamic parameters of the interaction between Cd^{2+} ions and synthesized AuNPs. Spectral changes of ligand moieties were observed by FTIR spectroscopy upon complexation, further verifying the binding process.

The size and ligand ratio of the nanoparticles were found to greatly affect their ion-binding abilities. The information obtained from conductivity experiments were projected on 2-D map of size vs. ligand ratio of synthesized AuNPs, resulting in phase diagram of Cd^{2+} binding behavior. This diagram could be used as a guide to understand different binding behavior of AuNPs towards Cd^{2+} ion depending on their core size and ligand ratio. In this chapter, we also concluded that AuNPs with certain ion-binding behavior (with certain selectivity profile) possess specific EG2 ligands configuration on the surface.

In **chapter 5**, monodispersed EG3:HT protected AuNPs were obtained after the fractionation method, and their ion-binding capabilities were investigated. These experiments showed the importance of the core size of AuNPs for ion-binding abilities.

To sum up, the configurations of EG2 ligands in dry state, which changes with respect to varying particle core size and composition, were found to be strongly correlated with ion-binding behavior.

6.2 Future Work

The configuration of EG2 ligands on the surface of different AuNPs showed no differences in the presence of water, in which the ion-binding studies were conducted. Therefore, the configurations of EG2 ligands in dry state cannot be directly correlated with ion-binding behavior. On the other hand, we concluded that the configuration of EG2 ligands at solid-state acts like some kind of index, which is indirectly related to binding capabilities.

In addition, both SSR values and molecular dynamic simulations suggested that observation of different alignment of EG2 ligands could be a result of the formation of different ligand arrangements on the surface. Consequently, a relationship between the binding capabilities of synthesized particles and their surface morphologies were observed. Since determination of exact surface ligand arrangement was not possible with the used techniques, the exact mechanism of the relationship between binding abilities and ligand shell morphology could not totally understood.

Depending on our results, we can speculate for now, referring to the theoretical explanation for the ion-capturing behavior of previously synthesized striped AuNPs (Section 2.4.2, Fig.2.14). They already showed that specific (stripe like) ligand arrangements on the surface is necessary to have some free space close to EG ligands. Therefore, configuration of EG2 ligands at solid-state could be an index to judge free space in the vicinity of EG2 ligands provided by shorter ligands. And, this free space can be modified by surface morphologies, which varies with respect to core size and ligand ratio of AuNPs.

More experimental evidences are still needed to show the direct correlation between selectivity (or ion-binding behavior) of AuNPs with the surface morphology. In addition, deeper examination is necessary to understand the links between the solid-state configuration of the ligands, the free space, and the ligand shell morphology. Then, it may be possible to relate these varying surface parameters with the selectivity of mixed-ligand coated AuNPs.

I believe that it is not an easy task to extract this information. A proper systematic study based on the synthesis, the characterization, and then the examination of binding behavior of series of particles is needed. A new series of particles should be studied by always keeping one of the ligand on the surface of the particles constant, and changing the other ligand in terms of length, bulkiness, and chemical functionality. SSR values can be great utility in future for the determination of surface arrangements. However, the reason behind obtaining different results for ligand ratio by two different techniques, namely; MALDI and NMR, should be examined. After validation of the accuracy of MALDI technique for a given system, data obtained from this method will be valuable. In addition, changing the core material to another metal with different lattice parameters such as silver may also help us to gain an understanding on the surface properties.

The patterned information, which relates the binding behavior of mixed-ligand coated AuNPs and ligand composition, size of the NPs, the configuration and morphology of ligands can open a new era in generating various recognition units based on AuNPs to develop array-based systems for the detection of multi-elements simultaneously.

6.2.1 Applicability of the AuNPs to the Real-World Systems

The ultimate goal of this study is to create numerous selective AuNP-based metal ion-sensing systems by tuning the surface properties in a controlled manner. Therefore, we wanted to examine whether the synthesized AuNPs still possess their binding abilities in different medium.

As stated in **Chapter 1**, rice samples already showed the presence of cadmium within the plants. Cadmium metal poses a high risk for the people, especially in Asia, who consume a lot of rice.¹ Therefore, we would like to test if our AuNPs could detect the cadmium contamination in rice extract medium. The aim of these preliminary experiments was just to see whether our AuNPs still retain their binding abilities or not.

However, the cadmium level in rice is typically at the order of few nano molar in our rice extract solution.¹ At this concentration level, one needs more sensitive technique to

detect the cadmium. Although, it is not possible to detect such low level of cadmium with conductometric method, the experiments were performed with the addition of concentrated solutions of CdBr_2 . Results are presented in **Fig.6.1**.

Prior to conductometric titrations, we extracted Cd^{2+} ions from rice.² The rice sample was purchased at supermarket from Lausanne, Switzerland. 2 g of rice was placed in a beaker and 10 ml of 65% HNO_3 (Sigma-Aldrich) was added and this content was evaporated to dryness at 130 °C. The sample was then cooled down to room temperature, and 2 ml of 30 % H_2O_2 (Sigma-Aldrich) were added. After 30 minutes, the sample was filtered, and diluted with ultrapure water in a 25 ml volumetric flask. Then, this solution was further diluted with MQ water. The protocol described in **Section 4.1.3** was followed. However, this time diluted rice extract was used instead of MQ water to dissolve AuNPs.

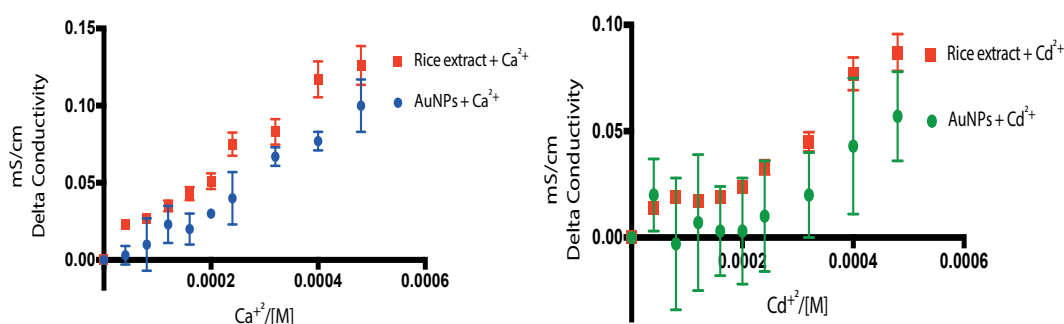


Figure 6.1: Left panel shows the addition of Ca^{2+} ions to control (red, rice extract), and (blue, AuNPs in rice extract). Right panel shows the addition of Cd^{2+} ions to control (red, rice extract), and (green, AuNPs in rice extract). Each set of measurements were done three times and the average values were plotted with standard deviations represented by error bars.

The AuNPs used in this study was from **binding regime-2**. In MQ water, they did not show any binding to Ca^{2+} ions, whereas; they showed strong affinity to Cd^{2+} ions (**Section 4.1.5**). When we compared the results of two titrations shown in **Fig.6.1**, AuNPs showed better binding performance against Cd^{2+} as it was predicted. This means that they still hold their binding abilities even in the rice extract solution. However, the error bars are quite high, making it difficult to come to a conclusion. The reason might be the high background noise (high conductivity value of the solution) coming from concentrated rice extract. Further experiments should be conducted at different solution pHs, and by

using different extraction protocols. In addition, more sensitive transduction mechanisms should be examined for enabling detection of Cd²⁺ at very low concentrations.

REFERENCES

- (1) Zhuang, P.; Zou, B.; Li, N. Y.; Li, Z. A. Heavy Metal Contamination in Soils and Food Crops around Dabaoshan Mine in Guangdong, China: Implication for Human Health. *Environ. Geochem. Health* 2009, 31 (6), 707–715.
- (2) Ju, S.; Liu, M.; Yang, Y. Preconcentration and Determination of Cadmium, Lead, and Cobalt in *Moringa Oleifera* (Moringaceae) Using Magnetic Solid-Phase Extraction and Flame Atomic Absorption Spectrometry. *Anal. Lett.* 2016, 49 (4), 511–522.

APPENDIX

A.1 NMR Spectra of EG2-n AuNPs

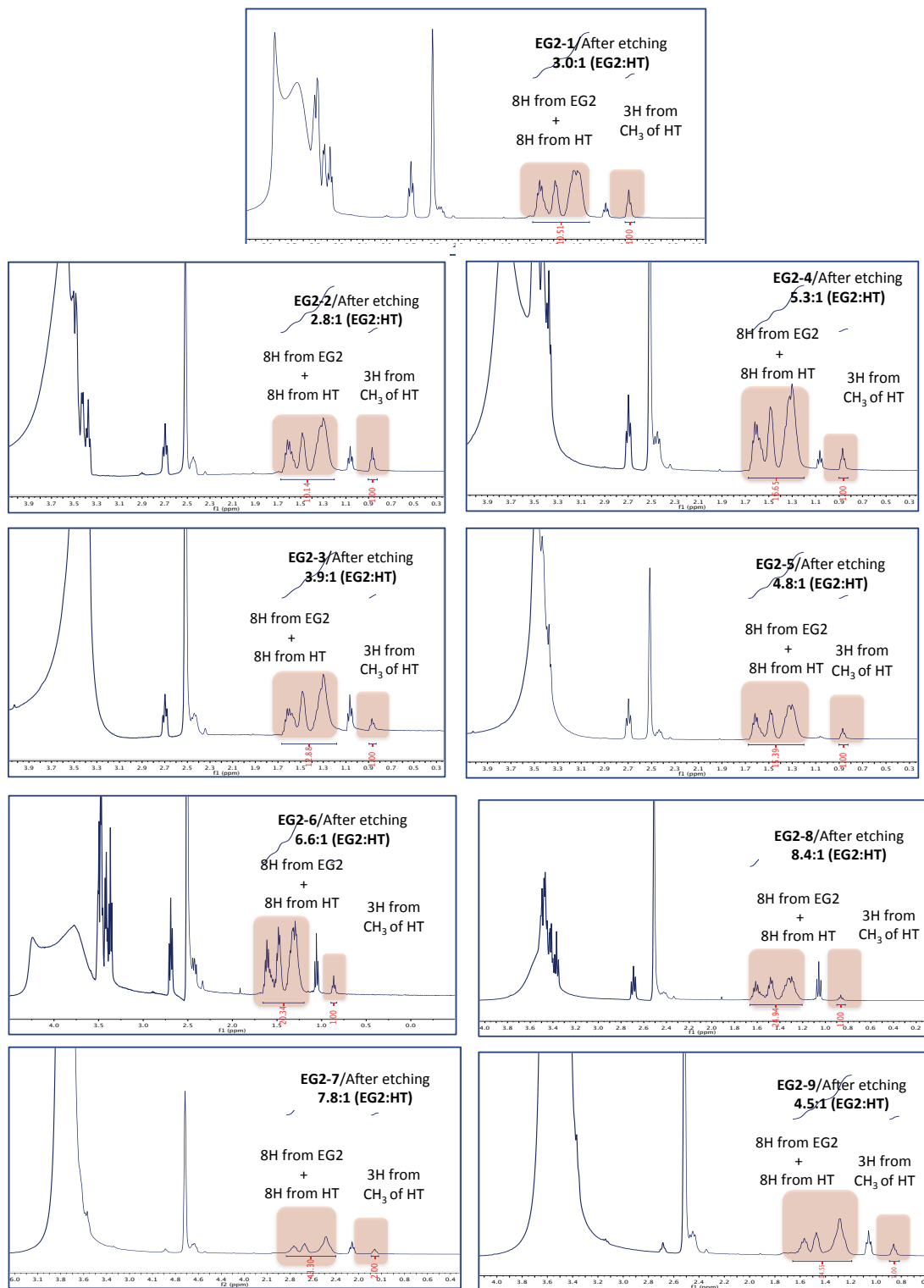


Figure A.1: NMR spectra of EG2-n (n, 1-9) after etching with iodine in DMSO-d₆

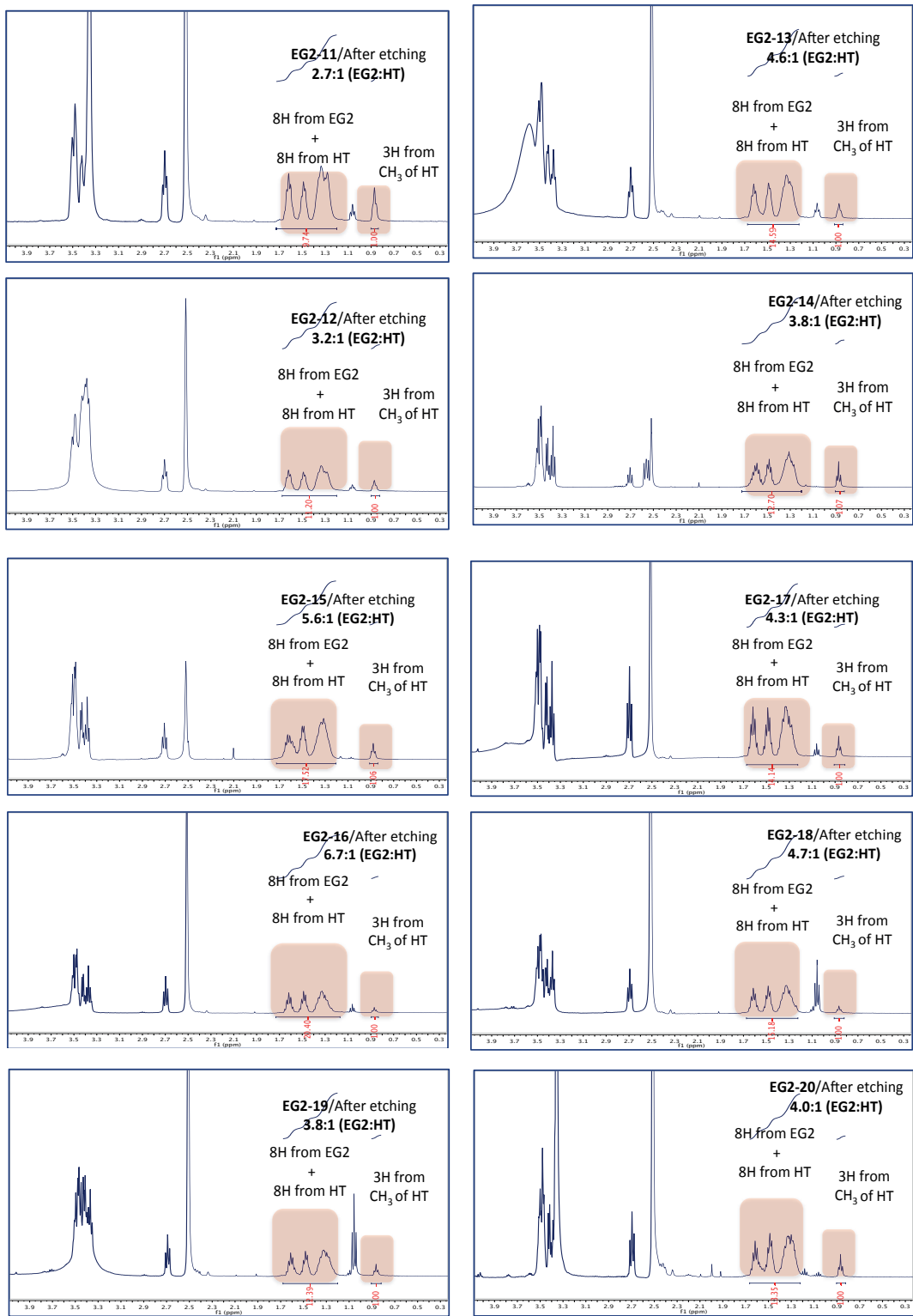


Figure A.2: NMR spectra of EG2-n (n, 11-20) after etching with iodine in DMSO-d₆

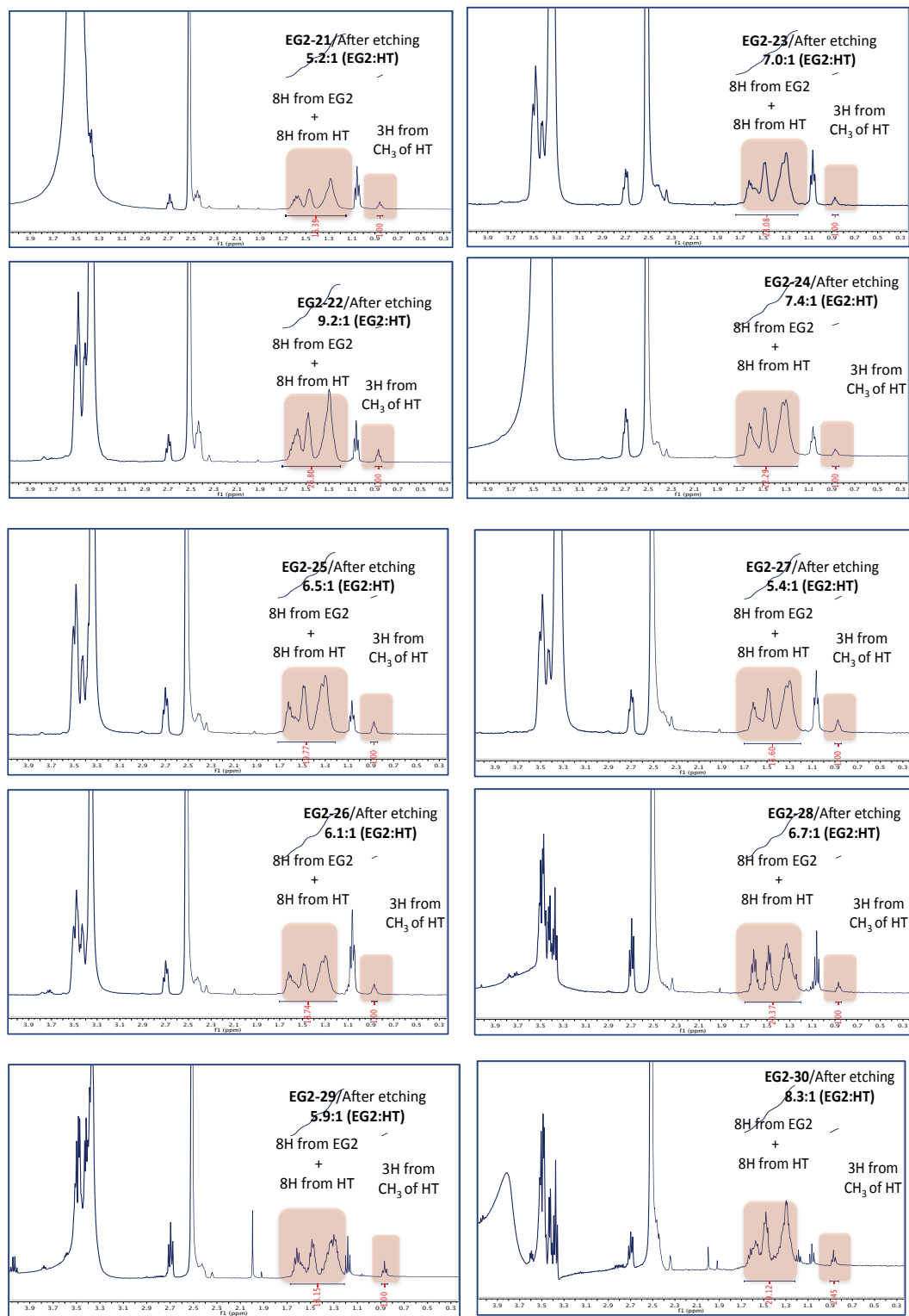


Figure A.3: NMR spectra of EG2-n (n, 21-30) after etching with iodine in DMSO-d₆

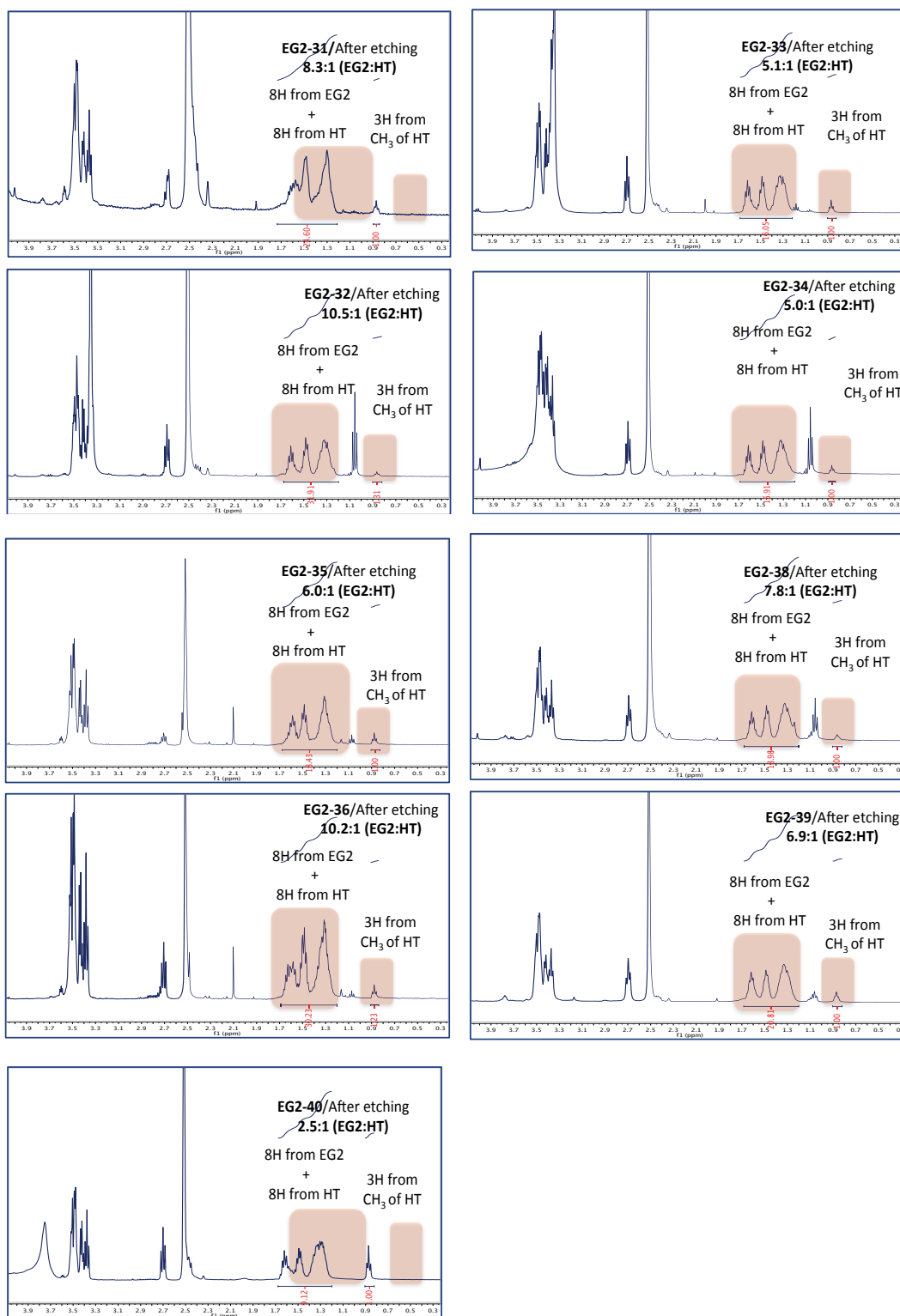


Figure A.4: NMR spectra of EG2-n (n, 31-40) after etching with iodine in DMSO-d_6

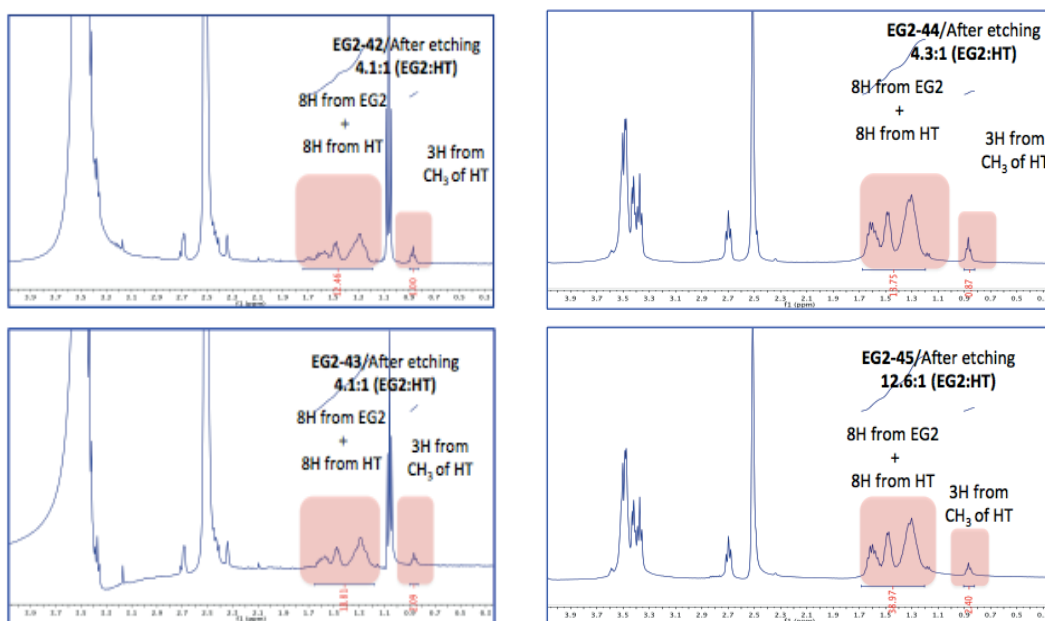


Figure A.5: NMR spectra of EG2-n (n, 42-45) after etching with iodine in DMSO-d₆

A.2 Representative TEM images and size distributions of EG2-n AuNPs

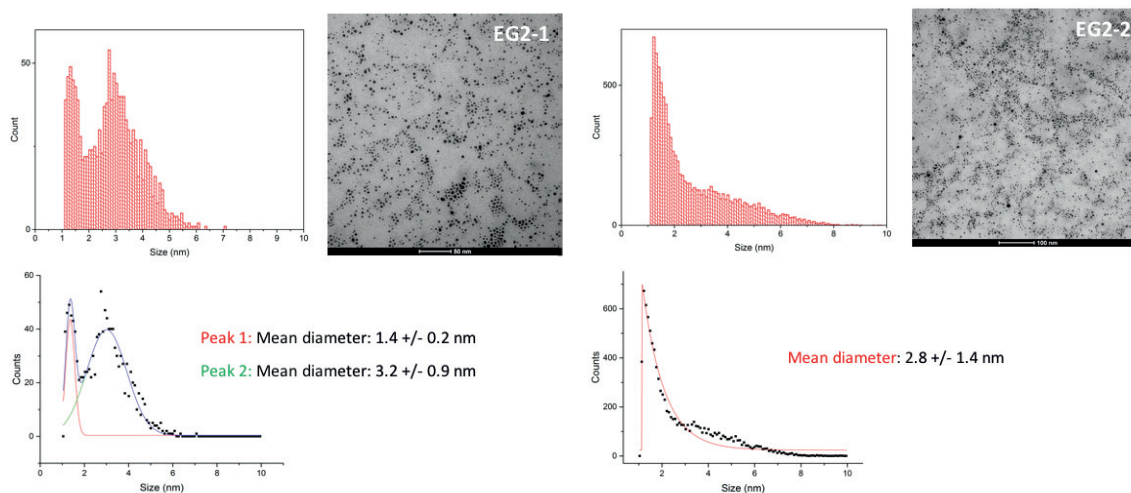


Figure A.6: Representative TEM images and size distributions of EG2-n (n, 1-2)

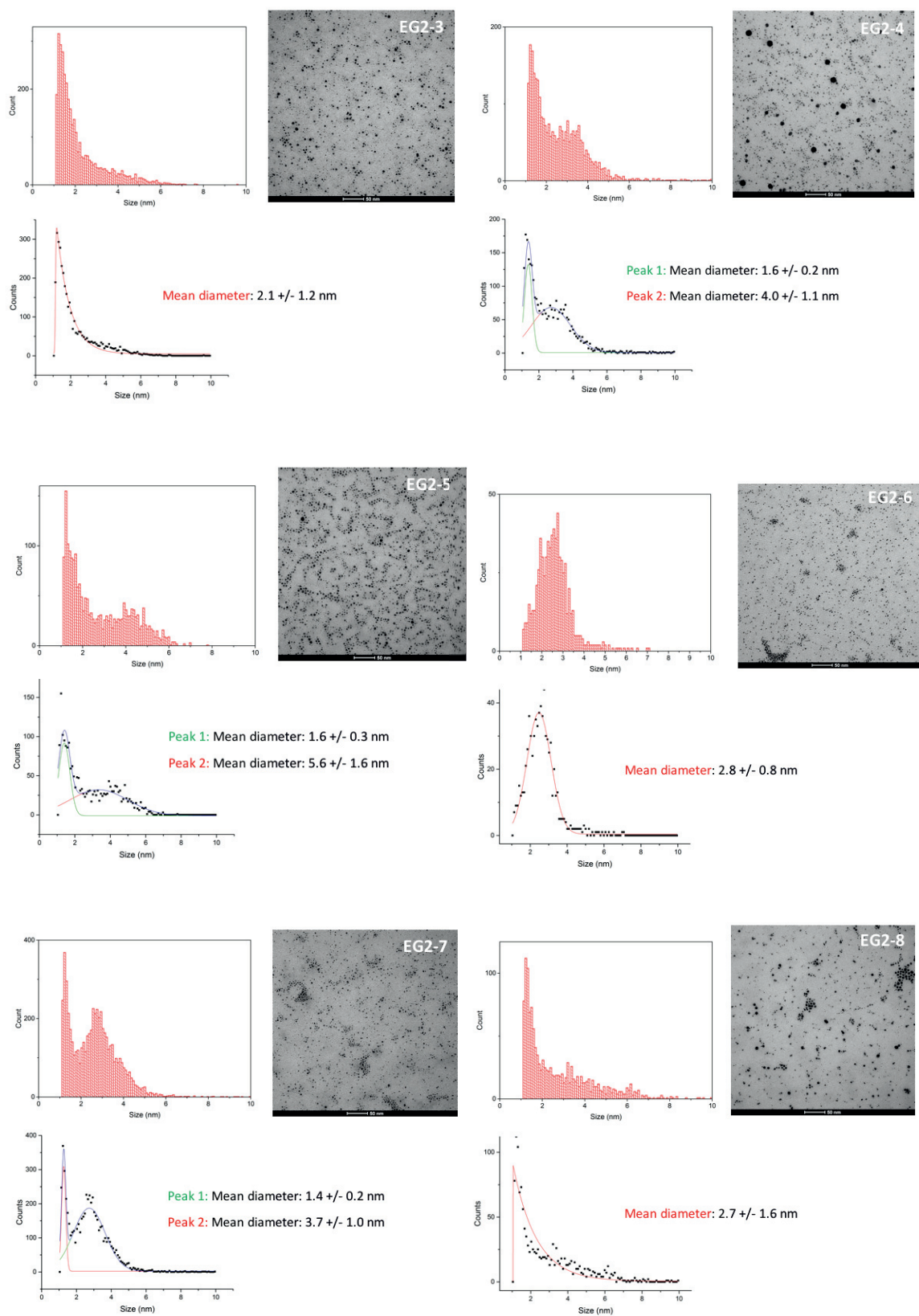


Figure A.7: Representative TEM images and size distributions of EG2-n (n, 3-8)

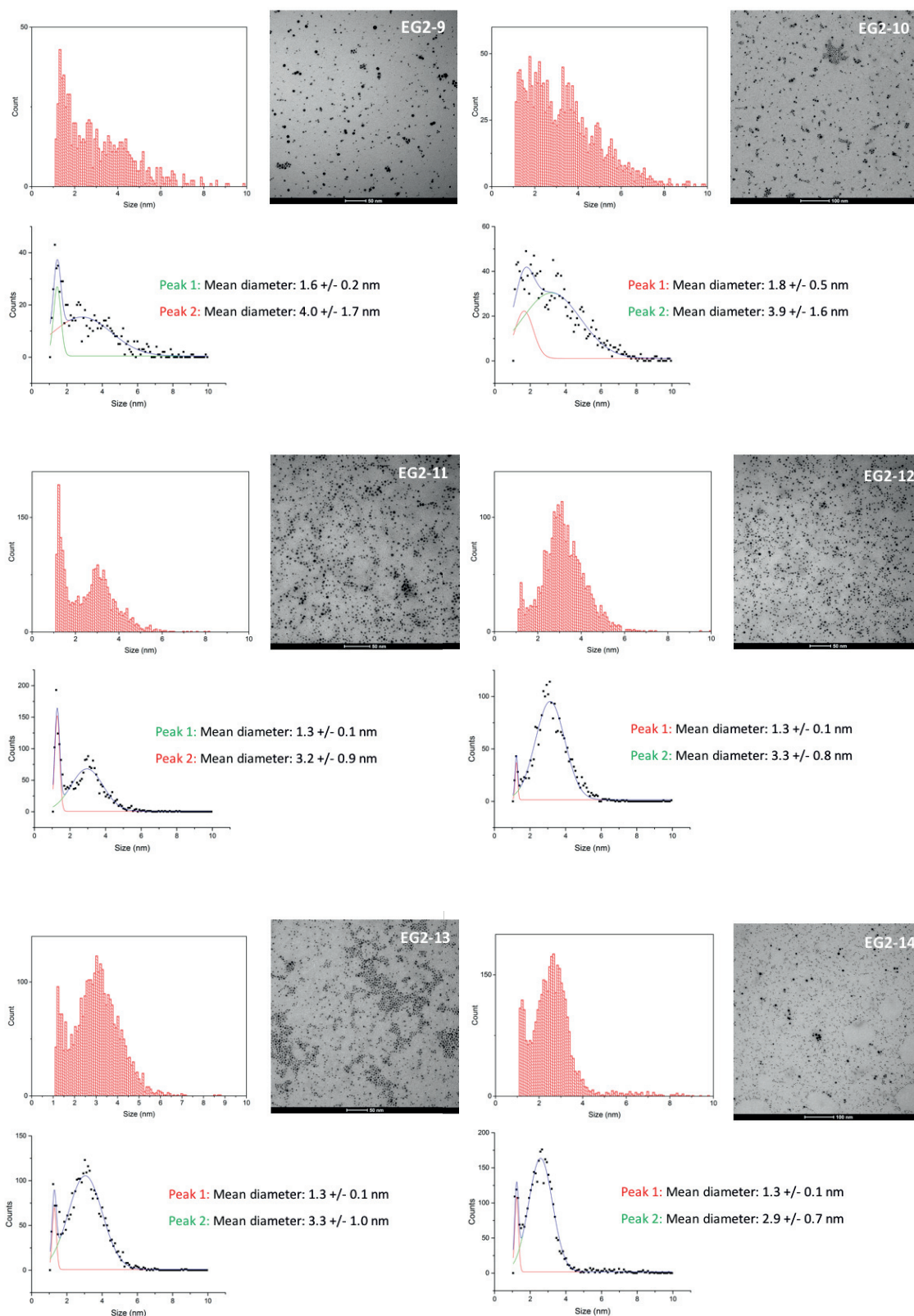


Figure A.8: Representative TEM images and size distributions of EG2-n (n, 9-14)

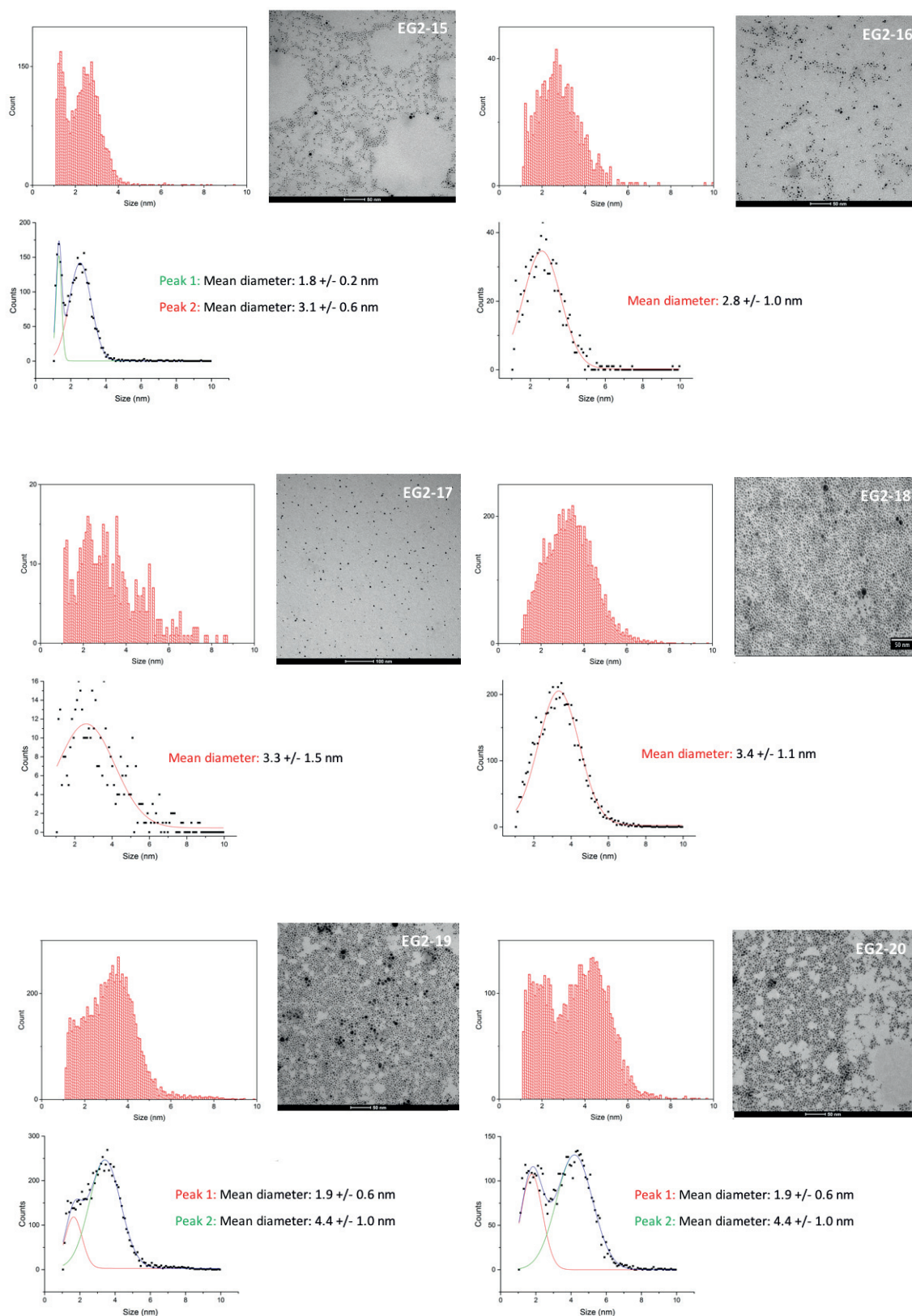


Figure A.9: Representative TEM images and size distributions of EG2-n (n, 15-20)

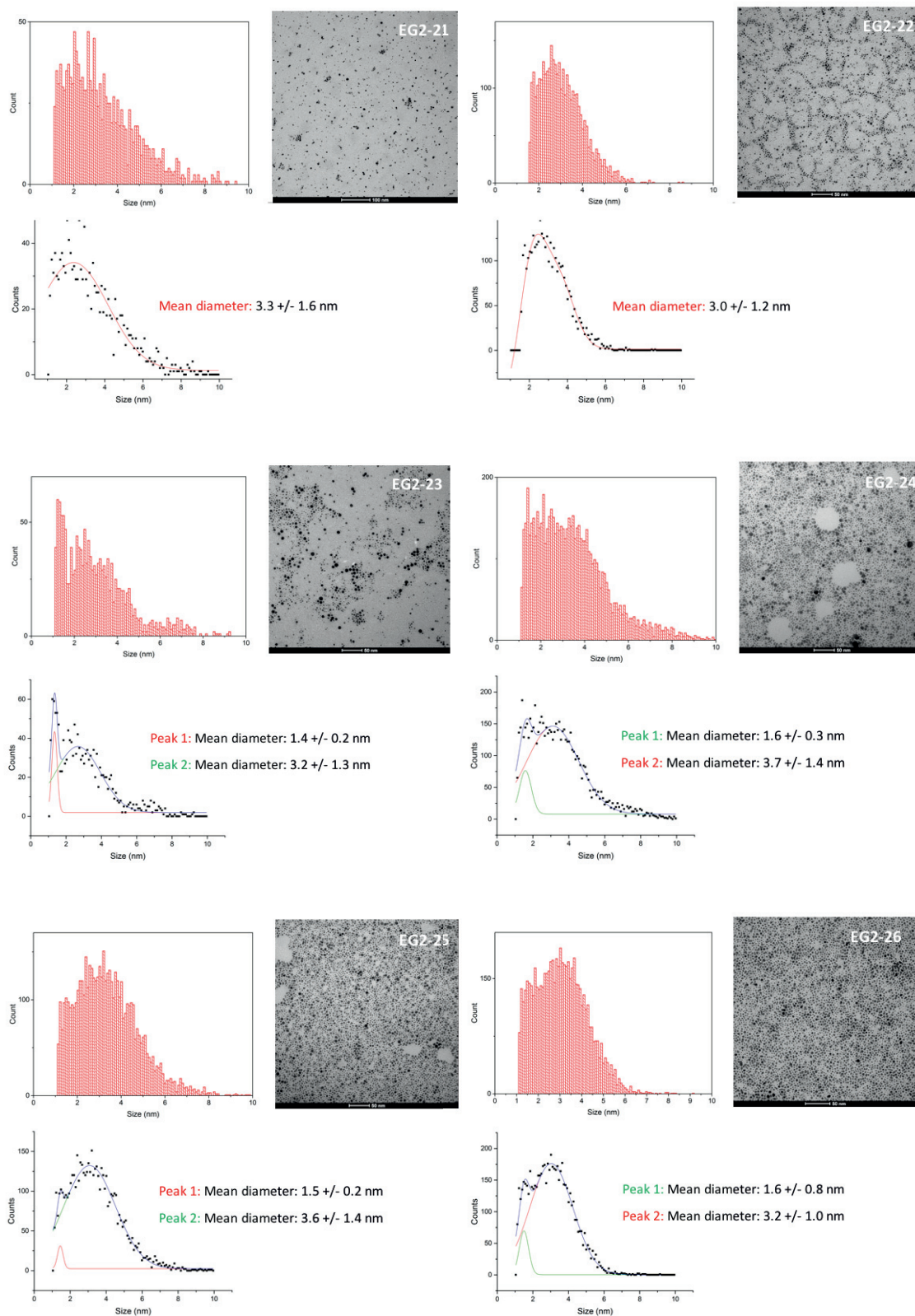


Figure A.10: Representative TEM images and size distributions of EG2-n (n, 21-26)

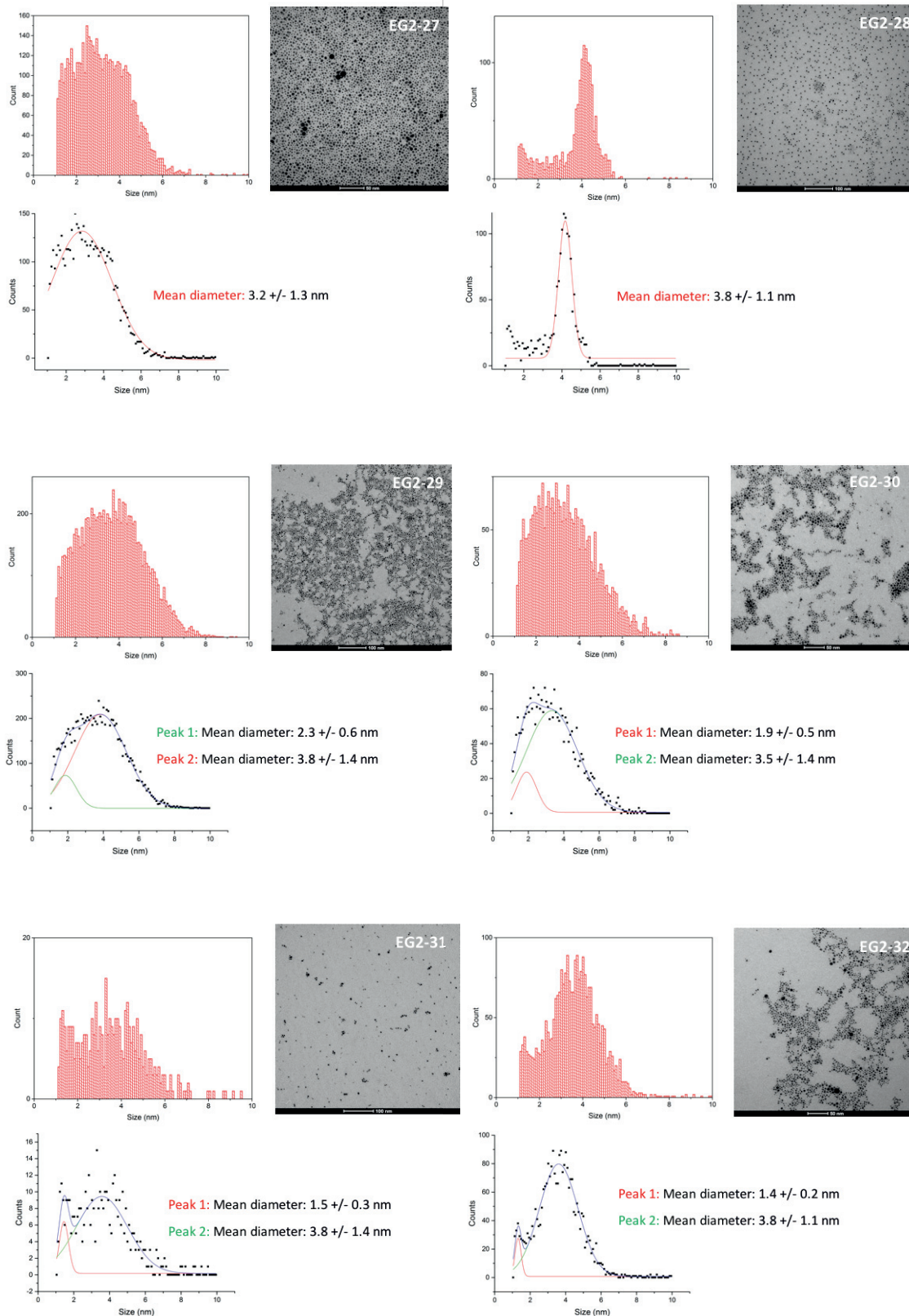


Figure A.11: Representative TEM images and size distributions of EG2-n (n, 27-32)

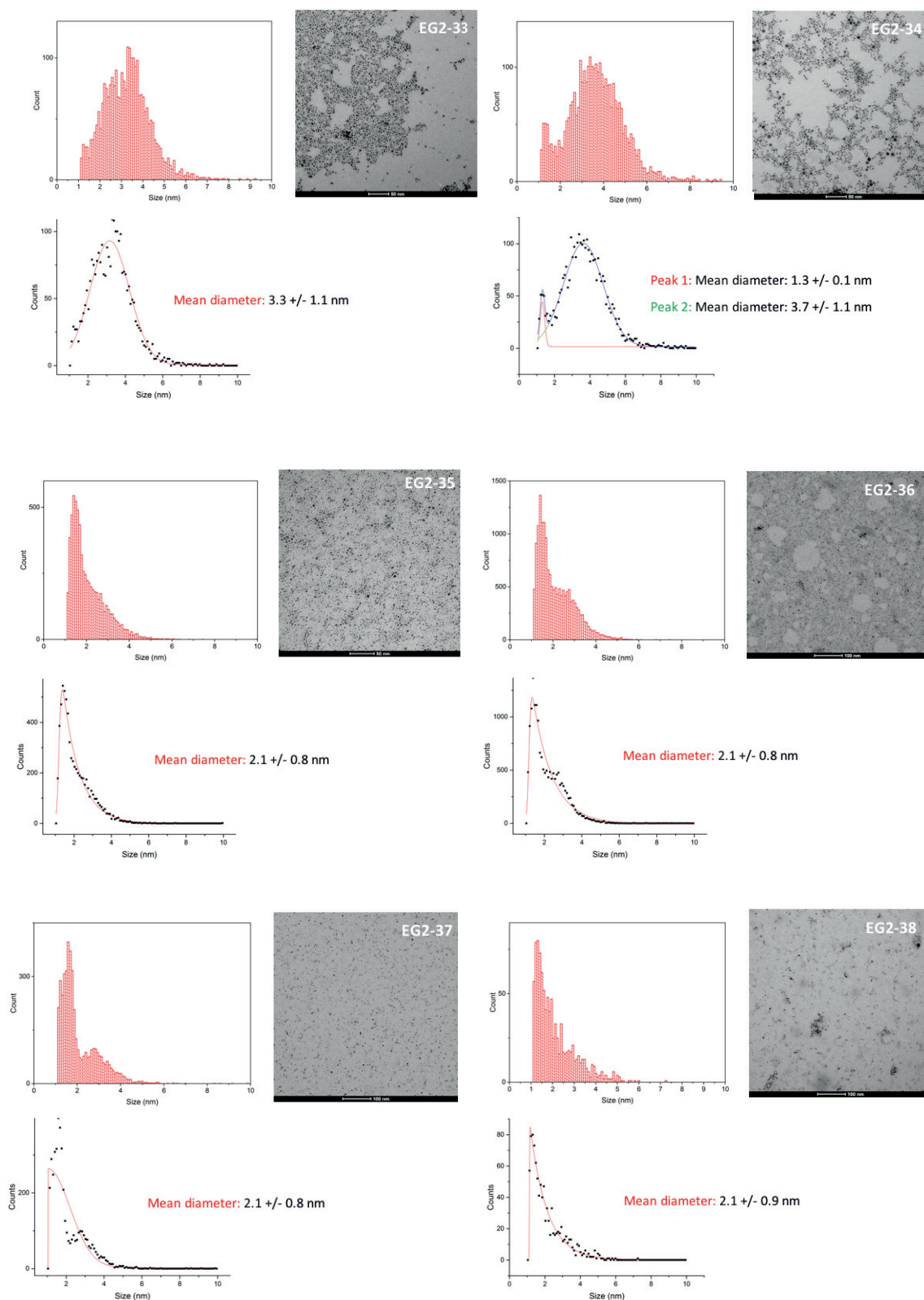


Figure A.12: Representative TEM images and size distributions of EG2-n (n, 33-38)

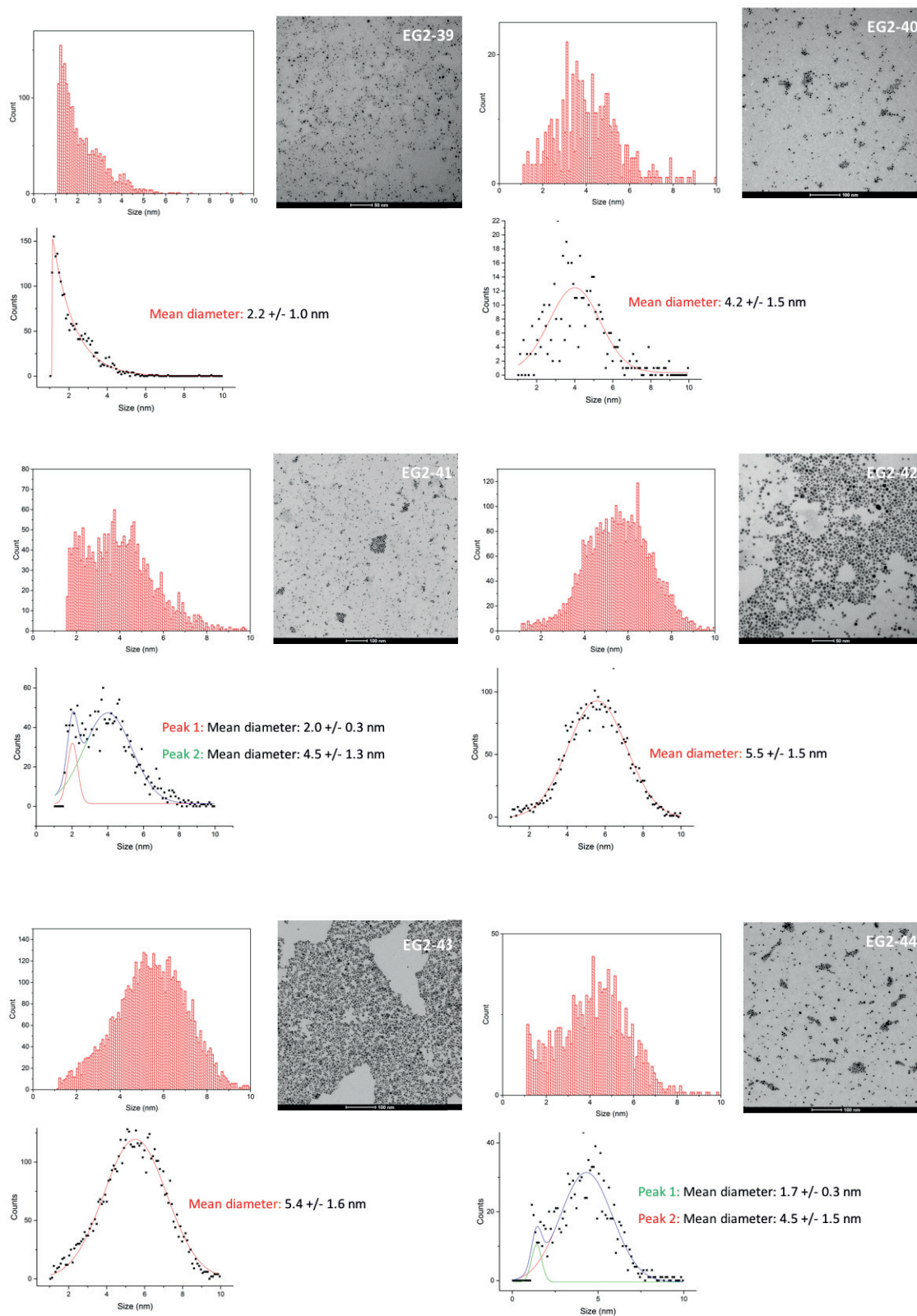


Figure A.13: Representative TEM images and size distributions of EG2-n (n, 39-44)

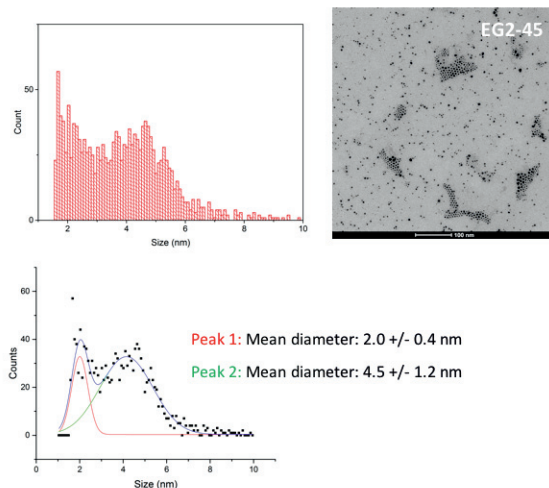


Figure A.14: Representative TEM image and size distribution of EG2-n (n, 45)

A.3 FTIR Spectra of EG2-n AuNPs

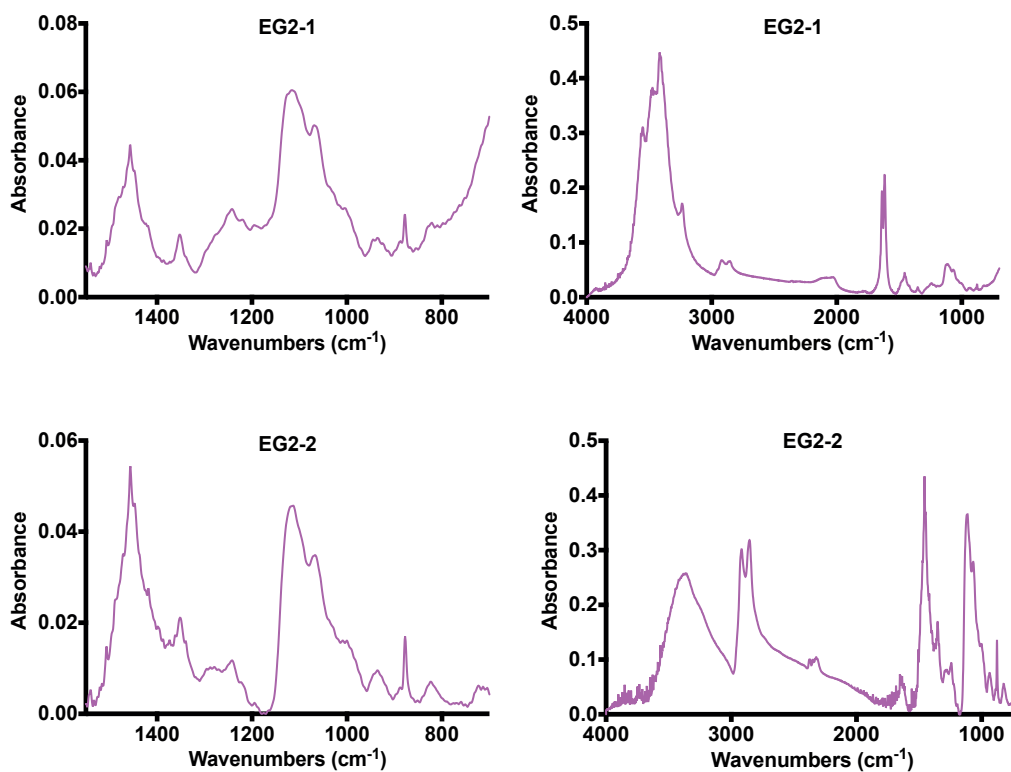


Figure A.15: Right panel shows the wavenumbers in the range of 700-4000 cm^{-1} , Left panel shows the wavenumbers in the range of 700-1550 cm^{-1} . Representative FTIR spectra of EG2-n (n, 1-2)

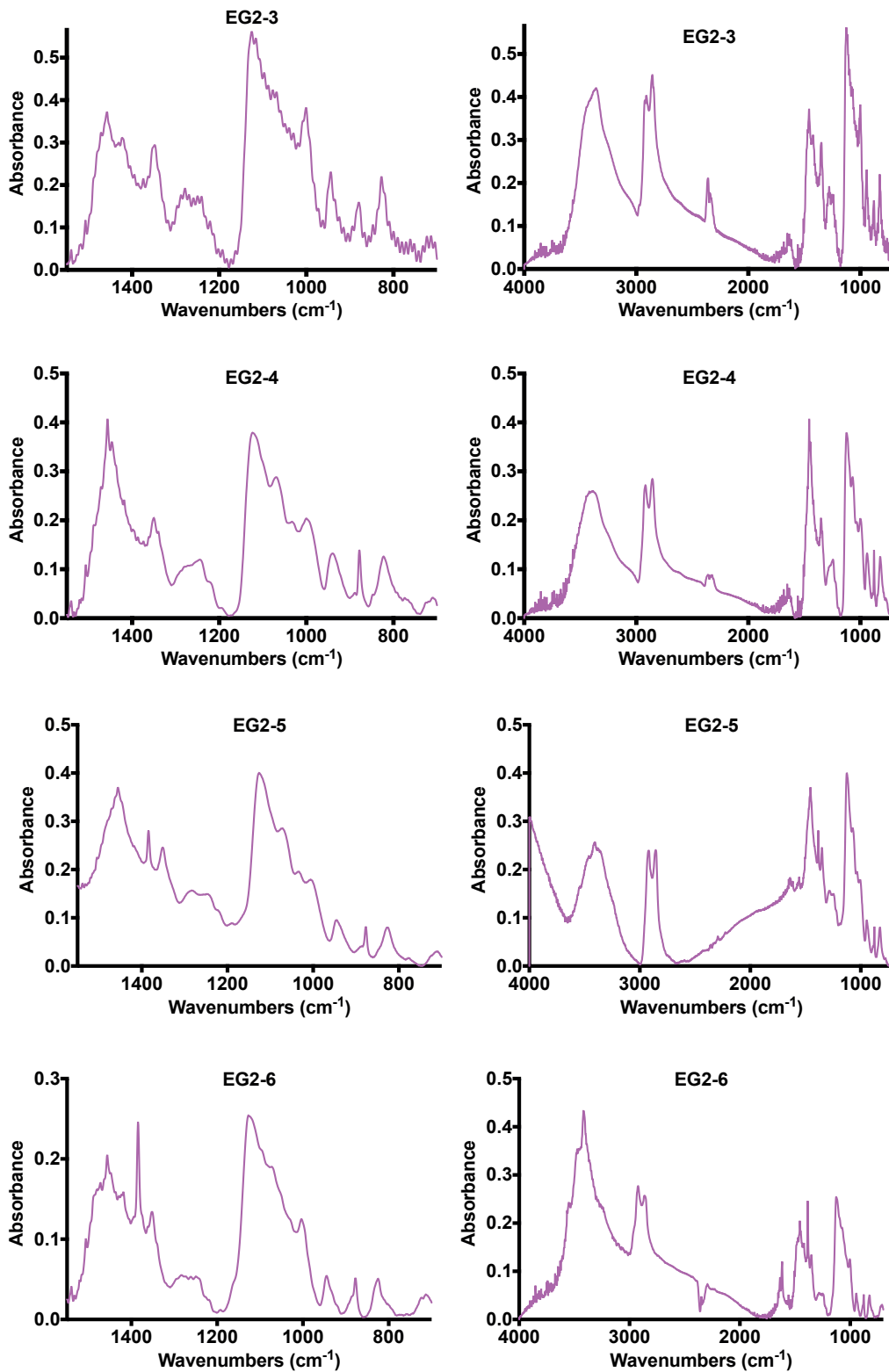


Figure A.16: Right panel shows the wavenumbers in the range of 700-4000 cm^{-1} , Left panel shows the wavenumbers in the range of 700-1550 cm^{-1} . Representative FTIR spectra of EG2-n (n, 3-6)

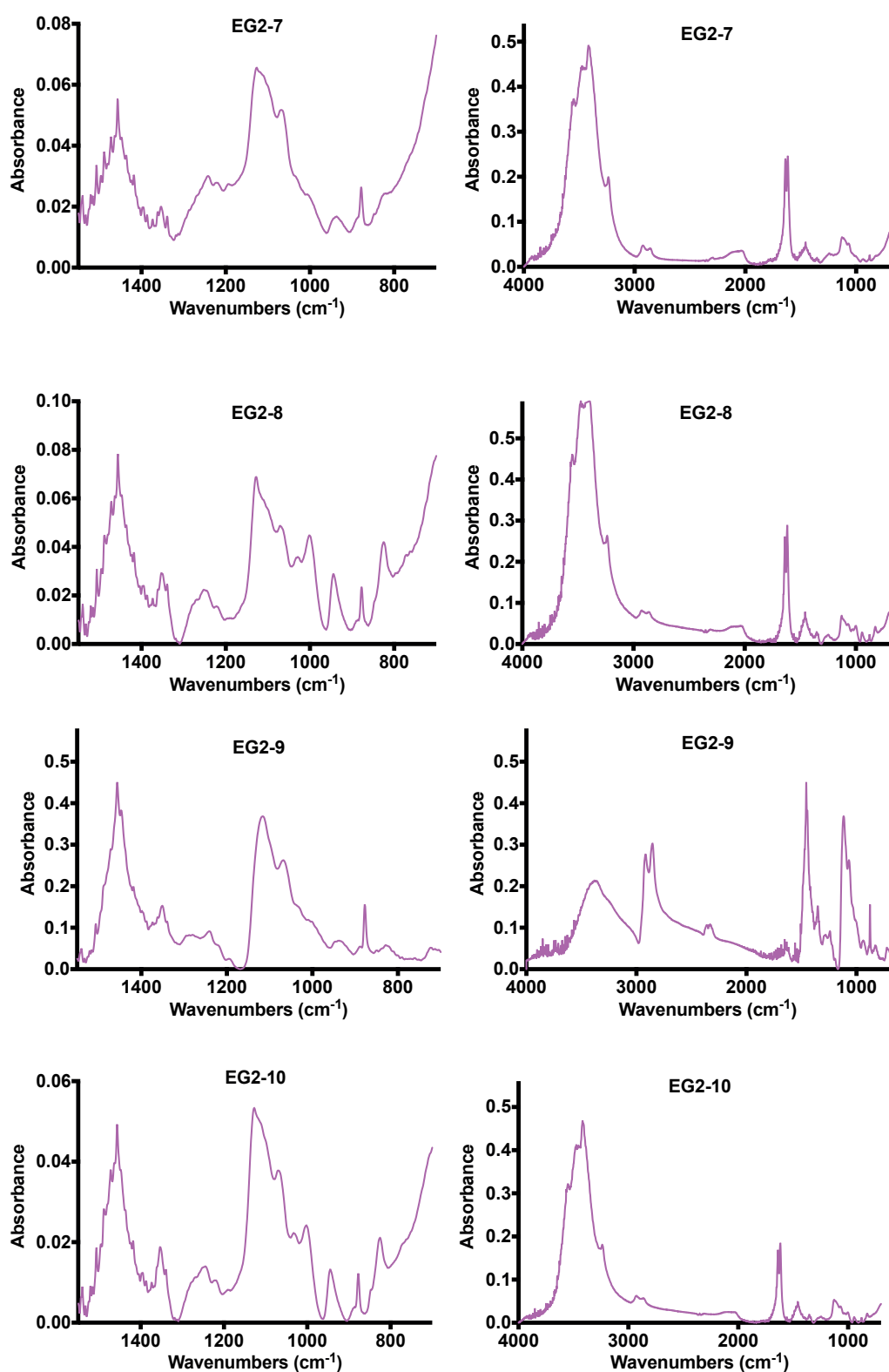


Figure A.17: Right panel shows the wavenumbers in the range of 700-4000 cm^{-1} , Left panel shows the wavenumbers in the range of 700-1550 cm^{-1} . Representative FTIR spectra of EG2-n (n, 7-10)

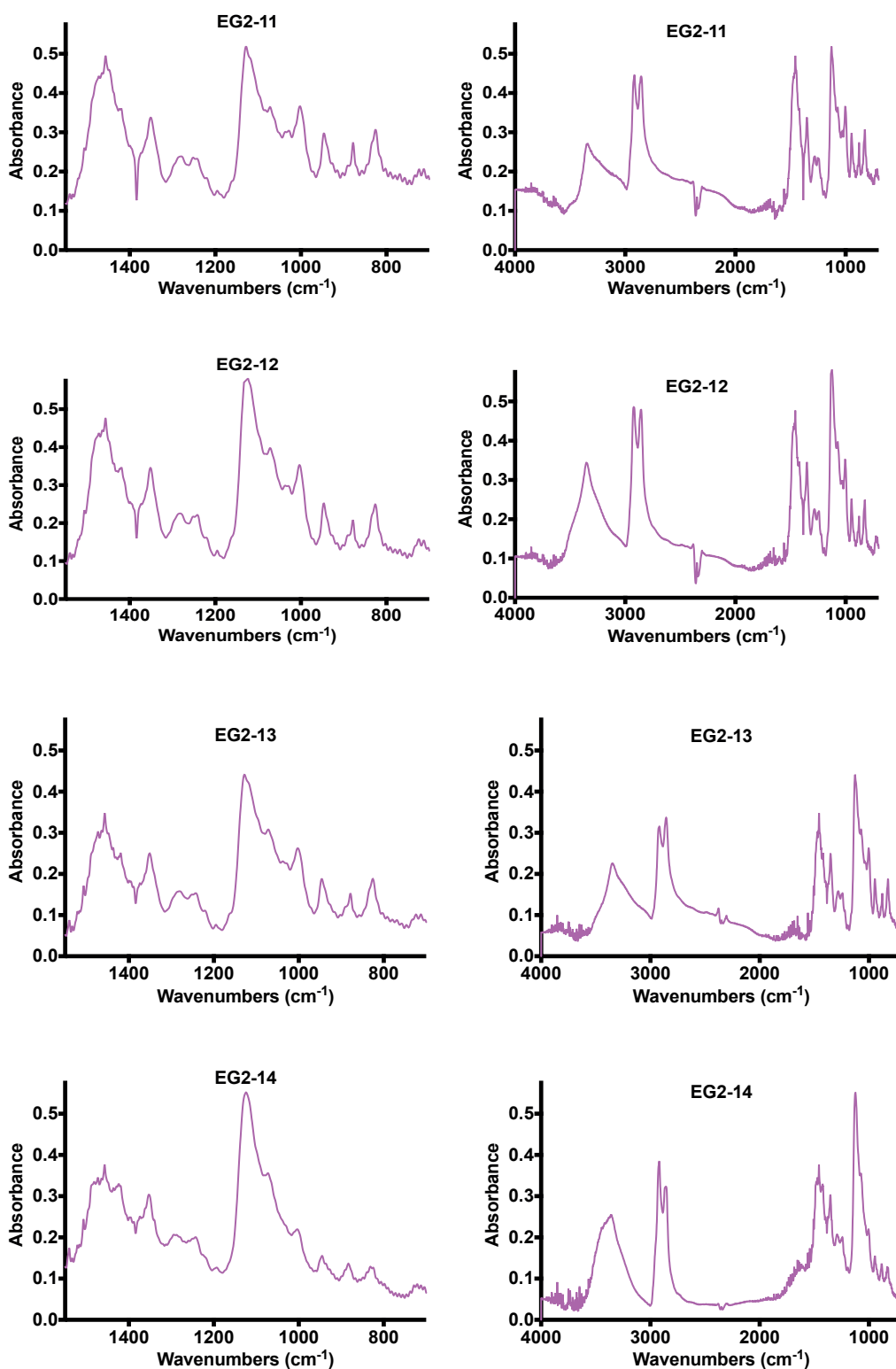


Figure A.18: Right panel shows the wavenumbers in the range of 700-4000 cm^{-1} , Left panel shows the wavenumbers in the range of 700-1550 cm^{-1} . Representative FTIR spectra of EG2-n (n, 11-14)

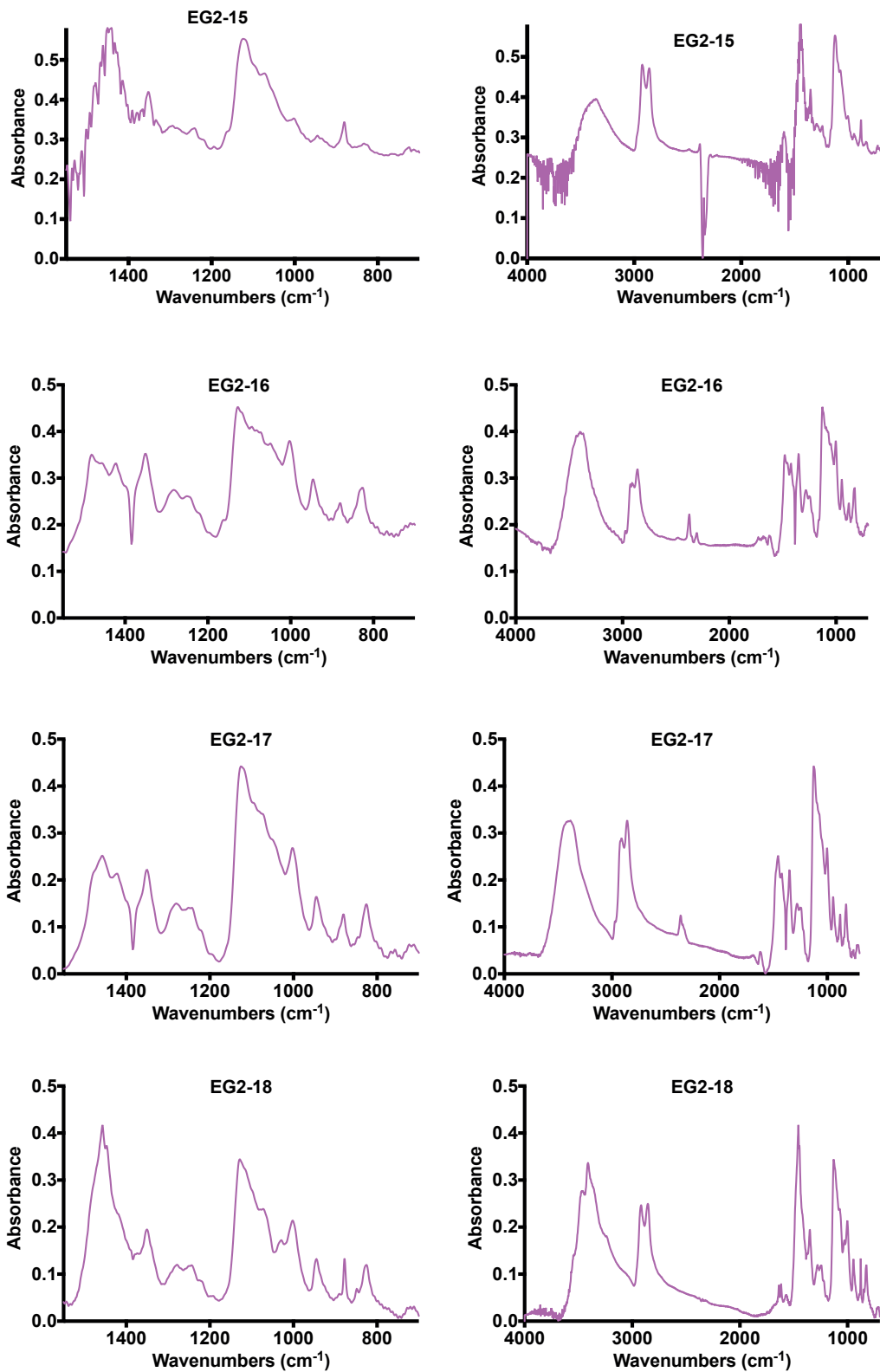


Figure A.19: Right panel shows the wavenumbers in the range of 700-4000 cm^{-1} , Left panel shows the wavenumbers in the range of 700-1550 cm^{-1} . Representative FTIR spectra of EG2-n (n, 15-18)

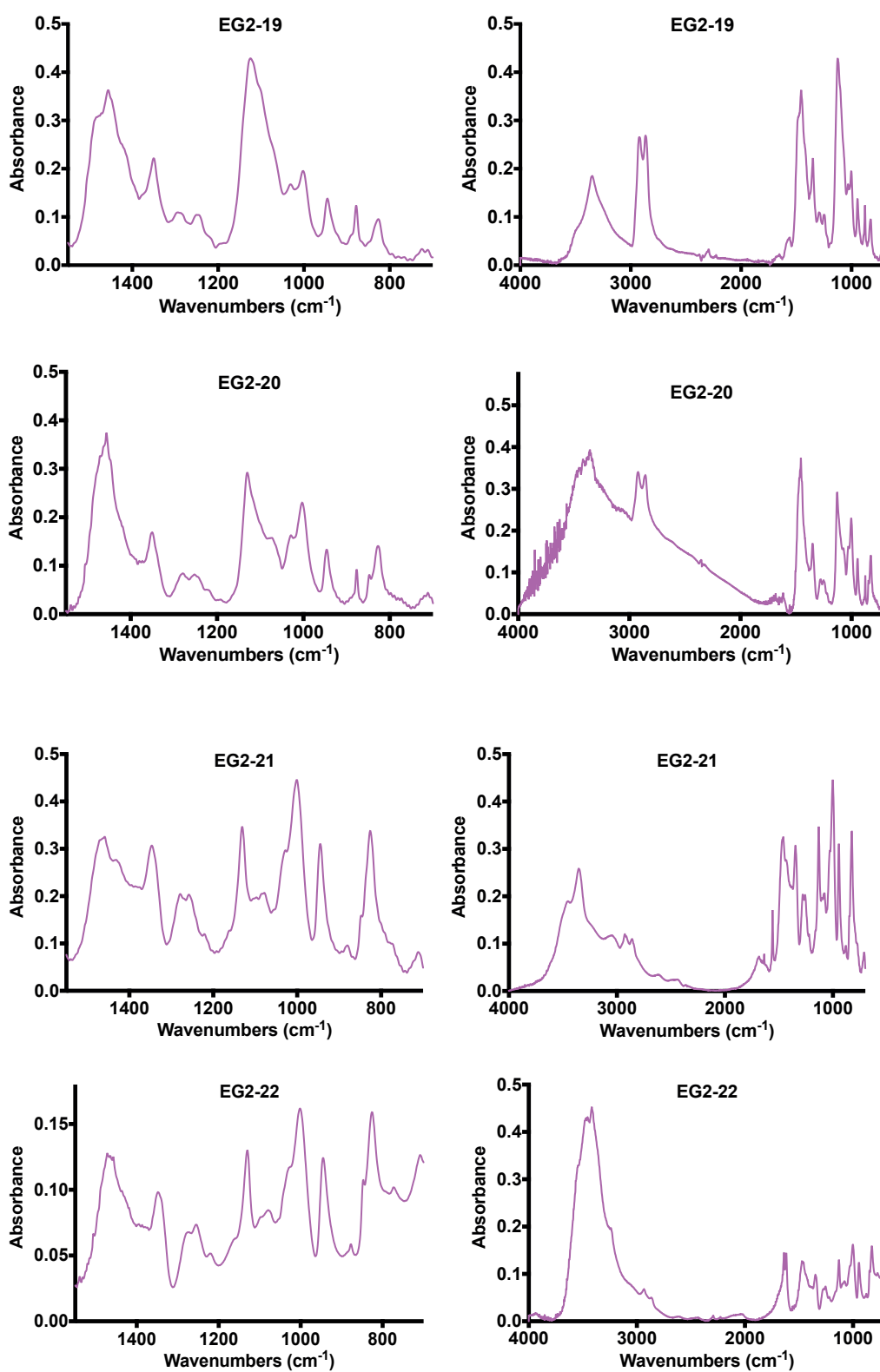


Figure A.20: Right panel shows the wavenumbers in the range of 700-4000 cm^{-1} , Left panel shows the wavenumbers in the range of 700-1550 cm^{-1} . Representative FTIR spectra of EG2-n (n, 19-22)

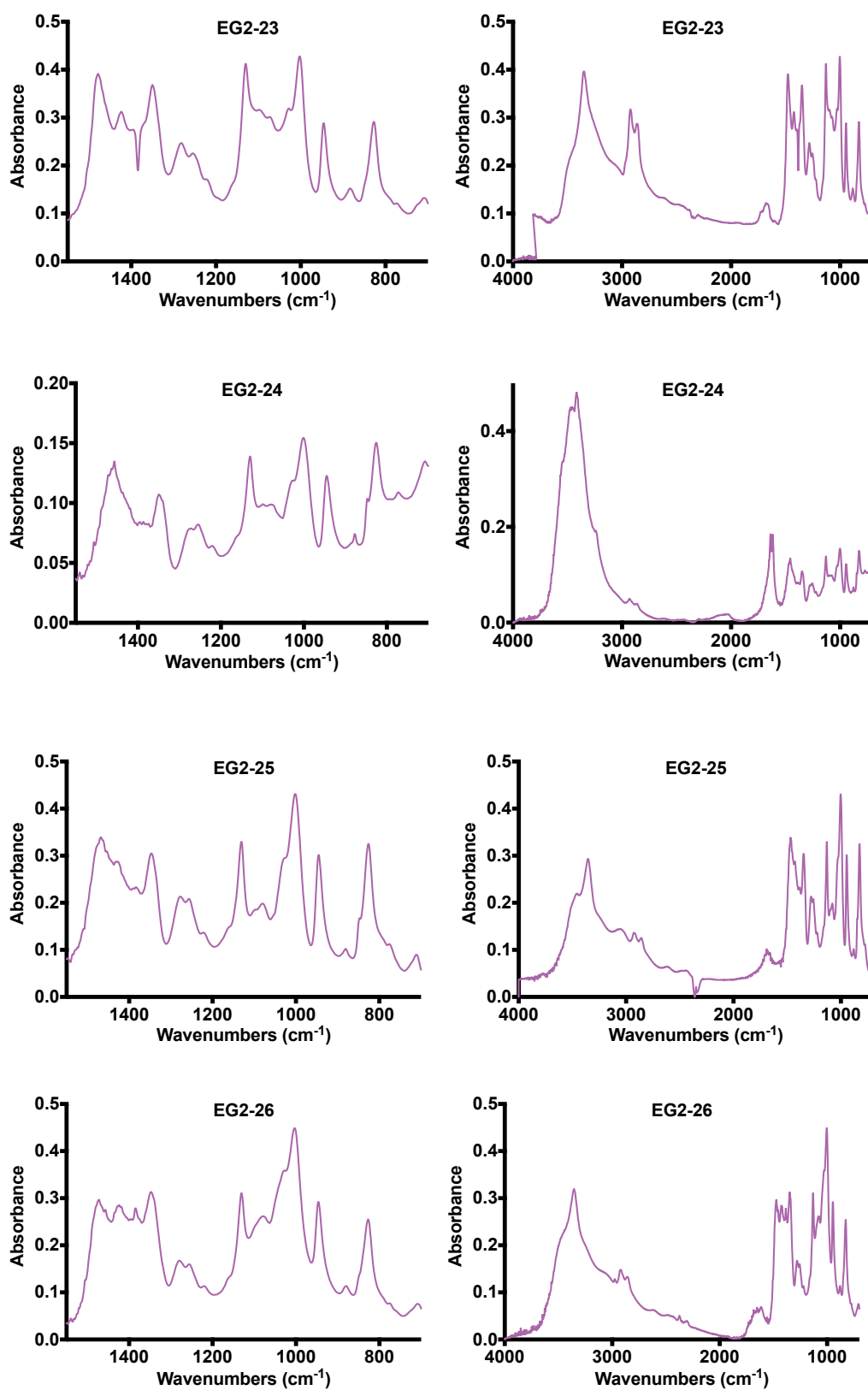


Figure A.21: Right panel shows the wavenumbers in the range of 700-4000 cm⁻¹, Left panel shows the wavenumbers in the range of 700-1550 cm⁻¹. Representative FTIR spectra of EG2-n (n, 23-26)

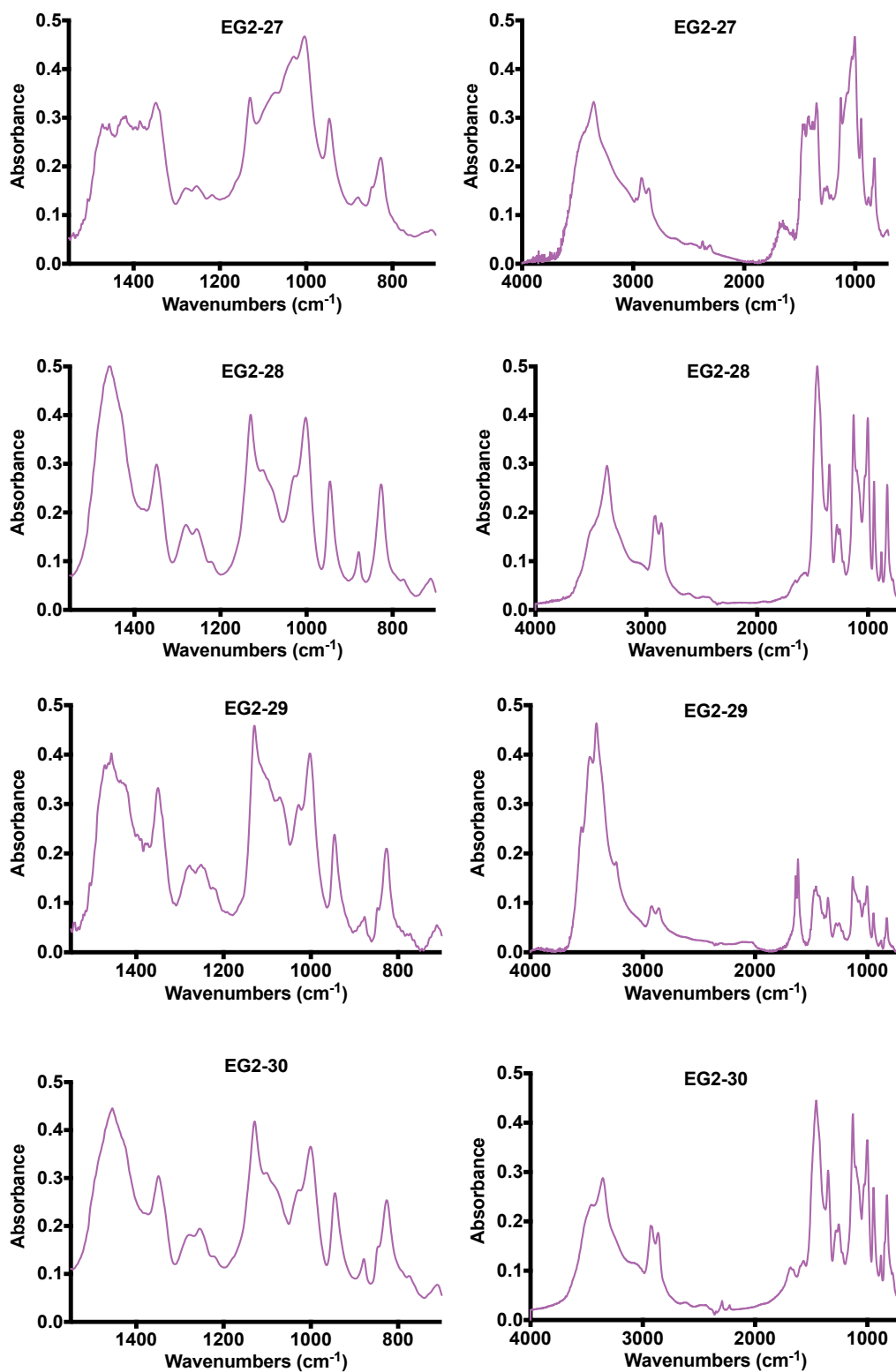


Figure A.22: Right panel shows the wavenumbers in the range of 700-4000 cm^{-1} , Left panel shows the wavenumbers in the range of 700-1550 cm^{-1} . Representative FTIR spectra of EG2-n (n, 27-30)

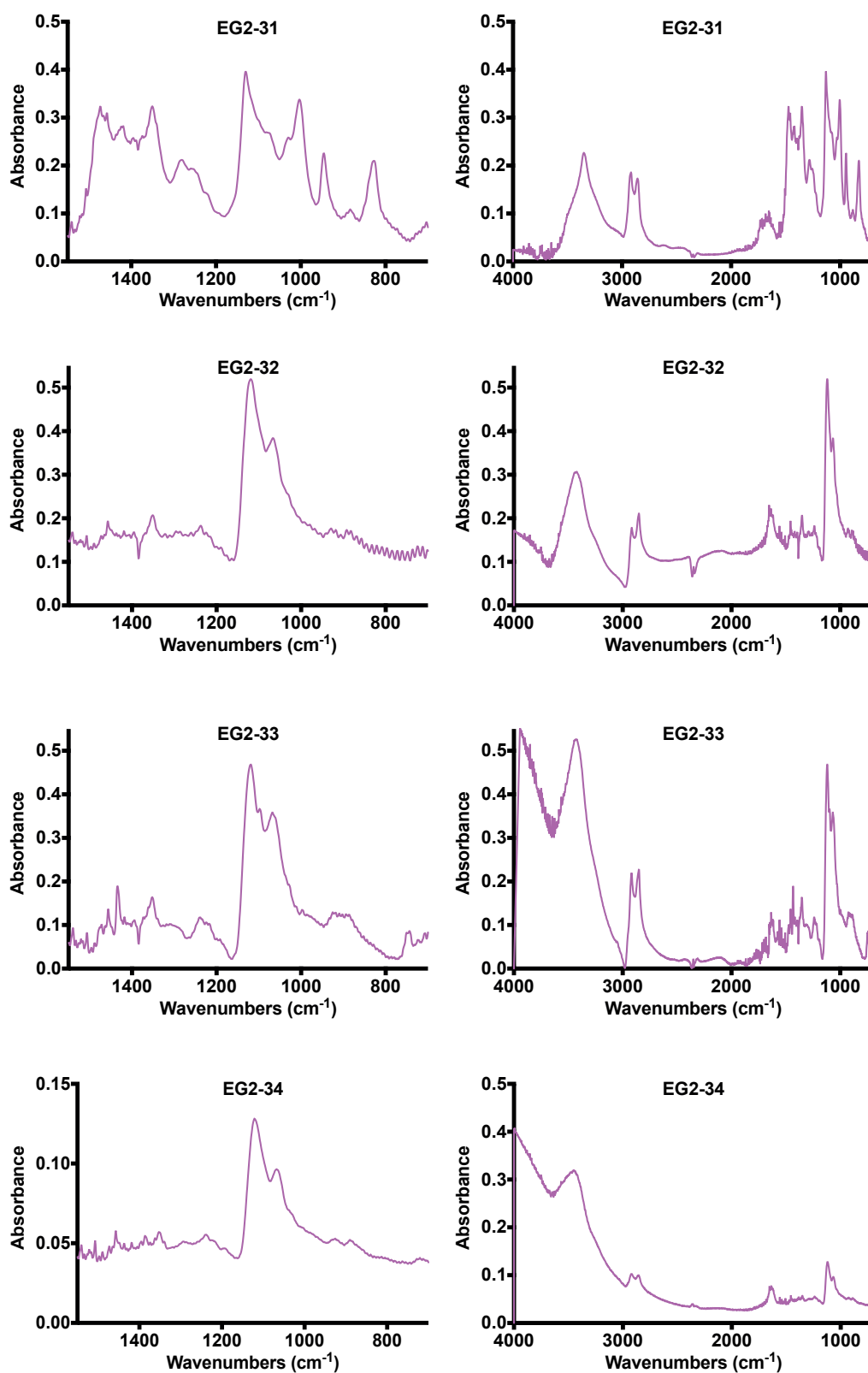


Figure A.23: Right panel shows the wavenumbers in the range of 700-4000 cm^{-1} , Left panel shows the wavenumbers in the range of 700-1550 cm^{-1} . Representative FTIR spectra of EG2-n (n, 31-34)

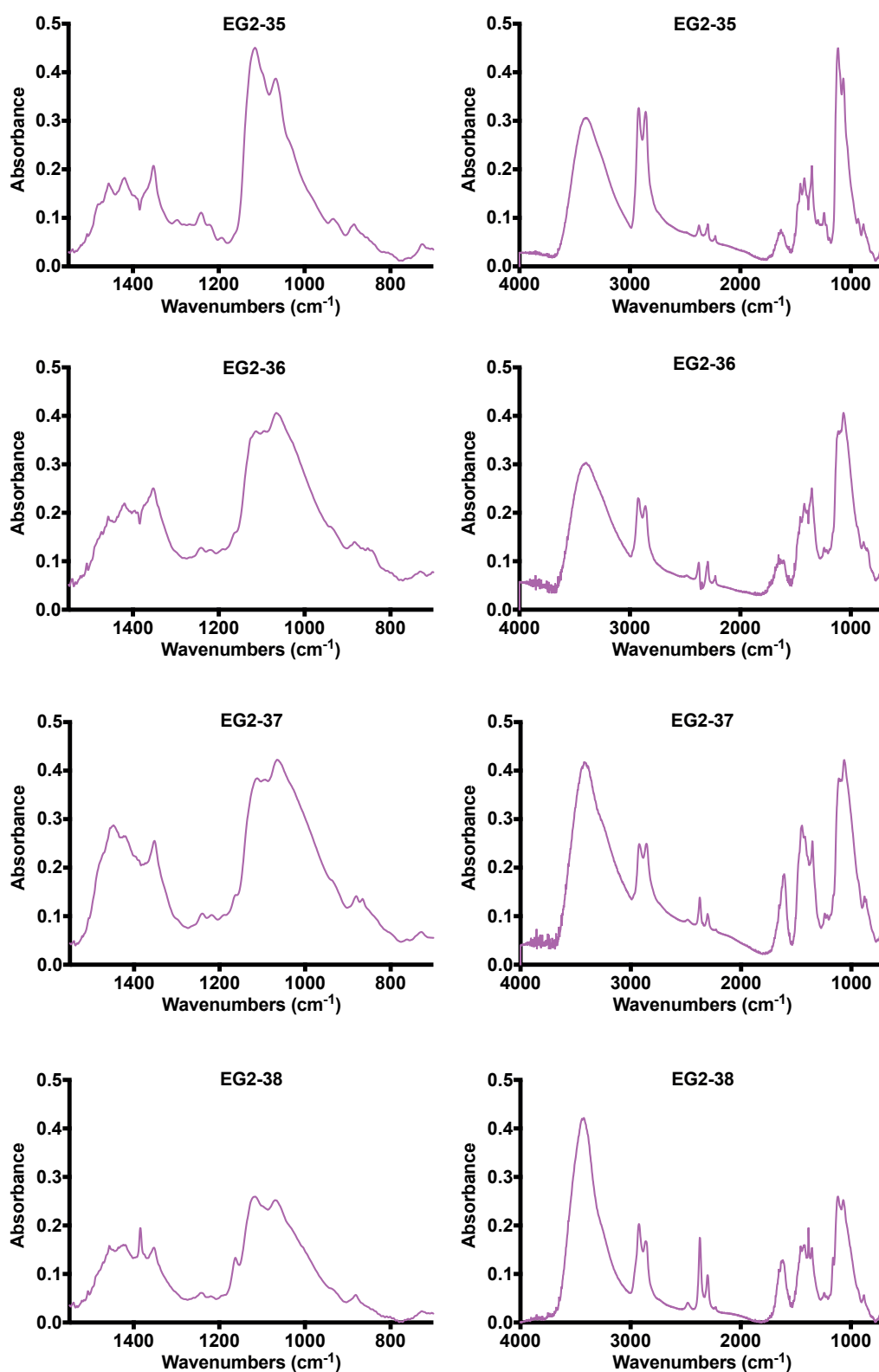


Figure A.24: Right panel shows the wavenumbers in the range of 700-4000 cm^{-1} , Left panel shows the wavenumbers in the range of 700-1550 cm^{-1} . Representative FTIR spectra of EG2-n (n, 35-38)

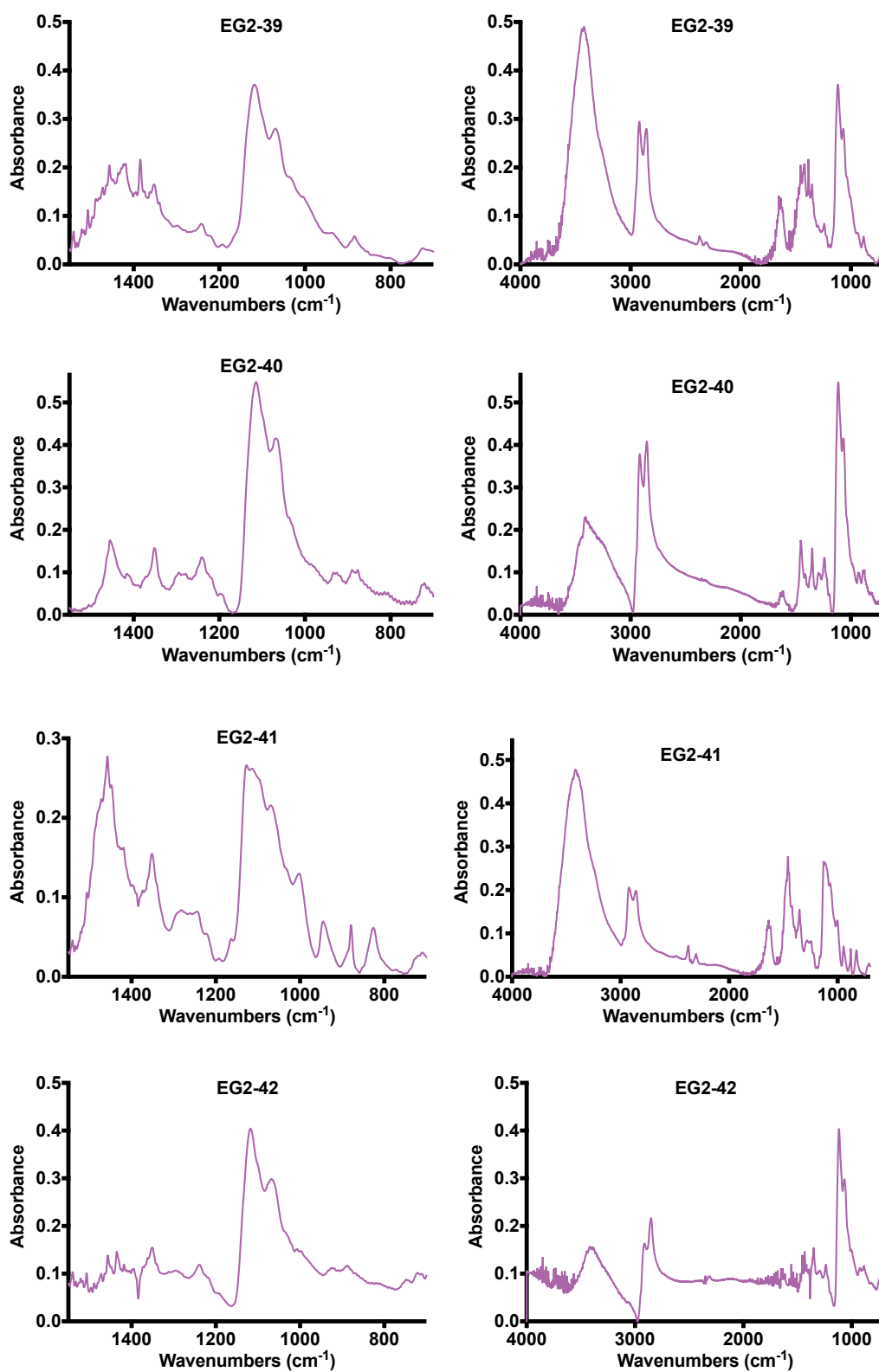


Figure A.24: Right panel shows the wavenumbers in the range of 700-4000 cm⁻¹, Left panel shows the wavenumbers in the range of 700-1550 cm⁻¹. Representative FTIR spectra of EG2-n (n, 39-42)

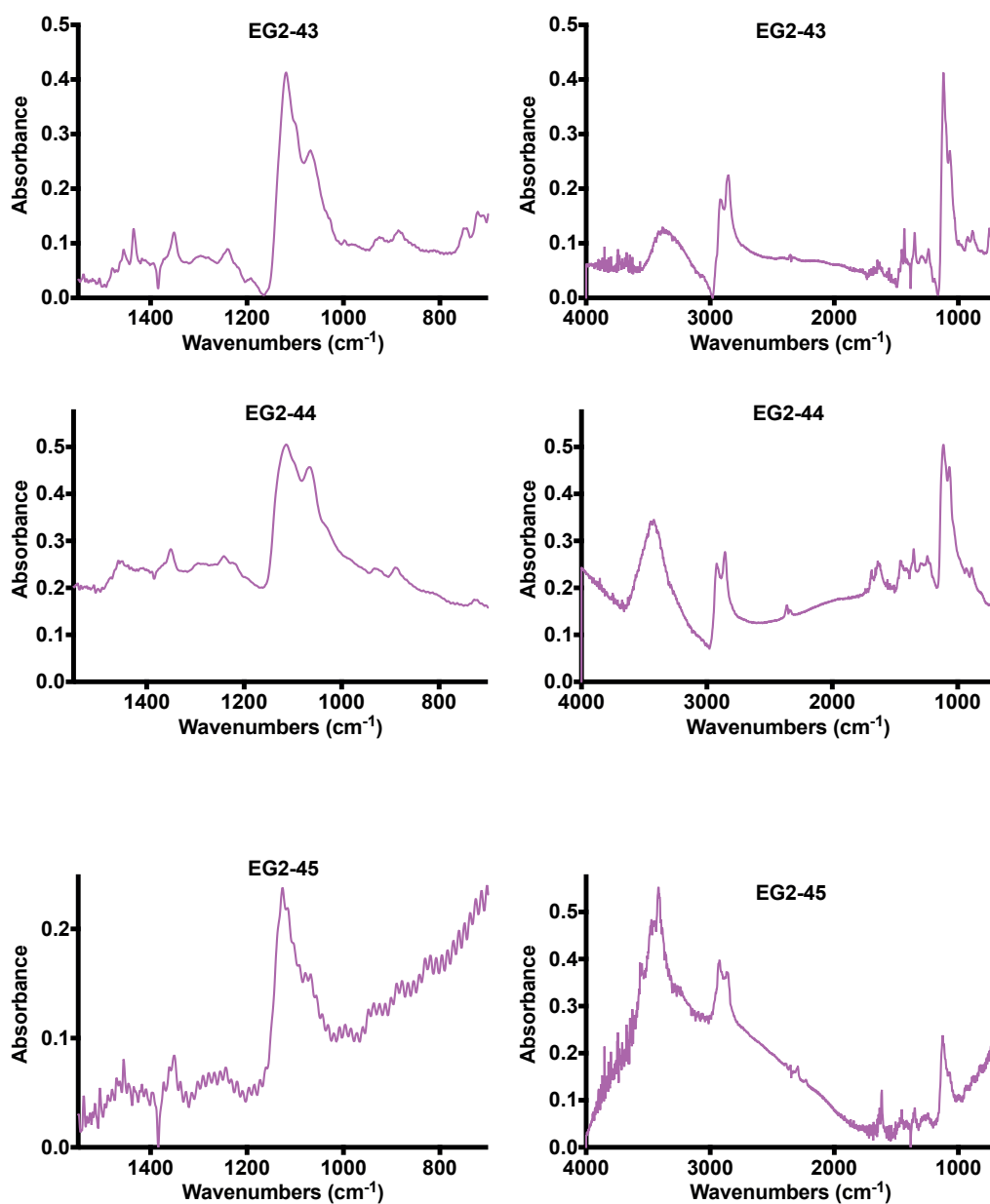


Figure A.25: Right panel shows the wavenumbers in the range of 700-4000 cm^{-1} , Left panel shows the wavenumbers in the range of 700-1550 cm^{-1} . Representative FTIR spectra of EG2-n (n, 43-45)

A.4 Conductivity Plots of EG2-n AuNPs

Delta conductivity (Δ) in the y-axis of the plots represents the conductivity of the solution from which the initial conductivity value is subtracted. Concentration of added metal salt is represented in x-axis as molarity (M).

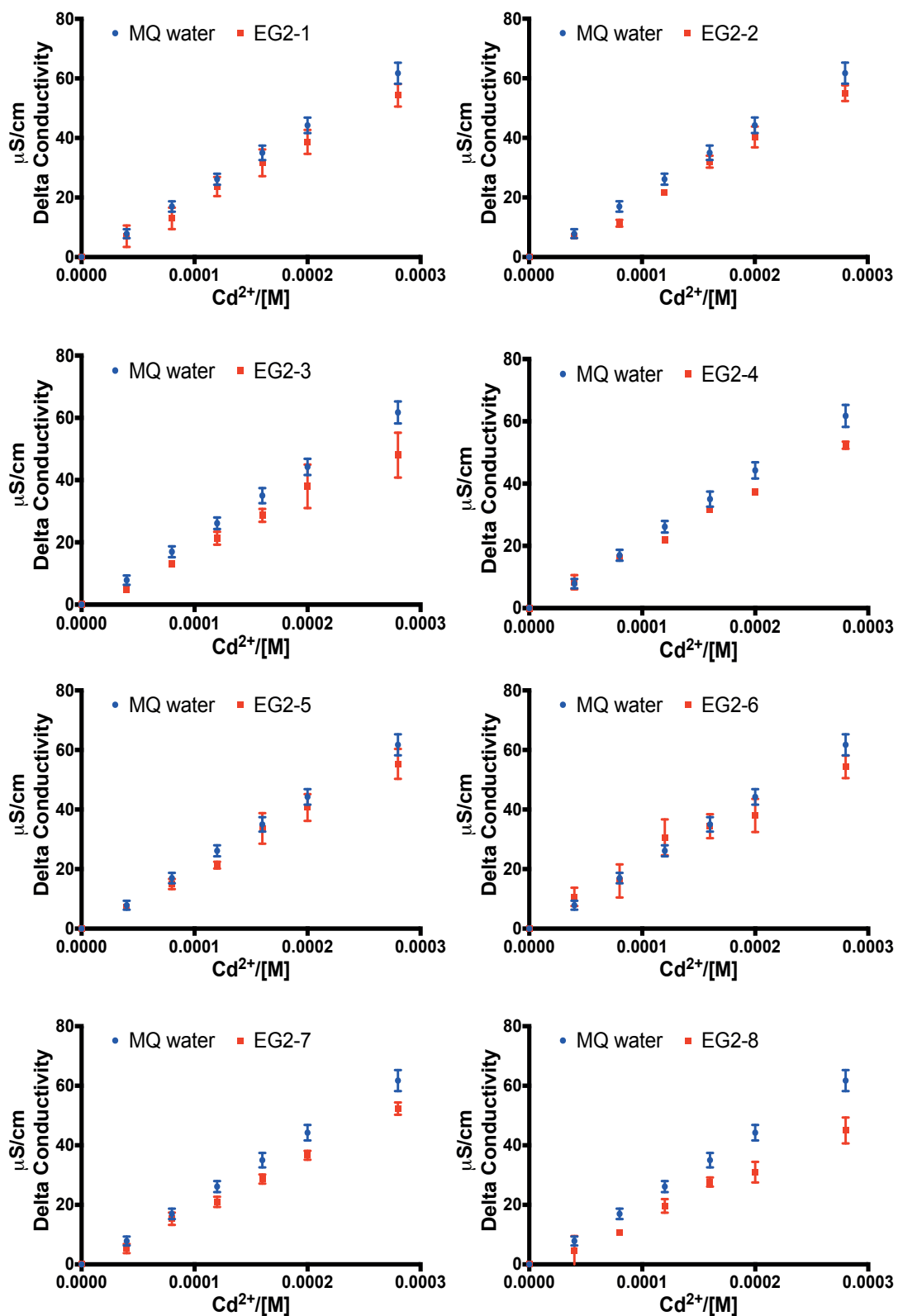


Figure A.26: The results of conductivity tests of EG2-n (n, 1-8) in MQ water.

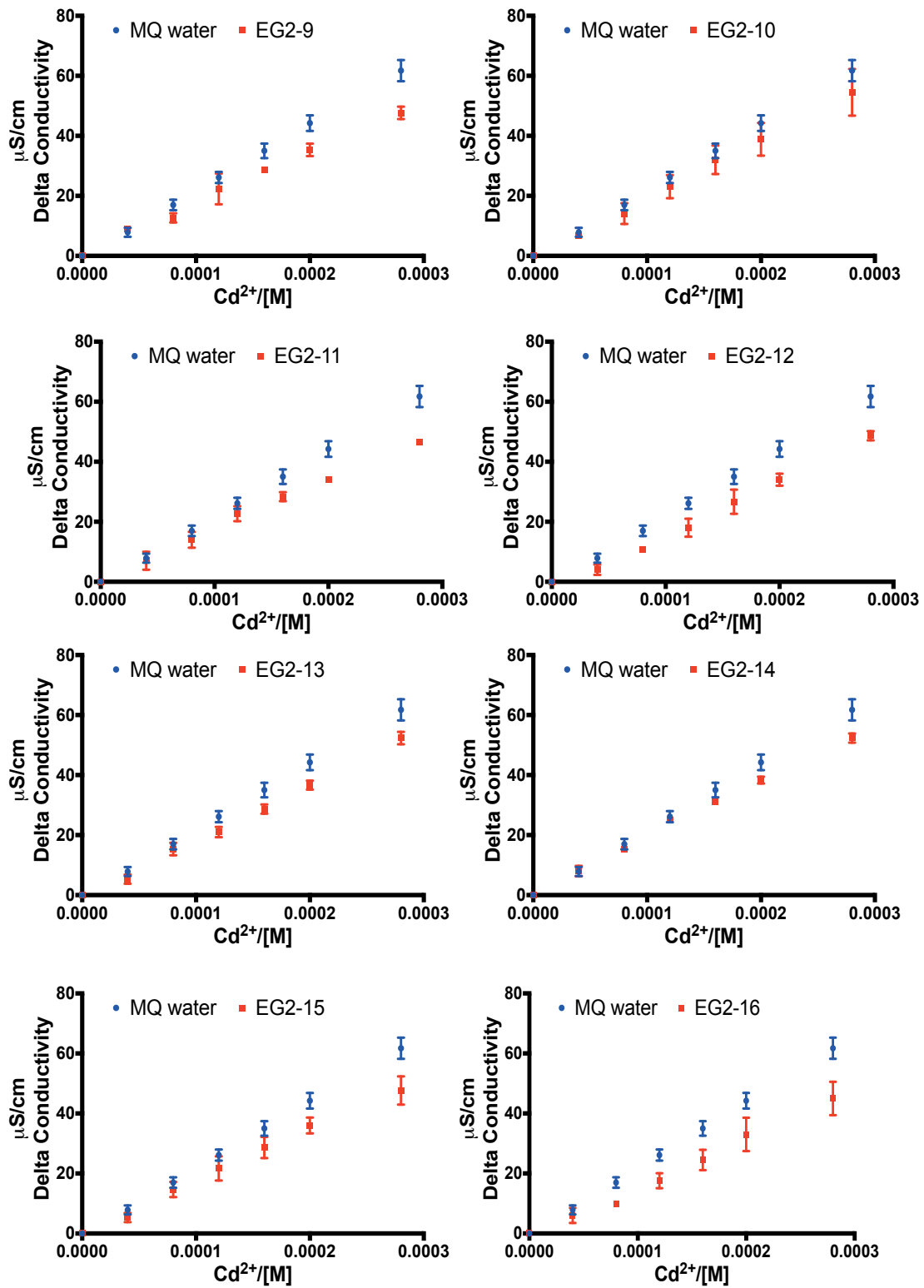


Figure A.27: The results of conductivity tests of EG2-n (n, 9-16) in MQ water.

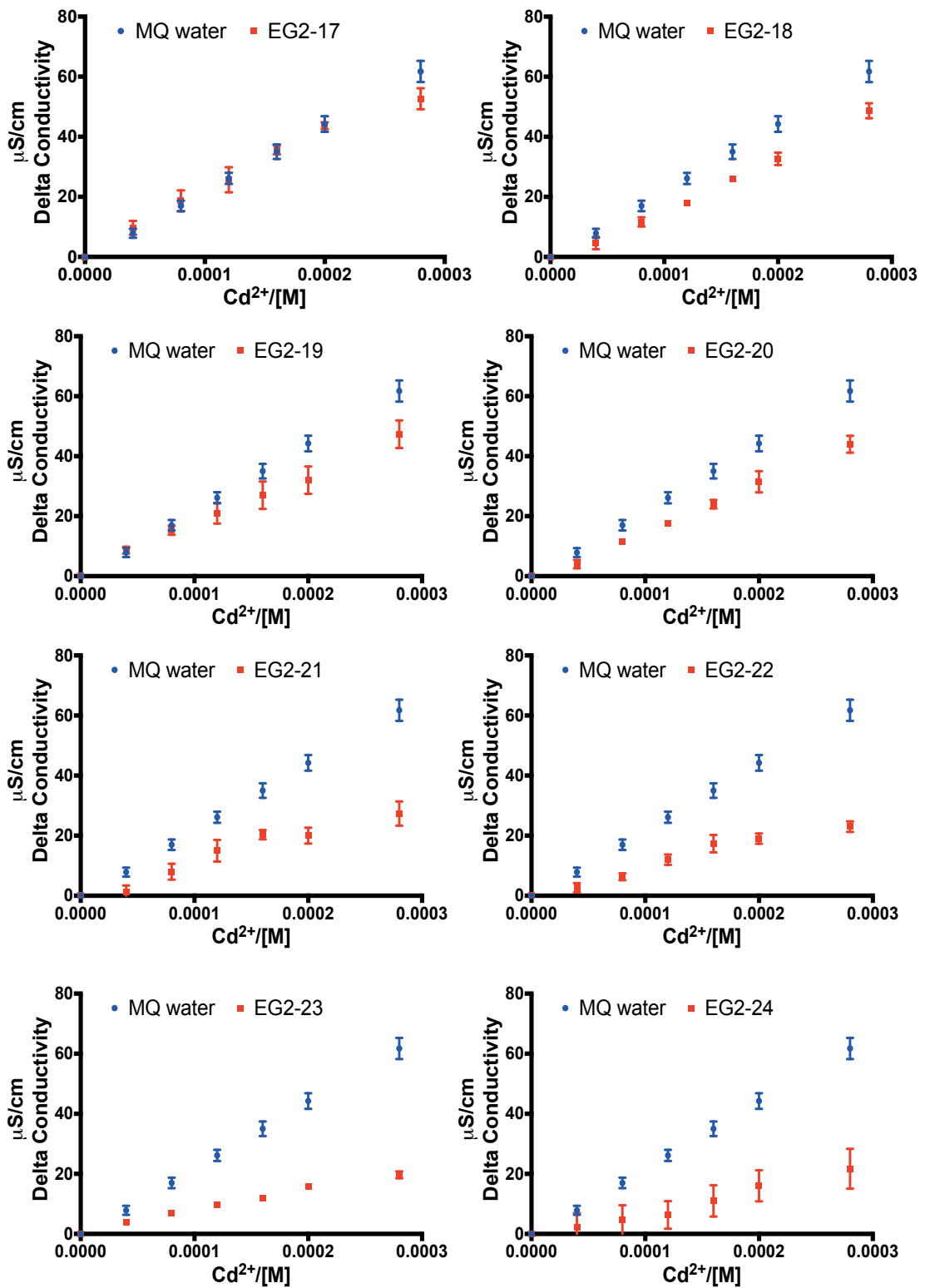


Figure A.28: The results of conductivity tests of EG2-n (n, 17-24) in MQ water.

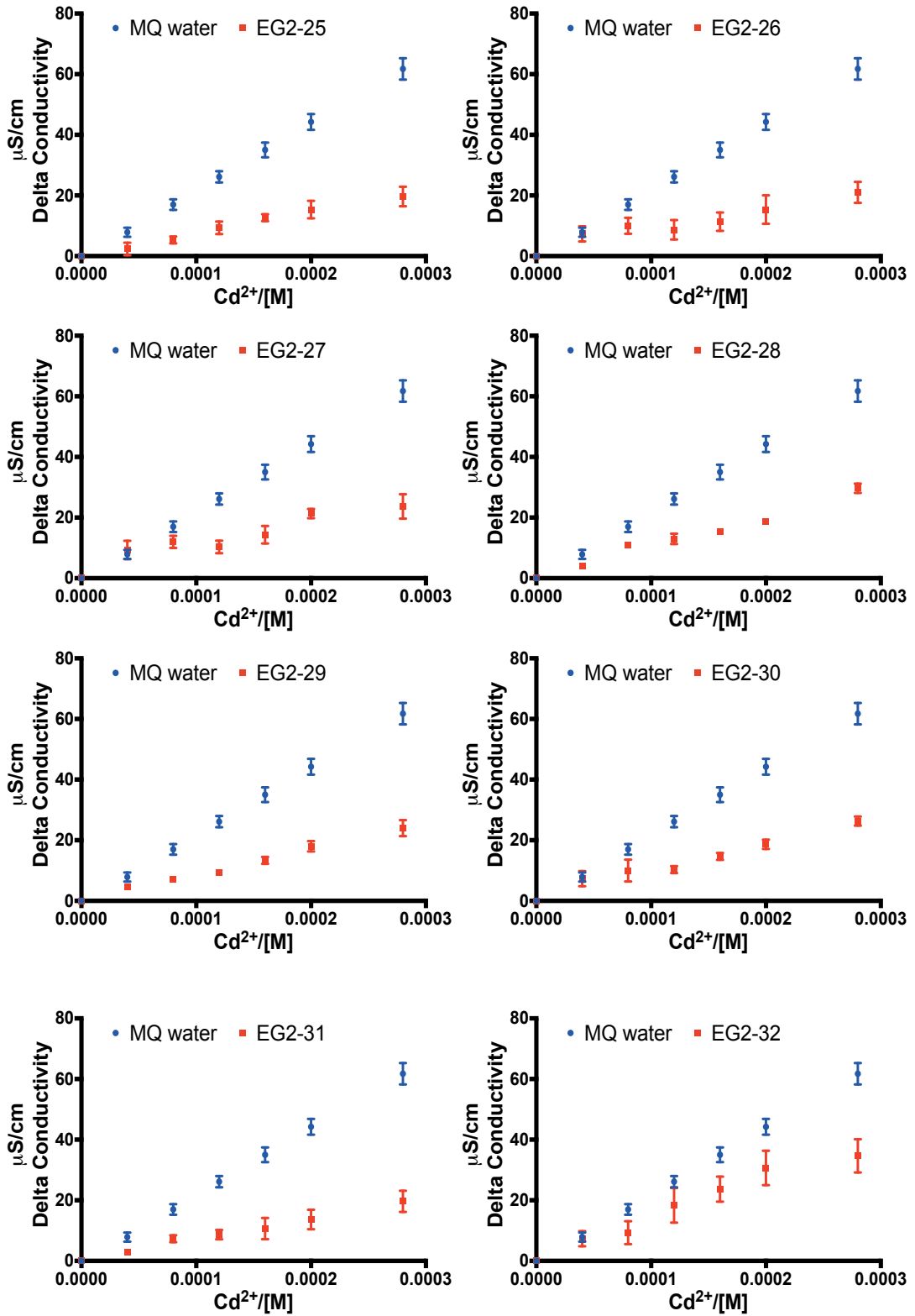


Figure A.29: The results of conductivity tests of EG2-n (n, 25-32) in MQ water.

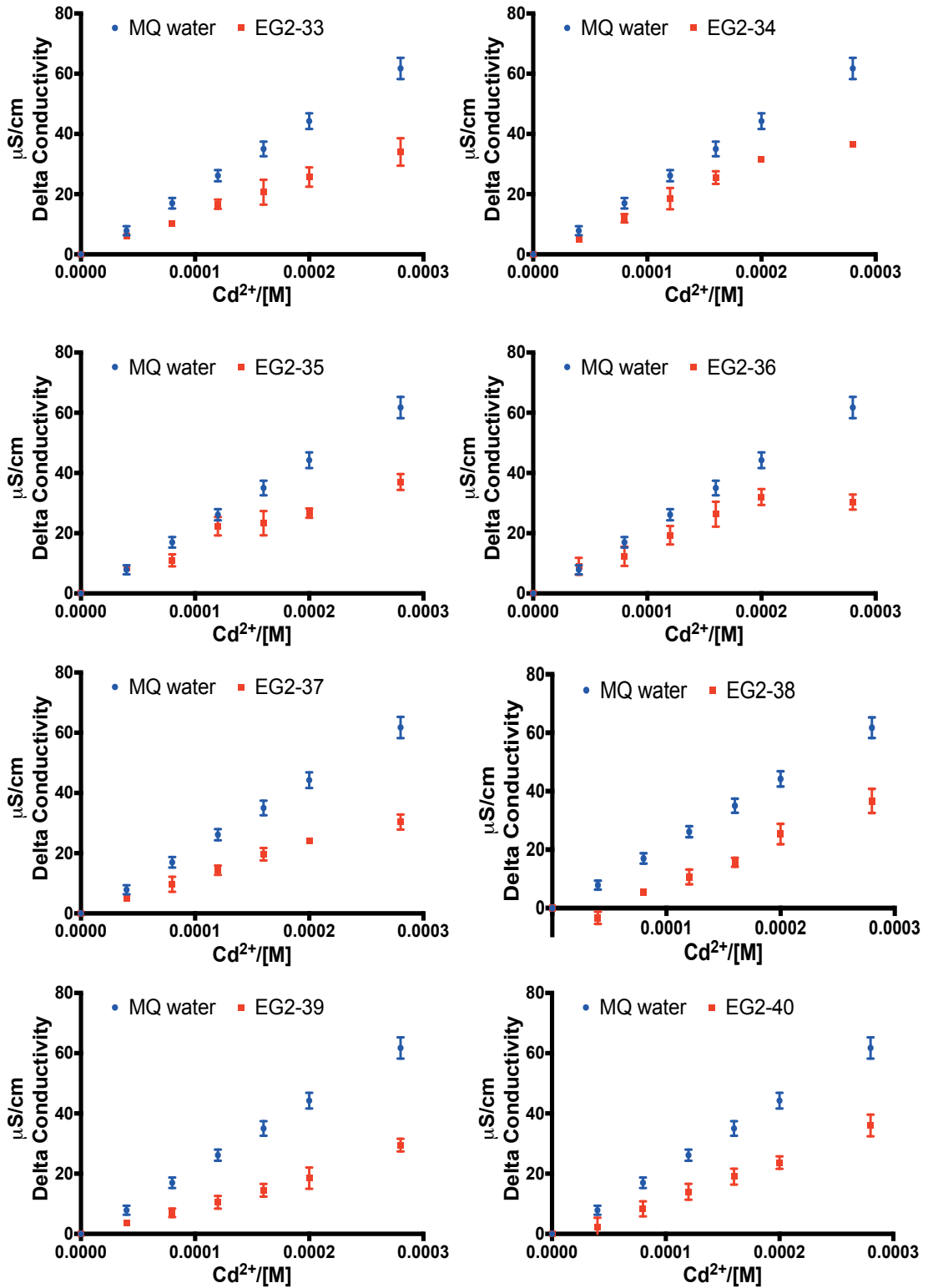


Figure A.30: The results of conductivity tests of EG2-n (n, 33-40) in MQ water.

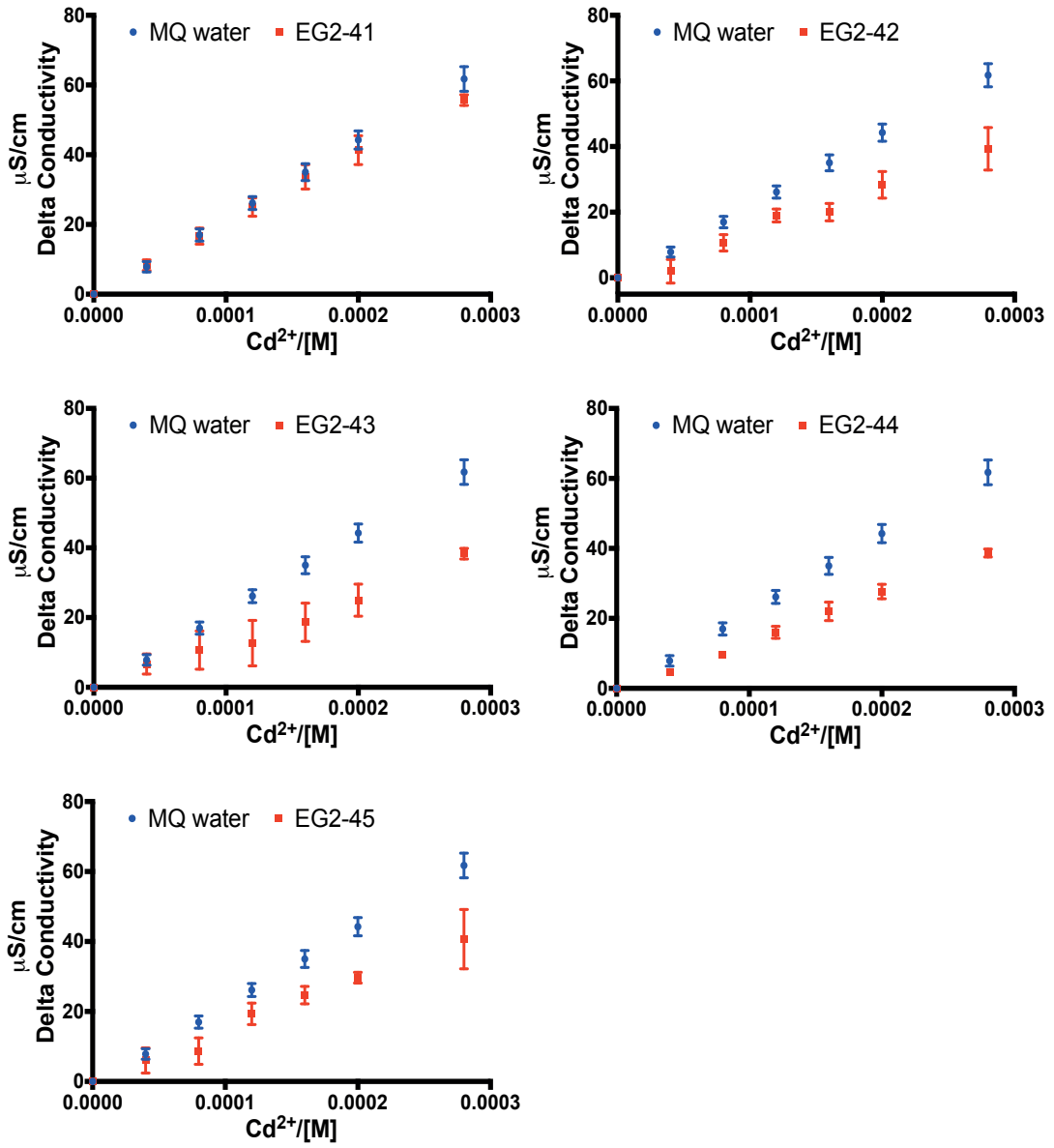


Figure A.31: The results of conductivity tests of EG2-n (n, 41-45) in MQ water.

ELIF ERTEM BEKDEMIR

PERSONAL DATA

Date of Birth: 6th December 1987

Email: elif.ertem@epfl.ch

Mobile: +41 78 8274837

Address: Chemin de Montelly 43A, 1007 Lausanne (CH)



SUMMARY

Graduated chemist with sound specialization on environmental chemistry. Experienced in managing medium to large scale projects as a research partner e.g. Swiss Commission for Technology and Innovation projects, worked closely with large industrial partners (Dentsply, Nestlé Institute of Health Sciences) and proven to be successful in competitive environments with high ranking achievements. Excelled on organic and inorganic nanomaterials synthesis as well as various physico-chemical characterization methods. Fluent in presentation of scientific data and technical communications.

EDUCATION

*Doctor of
Philosophy,
Ph.D.*

2012 – 2017 Material Science and Engineering, School of Engineering, **EPFL**, Lausanne, Switzerland

Advisor: Prof. Francesco Stellacci

Thesis Title: Investigation of key parameters effecting ion capturing abilities of mixed ligand protected gold nanoparticles

*Master of
Science,
M.S.(Magna
Cum Laude)*

2010 – 2012 Department of Materials Science and Nanotechnology, **National Nanotechnology Research Center, Bilkent University**, Ankara, TURKEY

Advisor: Prof. Engin Umut Akkaya

Thesis Title: Near-IR absorbing BODIPY functionalized SPIONs: a potential magnetic nanoplatform for diagnosis and therapy

*Bachelor of
Science, B.S.
(Major)
(Magna Cum
Laude)*

2006 – 2010 Department of Chemistry, Faculty of Arts and Sciences, **Middle East Technical University (METU)**, Ankara, TURKEY

*Bachelor of
Science, B.S.
(Minor)*

2008 – 2010 Environmental Engineering, Faculty of Engineering, **Middle East Technical University (METU)**, Ankara, TURKEY

ACADEMIC AND WORK EXPERIENCES

2012 - present *Research Assistant*, Supramolecular Nano-Materials and Interfaces Laboratory, **EPFL**, Lausanne, Switzerland.

Conducted multiple academic and industrial research projects individually and collaboratively. Specialized on design of nanoparticle-based metal ion sensing systems. Worked closely with International Dentsply Dental company and EMPA for development of silver nanoparticle based novel irrigation systems for root canal therapy.

2013 – 2015 *Teaching Assistant*, Thermodynamics for Material Science, EPFL, Switzerland.

2010 – 2012 *Research Assistant*, Supramolecular Chemistry Research Group, **National Nanotechnology Research center, Bilkent University**, Ankara, TURKEY

Excelled on organic molecules synthesis of highly potent supramolecular agents for photodynamic therapy for skin cancer.

2008- 2010 Undergraduate Research Assistant, Environmental Science Laboratory, **METU**, Ankara, TURKEY

Studied on development and validation of GC-Mass methods for determination of phthalates in milk.

June 2009- September 2009 Summer Internship, Chemical Biology-Inorganic Chemistry Laboratory, **University of Chicago**, Chemistry Department, Gordon Center for Integrative Science, Chicago, USA

Addressed metal-binding properties of Hpn from Helicobacter pylori and implications for therapeutic activity of bismuth under supervision of Prof.Chuan He.

June 2008- August 2008 Summer Internship, Analytical Electrochemistry Laboratory, **Ege University**, Department of Pharmacy, Izmir, TURKEY

Studied general aspects of DNA Biosensors: Carbon graphite electrode-DNA interaction, hybridization and denaturation of DNA.

KEY ACHIEVEMENTS

Publications

Ertem E., Castellnou M., Ong K.Q., Stellacci F., Novel Sensing Strategies based on Monolayer Protected Gold Nanoparticles for the Detection of Metal Ions and Small Molecules, Chem. Rec., 2017, just accepted.

Ertem E., Gutt B., Zuber F., Allegri S., Quay Le B., Mefti S., Stellacci F., Ren Q., Core-shell silver nanoparticles in endodontic disinfection solutions enable long-term antimicrobial effect on oral biofilms, ACS Appl. Mater. Interfaces., 2017, 40, 34762–34772.

Ertem E., Murillo-Cremaes N., Carney R.P., Laromaine A., Roig A., Janec k ER., and Stellacci F. A silica-based magnetic platform decorated with mixed ligand gold nanoparticles: Arecyclable catalyst for esterification reactions, *Chem. Commun.*, 2016, 52, 5573-5576.

Ertem, E.; Bekdemir, A.; Atilgan, A.; Akkaya, E. U. Near-IR absorbing Bodipy functionalized SPIONs: A potential magnetic nanoplatfrom for diagnosis and therapy, *Pure Appl. Chem.* 2014, 86, 899–903.

Cho, E.S., Yokoyama, T., **Ertem, E.**, Stellacci F. Change of luminescence properties of europium ions captured by mixed-ligand silver nanoparticles, *Isr. J. Chem.*, 2014, 54, 708-711.

Wegner, S., **Ertem, E.**, Sunbul M., He, C. Metal-binding properties of Hpn from *Helicobacter pylori* and implications for the therapeutic activity of bismuth, *Chem. Sci.*, 2011, 2, 451-456, Advanced Article.

Conferences

CTI₂₀₁₆ : *Swiss Medtech Day*, Kursaal Bern, Switzerland, 7 June, 2016 (Poster Presentation)

EDMX₂₀₁₅ : *EPFL STI-MX Research Day 2015*, EPFL, SwissTech Convention Center, Switzerland, 23 November 2015 (Poster Presentation)

CTI₂₀₁₅ : *Swiss Medtech Day*, Kursaal Bern, Switzerland, 8 September, 2015 (Poster Presentation)

GRC₂₀₁₄ : *Gordon Research Conference of Noble Metal Nanoparticles*, Mount Holyoke College, South Hadley, USA, 15-20 June 2014

ISMSC₂₀₁₁: *The 6th International Symposium of Macrocyclic and Supramolecular Chemistry*, University of Sussex, Brighton, UK, 3-7 July 2011 (Poster Presentation)

HONORS & AWARDS

The Swiss Federal Commission Scholarships for PhD students, 2012-2017

2010-2012 Awarded Prestigious Scholarship for Master of Science Studies, The Scientific and Technological Research Council of Turkey.

June, 2010- Ranked 2nd in graduation from department of chemistry, METU, Ankara, Turkey

June, 2005- Ranked 1st in graduation from Izmir High School, Izmir, Turkey.

ACTIVITIES AND VOLUNTARY WORK

Active member of the METU Chemistry Student’s Club Science (2008-2010) – Contributed to scientific fairs to raise public appreciation to fundamental sciences.

Member of METU Turkish Classical Music Club (2005 – 2006) – Participated in Turkish Classical Music Choir Activities.

Member of The International Association for the Exchange of Students for Technical Experience (IAESTE) - 2007

Voluntary Tutorship, The Scientific and Technological Research Council of Turkey (TUBİTAK) Summer Science Summer Camp (2008) - Guided 11-12 years old children in science activities and became responsible for nursing of a group of children.

LANGUAGES

Turkish – Native Language

English – Advanced Professional Fluency

French – Beginner (A2 level)

